

NORTHWESTERN UNIVERSITY

Structural Dynamics of Complex Fluids Subjected to Planar Extensional Flow Studied Using *In Situ* X-ray Scattering

A DISSERTATION

SUBMITTED TO THE GRADUATE SCHOOL
IN PARTIAL FULFILLMENT OF THE REQUIREMENTS

for the degree

DOCTOR OF PHILOSOPHY

Field of Chemical and Biological Engineering

By

Binbin Luo

EVANSTON, ILLINOIS

December 2018

© Copyright by Binbin Luo 2018

All Rights Reserved

ABSTRACT

Structural Dynamics of Complex Fluids Subjected to Planar Extensional Flow Studied Using *In Situ* X-ray Scattering

Binbin Luo

Complex fluids are ubiquitous, from natural materials to manufactured products. Understanding their behavior under flow is vital for engineering these materials. Extensional flow, despite being industrially relevant and often producing dominant impacts upon complex fluids, is an underserved topic compared to shear flow due to a lack of reliable apparatuses to apply well-defined extensional flow. The unusual behavior of complex fluids is manifested in the presence of microstructures at a mesoscopic length scale, frequently tens to hundreds of nanometers, where x-ray scattering is a powerful tool. This thesis reports the design and implementation of a high aspect ratio cross-slot flow instrument to facilitate *in situ* synchrotron x-ray scattering of low-to-moderate viscosity complex fluids subjected to planar extensional flow. This instrument is applied to two categories of complex fluids: dilute carbon nanotube suspensions and self-assembled surfactant solutions.

The structural dynamics of dilute carbon nanotube suspensions subjected to both homogeneous shear and planar extensional flow have been studied, under both transient and steady-state flow conditions. The transient dynamics of CNTs in shear follows the classic

behavior expected from Brownian rod-like particles. The relaxation behavior reflects polydispersity of our sample. Under steady-state conditions, planar extension aligns CNTs more effectively than shear flow. The orientation of CNTs can be mostly captured by simulation of orientation in dilute Brownian rods. However, the difference in orientation observed in shear and extension requires that the nanotubes be described with finite aspect ratio due to their bent and crooked shape. Finally, consistency in nanotube orientation measured under shear in the cross-slot flow cell and a dedicated homogeneous shear flow cell validates our design and implementation.

Two types of self-assembled surfactant solutions were studied under planar extensional flow: wormlike micelles and lamellar surfactants. The wormlike micelles exhibit increasing orientation as extensional rate grows for modest flow rates. Beyond a critical rate, viscoelastic flow instabilities set in, which disrupt the intended flow field. Two different lamellar surfactants display different inherent ordering: one exhibits negligible relaxation while the other loses most of its flow-induced orientation, though both align along the flow with little change of anisotropy to different flow rates.

ACKNOWLEDGEMENTS

This work would be impossible without help from many. Here I would like to dedicate my gratitude to a few of them. First of all, I would like to thank Professor Shengchun Zhou of History at Zhejiang University, who urged me to take a chance at a bigger institution. This journey would not happen if it was not for his strong encouragement. I would also like to express my appreciation to all of the professors and teachers I have had in schools in general. It was not until moving out of my home country that I realized that how extraordinary they are for dedicating as much effort and passion to students and teaching as those in private schools despite being paid far less. This generosity cannot be found anywhere else and is the foundation of my academic achievements.

I would also like to thank my committee members: Professor Linda Broadbelt, Professor John Torkelson, and Professor Ken Shull for their feedback. Particularly, I would like to thank Linda, who served as the Department Chair when I entered the program and helped me immensely in multiple ways, financially and academically.

I would like to thank my labmates, Erica and Matt, for being incredibly supportive and the best companions during many beam time experiments and conferences. I also owed a lot to them for numerous inspirational discussions in the office. I have learned a lot from each of them, including the information I need to navigate this society.

The work reported in the thesis could not be carried out without the help from Jeff Sundwall of the machine shop at Northwestern, and Steve Weigand and Denis Keane, of DND-

CAT at the Advanced Photon Source. Thanks to Jeff's patience and expertise, the flow cell used for this work finally became functional after many adjustments. Steve's help was indispensable for not only setting up every single experiment at the beamline, but also providing crucial support in integrating the flow control to x-ray scattering data acquisition at the synchrotron.

I would like to thank my collaborators Giovanniantonio Natale, Professor M. C. Heuzey and Professor P. J. Carreau at Polytechnique Montréal. Chapter 4 is inspired by their work on carbon nanotube suspensions and I am indebted to their generous supply of a range of samples, simulations, and discussions.

I would like to thank my parents, who have not raised an eyebrow with whatever news or decisions I have brought to them. This has allowed me to be completely honest with myself, and hence with others. They have also always encouraged me to formulate my own opinion regardless of others' views as I grew up. Despite the fact that neither of them are related to science in any way, this upbringing benefits me substantially.

Last but most importantly, my advisor, Wes. When I was still an undergraduate researcher and volunteered in a lab, I was rather overwhelmed with pipetting and other wet bench work. Therefore, when it was the moment to choose a lab for graduate studies, I was rather determined to make the most of my last chance of serious education to train my head instead of my hands. Though Wes was not actively recruiting students, I am really grateful that he still allowed me to join. Along this journey, Wes guided me with such patience and encouragements that now I can proudly claim that I am still curious, I am still passionate, and moreover, I have confidence. During the later stage of my graduate studies, I experienced a desperate identity

crisis. If it was not Wes' support of many years, I would not have ended up back on my feet. For that, I am forever grateful in this life.

LIST OF ABBREVIATIONS

SAXS – small-angle x-ray scattering

WAXD – wide-angle x-ray diffraction

CNTs – carbon nanotubes

MWCNT – multi-walled carbon nanotube

WLM – wormlike micelle

CTAB – cetyltrimethylammonium bromide

NaSal – sodium salicylate

CTAC - cetyltrimethylammonium chloride

DDAB – didodecyldimethylammonium bromide

CPyCl – cetylpyridinium chloride

SDS – sodium dodecyl sulfate

LVE – linear viscoelasticity

FT-IR – Fourier-transform infrared spectroscopy

iPP – isotactic polypropylene

PE – polyethylene

PB-1 – poly-1-butene

TABLE OF CONTENTS

ABSTRACT	3
ACKNOWLEDGEMENTS	5
LIST OF ABBREVIATIONS	8
LIST OF FIGURES	13
Chapter 1 Introduction	22
1.1 General introduction	22
1.2 Definition of flow fields and flow devices	24
<i>1.2.1 Shear flow</i>	24
<i>1.2.2 Extensional flow</i>	27
1.3 Techniques for probing microstructures of complex fluids	33
Chapter 2 Flow Devices for Applying Planar Extensional and Homogeneous Shear Flow to Low-Viscosity Fluids	36
2.1 High-aspect ratio cross-slot flow cell for applying planar extensional flow	36
<i>2.1.1 Background</i>	36
<i>2.1.2 Constructing a high-aspect-ratio cross-slot flow cell</i>	40
<i>2.1.3 Filling the flow cell</i>	46
<i>2.1.4 Flow cell operation</i>	49
<i>2.1.5 Integration with beamline systems</i>	52

	10
2.2 Cone and plate annular shear cell	57
2.2.1 <i>Shear cell geometry</i>	57
2.2.2 <i>Coordination of shear flow control with data acquisition</i>	59
Chapter 3 X-ray Scattering, Synchrotron Facility and Data Analysis	62
3.1 X-ray scattering basics	62
3.2 Synchrotron facility	69
3.3 Quantitative analysis of scattering patterns	75
3.4 Two-dimensional scattering pattern analysis	84
Chapter 4 Structural Dynamics of Carbon Nanotube Suspension under Homogeneous Shear and Planar Extensional Flow	90
4.1 Background	90
4.1.1 <i>Introduction</i>	90
4.1.2 <i>Relaxation in Brownian systems</i>	92
4.2 Materials	93
4.3 Methods	95
4.4 Results and discussion	101
4.4.1 <i>Structural dynamics of 0.05 wt% dilute CNT suspension in EPON 828 during shear flow inception, reversal and relaxation</i>	101
4.4.2 <i>Spatial distribution of orientation of 0.05 wt% CNT suspension in EPON 828 measured in cross-slot flow</i>	109

	11
4.4.3 Steady-state behavior of 0.05 wt % CNT suspension in EPON 828.....	113
4.4.4 Modeling of transient and steady-state orientation dynamics of rigid rods.....	121
4.4.5 Suspensions in low-viscosity matrix	130
4.4.6 The state of dispersion reflected by the absolute scattering intensity as a function of scattering vector q	136
4.5 Conclusion.....	138
Chapter 5 Structural Dynamics of Self-assembled Surfactants in Planar Extensional Flow	140
5.1 Wormlike-micelle solution.....	140
5.1.1 Introduction	140
5.1.2 Material and methods.....	146
5.1.3 Structural dynamics of WLMs in cross-slot flow.....	152
5.2 Lamellar surfactants.....	170
5.2.1 CTAC/Pentanol/ Water.....	171
5.2.2 Aqueous DDAB.....	180
5.3 Summary	188
Chapter 6 Conclusions and Future Directions.....	189
Appendix A (Previous Research): <i>In situ</i> SAXS/WAXD studies of shear-induced crystallization of poly(1-butene) in shear flow	197
A1. Introduction	197

	12
A2. SAXS/WAXD data analysis background	203
<i>A2.1 Kinetics of Crystallization</i>	204
<i>A2.2 Orientation of microstructures</i>	206
A3. Experimental methods	209
<i>A3.1 Materials</i>	209
<i>A3.2 Shear flow device</i>	210
<i>A3.3 Temperature and flow protocols</i>	211
<i>A3.4 Synchrotron x-ray scattering</i>	212
<i>A3.5 X-ray scattering data analysis</i>	214
<i>A3.6 Turbidiy measurements</i>	223
<i>A3.7 Linear viscoelasticity</i>	223
A4 Results and discussion	224
<i>A4.1 X-ray scattering results and discussion</i>	224
<i>A4.2 Turbidity measurements versus x-ray scattering</i>	230
<i>A4.3 Linear viscoelasticity versus x-ray scattering</i>	232
A5 Conclusions	235
Appendix B: Quantitative Impact from Isotropic Background Scattering and Correction	236
Reference	243

LIST OF FIGURES

Figure 1.1 Schematic illustration of shear flow and the deformation	25
Figure 1.2 Shear rheometry often uses (a) cone and plate (b) Couette cell (c) parallel plate (d) press-driven (slit) flow	26
Figure 1.3 Illustration of (a) uniaxial extension (b) equibiaxial extension (c) planar extension	28
Figure 1.4 An illustration of ideal two-dimensional cross-slot flow, producing planar extensional flow at the stagnation point	32
Figure 2.1 A schematic illustration of velocity profile for a high aspect-ratio cell (a) versus a low aspect-ratio flow cell (b)	37
Figure 2.2 (a) An improved cross-slot shape based on numerical simulation of upper-convected Maxwell fluids at $De = 4$ (figure reprinted from [103]) (b) Strain rate field of numerically simulated Newtonian creeping flow in the optimized cross-slot geometry (figure reprinted from [104])	39
Figure 2.3 Overview of cross-slot flow system	41
Figure 2.4 Cross-slot flow cell design. (a) cross-slot flow cell body with four ports; (b) the cross-slot flow cell “sandwich” sealed by Kapton® windows and brass plates	42
Figure 2.5 Illustration of how to fill a syringe with sample	47
Figure 2.6 Installation of the cross-slot flow cell and syringe pump in the beam line station	51
Figure 2.7 An illustration of a typical set of positions used in “mapping” experiments, used to study microstructure at different locations within the cross-slot flow cell	52
Figure 2.8 The beam path for the 1-2 plane annular cone and plate shear cell	57
Figure 2.9 X-ray beam travelling perpendicular to 1-2 plane of shear flow	58
Figure 2.10 (a) The DAC1-5 signal measured from all frames collected during an experimental run. These data allow determination of exactly when flow is turned on and off, and the associated shear rate. (b) Calibration curve for shear rate based on measured counts from DAC1-5 channel	61
Figure 3.1 An illustration of Bragg’s law	64

- Figure 3.2** (a) An illustration of scattering from two electrons (b) definition of incident and scattered wave vectors, and the scattering vector q **65**
- Figure 3.3** Demonstration of the Ewald sphere, demonstrating how reciprocal space is probed in x-ray scattering experiments **69**
- Figure 3.4** Small-, medium-, and wide-angle x-ray scattering detectors setup at Station 5ID-D of Sector 5, DND-CAT **70**
- Figure 3.5** Sample scattering patterns of several complex fluids systems: (a) and (b) for lamellar surfactants, (c) for wormlike micelles solution (d) for dilute carbon nanotube suspension. **74**
- Figure 3.6** Scattering patterns from different anisotropic microstructures (a) rods (b) lamellar stacking **78**
- Figure 3.7** Selecting a q range on the scattering pattern for quantitative analysis. (a) 60 mM CTAB with 350 mM NaSal wormlike micelle solution (b) 0.05 wt% CNT suspension in EPON828 scattering under shear flow on SAXS detector (c) 17.4 wt% CTAC/ 20.0 wt% pentanol/ 62.6 wt% water lamellar surfactant (d) 60 mM DDAB lamellar surfactant. (a) and (c) are patched images obtained by rotating the MAXS pattern through 180°. **79**
- Figure 3.8** An illustration of sub-image of the 2-dimensional scattering pattern for quantitative analysis **86**
- Figure 4.1** a TEM micrograph of 3 wt% CNT suspension (figure reprinted from [66]). The CNTs are long tubes with varying lengths and curvature or bending present. **94**
- Figure 4.2** Time evolution of anisotropy factor measured in 0.05 wt% CNT suspension in EPON 828 using SAXS, subjected to a shear rate of 0.25 s⁻¹. Flow direction is reversed at $t = 130$ second. Data collected at an exposure time of 0.4 second and a frequency of 1 frame/second during experiments conducted in March 2015. **97**
- Figure 4.3** Representative SAXS patterns measured in 0.05 wt% CNT suspension in EPON 828 under flow (a) Homogeneous shear at different rates; (b) Shearing in opposite directions, and then after relaxation; (c) Planar extension along vertical direction at different rates; (d) Planar extension along horizontal direction at different rates **99**
- Figure 4.4** Transient evolution of AF and χ measured in 0.05 wt% CNT suspension in EPON 828 during shear flow inception at various shear rates, plotted against both time and strain. **101**

- Figure 4.5** Transient evolution of the components of the second moment tensor, AF and orientation angle measured in 0.05 wt% CNT suspension in EPON 828, during shear reversal experiments. **103**
- Figure 4.6** Representative data for anisotropy factor and orientation angle measured in 0.05 wt% CNT suspension in EPON 828 upon cessation of shear flow at a rate of 1.6 s^{-1} . Solid curve indicates stretched exponential fit of the data (Equation 4.6) **105**
- Figure 4.7** Fitting parameters α (a) and β (b), and the average relaxation time (c) and rotational diffusivity (d) determined from SAXS measurements on 0.05 wt% CNT suspension in EPON 828 **106**
- Figure 4.8** Relaxation of orientation angle data upon shear flow cessation at 0.04 and 0.25 s^{-1} , measured in 0.05 wt% CNT suspension in EPON 828 **108**
- Figure 4.9** The degree and direction of orientation measured via SAXS in a 0.05 wt% CNT suspension in EPON 828 subjected to (a) no flow (b) planar extension along horizontal direction, and (c) planar extension along vertical direction **111**
- Figure 4.10** Evolution of simplified AF in 0.05 wt% CNT suspension in EPON 828, measured along the centerline of cross-slot flow. The origin is defined at the stagnation point. Negative positions correspond to distance upstream of the stagnation point, while positive positions are measured downstream of the stagnation point. (a) Stretching along horizontal direction, denoted by positive nominal extensional rates. (b) Stretching along vertical direction, denoted by negative nominal extensional rates. **112**
- Figure 4.11** Steady state anisotropy factor and orientation angle measured in 0.05 wt% CNT suspension in EPON 828 in both homogeneous shear and planar extension. Different symbols in the shear flow data represent repeated measurements with different sample loadings. **115**
- Figure 4.12** (a) Schematic of parabolic Poiseuille velocity profile expected in fully-developed slit flow upstream of the slot intersection. (b) Specific locations at which x-ray data collected in cross-slot flow are used to extract steady shear flow measurement of anisotropy and orientation angle **117**
- Figure 4.13** Shear flow-induced anisotropy factor (a) and orientation angle (b) in 0.05 wt% CNT suspension in EPON 828, measured in homogenous shear (open symbols) and in the upstream channels of the cross-slot flow cell (filled symbols) **118**
- Figure 4.14** Comparison of (a) degree of orientation, and (b) orientation angle measured in dilute CNT suspensions in EPON 828, using SAXS (black) and optical dichroism (red) (dichroism data extracted from [66]) **120**

Figure 4.15 Transient anisotropy factor (<i>a</i>) and orientation angle (<i>b</i>) data measured upon flow inception of 0.05 wt% CNT suspension in EPON 828. Solid lines represent predictions of a rigid rod orientation model, with <i>AF</i> values scaled by a factor of 0.1.	123
Figure 4.16 Modeling of rigid rods dynamics in steady-state shear or planar extension (curves) compared with experimental data (symbols) for 0.05 wt% CNT suspension in EPON 828 (<i>a</i>) anisotropy factors, the model <i>AF</i> for planar extension is scaled by 0.15 and the model <i>AF</i> for steady shear is scaled by 0.1 (<i>b</i>) orientation angle in shear	124
Figure 4.17 Tumbling motion of finite aspect-ratio particle	126
Figure 4.18 Simulated anisotropy factor of particles with changing particle aspect ratios in steady shear and planar extension	127
Figure 4.19 (<i>a</i>) Modeling rigid rods dynamics with an aspect ratio of $\lambda = 0.9$ (solid curves) plotted with experimental data (symbols) obtained from 0.05 wt% CNT suspension in EPON 828; Model <i>AF</i> in both planar extensional and shear flow is scaled by 0.15; (<i>b</i>) Model orientation angle in shear	129
Figure 4.20 Schematic scattering patterns for perfectly aligned straight rods versus oriented but bent and crooked tubes	130
Figure 4.21 Steady-state anisotropy factor (<i>a</i>) and orientation angle (<i>b</i>) measured in 0.05 wt% CNT suspension in EPON 815c	132
Figure 4.22 Anisotropy factor of CNT suspended in EPON 828 and EPON 815c subjected to homogeneous shear (<i>a</i>) and planar extension (<i>b</i>) scaled to Peclet number using rotational diffusivity	134
Figure 4.23 0.05 wt% (dilute) and 0.17 wt% (semi-dilute) CNT suspension in EPON 815c, subjected to planar extension	135
Figure 4.24 Scattered intensity of 0.05 wt% CNT suspension in EPON 828 versus scattering vector q (\AA^{-1}) in (<i>a</i>) homogeneous shear and (<i>b</i>) planar extensional flow	138
Figure 5.1 Small-amplitude oscillatory shear and steady shear viscosity for wormlike micelle solution 60 mM CTAB /350 mM NaSal measured at 25 °C	147
Figure 5.2 Representative medium-angle scattering pattern measured on the 60 mM CTAB/ 350 mM NaSal WLM solution.	149
Figure 5.3 A 2- <i>d</i> scattering pattern collected with an empty cell	151
Figure 5.4 A sample background correction for scattering data on the medium angle detector.	152

Figure 5.5 Vector plot representing anisotropy factor and orientation angle throughout the cross-slot flow cell, for 60 mM CTAB/ 350 mM NaSal solution subjected to a flow rate of 0.283 ml/min (Nominal Wi : 0.293)	153
Figure 5.6 Vector plot representing anisotropy factor and orientation angle throughout the cross-slot flow cell, for 60 mM CTAB/350 mM NaSal solution subjected to a flow rate of 0.712 ml/min (Nominal Wi : 0.736)	154
Figure 5.7 Vector plot representing anisotropy factor and orientation angle throughout the cross-slot flow cell, for 60 mM CTAB/350 mM NaSal solution subjected to a flow rate of 1.78 ml/min (Nominal Wi : 1.84)	154
Figure 5.8 Vector plot representing anisotropy factor and orientation angle throughout the cross-slot flow cell, for 60 mM CTAB/350 mM NaSal solution subjected to a flow rate of 4.49 ml/min (Nominal Wi : 4.64)	155
Figure 5.9 An illustration of bifurcation, incoming wormlike micelle solution unevenly splitting to the outgoing channels	157
Figure 5.10 Anisotropy factor data measured along (a) extension axis x and (b) compression axis y for 60mM CTAB/ 350 mM NaSal solution in cross-slot flow	163
Figure 5.11 Anisotropy factor data measured along (a) extension axis x and (b) compression axis y for 60mM CTAB/ 350 mM NaSal solution in cross-slot flow	164
Figure 5.12 Anisotropy factor data measured along (a) extension axis x and (b) compression axis y for 60mM CTAB/ 350 mM NaSal solution in cross-slot flow	165
Figure 5.13 Anisotropy factors and orientation angles of WLMs at stagnation point as a function of nominal Weissenberg number.	167
Figure 5.14 AF measured in upstream slots and at stagnation point of cross-slot flow cell	169
Figure 5.15 Shear rheology of CTAC/Pentanol/Water lamellar surfactant solution in (a) small-amplitude oscillatory shear, and (b) steady shear	173
Figure 5.16 Representative scattering patterns from CTAC/Pentanol/Water solution at two locations in the cross-slot flow cell, during flow at a nominal extension rate of 1 s^{-1}	174
Figure 5.17 Vector plots representing orientation state measured in lamellar surfactant CTAC/Pentanol/Water in cross-slot flow at nominal extensional rates of (a) 0.01, (b) 0.1, and (c) 1 s^{-1}	176

- Figure 5.18** Distribution of simplified $AF \langle q_y q_y \rangle - \langle q_x q_x \rangle$ measured in CTAC/Pentanol/Water along the vertical centerline axis of cross-slot flow cell ($x = 0$) at indicated nominal extension rates **177**
- Figure 5.19** Steady-state anisotropy factor measured in CTAC/Pentanol/Water at stagnation point in cross-slot flow, as a function of nominal extension rate. **178**
- Figure 5.20** Relaxation of lamellar orientation in CTAC/Pentanol/Water measured at stagnation point of cross-slot flow cell, after cessation of planar extensional flow at a nominal extension rate of 1.0 s^{-1} . (a) Series of azimuthal intensity scans measured at time intervals of 41 seconds. (b) AF vs time. **179**
- Figure 5.21** Shear rheology of aqueous DDAB lamellar surfactant solution in (a) small-amplitude oscillatory shear, and (b) steady shear flow **181**
- Figure 5.22** Representative scattering patterns from 60 mM DDAB solution, measured at the stagnation point in cross-slot flow at a nominal extension rate of 3.33 s^{-1} . Flow direction is indicated **182**
- Figure 5.23** Vector plots representing orientation state measured in aqueous DDAB in cross-slot flow at a nominal extensional rate of 0.1 s^{-1} . (a) extension along horizontal axis; (b) extension along vertical axis. **185**
- Figure 5.24** Steady-state (a) anisotropy factor and (b) orientation angle measured in 60 mM DDAB at stagnation point in cross-slot flow, as a function of nominal extension rate. **186**
- Figure 5.25** Relaxation of AF in the 60 mM DDAB solution fitted to a single-mode exponential decay **187**
- Figure A1** (a) An schematic illustration of chains folding into lamellae, which further piled to formulate the spherulite (figure reprinted from [205]) (b) spherulites from peptide crystallization visualized by polarized light microscopy (figure reprinted from [206]) **198**
- Figure A2** An illustrations of crystalline (blue) and amorphous phases in semi-crystalline polymer (figure reprinted from [208]) **199**
- Figure A3** “Shish-kebab” morphology of semi-crystalline polymers (a) a schematic illustration (figure reprinted from [211]) (b) an SEM image of shish-kebab crystallites of ultrahigh-molecular-weight polyethylene (figure reprinted from [212]) **199**
- Figure A4** Illustrations of (a) lamellae and its scattering (SAXS); (b) unit cell and its x-ray scattering (WAXD) **201**

- Figure A5** A sequence of SAXS patterns collected during shear-induced crystallization, subjected to a shear rate of 4 s^{-1} and a strain of 12, at (a) $t = 0$ min (at the time when flow was applied) (b) $t = 20$ min (c) $t = 40$ min **204**
- Figure A6** A sequence of WAXD patterns collected during shear-induced crystallization, subjected to a shear rate of 4 s^{-1} and a strain of 12, at (a) $t = 0$ min (at the time when flow was applied) (b) $t = 20$ min (c) $t = 40$ min **206**
- Figure A7** (a) scattering of lamellae perfectly aligned perpendicular to the flow axis versus uniaxially symmetrically aligned with a tilted angle β (b) scattering of unit cells perfectly aligned along the flow axis versus uniaxially symmetrically aligned with a tilted angle β (figure adapted from [239]) **207**
- Figure A8** G' (filled) and G'' (open) of PB 0300M, measured at 135, 150, 165, and 180 °C, shifted to a reference temperature at 135 °C **209**
- Figure A9** (a) the Linkam CSS-450 high temperature shearing stage (b) an illustration of the beam path through parallel-plate geometry of the shearing stage (c) an illustration of beam path in the shear flow field **210**
- Figure A10** Temperature and flow protocol **211**
- Figure A11** An illustration of the grid for extracting the intensity profile as a function of scattering angle and azimuthal angle with respect to the flow axis (a) on SAXS patterns (b) on WAXD patterns **213**
- Figure A12** An illustration of calculation of lamellae growth induced by shear flow at a rate of 4 s^{-1} and a strain of 12 units, collected at $t = 0$ (black), 4 (red), 12 (blue), 20 (magenta), 40 (olive) min (a) the azimuthally integrated intensity as crystallization progresses (b) subtracted intensity profile using the intensity profile while flow was applied as the background **216**
- Figure A13** WAXD intensity as a function of q measured perpendicular to the flow direction **217**
- Figure A14** A demonstration of the calculation of integrated peak area, for the experiment when flow was applied at a shear rate of 4 s^{-1} and a strain of 12 units, intensity collected at $t = 40$ min **218**
- Figure A15** WAXD integrated peak area as a function of ϕ , the corrected azimuthal angle according to the curvature of Ewald sphere, collected in the experiment where flow was at a shear rate of 4 s^{-1} and a strain of 12 units, collected at $t = 0$ (black), 4 (red), 12 (blue), 20 (magenta), 40 (olive) min **219**

- Figure A16** WAXD integrated peak area fitted to a double Gaussian function, collected in the experiment of a shear rate of 4 s^{-1} and a strain of 12 units, collected at $t = 0$ (black), 4 (red), 12 (blue), 20 (magenta), 40 (olive) min **220**
- Figure A17** (a) $I(\varphi)$ obtained by integrated $I(q, \varphi)$ over the q range of 0.00819 \AA^{-1} and 0.0143 \AA^{-1} (b) background subtracted $I_{SAXS}(\varphi)$ using $I_{flow}(\varphi)$, integrated from the scattering pattern subjected to a shear rate of 4 s^{-1} and a strain of 12 units, collected at $t = 0$ (black), 4 (red), 12 (blue), 20 (magenta), 40 (olive) min **221**
- Figure A18** Setup for turbidity measurements of shear-induced crystallization **223**
- Figure A19** Kinetics for shear-induced crystallization with the shear rate fixed at 4 s^{-1} and the applied strain is varied at 4 (black), 8 (red), and 12 (blue) units (a) the evolution of SAXS invariant, indicative of lamellae growth (b) the growth of WAXD integrated peak area, representative of unit cell growth (c) scaled SAXS invariant Q (open) plotted together with WAXD integrated peak area A (filled) **225**
- Figure A20** Evolution of Hermans' orientation parameter for (a) lamellae (b) unit cells (c) both structural features with unit cell (filled) and lamellae (open) when the shear rate is fixed at 4 s^{-1} and the applied is varied at 4 (black), 8 (red), and 12 (blue) units **227**
- Figure A21** Kinetics for shear-induced crystallization with flow of a fixed strain and varying shear rates at 1 (black), 2 (red), and 4 (blue) s^{-1} (a) the evolution of SAXS invariant, indicative of lamellae growth (b) the growth of WAXD integrated peak area, representative of unit cell growth (c) scaled SAXS invariant Q (open) plotted together with WAXD integrated peak area A (filled) **228**
- Figure A22** Hermans' orientation parameters (a) lamellae (b) unit cells (c) both lamellae (open) and unit cells (filled) for shear-induced crystallization when the applied strain is fixed at 12 units and the shear rate is varied at 1 (black), 2 (red), and 4 (blue) s^{-1} **229**
- Figure A23** Quiescent crystallization from PB-1 melt (black) as well as shear-induced crystallization at a fixed strain of 8 units and shear rates are varied from 0.5 (red), 1 (green), 4 (blue), and 8 (magenta) s^{-1} , measured using (a) WAXD integrated peak area A (filled) and scaled SAXS invariant Q (open) (b) turbidity **231**
- Figure A24** Kinetics of shear-induced crystallization under a strain of 12 units and shear rates of 1 (black), 2 (red), and 4 (blue) s^{-1} measured using (a) WAXD integrated peak area A (filled) and scaled SAXS invariant Q (open) (b) small-amplitude oscillatory shear **233**

Figure A25 Kinetics of shear-induced crystallization under a shear rate of 4 s^{-1} and varied strain of 4 (black), 8 (red), and 12 (blue) units, measured using (a) WAXD integrated peak area A (filled) and scaled SAXS invariant Q (open) (b) small-amplitude oscillatory shear **234**

Chapter 1 Introduction

This thesis reports on the design, implementation and application of an instrument to facilitate x-ray scattering of low-to-moderate viscosity complex fluids subjected to planar extensional flow. This chapter lays out a general motivation for the work in this thesis and presents technical details regarding the exact definitions of flow fields relevant to this work. Flow devices are discussed, and a number of structural probes available for studying complex fluids are compared and contrasted.

1.1 General introduction

Complex fluids are ubiquitous in the natural environment. For example, almost all biological and geological fluids are suspensions — blood, cytoplasm, mucus, and mud. Complex fluids are also extensively found in numerous consumer products and industrial applications, such as paints, cosmetics, detergents, food additives, lubricants, and drag-reducing agents. The behavior of complex fluids under flow is vital for understanding these materials and their functions, and hence crucial for engineering these products and developing new applications. For these reasons, rheology, the study of flow and deformation of matter, with an emphasis on non-Newtonian fluids, has been a keen interest of industry and academia.

In the field of rheology, extensional flow is a traditionally underserved topic compared to shear flow, which is studied abundantly due to easy access to shear rheometry. Contrasts between extensional versus shear flow were first drawn by Trouton,¹ who discovered the ratio of uniaxial extensional viscosity over shear viscosity is 3 for Newtonian fluids. The practical

significance of extensional flow was recognized with the emergence of polymer processing, as extensional rheology plays a decisive role in the fiber spinning process of polymer melts and solutions. Later, its relevance was again highlighted as polymer or surfactant solutions found use as drag-reducing agents. Apart from the frequent presence of extensional flow in industrial processes, it has been found that when both shear and extensional kinematics are present, the extensional flow normally has the dominant influence.² In addition, for non-Newtonian fluids, the behavior in extensional flow cannot be predicted from their behavior in shear.^{2,3} Since Trouton, numerous efforts have been made to characterize the extensional rheology of various samples – polymer melts⁴⁻⁸ and solutions,^{9,10} surfactant solutions,¹¹⁻¹⁴ and suspensions.¹⁵⁻¹⁷

The unusual rheological behavior exhibited by complex fluids usually results from the presence of microstructures at a mesoscopic length scale, intermediate between molecular and macroscopic dimensions.¹⁸ For example, the persistence length of wormlike micelles, the end-to-end distance of polymer chains, the interlayer spacing of lamellar surfactant solutions, the dimensions of carbon nanotubes (radius or length) in suspensions, the dimension of a separated microphase in block copolymers, *etc.* These microstructures are often on the order of tens to hundreds of nanometers. Understanding these microstructures and their responses to flow and deformation, especially to extensional flow, is key to unraveling the macroscopic rheological behavior of complex fluids and understanding their role in practical applications.

Ideally, constitutive equations grounded in realistic descriptions of fluid microstructure would be the ultimate tool to predict non-Newtonian flow phenomena. However, given the range of behavior exhibited by complex fluids when subjected to extensional flow and the challenge of producing well-defined extensional flow, such theories or modelling approaches have only been

developed for restricted categories of fluids, such as dilute solutions of flexible polymers. To address the challenges of other classes of fluids, a worthy goal is to expand capabilities for *in situ* structural studies in extensional flow, as this information will contribute in either facilitating development of theories or constitutive equations for the scientific community, or in elucidating the phenomena that underlie complex fluids' industrial applications.

1.2 Definition of flow fields and flow devices

Shear has been the predominant type of flow studied in rheology. Extensional flow, on the other hand, is much less researched despite its scientific complexity and practical importance, due to difficulties in experimental realization. Given the contrast in behavior of complex fluids in shear versus extensional flow, fluids should ideally be studied using both types of flow fields where possible. In this section, shear and extensional flows will be defined, and their main characteristics discussed, together with a historical account of extensional flow devices.

1.2.1 Shear flow

In simple shear, material planes slide over one another (Figure 1.1). Kinematic analyses of shear flow show a balance between deformation and solid body rotation (due to the presence of vorticity). Material elements are stretched linearly with time, on average. Polymer molecules in shear flow are both stretched and rotated. With increasing flow strength, molecules increasingly align along the flow direction. In other classes of materials, the rotational character of shear leads to “tumbling” motion, first described by Jeffery¹⁹ for elongated particles of finite aspect ratio. Certain classes of liquid crystalline materials also exhibit tumbling in shear.^{20–22}

The formal definition of simple shear flow is:

$$\begin{aligned} v_1 &= \dot{\gamma}x_2 \\ v_2 &= v_3 = 0 \end{aligned} \quad (1.1)$$

Here “1” is the flow direction, “2” is the gradient direction, and “3” is the vorticity direction, and $\dot{\gamma}$ is the shear rate. Most rheological characterization is reported in terms of shear material functions, which describe the stresses produced in materials subjected to steady or time-dependent shear flow. These include steady shear viscosity, transient shear viscosity, stress relaxation after steady shear or step strain, and storage and loss moduli to characterize the viscoelastic response to small-amplitude oscillatory shear.

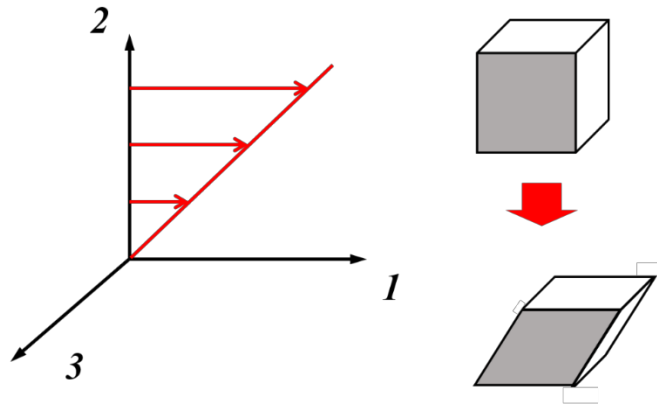


Figure 1.1 Schematic illustration of shear flow and the deformation

Numerous flow geometries are used to produce shear flow (Figure 1.2). Rotational rheometers frequently employ cone and plate, Couette, and parallel plate flows, in which motors control shear rate by varying rotation rate, while torque transducers allow measurement of the resulting stress. Cone and plate geometries are particularly useful in that, for small cone angles, the flow is “homogeneous”, meaning that the shear rate is uniform throughout the device.

However, the circular streamlines make cone-and-plate flow susceptible to flow instabilities (such as edge fracture and secondary flows) in highly elastic samples.

Fully-developed pressure-driven flow in a slit (Figure 1.2 *d*) is an example of an “inhomogeneous” flow in which shear rate and shear stress vary with position. Specifically, the shear stress is a linear function with respect to the distance away from the center of the slit:

$$\tau_{21} = \frac{x_2}{H} \tau_{wall} \quad (1.2)$$

For a Newtonian fluid, the linear relationship between shear stress and velocity gradient leads to the familiar parabolic velocity profile. For non-Newtonian fluids, more complex velocity profiles

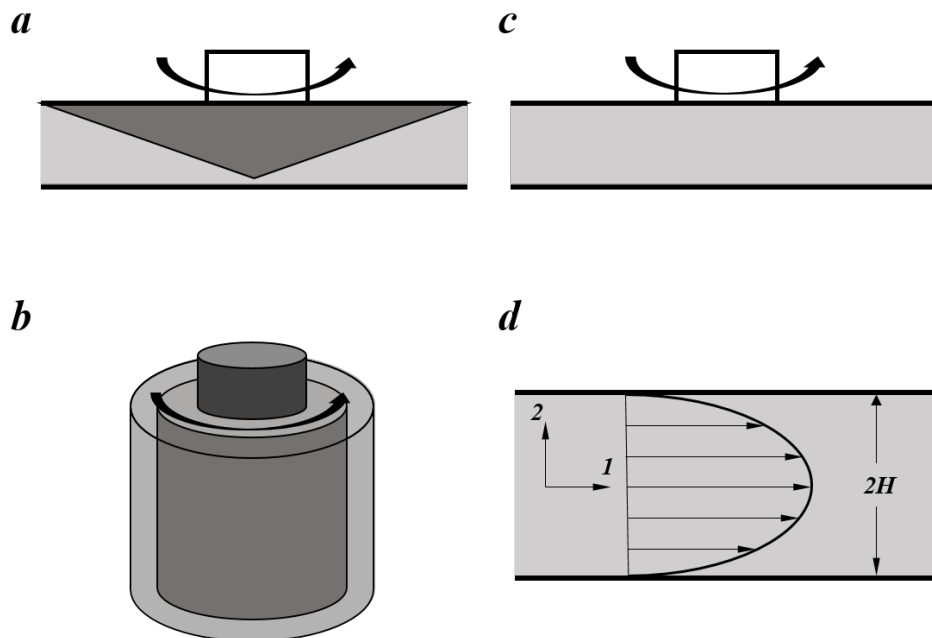


Figure 1.2 Shear rheometry often uses (a) cone and plate (b) Couette cell (c) parallel plate (d) press-driven (slit) flow

are found, although strategies exist for extracting viscosity from measurement of pressure drop versus volumetric flow rate.²³

1.2.2 Extensional flow

The most notable distinction between extensional and shear flow is the direction of velocity gradients relative to flow. In shear, velocity changes *transverse* to the flow direction, while in extension, velocity changes *along* the flow direction. Several particular forms of extensional flow are most frequently considered. *Uniaxial* extensional flow is defined as:

$$\begin{aligned}v_1 &= \dot{\epsilon}x_1 \\v_2 &= -\frac{\dot{\epsilon}}{2}x_2 \\v_3 &= -\frac{\dot{\epsilon}}{2}x_3\end{aligned}\tag{1.3}$$

and is characterized by stretching along the 1-axis and compression along the 2- and 3-axes (Figure 1.3 a). *Equibiaxial* extension is defined as:

$$\begin{aligned}v_1 &= \dot{\epsilon}x_1 \\v_2 &= \dot{\epsilon}x_2 \\v_3 &= -2\dot{\epsilon}x_3\end{aligned}\tag{1.4}$$

and is characterized by compression along 3-axis and stretching along 1- and 2-axes (Figure 1.3 b). Both of these flows are three dimensional. *Planar* extension is a two-dimensional extensional flow:

$$\begin{aligned}v_1 &= \dot{\epsilon}x_1 \\v_2 &= -\dot{\epsilon}x_2 \\v_3 &= 0\end{aligned}\tag{1.5}$$

in which fluid is stretched along the 1-axis, compressed along the 2-axis, and nothing happens along the 3-axis (Figure 1.3 *c*).

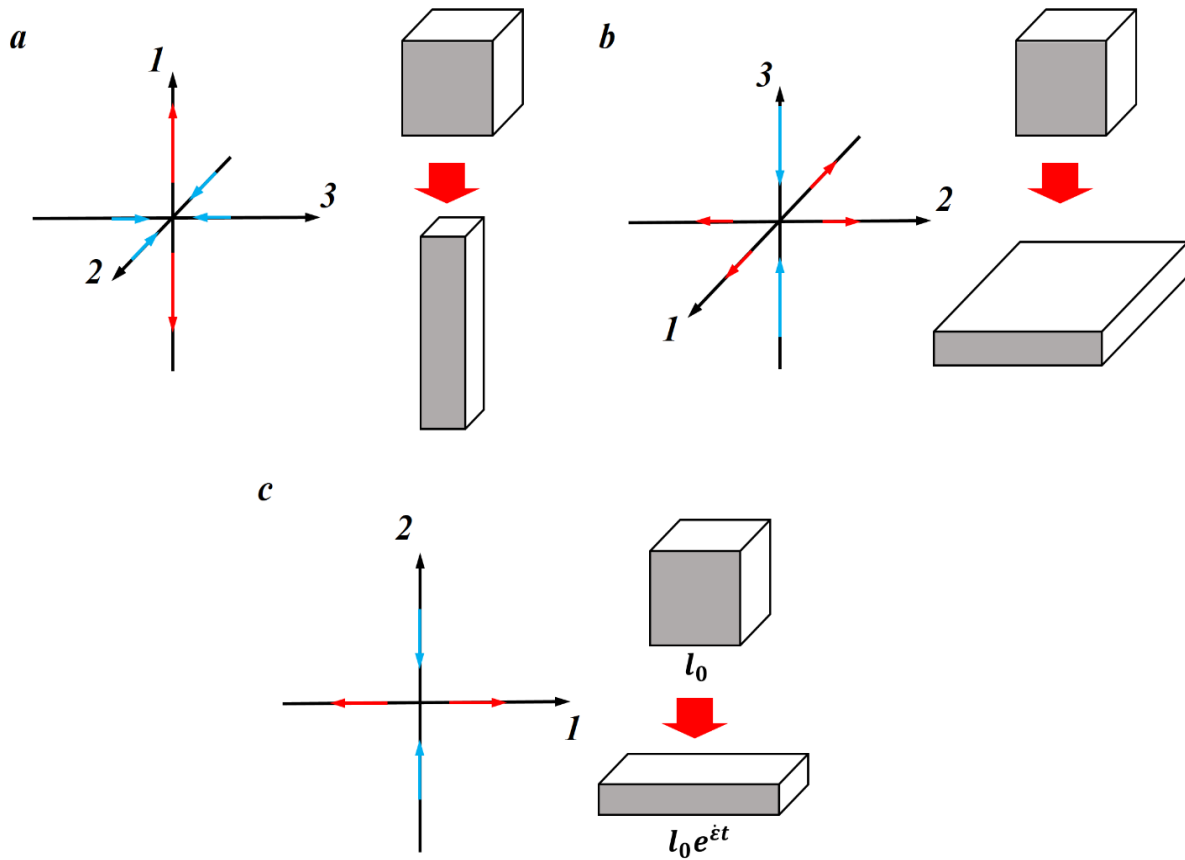


Figure 1.3 Illustration of (a) uniaxial extension (b) equibiaxial extension (c) planar extension

Unlike shear flow, extensional flows have no rotational character (*i.e.*, zero vorticity), and thus consist of pure deformation. Investigation of the velocity component along the stretching direction (1-axis) shows that a material element with initial length l_0 grows exponentially in time:

$$l(t) = l_0 e^{\dot{\epsilon}t} \quad (1.6)$$

in contrast to the linear stretching present in shear flow. This strong stretching, and its impact on microstructure in complex fluids, is a key reason why extensional flows are scientifically and technologically interesting, but also makes them difficult to produce in a controlled way. The product $\dot{\epsilon}t$ is known as Hencky strain, and is a measure of total deformation in an extensional flow.

Kinematically complex flows generally have regions where extension is present, and hence extensional behavior is important in non-Newtonian fluid mechanics. For example, in flow past a sphere, equibiaxial extension is present in upstream of the sphere, while uniaxial extension is present downstream. In flow through axisymmetric contractions or expansions, uniaxial extension or biaxial extension is present. Planar extension is present in flow past a cylinder, or in two-dimensional expansion/contraction flow. Industrially, uniaxial extension plays a key role in producing synthetic fibers, such as amid, nylon, and spandex. Equibiaxial extension is the dominant deformation in blow molding or blown film extrusion.

Efforts to investigate extensional behavior began with highly viscous materials such as polymer melts. In the early days, instruments to apply constant-force, -stress, or -velocity stretching were developed for uniaxial extension. Bubble inflation and film blowing were used for biaxial extension. These experimental techniques and results were reviewed in detail by Petrie.² Contraction flows^{24,25} were also utilized to estimate extensional viscosity. Later, instruments to produce better-defined deformation were developed. These include Meissner's rotating-clamp rheometer^{5,26-28} and Münstedt's fiber stretching apparatus.²⁹ Sentmanat *et al.*³⁰ developed a variant on Meissner's design, known as the SER, in which polymer melt is stretched on a pair of counter-rotating drums. The SER fixture can be mounted to conventional

rheometers, and has rapidly become the most common instrument for applying uniaxial extensional flow to highly viscous materials. An instrument for *in situ* scattering studies for polymer melts has been constructed in our lab using the SER fixture.^{31,32} For less-viscous complex fluids, however, devices capable of producing well-defined extensional flow have developed at a slower pace.

Early efforts to measure extensional viscosity in solutions fell short of the goal of rheometry, in that the designated extensional flow kinematics are only present in a particular region of the flow, and stresses are inferred from indirect methods such as pressure drops that may be influenced by fluid inertia and shear stresses. Contraction flows, fiber spinning, tubeless siphons and various stagnation point flows (opposed-jets, four-roll mill, cross slots) have all been employed. However, from these early efforts, a disconcerting observation was found: large disparities existed between data obtained on polymer solutions using different experimental techniques. James and Walters³³ summarized extensional viscosity values of a dilute polyisobutylene solution in a relatively viscous solvent (viscosity around 3 Pa·s at room temperature). Results from multiple methods, including fiber spinning, filament stretching and opposing jets, showed a three-decade variation in apparent extensional viscosity.

More recently, filament-stretching (FiSER)^{34,35} and capillary thinning (CaBER)^{36,37} extensional rheometers have emerged as more robust methods for extensional rheometry. FiSER and CaBER measure the extensional viscosity, respectively, through exponential stretching of a fluid filament (see Equation 1.6), or through thinning of a liquid bridge driven by surface tension. With appropriate control, FiSER is acknowledged as the most reliable way to measure true extensional viscosity of moderate-viscosity materials.³⁵ FiSER instruments produce well-

defined uniaxial extensional flow, and allow direct measurements of the resulting stress from which a true extensional viscosity may be computed. In dilute polymer solutions, FiSER data show that extensional viscosity grows remarkably – by several orders of magnitude, as increasing degrees of strain are imposed during a flow inception experiment. This highlights the important role that strain history plays in extensional behavior, and helps explain why early measurement strategies failed, since early devices fail to control deformation history, and report a single viscosity value that does not capture the strong time-dependence that is often intrinsic to a sample's response. Applications of FiSER have included polymer solutions,⁹ surfactant solutions,^{14,38} and particulate suspensions.¹⁵ However, FiSER still presents several difficulties. First, it still requires some minimal sample viscosity to reduce the relative magnitude of complicating factors such as surface tension, gravity and inertia. Second, devices are large and complicated. The maximum amount of strain that FiSER can apply is rather limited due to spatial constraints. CaBER has been employed to measure a range of low-viscosity materials by applying an extensional step strain and subsequently measuring the time evolution of the midpoint diameter of the thinning filament. Applications have included polymer solutions,^{39,40} wormlike micelle solutions,^{14,41,42} and particle suspensions.^{16,17,43,44}

The above discussion illustrates that available options for producing extensional flows in low-viscosity fluids for the purposes of structural investigations are limited. FiSER, though offering the most robust capabilities for measuring extensional viscosity, is a less desirable candidate for structural studies because special design is necessary to allow measurements in the region in the stretching filament at which ideal kinematics are produced.^{9,10} Further, for many samples, the transient dynamics may be too fast to capture. Although examples of flow-induced

birefringence measurements in FiSER exist,^{9,10} it is still a formidable challenge to implement FiSER for *in situ* structural studies. Likewise, CaBER suffers from very small sample thickness, and the lack of a fixed location within the thinning filament guaranteed to be suitable for structural characterization. The stagnation-point extensional flows discussed earlier, though poorly suited for quantitative measurement of extensional viscosity, are nevertheless promising

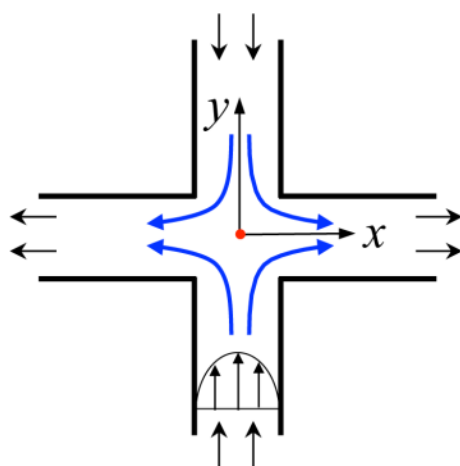


Figure 1.4 An illustration of ideal two-dimensional cross-slot flow, producing planar extensional flow at the stagnation point

candidates for structural studies. The presence of a stagnation point allows for accumulation of a large amount of strain in its immediate vicinity. Unlike FiSER and CaBER, samples may be readily studied under steady-state conditions. Indeed, there is a long history of applying structural probes such as birefringence or light scattering in opposed-jets,^{45–48} four-roll mill,^{49–52} and cross-slot^{53–63} flow cells.

Among candidate flow geometries for structural studies, cross-slot flow cells have been favored because of their simple geometry (Figure 1.4) and ease of manufacture and control. The extensional flow is produced by two streams with the same flow rate entering opposite channels

and exiting via the other two orthogonal slots, ideally creating a symmetrical flow field. The kinematics near the center of the cross-slot flow cell should, ideally, follow Equation 1.5. At the center, the velocity is zero, producing a purely extensional flow, with, locally, an infinite residence time. Away from the stagnation point, the flow will deviate from Equation 1.5. For instance, in the entry and exit slots the flow is shearing rather than extensional. The suitability of cross-slot flow for structural studies thus depends, in part, on how well localized the structural probe may be within the region of ideal kinematics.

1.3 Techniques for probing microstructures of complex fluids

As discussed in Section 1.1, the unusual rheological behavior of complex fluids results from the presence of microstructures at mesoscopic length scale. Thus, a technique that can probe microstructures, at length scale from tens to hundreds of nanometers is necessary for pursuing structural investigations to elucidate their non-Newtonian behavior. Techniques with good time resolution can also facilitate measurements of transient dynamics.

So far, the most commonly used techniques to study fluid microstructures during flow are optical microscopy, polarimetry (birefringence and dichroism), light scattering, neutron scattering and x-ray scattering. Direct visualization of microstructure via microscopy is powerful, but requires that the structure of interest (*e.g.*, particles in suspensions; polymer molecules) be large enough to visualize. An outstanding example is provided by seminal visualization of coil-stretch phenomena in dilute DNA solutions subjected to extensional flow in cross-slot devices.^{54,64} However, for many materials, this approach is not possible. Birefringence and dichroism detect anisotropy in the refractive index of the material produced when flow-induced orientation or stretching of microstructure renders the macroscopic optical properties

anisotropic. Flow-induced birefringence has a particularly rich history as a probe of microstructural change in complex fluids. Birefringence and dichroism have been coupled with all kinds of flow devices discussed in Section 1.2, such as parallel plate,^{65,66} and Couette cells^{67–70} in shear flow, and opposed-jet,^{48,71,72} four-roll mill,⁵¹ FiSER^{9,10} and cross-slot^{57,58,61,73,74} devices for extensional flow. Various categories of complex fluids have been studied, such as polymeric solutions,^{9,10,48,51,71} surfactant solutions,^{58,68–70} and dilute and semi-dilute carbon nanotube suspensions.^{65–67} In the case of carbon nanotube suspensions, due to low light transmittance, the maximum concentration of the CNT suspension or the sample thickness is limited. This illustrates one limitation of optical techniques, namely that samples must be transparent. Certain classes of materials that form ordered phases at rest (*e.g.*, liquid crystals) also present a challenge that birefringence is difficult to measure and interpret when the optical anisotropy becomes very large. Finally, birefringence and dichroism also reduce all information about microstructural anisotropy to a single number, such that details of the orientation distribution are not detected.

Scattering is a powerful technique to probe microstructures at length scales comparable or larger than the wavelength of the radiation employed (typically visible light, x-rays or neutrons). Light scattering, a classical method for measuring polymer coil sizes in dilute solutions, has been employed to investigate the global chain deformation under shear⁷⁵ and extensional^{46,52} flow. Over several decades, small-angle neutron and x-ray scattering have contributed immensely to understanding microstructures of diverse complex fluids. In the case of scattering in the quiescent state, many microstructural details can be measured, such as the state of dispersion for carbon nanotube suspensions,^{76–81} quantitative determination of microstructural

dimensions such as persistence length or lamellar spacing in surfactant aggregates,^{82–89} and the radius of gyration for polymer molecules.⁹⁰ When coupled with flow, the degree and direction of orientation induced can be determined,^{20,91–99} as well as flow-induced structures.¹⁰⁰ Neutron scattering is particularly useful for hydrogen-rich materials, as isotopic labelling with deuterium can selectively highlight certain structural features within a sample. Conversely, x-ray scattering relies on the contrast of electron density and thus does not need extra sample preparation. It can probe suspensions of a wide range of concentrations, from dilute⁹⁷ to concentrated,⁹⁵ regardless of whether samples are optically transparent. Compared to neutron scattering, another advantage of x-ray scattering is that it is less affected by multiple scattering, which dramatically complicates data analysis. Finally, high brilliance synchrotron sources facilitate time-resolved studies, while neutron scattering is comparatively sluggish due to the limited flux of available neutron sources. In this thesis, small-angle x-ray scattering is chosen as our structural probe.

Chapter 2 Flow Devices for Applying Planar Extensional and Homogeneous Shear Flow to Low-Viscosity Fluids

Devices that can apply well-defined flow fields and allow for *in situ* x-ray scattering studies are vital to our work. This chapter introduces the two devices used in this work, namely a high-aspect-ratio cross-slot flow cell to apply planar extensional flow, and a cone and plate shear flow cell to apply homogeneous shear flow.

2.1 High-aspect ratio cross-slot flow cell for applying planar extensional flow

Building on the historical account of extensional flow devices in Section 1.2, this section describes the rationale for development of a high-aspect-ratio cross-slot flow cell to apply planar extensional flow. Details on its construction are laid out, and practical factors regarding its use at the synchrotron for *in situ* x-ray structural studies are described.

2.1.1 Background

While planar extensional flow (Equation 1.5, Figure 1.3 *c*) and the idealized cross-slot flow depicted in Figure 1.4 are two-dimensional, practical implementation of such flow devices requires confining the sample in the third (z) direction with windows. Due to the no-slip condition imposed by the windows, the flow field is rendered 3-dimensional, with variations along the depth of the flow cell (Figure 2.1). The aspect ratio, t/w , where w is the slot width and t is the thickness, is a crucial parameter for such a cell. If the aspect ratio is sufficiently large, the flow may be treated as quasi-two-dimensional, with a well-defined extension rate at the stagnation point through most of the cell thickness. Conversely, if the aspect ratio is small, shear

gradients across the thickness of the cell dominate over the planar extensional flow produced in the mid plane of the flow cell, which means that fluid is subjected primarily to shear rather than the desired planar extensional flow, and that there is no single well-defined extension rate even at the stagnation point.

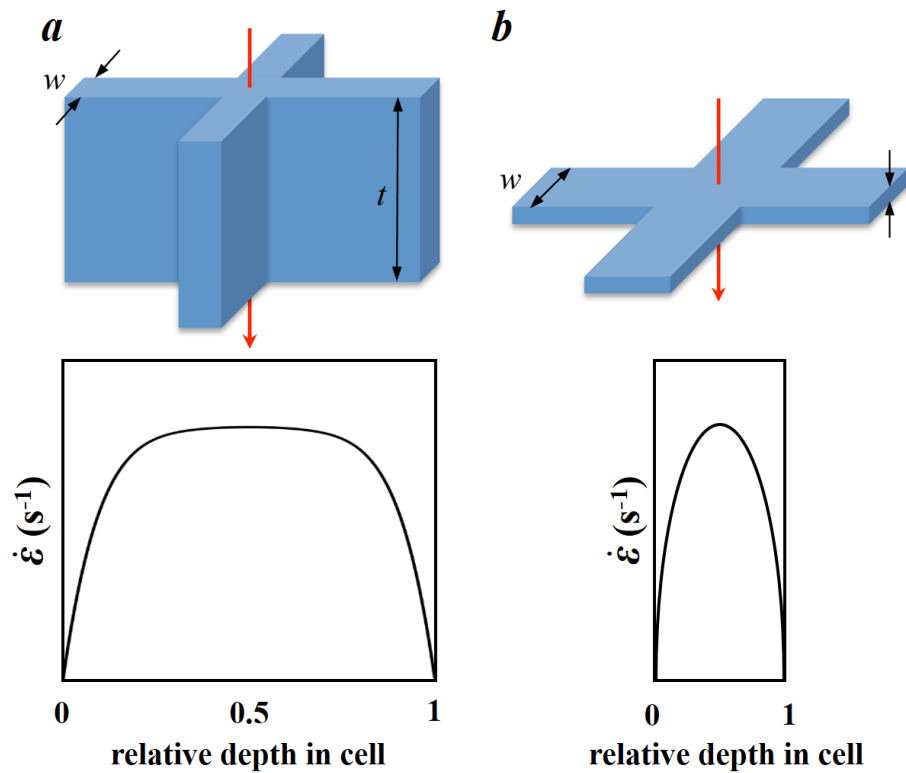


Figure 2.1 A schematic illustration of velocity profile for a high aspect-ratio cell (*a*) versus a low aspect-ratio flow cell (*b*)

With the cross-slot flow cell, a nominal extensional rate is determined from the volumetric flow rate, Q , in one slot and cell dimensions by:

$$\dot{\epsilon}_{nom} = \frac{Q}{w^2 t} \quad (2.1)$$

This may be compared to the characteristic *shear* rate produced in the slot flows upstream and downstream of the stagnation region:

$$\begin{aligned}\dot{\gamma}_{char} &= \frac{Q}{(\text{cross-sectional area}) \cdot (\text{characteristic length})} \\ &= \begin{cases} \frac{Q}{(wt)w} = \frac{Q}{w^2t}, \text{ high aspect ratio} \\ \frac{Q}{(wt)t} = \frac{Q}{wt^2}, \text{ low aspect ratio} \end{cases} \end{aligned} \quad (2.2)$$

For a high aspect ratio flow cell, extensional and shear rates are comparable, and regions of shear- and extension-dominated kinematics are spatially isolated from one another. Conversely, for a low aspect ratio channel, the extension rate is *small* compared to the characteristic shear rate in the device, and these dominant shearing gradients persist closer to the stagnation point. These considerations make clear that high aspect ratio geometries are crucial to producing well-defined planar extensional flow in cross-slot flow cells.

Of previous work employing cross-slot flow cells, Idziak's¹⁰¹ and Penfold's work⁶⁰ is particularly relevant to us because they used x-ray or neutron scattering as their structural probe. Idziak *et al.*¹⁰² studied the microstructures of lamellar surfactant using x-ray scattering. Penfold *et al.* studied both wormlike mixed micelles and lamellar surfactant using neutron scattering. In both cases, however, the aspect ratios of their flow cells were alarmingly small: With Idziak's flow cell, the slots were 11.1 mm wide and had a thickness of 2.5 mm ($t/w = 0.23$). With Penfold's flow cell, the width was around 1 cm and the thickness was around 0.5 cm ($t/w = 0.5$). Given these aspect ratios, velocity gradients along the beam path (z -direction) dominate over the desired planar extensional flow in the x - y plane. One reason for the large width (and hence low

aspect ratio) was the incident beam dimension. Idziak used a $1\text{ mm} \times 1\text{ mm}$ x-ray beam, while Penfold used 2 mm diameter neutron beam. Since the desired extensional flow is localized in the

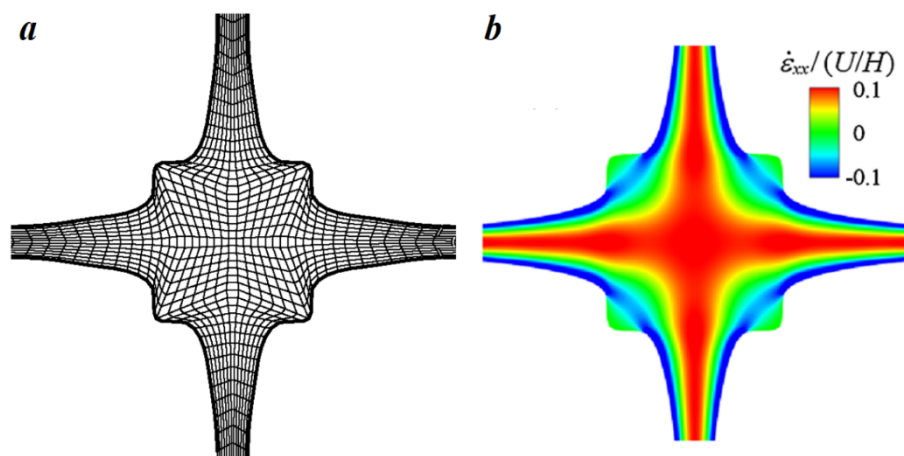


Figure 2.2 (a) An improved cross-slot shape based on numerical simulation of upper-convected Maxwell fluids at $De = 4$ (figure reprinted from [103]) (b) Strain rate field of numerically simulated Newtonian creeping flow in the optimized cross-slot geometry (figure reprinted from [104])

stagnation region, the corresponding width must be made significantly larger. At the same time, the sample thickness was limited by concerns of x-ray absorption or, with neutrons, multiple scattering. These experimental constraints combined to necessitate the use of low-aspect-ratio geometries.

As discussed earlier, away from the stagnation point, the deformation will typically be some mix of shear and extension. Researchers have sought to design optimized cross-slot flow geometries to maximize the extent of the homogenous extensional flow region, based on numerical simulations of flow kinematics.^{103,104} Such optimized cross-slot flow cells offer improved prospects for measuring extensional viscosity (Figure 2.2). However, such a geometry has a large internal volume. Higher flow rates are necessary to produce comparable extension

rates at the stagnation point. And, the larger internal dimensions make it considerably harder to execute a higher aspect ratio design to reduce the impact of the windows along the beam direction. For these reasons, we adhere to the simple cross-slot design in this work.

Because the strain history is not the same for fluids following different trajectories through the flow cell, it is important to study fluid structure in the vicinity of the stagnation point, as well as at the stagnation point itself, in order to probe the extent of localization of the structural features observed at the stagnation point. A second concern is a flow bifurcation that has been observed with viscoelastic fluids in cross-slot flows.^{33,55,62} Since structural data will reveal if the flow pattern deviates from presumed symmetrical pattern, there is little risk that such flow instabilities would be undetected. Moreover, velocity fields in the simple cross-slot geometry have been copiously studied,^{55,56,58,59,62} providing a good foundation of understanding for this work.

2.1.2 Constructing a high-aspect-ratio cross-slot flow cell

Our flow system consists of three major parts: a cross-slot flow cell, a set of four syringes to hold sample fluids, and a syringe pump to precisely control the flow (Figure 2.3). The flow cell is connected to the four syringes using plastic tubing. Planar extensional flow is created by two streams entering the two opposing slots and exiting in the other two perpendicular slots, all at the same rates. The syringe pump can simultaneously push and pull two syringes at the same rate. This ensures that both supply lines and both withdraw lines provide precisely the same flow rate. Details on each of the components are provided below.

2.1.2.1 Cross-slot flow cell

The main flow cell body is machined from aluminum. As shown in Figure 2.4, rectangular slots are machined through the aluminum body's thickness to produce the cross-slot geometry. Each slot is 1 mm wide, 5 mm thick, and 30 mm long. Four additional 30-mm long circular channels connect the slots to the outer edge of the flow cell. The diameter of these circular channels is selected so that they have the same cross-sectional area as rectangular slots, so as to minimize large changes in average velocity as fluid enters the slot. Still, there is a flow disturbance as fluid enters the rectangular slots. These slots were made as long as practical in

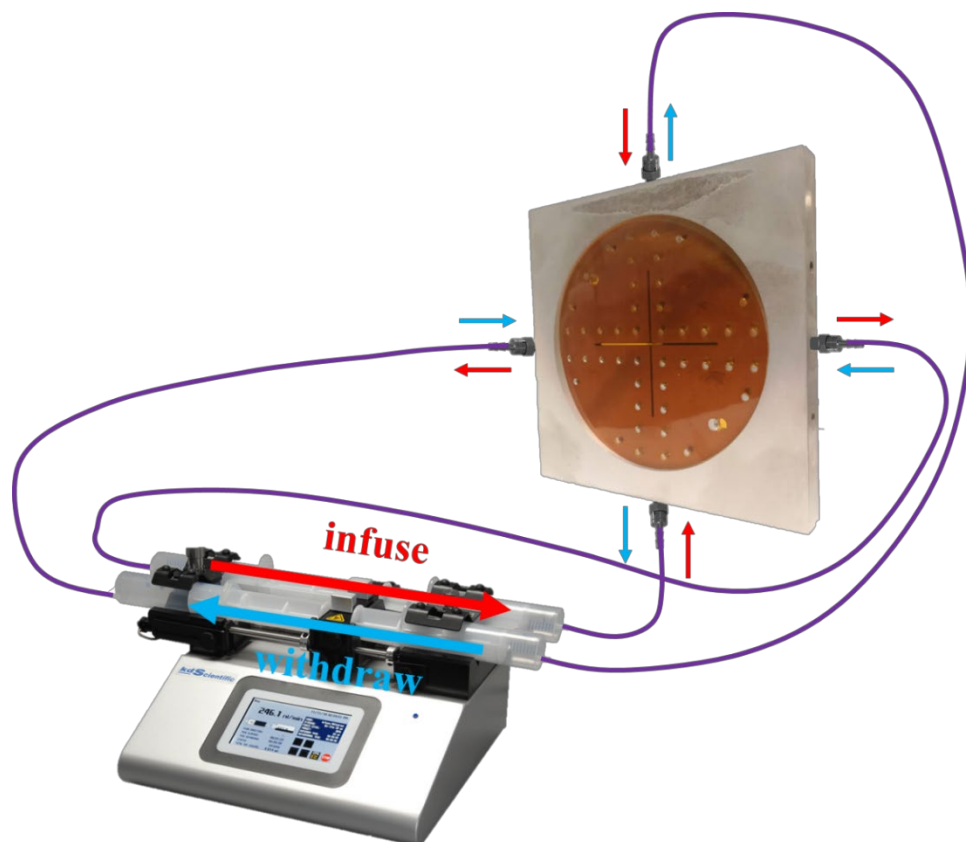


Figure 2.3 Overview of cross-slot flow system.

order to maximize the chance that the fluid structure become fully developed, and effects of prior disturbances washed out, prior to entering the stagnation zone. The aspect ratio, thickness/width, is 5. This value is a significant improvement compared to 0.23 with Kisilak's x-ray cell,¹⁰¹ or 0.5 with Penfold's neutron cell.⁶⁰

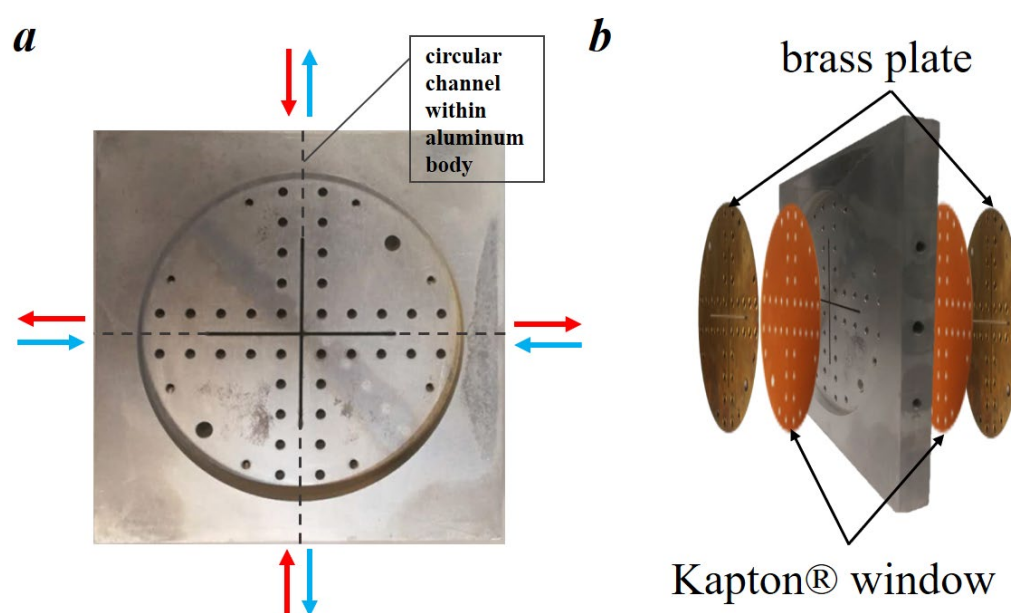


Figure 2.4 Cross-slot flow cell design. (a) cross-slot flow cell body with four ports; (b) the cross-slot flow cell “sandwich” sealed by Kapton® windows and brass plates

We used 0.13-mm (5 mil) non-adhesive polyimide film (Kapton®, Argon Tape PC555FILM) as the x-ray scattering window. This thickness was chosen as a compromise between a desire to minimize the deflection of the window produced by pressures in the flow cell (which favors thick windows), and to reduce parasitic background scattering from the window itself. To mount the two Kapton windows, two brass plates are used to press the Kapton film firmly to the flow cell. The brass plates were machined with matching cross-slots of 1.1 mm

width. The “sandwich” flow cell is aligned and assembled using 36 screws and nuts. Although we didn’t use adhesives, the flow cell successfully contains the samples with viscosity of up to 13 Pa·s without leaking.

Four threaded ports (10-32) and Nylon extra-grip barbed tube fittings (McMaster-Carr 5153K32) were used to connect the flow cell to plastic tubing. Teflon tape aids in ensuring a completely sealed connection here. The tubing itself needs to satisfy several requirements. First, it must withstand the pressure drop produced by flowing samples. Second, the wall of the tubing must be as hard as possible to increase the responsiveness of the device. If the tubing wall is too compliant, it may produce a significant lag between the command exerted by the syringe pump and the actual flow in the cross-slot cell, as some of the volumetric flow produced by the pump is diverted into dilation of the tubing. Harder tubing materials reduce this effect, and allow greater operating pressures, important for higher viscosity samples. However, the tubing still must be sufficiently flexible to enable the device to be readily mounted and moved about within the beam line. Last, but most importantly, we found that plasticizers in certain tubing could substantially alter sample rheology. For instance, the wormlike micelle solution 60 mM CTAB/ 350 mM NaSal studied in this work was a strongly viscoelastic Maxwellian fluid, but turned into a watery liquid after contacting tubing containing plasticizers or other additives. (This impact of plasticizer or surfactant solutions has also been reported by Lutz-Bueno *et al.*¹⁰⁵) In the end, polyurethane clear tubing for drinking water (McMaster-Carr 5648K68) with 3/32" ID and 5/32" OD, was found to be the best option. The length of the four pieces of tubing was chosen to be 56 cm (corresponding to an internal volume of 2.5 ml), to accommodate the physical distance between the cross-slot cell and the syringe pump when mounted in the synchrotron hutch. The

length of the tubing was cut to be exactly the same for all four ports, to promote flow symmetry within the cross-slot cell, which is further enhanced by the reciprocating design of the syringe pump. A female luer bulk head fitting (Cole-Parmer UX-45508-32) was used at the other end of the tubing for connection to the syringes. This particular fitting was chosen because its extra-long-barbed head secures the tubing and seals the fitting well, so as to minimize entrainment of air bubbles despite the stresses produced of the tubing connection by the bending of tubing in the mounted flow cell. The luer lock fitting then connects to a syringe.

2.1.2.2 Syringes

10-ml SGE gas-tight glass syringes with removable luer lock (SGE 008960) were used for all the work discussed in this document. This syringe can operate between 5 to 100 C°. This syringe has an outer diameter of 18 mm, a scale length of 60 mm, and a barrel length of 106 mm. Its overall length with the plunger is 120 mm. The syringe can hold 12 ml of sample at the maximum. The plunger and the barrel head both have non-stick PTFE (polytetrafluoroethylene) coatings, providing corrosion resistance and a low coefficient of friction. This coating also reduces concerns about compatibility of the test fluid with the syringe. At the same time, it poses a challenge for sample loading because the two end surfaces are hard to wet and air bubbles may easily be trapped during the filling process (see Section 2.1.3). An additional aluminum cap is attached to the syringe plunger, so that the syringe can be firmly mounted on the syringe pump rack to be either pushed or pulled.

2.1.2.3 Syringe Pump

The syringe pump (KDS Legato 270P) can hold four syringes ranging in size from 0.5 μ l to 140 ml. It can exert a maximum force of 34 kg. The force is automatically adjusted based on

the sample and the flow rate. The pump also allows a maximum force to be set, to prevent syringes from breaking. A mechanical limit on the rack further prevents excessive pushing of the plunger that might break the syringe. The pusher travel velocity has a range of 0.36 $\mu\text{m}/\text{min}$ to 190.80 mm/min . Combined with syringes of different sizes, this can achieve flow rates between 3.06 pl/min and 216 ml/min . The accuracy is reported to be at $\pm 0.35\%$ and the reproducibility is 0.05 %. The operating temperature is between 4 to 40 $^{\circ}\text{C}$. It offers control through its touch screen, or through pump commands sent through a serial interface, which is essential for conducting experiments at the synchrotron. The programmable syringe pump offers various external input/output ports to trigger pump event or export flow rate. The functions relevant to this work will be described in detail in Section 2.1.4. Although the syringe pump offers a range of flow modes allowing for various injection profiles (including ramp, stepped, and pulse injection), in this work, only the “constant rate” mode is used.

With the 10-ml syringe used here, the range of pump speeds corresponds to flow rates from 61.3 nl/min to 31.8 ml/min , or nominal extensional rates of $2 \times 10^{-4} \text{ s}^{-1}$ to 106 s^{-1} , according to Equation (2.1). However, the actual achievable extensional rates have additional boundaries due to sample viscosity. If the viscosity is too high, the required force can exceed the preset maximum force of the syringe, which leads to a sudden stop of the pump. This is inconvenient because this error shuts down the external connections to the pump and it must be reset through the touch screen. When this happens, experiments must be stopped and the flow control and structural studies must be reinitiated. To avoid such a scenario, a functional maximum flow rate must be determined prior to synchrotron experiments. The criterion we adopt is the maximum flow rate which allows the syringe pump to continuously run in both infuse and withdraw modes

twice for each direction. The pump may still stall abruptly due to a small fluctuation above the force limit, thus the status of the pump needs close attention during the experiment. But this criterion has been effective most of the time in ensuring a smooth run for our experiments.

2.1.3 Filling the flow cell

The entire flow cell and syringes must be filled without air bubbles and sealed completely, as quickly as possible. Additionally, the sample volumes in the four syringes need to be coordinated so that simultaneous control over flow rates in the four slots can be achieved. Experience has led to the protocol outlined here.

2.1.3.1 Preparation

The sample should start in a bubble-free state. This is usually achieved by letting the sample sit undisturbed for a day or two. But, for samples with nonzero yield stress (such as lamellar surfactants), low-speed centrifugation facilitates the separation of air bubbles from samples. If centrifugation is employed, the centrifuge tube must be carefully chosen to avoid contamination from plasticizers, as described above with the flow cell tubing. The cross-slot flow cell with Kapton® windows and brass plates is assembled, and the required connectors are attached to the ends of the tubing prior to arriving at the beam line. At the start of a run, the empty cross-slot flow cell is first connected to the four pieces of tubing and then used for alignment and collecting background scattering. The four syringes are then filled with the sample fluid.

2.1.3.2 Syringe filling

The removable luer lock tip on each syringe is screwed as tightly as possible, to prevent sample leaking during loading and operation. The syringe plunger is then removed and the head

of the syringe is capped with a lightweight quick-turn tube plug (McMaster-Carr 51525K315) so that the sample can be poured into the barrel of the syringe. During sample loading, extra care is needed to avoid introducing new bubbles as the sample wets the PTFE-coated head and the inner glass wall of syringes. The usual practice is to use a small amount of sample to wet PTFE surface completely and then pour in additional fluid to fill the syringe. 10 ml of sample is typically loaded in each syringe at this step so that there is enough volume to fill the tubing and flow cell later, and to squeeze any unexpected air bubbles out. This volume must not be larger than 11 ml, or the syringes will not be able to fit into the pump after filling the tubing. (The maximum sample volume for which these syringes can be mounted onto the pump rack is 8.5 ml).

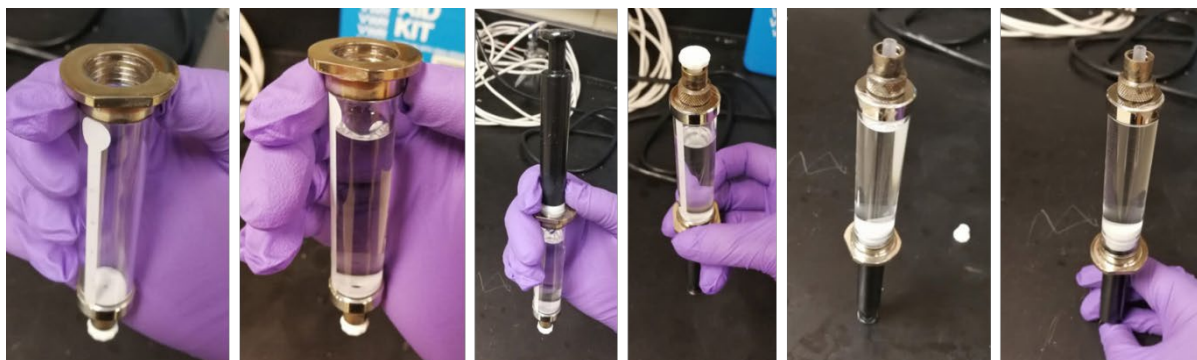


Figure 2.5 Illustration of how to fill a syringe with sample

After loading sample into the syringe, the plunger is gently pushed into the barrel for a bit and the syringe slowly reversed to be upright, with the capped luer lock connector on top. The goal is to keep the air inside the syringe as one big bubble as the sample now flows down against the plunger, vacating the tip of the syringe. Pushing the plunger into the barrel creates a positive pressure inside the syringe. Thus, the plunger and barrel must be held firmly together during this procedure. The syringe is kept upright long enough for the air bubble to fully rise to the tip.

Finally, the cap is opened and the air slowly squeezed out with the plunger. The entire process should be conducted slowly to avoid creating small air bubbles, which tend to accumulate at one of the fitting connections in the system. The whole process is graphically illustrated in Figure 2.5.

2.1.3.3 Flow cell filling and sealing

Three of the filled syringes are connected to the lengths of tubing connected to the bottom and the two horizontal flow cell slots. Filling tubing with the sample is straightforward as long as the air is always kept above the sample and the filling rate is kept slow to avoid creation of tiny air bubbles. A Loggerhead® bionic grip wrench is used to connect the syringe to the female luer bulk head, to assure complete and firm connection. Then the plunger is slowly pushed until sample solution appears in the tubing. The sample is fed into the tubing until it just reaches the Nylon extra-grip barbed fitting at the flow cell. This step is repeated for all three sides: bottom, left and right.

To fill the Nylon extra-grip barbed fitting and the flow cell slot, the syringe pump is used to ensure a slow and even feeding speed, because this step is mostly invisible, particularly where the channel cross-section changes from circular to a rectangular slot. The two shapes join head-on without a transitional bridge which can induce hidden air bubbles during filling. The flow cell is mounted upright on optical posts. The bottom slot is the first to be filled. The syringe pump is set to push the solution upwards at 300 $\mu\text{l}/\text{min}$, until the sample appears in the middle of the slot. This usually requires 0.4 ml sample. To fill the horizontal slots, the flow cell is rotated by 90 degrees so that the sample is always fed from below during filling, again using the syringe pump for each slot.

Once filling of the bottom and horizontal slots is completed, the flow cell is reset to an upright position. The three syringes are all used to fill the rest of the flow cell and the top tubing, with the aim that the sample volumes in all four syringes are coordinated to allow mounting on the syringe pump together. The sample volume for each syringe is adjusted and any remaining air bubbles are squeezed out by flushing extra sample. Using V_1 , V_2 , V_3 , and V_4 to designate the sample volume in the syringe connecting to bottom, left, top, and right slots, these volumes must satisfy: 1) $V_1=V_3$, 2) $V_2=V_4$, 3) $V_1+V_2=9.0$ ml. This volume matching step is crucial for creating a symmetrical flow in the cross-slot intersection and the durability of the flow cell to be tested for 20 hours. A mis-match of 0.1 ml can lead to an unsymmetrical flow pattern appearing at low flow rates and air bubbles being produced as the experiment proceeds. After all the volumes are adjusted and the flow cell and remaining tubing connected to the top slot are filled, the last step is to close the connection between the last syringe and the top tubing fitting, avoiding air bubbles. Finally, the syringes are mounted into the pump.

2.1.4 Flow cell operation

To achieve simultaneous push and pull flow within all four syringes at the exact same rate, syringe barrels and the ends of the plungers must be secured. Detailed procedures for securing syringes on the rack are available in a manual provided by the KDS company. To avoid risk of breaking the syringe by pushing the plunger too far, the pump is configured to use only 8 ml of sample as an active experimental volume. Thus, each syringe has an unused 0.5-ml buffer volume. Two mechanical stop collars are set on the rail at the position where 0.5 ml is left to prevent the pusher block from further advancing and creating unwanted excessive force.

The arrangement of the syringes affects the extension direction in the flow cell. To ensure consistency across all experiments, the syringes connecting to the horizontal channels are always placed in the left part of the rack and syringes connecting to the vertical channels in the right part of the rack. With this arrangement, when the pump runs in the “infuse” mode (Figure 2.3), the pusher moves towards the right, and the fluid runs from vertical channels to horizontal channels. Planar extension along the horizontal direction is thus produced. When the pump is switched to “withdraw” mode, planar extension along the vertical direction is generated.

During x-ray experiments, the pump must be operated remotely, via commands sent through a serial interface. To enable the syringe pump to receive chain commands from an external source, the configuration of the pump must first be set at “infuse only” or “withdraw only” mode. This is manually setup through the touch screen. To monitor the pump status, a hutch camera is focused on the pump’s screen, including a view of the position of the pusher on the rack, and the LED indicator of whether the pump is running. The manual provided by KDS company lists all the chain commands recognized by the syringe pump. The flow control chain commands most frequently used in our experiments are: “irate”, “wrate”, “irun”, “wrun”, “stop”, and “ctvolume”. The “irate” and “wrate” commands set or display the infuse and withdraw flow rates. The “irun” and “wrun” commands set the pump to run in infuse or withdraw mode. The “stop” command is to stop the pump immediately. The pump can also automatically stop if a designated target volume or a flow time is reached. To prevent unexpected stop of the syringe pump during x-ray scattering data collection, the “ctvolume” command (“clear target volume”) is often executed between experiments.

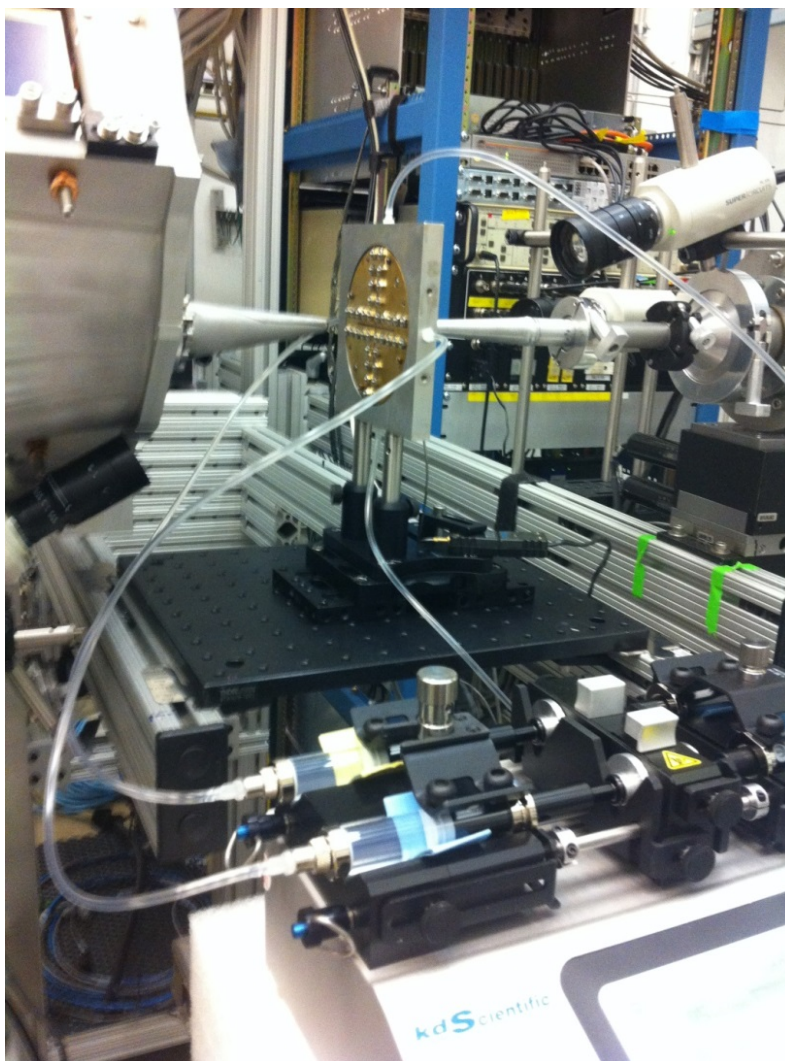


Figure 2.6 Installation of the cross-slot flow cell and syringe pump in the beam line station.

2.1.5 Integration with beamline systems

Figure 2.6 shows the flow cell and pump installed at the beamline (5ID-D at the APS). The flow cell is mounted on a cantilevered arm that allows precise control of positioning in the horizontal and vertical directions. The syringe pump is placed close to the cross-slot flow cell due to spatial constraints posed by the tubing length. The flexibility of the tubing does allow a sufficient range of motion to allow the flow cell position to be scanned through several millimeters in each direction to allow “mapping” experiments in which structural data are collected at a range of location in the cross-slot flow cell.

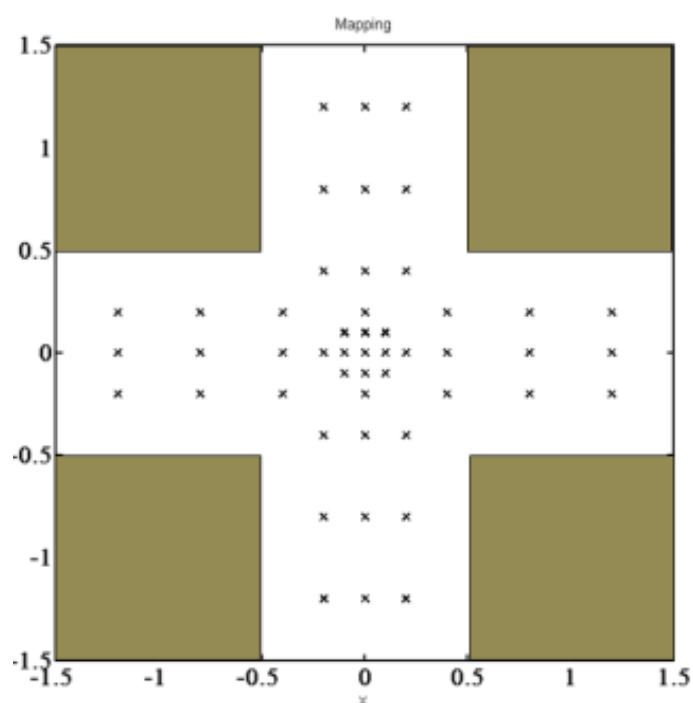


Figure 2.7 An illustration of a typical set of positions used in “mapping” experiments, used to study microstructure at different locations within the cross-slot flow cell

Smooth execution of experiments requires integration of flow control with the beamline software that governs acquisition of x-ray scattering patterns. In addition to automating data

acquisition, a record of flow condition, flow cell location, and scattering parameters for each data point should be produced. The beamline software at 5ID-D provides two modes of data acquisition. In “slow” mode, scattering images are collected one at a time, and data files are written immediately. As a result, several seconds are required between successive image frames. This mode is typically used for mapping experiments, in which scattering patterns are collected at different locations within the cell while flow is kept at steady state (Figure 2.7). In “fast” mode, a block of images is stored into a memory buffer, and subsequently stored to disk at some later time. This allows much faster data frame rates, and is thus used for transient studies of structural dynamics at the stagnation point, particularly for experiments when the exposure time is less than 1 second.

2.1.5.1 Slow mode

When experiments are conducted using slow mode, the flow control for the syringe pump can be entirely integrated into SPEC, the operating software used for beamline control and x-ray data acquisition. A macro file which include all commands for scattering data collection, pump control, and positioning stage movement is written to execute a pre-designed sequence of experiments.

The syringe pump is connected to the intranet at the beamline station through a RS-232 connection. The baud rate is set at 19200. The communication is through telnet protocol. A prefix “kdscmd” is used to direct chain commands to the pump. A representative excerpt from such a macro, including both pump and SPEC commands, is given below:

```
kdscmd irate 0.3 m/m  
kdscmd irun
```

```
do_countdown time()+200.0  
mv samp_v 0  
ascan samp_h -0.1 0.1 2 1.0
```

The first line sets the pump infuse rate at 0.3 ml/min. The second line starts the syringe pump in infuse mode. The third line counts down 200 seconds so that the flow can reach steady state. The fourth line moves the y coordinate of the flow cell to 0. The last line collects the scattering patterns at x equal to -0.1, 0 and 0.1 mm with an exposure time of 1.0 second, by executing a “scan” of the horizontal sample position motor. Each macro command requires a certain amount of time to execute. As the flow keeps running during the time-lag, sample volume is continually dispensed. This dispensed volume needs to be accounted for, especially when flow rate is large enough that the 8 ml active sample volume is used up before the desired data collection is completed. Experience at the synchrotron shows that stage motion usually takes about 2 seconds, and that transferring data from the detector to the beamline computer takes about another 2 seconds. Therefore, a command like “ascan samp_h -0.1 0.1 2 1.0” costs about 11 seconds. Knowing the limit of 8 ml active volume and flow rate, the number of scattering patterns that can be collected while pumping in one direction (infuse or withdraw) can be determined. Macros are thus written to automatically execute a large number of experiments at the desired flow rate, flow cell positions, and flow direction.

This fully automated flow control and data collection system enables a large number of scattering patterns to be generated. This, in turn, requires generation of an automated record of pump status for each scattering pattern. A programmable analog voltage source at the beamline (DAC1-5) can be used to build this function. The analog source can generate a voltage signal

between 0 and 5000 mV. Based on the flow rate applied in each experiment, a function $f2v(Q)$ defines a voltage output based on the flow rate. The function is constructed with the idea that the whole voltage range can be fully utilized. The static condition ($Q = 0$) is set to an output of 2500 mV. Any voltage larger than 2500 mV indicates pump running in the infuse mode, with extensional flow along the horizontal direction. Likewise, a voltage output below 2500 mV indicates the pump running in the withdraw mode, with extension along the vertical direction. The smallest flow rate to be applied is designated Q_{\min} , and the largest flow rate Q_{\max} , Q is taken as positive sign for infuse mode and negative for withdraw mode. Since we will usually specify that all the intermediate flow rates be evenly spaced out on a log scale, the function $f2v(Q)$ may be formulated:

$$f2v(Q(\text{ml}/\text{min})) = 2500 + \text{sign}(Q + 1 \times 10^{-6}) \cdot (\log_{10}(|Q| + 1 \times 10^{-6}) + a) \times M \quad (2.3)$$

Here a is the smallest integer to make $(\log_{10} Q_{\min} + a)$ a positive number, and M is a magnification factor chosen to fully utilize the whole available voltage range. It is typically assigned a value, slightly smaller than $2500/(\log_{10} Q_{\max} + a)$. For example, one of our experiments required flow to be performed from 0.0014 to 0.64 ml/min for both infuse and withdraw modes. We formulated the voltage function as following:

$$f2v(Q(\text{ml}/\text{min})) = 2500 + \text{sign}(Q + 1 \times 10^{-6}) \cdot (\log_{10}(|Q| + 1 \times 10^{-6}) + 3) \times 781.25 \quad (2.4)$$

The small value 10^{-6} is inserted to avoid the undefined $\log_{10}(0)$. In the macro file, after changing flow status, this $f2v(Q)$ function is executed to designate a voltage output from DAC1-5. If the pump is stopped, $f2v(0)$ is the input, and the export voltage is 2500 mV.

The voltage signal is sent to a voltage-to-frequency counter, and then recorded into SPEC during each image exposure. Since the counter accumulates during the exposure, the SPEC data must be divided by the exposure time to recover the voltage in mV. From this, the value of Q associated with each data frame may be recovered by inverting equation (2.4):

$$v2f(U(mV)) = \text{sign}(U - 2500) \cdot \left(10^{\frac{|U-2500|}{M}-a} - 1 \times 10^{-6} \right) \quad (2.5)$$

The flow cell position is recorded with “samp_h” and “samp_v” for horizontal and vertical position, respectively. If the center of the cross-slot flow cell is defined as the origin (0,0), moving “samp_v” to a positive value means to lift the sample stage upward for “samp_v” mm. Since the synchrotron x-ray beam is fixed, the position where the microstructure is probed is actually below the center of the cross-slot flow cell.

2.1.5.2 Fast mode

The fast mode is used to probe fast dynamics when exposure time is less than 1 second and the data acquisition reaches as fast as 1 frame/second. Also, the fast mode is used for experiments with multiple stages of different data collection frequency. While conducting experiment in this mode, the syringe pump is commanded usually through telnet communication outside of the SPEC software. A SPEC command initiates acquisition a block of data frames. Once the shutter voltage signal shows that data acquisition has begun, the relevant command is issued to the pump (typically flow inception or flow cessation). The precise timing of the flow event relative to data acquisition is variable. Thus, the 15-pin digital I/O connector of the syringe pump is used to export and record the direction and pump status. Pin 7 is a direction indicator and Pin 15 is the run indicator. Both are directly connected to beamline data acquisition

channels, and recorded during each data frame exposure. In this way, it is possible to identify the exact frame in the block of scattering patterns at which flow was started or stopped. When operating in this mode, the flow rate for each experiment needs to be manually recorded.

2.2 Cone and plate annular shear cell

As discussed in Chapter 1, most research using *in situ* methods for studying complex fluids under flow has been performed in shear flow. In Chapter 4, measurements of structural dynamics of carbon nanotube suspension in planar extensional flow will be complemented by experiments in shear. These shear flow experiments were conducted using a cone and plate annular cell developed previously in the group⁹⁴ to probe microstructural dynamics in the velocity-gradient (1-2) plane of homogeneous shear. Here we briefly describe this device, and certain enhancements that were introduced to accommodate experiments with faster data acquisition.

2.2.1 Shear cell geometry

An illustration of the annular cone and plate geometry used in this shear cell is presented in Figure 2.8. The lower annular plate is fixed while the upper annular cone rotates. The annular

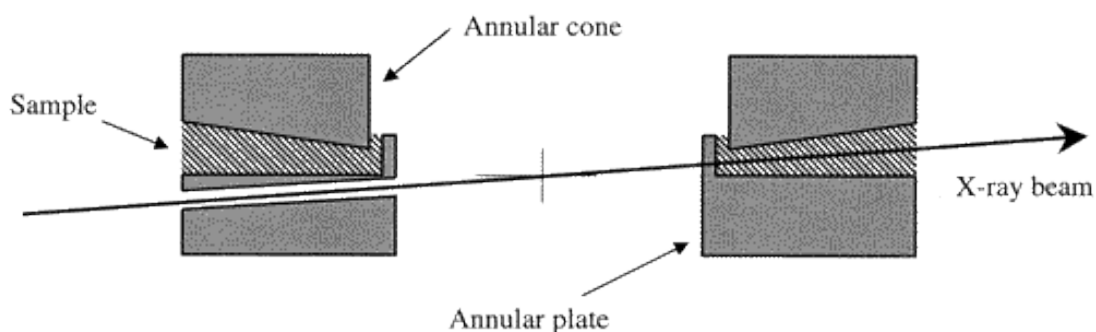


Figure 2.8 The beam path for the 1-2 plane annular cone and plate shear cell

fixtures have a 1.5-cm inner radius and 2.5-cm outer radius, with a cone angle of 5° and hold about 2.5 ml of sample. The incident x-ray beam travels through an aperture in the bottom plate and then through the 1-cm-thick sample on the opposite side. The comparatively long beam path through the sample is required to reduce the impact of edge effects, similarly to the high aspect channel in the cross-slot flow cell design. Use of high energy x-rays reduces absorption to allow experiments with this thicker sample. The whole flow cell is tilted by 2.5° to accommodate the horizontal x-ray beam at the synchrotron.

The flow cell is driven by a microstepping motor, and can apply a shear rate from 0.1 s^{-1} up to around 100 s^{-1} . With an added gear reducer, the shear cell can access a shear rate as low as 0.002 s^{-1} . However, installation of the gear reducer requires realignment of the shear cell with respect to the beam, due to the added weight. The shear cell has temperature control capability, but the experiments in this work were all conducted at room temperature.

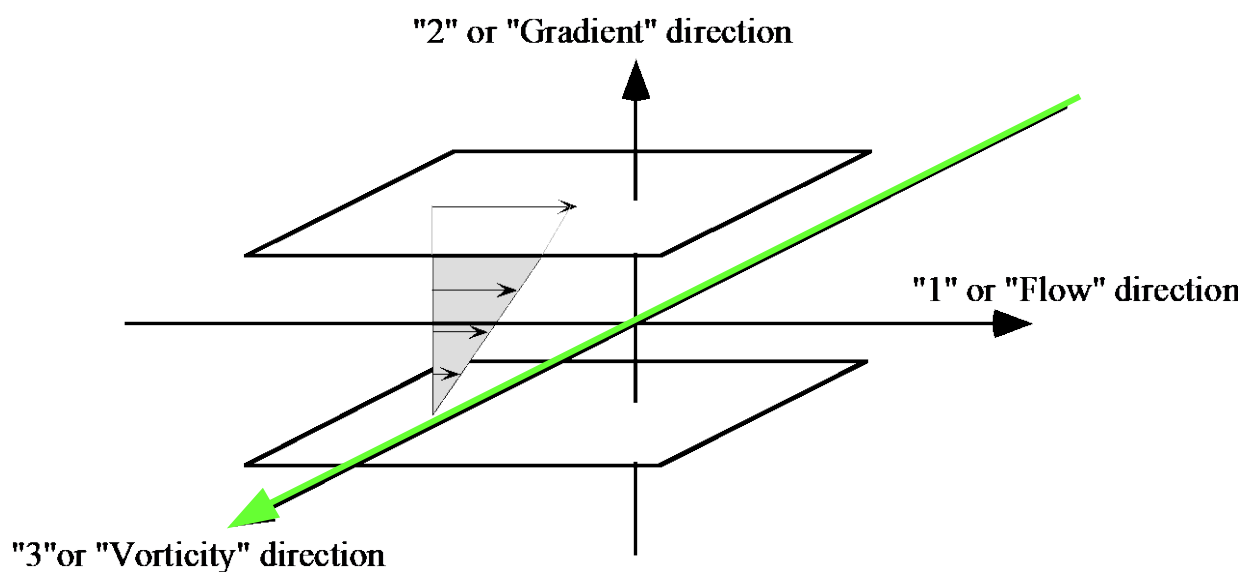


Figure 2.9 X-ray beam travelling perpendicular to 1-2 plane of shear flow

The advantage of this flow cell is that it is one of the rare instruments that offers the capability to probe microstructures in the 1-2 plane under homogeneous shear flow (Figure 2.9). However, this design also poses limitations. Samples must be sufficiently viscous enough to resist gravitational sag when loaded in the tilted fixtures. The relatively large cone angle and free surface create susceptibility to normal stress-driven instabilities, such as edge fracture or secondary flows in highly viscoelastic materials at high shear rates. The usable operating range must therefore be determined carefully for each new sample. The carbon nanotube suspension studied here was not too challenging, since its rheology is essentially Newtonian. Unfortunately, the wormlike micelle solution (CTAB/NaSal) studied in this work was too viscoelastic to be studied with this shear flow cell.

2.2.2 Coordination of shear flow control with data acquisition

The shear cell is controlled from a stand-alone programmable motor controller that is not integrated with other beamline components. Traditionally, users have had to manually record how events in the flow protocol (flow inception, cessation, reversal, *etc.*) relate to the acquisition of a sequence of x-ray scattering frames. As faster detectors allow for more rapid data acquisition, it became necessary to implement improved methods for recording parameters from the flow protocol into the x-ray data record. Specifically, an automated method has been developed to record the motor status for each scattering frame. Signals from the motor output connection on the controller are split, and the voltage signals specifically associated with motor direction and motor speed are read into the DAC1-5 and DAC1-6 data acquisition channels at the beam line. Signals are fed to a voltage-frequency counter, and then counted, gated by the

beamline shutter. Values thus accumulate throughout the whole exposure time, and are saved for each frame of scattering data.

To reconstruct the motor status, values recorded from DAC1-5 and DAC1-6 must first be normalized by the exposure time in seconds. The motor direction is straightforward with the “forward” direction exporting 3 V and the “reverse” direction exporting 1 V. The motor speed calculation requires more effort because the analog signal extracted from the motor output connection often fluctuates. For this reason, for each experiment, the motor speed is also manually recorded as a back-up reference. A calibration curve has been developed by averaging the DAC1-5 signal for all experiments at a given same shear rate. As shown in Figure 2.10, the shear rate and DAC1-5 signal are directly proportional. This relationship is then applied back to the voltage signals of each individual frame to determine the shear rate for each image. It is possible that a flow inception or cessation event occurs while a scattering frame is being collected. In such circumstances, the exact time of the event can be inferred from the ratio of the measured voltage to the standard full voltage for that shear rate.

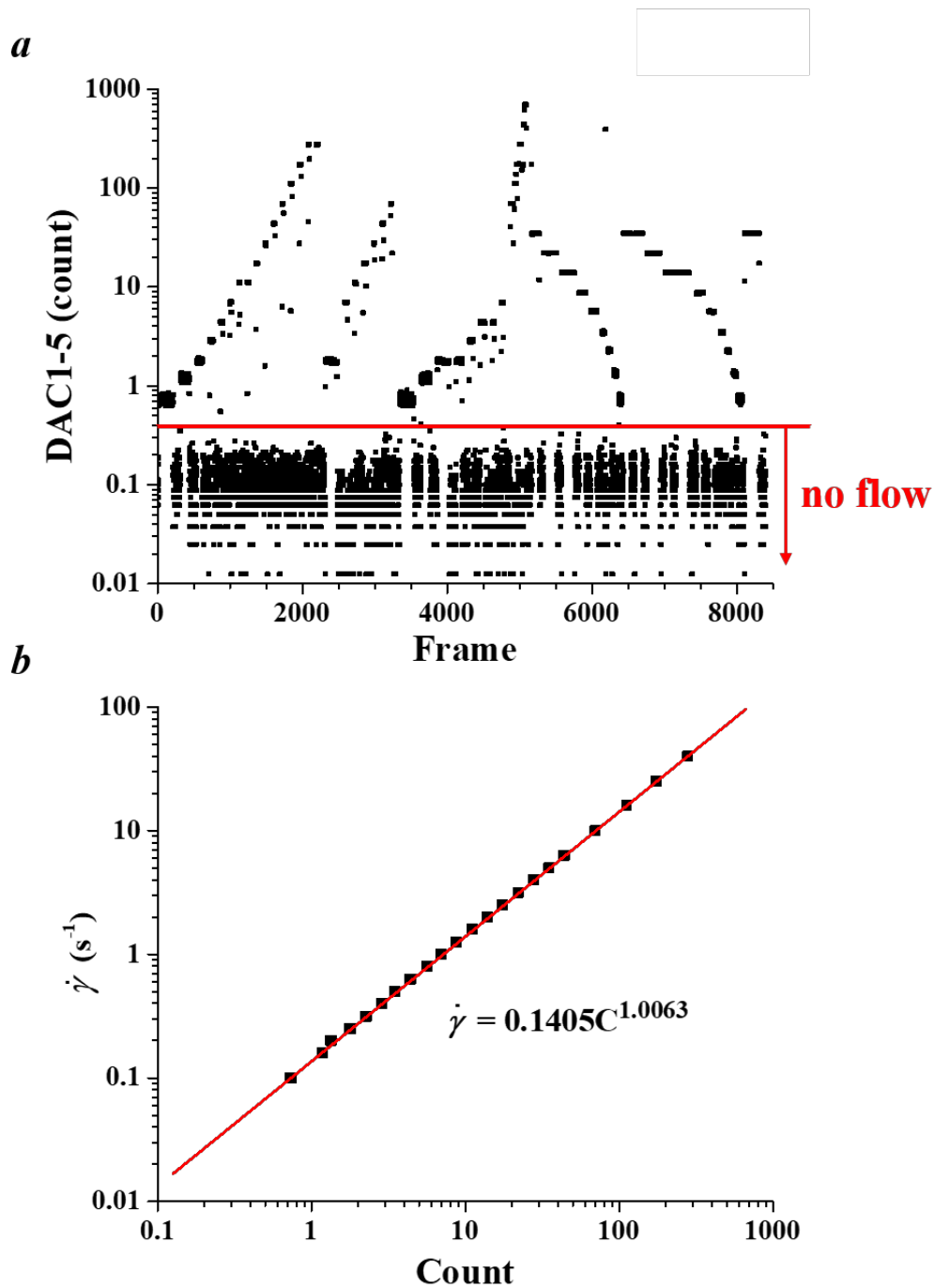


Figure 2.10 (a) The DAC1-5 signal measured from all frames collected during an experimental run. These data allow determination of exactly when flow is turned on and off, and the associated shear rate. (b) Calibration curve for shear rate based on measured counts from DAC1-5 channel

Chapter 3 X-ray Scattering, Synchrotron Facility and Data Analysis

3.1 X-ray scattering basics

X-rays are electromagnetic waves of the same nature as light but with much shorter wavelength. The wavelength of x-rays varies from 0.001 nm to 10 nm; sources for scattering and diffraction methods of interest here typically produce x-rays with wavelengths near 0.1 nm or 1 Å. Before x-rays were fully understood, radiography was already used to study the internal structure of opaque objects such as bones or metals. Later, in 1912 the nature of x-rays was established and the phenomenon of x-ray diffraction by crystals was discovered. This provided a new tool for investigating the fine structure of matter.¹⁰⁶ The wavelength of x-rays makes x-ray scattering a powerful tool for probing structures on length scales ranging from a few Ångströms to tens of nanometers. This overlaps with the length scales at which a wide range of non-Newtonian fluids exhibit characteristic microstructures whose dynamics in response to the flow governs their rheology. Neutron scattering is also capable of probing similar length scales, but often requires the use of deuterated solvents or samples, and limitations on neutron source strength is an impediment to time-resolved studies. Given advantages such as easy sample preparation, availability of high brilliance sources and its noninvasive nature, x-ray scattering is well-suited for probing the behavior of complex fluids.

X-ray beams interact with matter through the electrons contained in the atoms. When exposed to an incident x-ray beam, the electrons of the atomic shell begin oscillating, producing

scattered radiation. Depending on whether or not the kinetic energy of the incident wave is conserved, elastic or inelastic scattering can occur. When the oscillation of the electron is induced by the electromagnetic field of the incident photon, the scattered wave has the same wavelength and the phase information is preserved. Only the direction of the incident beam is changed and the kinetic energy is conserved. This is elastic (or coherent) scattering. Inelastic (or Compton) scattering occurs when the interaction between the electron and the incident photon is a particle collision governed by energy and momentum conservation. Here, the electron acquires kinetic energy from the incident photon through collision, the energy of the photon is reduced (the scattered beam is redshifted), and the phase information is lost. For structural investigation using scattering and diffraction methods, the phase difference is a key factor in determining whether the constructive and destructive interference occurs. Thus, we focus here solely on elastic scattering.

When x-rays encounter matter, they may also be absorbed. X-ray absorption depends on the material's chemical makeup, its density, and the wavelength of the incident beam. Away from characteristic absorption "edges", absorption is proportional to λ^3 . Therefore, using an x-ray beam with shorter wavelength can significantly reduce absorption. Hence hard x-rays with high energy, typically above 10 keV, are often employed.

In elastic scattering, the phase relationship between incident and scattered waves, and hence between x-rays scattered from neighboring locations in the sample is preserved. Scattered x-rays may thus be subject to constructive or destructive interference, which is the basis for diffraction and scattering techniques. A simple example is provided by Bragg's law, which describes the condition when a diffraction peak emerges as a result of constructive interference

in a material with periodic internal structure (Figure 3.1). If the interplanar spacing of the lattice is d , and the incident beam is displaced by 2θ degrees after scattering, then the pathlength difference between the beams scattered from successive layers is $2d \sin \theta$. For a diffraction peak to appear, the pathlength difference must be an integer multiple of the wavelength: ¹⁰⁷

$$2d \sin \theta = n\lambda \quad (3.1)$$

Using Braggs' Law, the dimensions of a crystal lattice can be inferred from the location of diffraction peaks.

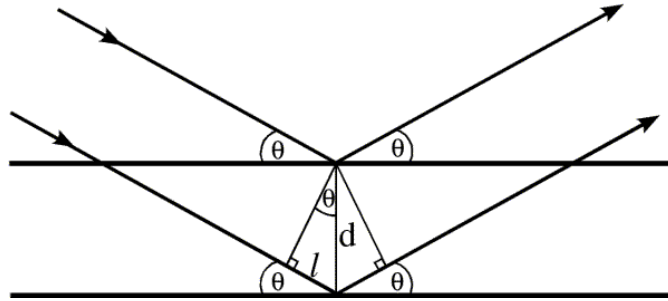


Figure 3.1 An illustration of Braggs' law

Scattering patterns from amorphous materials do not exhibit well-defined Bragg peaks. Even in this case, however, constructive and destructive interference of scattered x-rays can still provide a basis for investigating microscopic structure. To understand this, we consider first the interference from two electrons (Figure 3.2 a), and then generalize to a continuous distribution of electrons in the sample. If two electrons O and P are separated by a vector \mathbf{r} and scattering is observed at an angle 2θ , the phase difference between the two scattered beams is

$$\Delta\phi = -\mathbf{k} \cdot \mathbf{r} + \mathbf{k}_0 \cdot \mathbf{r} \quad (3.2)$$

where the incident beam is represented by the wave vector \mathbf{k}_0 and the scattered beam is represented by the wave vector \mathbf{k} . Both wave vectors point along the direction of wave propagation with a magnitude of $2\pi/\lambda$. The scattering vector \mathbf{q} is defined as the scattered wave vector \mathbf{k} minus the incident wave vector \mathbf{k}_0 (Figure 3.2 *b*):

$$\mathbf{q} = \mathbf{k} - \mathbf{k}_0 \quad (3.3)$$

Its magnitude, q , is given by

$$q = |\mathbf{q}| = \frac{4\pi \sin \theta}{\lambda} \quad (3.4)$$

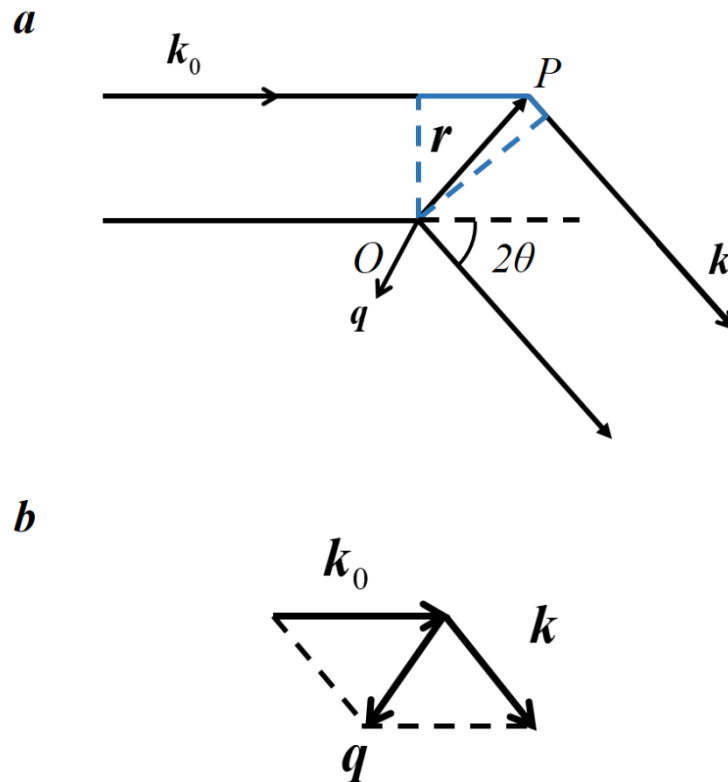


Figure 3.2 (a) An illustration of scattering from two electrons (b) definition of incident and scattered wave vectors, and the scattering vector \mathbf{q}

The amplitude $A(\mathbf{q})$ of the scattered wave is obtained by summing the scattering from O and P, allowing for interference due to the phase difference:

$$A(\mathbf{q}) = A_0 b (1 + e^{-i\mathbf{q}\cdot\mathbf{r}}) \quad (3.5)$$

Here A_0 is the amplitude of the incident wave and b is the scattering length of the electron. For the scattering from amorphous materials where electrons are continuously dispersed, a generalization of this concept leads to the following expression for the scattered amplitude:

$$A(\mathbf{q}) = A_0 b \int_V n(\mathbf{r}) e^{-i\mathbf{q}\cdot\mathbf{r}} d\mathbf{r} \quad (3.6)$$

where $n(\mathbf{r})$ is the electron density distribution, and the integration domain is the whole illuminated sample. We see, then, the scattered amplitude is the 3-dimensional Fourier transform of the electron density distribution, and is a function of the scattering vector \mathbf{q} in a 3-dimensional “reciprocal space”. Bragg diffraction is a special case of equation (3.6) in which periodic structure in real space, upon Fourier transformation, leads to concentration of scattering at discrete locations (Bragg peaks) in reciprocal space. Recasting Bragg’s law in terms of the scattering vector q , we see:

$$q = \frac{2n\pi}{d} \quad (3.7)$$

There is thus a reciprocal relationship between the length scales within a sample and the value of q (or scattering angle) at which these features will be manifested in scattering or diffraction.

In an x-ray scattering experiment, only the scattered intensity is measured. This is the conjugate product of the amplitude: ¹⁰⁸

$$\begin{aligned}
I(\mathbf{q}) &= A(\mathbf{q}) \cdot A^*(\mathbf{q}) = A_0^2 \left[\int \rho(\mathbf{u}') e^{-i\mathbf{q} \cdot \mathbf{u}'} d\mathbf{u}' \right] \left[\int \rho(\mathbf{u}) e^{-i\mathbf{q} \cdot \mathbf{u}} d\mathbf{u} \right] \\
&= A_0^2 \int_V \left[\int \rho(\mathbf{u}) \rho(\mathbf{u} + \mathbf{r}) d\mathbf{u} \right] e^{-i\mathbf{q} \cdot \mathbf{r}} d\mathbf{r} = A_0^2 \int_V \Gamma(\mathbf{r}) e^{-i\mathbf{q} \cdot \mathbf{r}} d\mathbf{r}
\end{aligned} \tag{3.8}$$

Therefore, the measured intensity is the Fourier transform of the autocorrelation function of “scattering length distribution”, $(\mathbf{r}) = bn(\mathbf{r})$. The scattered intensity can also be separated into two terms: ¹⁰⁸

$$I(\mathbf{q}) = A_0^2 \int_V \Gamma(\mathbf{r}) e^{-i\mathbf{q} \cdot \mathbf{r}} d\mathbf{r} = A_0^2 \left(\int_V \Gamma_\eta(\mathbf{r}) e^{-i\mathbf{q} \cdot \mathbf{r}} d\mathbf{r} + \langle \rho \rangle^2 V \delta(\mathbf{q}) \right) \tag{3.9}$$

Here $\Gamma_\eta(\mathbf{r})$ is the autocorrelation of a *relative* scattering density function $\eta(\mathbf{r})$, defined as

$$\eta(\mathbf{r}) = \rho(\mathbf{r}) - \langle \rho \rangle \tag{3.10}$$

Where $\langle \rho \rangle$ is the average value of $\rho(\mathbf{r})$. This shows that $\langle \rho \rangle$ only affects the zero-angle scattering which is experimentally unobservable because it is coincident with the much stronger directly transmitted beam. The observable scattering pattern only arises from spatial variations of scattering power within the sample. Scattering experiments are thus easier when there is significant electron density contrast between the different constituents of a sample. This enables short exposure time, making it easier to perform time-resolved studies of dynamics in transient flows. Unfortunately, while scattering contrast may be manipulated in neutron scattering through selective deuteration, in x-ray scattering one typically must work with intrinsic properties of a sample of interest.

The scattered intensity, as the Fourier transform of the autocorrelation function of the sample's scattering length density, theoretically pervades all of three-dimensional reciprocal space. However, only a small portion of reciprocal space is accessible in a typical scattering experiment (Figure 3.3). As shown in Figure 3.2, the scattering vector \mathbf{q} bisects the angle between the incident and scattered wave vectors. As the scattering angle 2θ , increase from 0° to 180° , the tip of \mathbf{q} defines a spherical surface in reciprocal space, known as the Ewald sphere (Figure 3.3). Point O is the origin of reciprocal space. \overline{MO} indicates the direction of the incident beam. The radius of the Ewald sphere is $2\pi/\lambda$. It defines the explorable portion of reciprocal space for a beam of fixed wavelength. The size of the detector and the sample-to-detector distance further limit access to reciprocal space by constraining the maximum scattering angle, and hence maximum q that may be accessed. The shaded blue surface in Figure 3.3 provides an example of how the experimentally attainable \mathbf{q} may be limited. For small-angle scattering, \mathbf{q} becomes increasingly limited to a patch of the Ewald sphere near the origin of reciprocal space, effectively sampling \mathbf{q} in a plane perpendicular to the incident beam direction.

For systems under flow, 2-dimensional scattering patterns are often analyzed in terms of the azimuthal dependence of intensity, measured away from some reference direction (*e.g.*, the flow direction). For wide-angle scattering, Figure 3.3 demonstrates that the azimuthal angle on the 2-dimensional scattering pattern may not reflect the true orientation angle away from the flow direction in the reciprocal space. For example, if the microstructure has a uniaxial symmetry with respect to the flow axis, the azimuthal angle read from the scattering pattern ϕ' is related to the true orientation angle ϕ through the scattering angle 2θ :

$$AP \cdot \cos \phi' = OA \cdot \cos \phi$$

$$AP = \frac{2\pi}{\lambda} \cdot \sin 2\theta$$

$$OA = \frac{4\pi \sin \theta}{\lambda} = q$$
(3.11)

$$\cos \theta \cdot \cos \phi' = \cos \phi$$
(3.12)

In SAXS, the scattering angle is so small that the curvature of the Ewald sphere can be neglected, and this correction is not required ($\cos \theta \approx 1$).¹⁰⁹

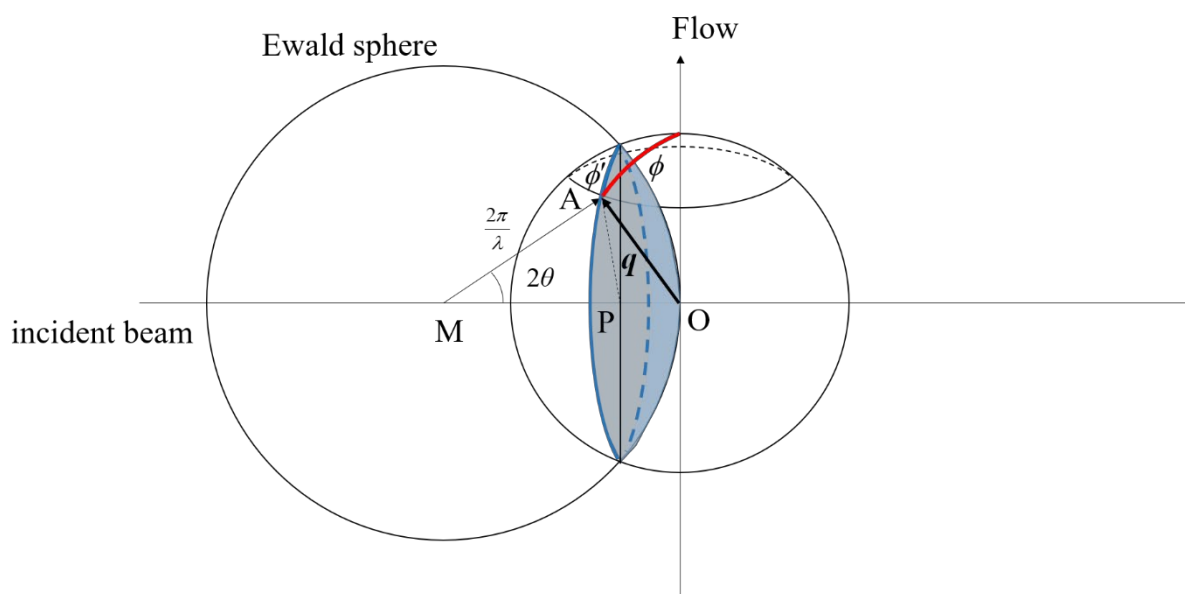


Figure 3.3 Demonstration of the Ewald sphere, demonstrating how reciprocal space is probed in x-ray scattering experiments

3.2 Synchrotron facility

X-ray experiments were carried out at Station 5ID-D of Sector 5, operated by the Dupont-Northwestern-Dow Collaborative Access Team (DND-CAT), at the Advanced Photon Source, located at Argonne National Laboratory. Station 5-ID-D has an integrated system of

three detectors which can simultaneously collect x-ray scattering intensity at small, medium and wide angles spanning a range of scattering angle 2θ from 0.02° to 23° (Figure 3.4). This allows structure to be probed over a wide range of length scales (0.2 ~ 300 nm) of relevance to complex fluids such as polymers, solutions, suspensions, *etc.*

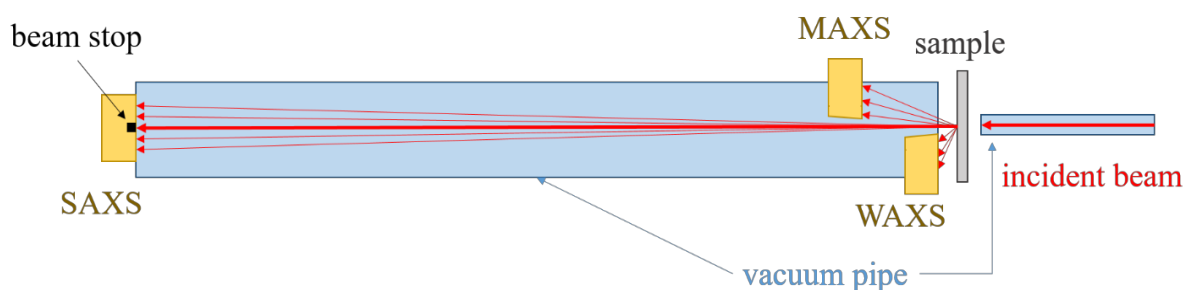


Figure 3.4 Small-, medium-, and wide-angle x-ray scattering detectors setup at Station 5ID-D of Sector 5, DND-CAT

The x-ray beam is produced by an Undulator A insertion device and, with the existing double crystal monochromator, its energy can be tuned from 5 to 19 keV. The beam dimension can be adjusted from $50\ \mu\text{m} \times 50\ \mu\text{m}$ to $1\ \text{mm} \times 2.5\ \text{mm}$. In our experiments, the target beam dimension has been $(100\ \mu\text{m})^2$, though the actual beam size varied from 90 to 135 μm in different synchrotron runs. The standard detector-to-sample distances for wide, medium and small angle detectors are, respectively, 0.2 m, 1 m and 8.5 m. The unfocused, uncollimated beam has a flux of about 1×10^{13} ph/s. This high flux beam is pivotal in reducing the exposure time for each frame, facilitating rapid data acquisition. To reduce air absorption and background scattering, long vacuum pipes are placed between the source and sample location, and between the sample and the detectors. If space allows, aluminum cones are used to extend the vacuum pipes upstream and downstream of the sample as close as possible to the flow cell (Figure 2.7). A beam stop is used to prevent the powerful transmitted beam from damaging the SAXS

detector. The station has a sample “tower”, with heavy duty, long range, motorized translation stages that allow positioning of our home-built flow cells relative to the x-ray beam, and precise movement of the flow cell to allow x-ray beam to probe different locations within the cell. The flow cell is aligned to the beam by scanning the flow cell position both vertically and horizontally, while monitoring the transmitted intensity.

The detectors are fiber-optic taper coupled modules from Rayonix, L.L.C. These detectors employ frame-transfer technology, which facilitates high speed frame rates without compromising data quality. This technology is also crucial to capturing the microstructural dynamics of complex fluids, when transient phenomena are being studied. With this technology, the frame rate is primarily limited by the exposure time. For experiments reported in this thesis, the exposure time ranged from 0.2 second to 30 second (largely determined by the scattering power of the sample), and the frame collection frequency varied from 1 second/frame to 1 min/frame. Specifically, the SAXS detector model is MX170-HS. It consists of a 2×2 tiled array, with $(170 \text{ mm})^2$ active area without gaps between modules. The pixel dimension is $(0.0443 \text{ mm})^2$, producing a full resolution 3840×3840 pixels. However, we usually have used a 4×4 or 6×6 binning, to reduce image size and readout time, and to improve signal-to-noise ratio. The MAXS detector model is LX170-HS. It consists of a 2×1 tiled array of the high-speed frame-transfer device. In addition, a special notch is constructed to allow small-angle scattering and the direct beam to pass. The MAXS imaging area is $85 \times 170 \text{ mm}^2$. The full resolution in pixels is 1920×3840 . The WAXS detector is identical to the MAXS detector, with a similar notch, to allow passage of both medium- and small-angle scattering. The MAXS and WAXS detectors are

positioned on opposite sides of the direct beam (Figure 3.4), so that either only allows access to an azimuthal range of 180°.

Although the detector system allows seamless coverage of scattering angle with overlap between the detectors, access to a full 180° azimuthal angle (necessary for the analyses of anisotropy described below) is only available within certain ranges of scattering angle for each detector. Energy is selected, in turn, to position the scattering features of interest in these regions. For the experiments reported in this thesis, an energy of either 9.4 keV or 15 keV has been used.

Since the detectors all read out to a resolution of 16 bits, the scattering intensity at each pixel is an integer from 0 to 65535. The raw detector intensity can be calibrated to absolute scattering units through use of a glassy carbon scattering standard. A calibration procedure is performed by the beamline scientist at the beginning of each experimental run, resulting in a calibration factor to correct the raw image intensity. The intensity in absolute units (cm⁻¹) can then be computed from the raw image intensity:

$$I_{absolute} = \frac{DetectorReadout - DetectorDark}{TransmittedIntensity - TransmittedDark} \cdot \frac{CalibrationFactor}{SampleThickness} \quad (3.13)$$

The “*DetectorReadout*” is the raw integer intensity reported by the detector. The “*DetectorDark*” is a baseline output when there is no scattering signal. This baseline has an average value of about 10 for these detectors. Hence, we use this number as the dark baseline. The “*TransmittedIntensity*” is measured at beam stop using a photo diode. Similarly, “*TransmittedDark*” is the baseline signal when no beam is present. The “*TransmittedIntensity*” is affected by the flux of the incident beam. In addition, “*TransmittedIntensity*”, “*TransmittedDark*”, “*DetectorReadout*”, and “*DetectorDark*” are additive and proportional to

exposure time. The normalization in equation 3.13 thus compensates for any fluctuation or drift in the incident beam intensity, or for variations in exposure time. The “*CalibrationFactor*” is the coefficient provided by the beamline scientist to calibrate intensity to the absolute units based on glassy carbon standard. “*SampleThickness*” is the thickness of the sample through which the beam passes. Except that the “*DetectorReadout*” comes from the scattering image file and the “*SampleThickness*” is determined by the flow cell geometry, all the other parameters are saved in a “sav” file associated with each scattering image.

Figure 3.5 shows two-dimensional sample scattering patterns from lamellar surfactants (*a*) and (*b*), wormlike micelles (*c*), and carbon nanotube suspensions (*d*), all materials studied in this work. The lamellar surfactants (patterns (*a*) and (*b*)) exhibit long range 1-dimensional ordering, which produces a sharp Bragg reflection at a characteristic scattering angle. It so happens that the lamellar spacing in DDAB is larger than that of CTAC, so that, according to Bragg’s law (equation 3.1) the diffraction peak occurs at lower angle. Thus, pattern (*a*) was collected on the SAXS detector, while pattern (*b*) was collected on the MAXS detector. Patterns (*a*) and (*b*) both exhibit a secondary peak in addition to a primary peak. The narrower peak width and sharper second-order diffraction peak in CTAC are indication of more persistent long-range order. Likewise, intensities are unevenly distributed azimuthally due to the preferred microstructure orientation induced by flow (see following section).

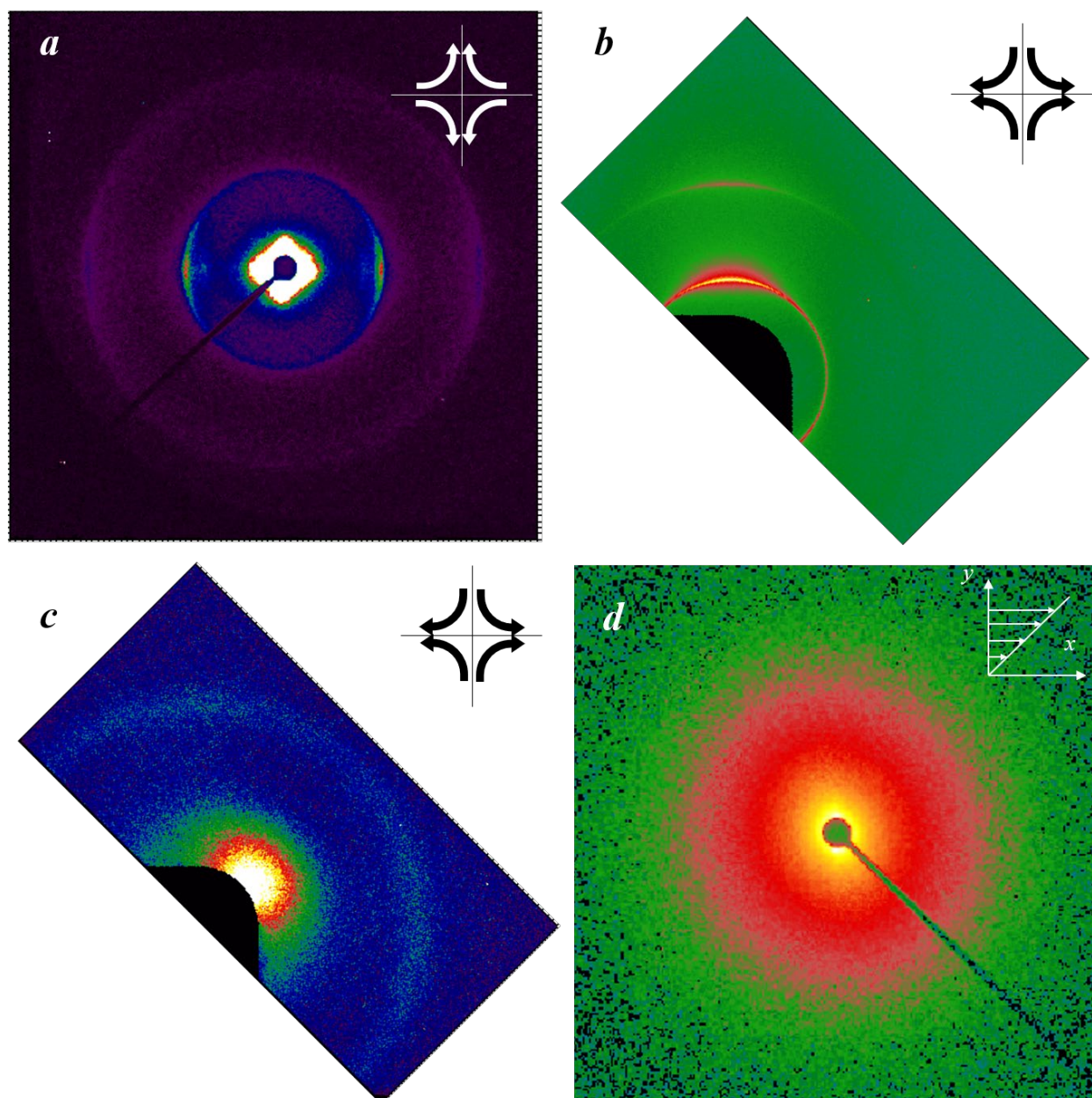


Figure 3.5 Sample scattering patterns of several complex fluids systems: (a) and (b) for lamellar surfactants, (c) for wormlike micelles solution (d) for dilute carbon nanotube suspension.

- (a) DDAB (didodecyldimethylammonium bromide) in water;
 - (b) CTAC (cetyltrimethylammonium chloride) and 1-pentanol in water;
 - (c) CTAB (cetyltrimethylammonium bromide) and NaSal (sodium salicylate) in water;
 - (d) dilute suspension of multiwalled carbon nanotubes (CNTs) in uncured epoxy resin.
- Specific concentrations are given in Chapter 5.

Wormlike micelles (*c*) and suspended carbon nanotubes (*d*) do not possess long range periodic order, so there are no diffraction peaks. Still, the length scale of the microstructure influences the scattering. Typical diameters of wormlike micelles are 5 to 20 nm,¹¹⁰ while the average CNT diameter used in (*d*) is 15 nm. As a result, the observed CNT scattering occurs at smaller angles than in the CTAB solution. However, their scattering is still rendered anisotropic by the application of flow. The anisotropic scattering patterns reflect the preferred orientation of these materials under flow. Pattern (*c*) is substantially more anisotropic than Pattern (*d*), demonstrating that classes of materials differ in their susceptibility of flow alignment, and types of flow fields differ in their capability in inducing orientation.

Extracting quantitative insights into the effects of flow on the microstructures of the samples requires quantitative analysis of these patterns.

3.3 Quantitative analysis of scattering patterns

As discussed in Section 3.1, scattering intensity can be separated into observable scattering pattern that rises from spatial variation in the sample's scattering length density, and an unobservable zero-angle intensity arising from the average scattering length density within the whole sample.¹⁰⁸ The observable portion can be rewritten as:

$$I(q) = \int_V \Gamma_\eta(\mathbf{r}) e^{-i\mathbf{q}\cdot\mathbf{r}} d\mathbf{r} \quad (3.14)$$

If scattering intensity is integrated with respect to the reciprocal scattering vector throughout all of reciprocal space, the contrast term cancels out and the integral turns out to be:¹⁰⁸

$$Q = \frac{1}{(2\pi)^3} \int I(\mathbf{q}) d\mathbf{q} = \int \Gamma_\eta(\mathbf{r}) \left[\frac{1}{(2\pi)^3} \int e^{-i\mathbf{q}\cdot\mathbf{r}} d\mathbf{q} \right] d\mathbf{r} = \int \Gamma_\eta(\mathbf{r}) \delta(\mathbf{r}) d\mathbf{r} = \Gamma_\eta(\mathbf{0}) = V \langle \eta^2 \rangle \quad (3.15)$$

This tells us that the integral of the scattering intensity throughout the reciprocal space yields an invariant equal to the product of the illuminated sample volume and the mean of squared relative scattering length density. As long as the material composition and the sample volume remain the same, the invariant should stay constant even if the microstructure has been perturbed (*e.g.*, aligned by flow). In our experiments, it is impossible to detect scattering from all of reciprocal space. An approximate integration of scattering intensity may be performed over a finite q range on the two-dimensional plane within reciprocal space sampled in a typical scattering experiment. Such an “invariant” can provide useful insights, despite its lack of rigor. One application is to track the fluctuations of sample thickness during flow in a 1-2 shear geometry with a free surface (see Section 2.2). Another application is to provide firmer basis for quantitative comparisons of data collected during different synchrotron runs. In addition, the scattering invariant provides a classic method to quantify the growth of a second phase as in semi-crystalline polymers (see Appendix A). In practical terms, we set the lower q integration limit on the edge of the beam stop, and impose an upper limit where the sample’s scattering intensity has dropped to background levels, to prevent random noise at large q from masking the invariant’s value when weighted with q^2 (the volume in reciprocal space associated with an incremental increase, dq , of the scattering vector is proportional to q^2).

Based on the scattering process principle introduced earlier, the real space where the material sits is connected to the material’s reciprocal space structure (the corresponding distribution of scattered or diffracted intensity in reciprocal space), related through Fourier transformation. The scattering from anisotropic features will be distributed anisotropically in reciprocal space, leading to an anisotropic pattern in two-dimensional scattering images. Figure

3.5 schematically illustrates how scattering from (a) rod-like and (b) lamellar microstructures leads to anisotropic patterns, reflecting the distribution of orientation in the sample. For a long rod, whose length is much larger than its diameter, the scattering pattern has an inverse character, where the intensity measured in the direction of the diameter persists to much higher angles than when measured in the direction along the particle's length. When a distribution of rod orientation is present, the anisotropic features at the single-particle scattering are smeared azimuthally; the breadth of the azimuthal distribution of scattered intensity reflects the breadth of the distribution of orientation in real space. For a random distribution of particle orientation, the pattern becomes fully isotropic. A lamellar structure (Figure 3.6 b) leads to well-defined scattering peaks oriented in the normal direction of lamellae. The interlamellar spacing determines the scattering angle 2θ (or equivalently, scattering vector q), where the peak emerges (Equation 3.1, Braggs' law). The quality of the ordering and details of the electron density distribution will affect the brightness of the peak, and whether second or higher order peaks are observed. As is the case with rods, the orientation distribution of lamellar domains will be reflected in the azimuthal distribution of diffracted intensity in the scattering pattern.

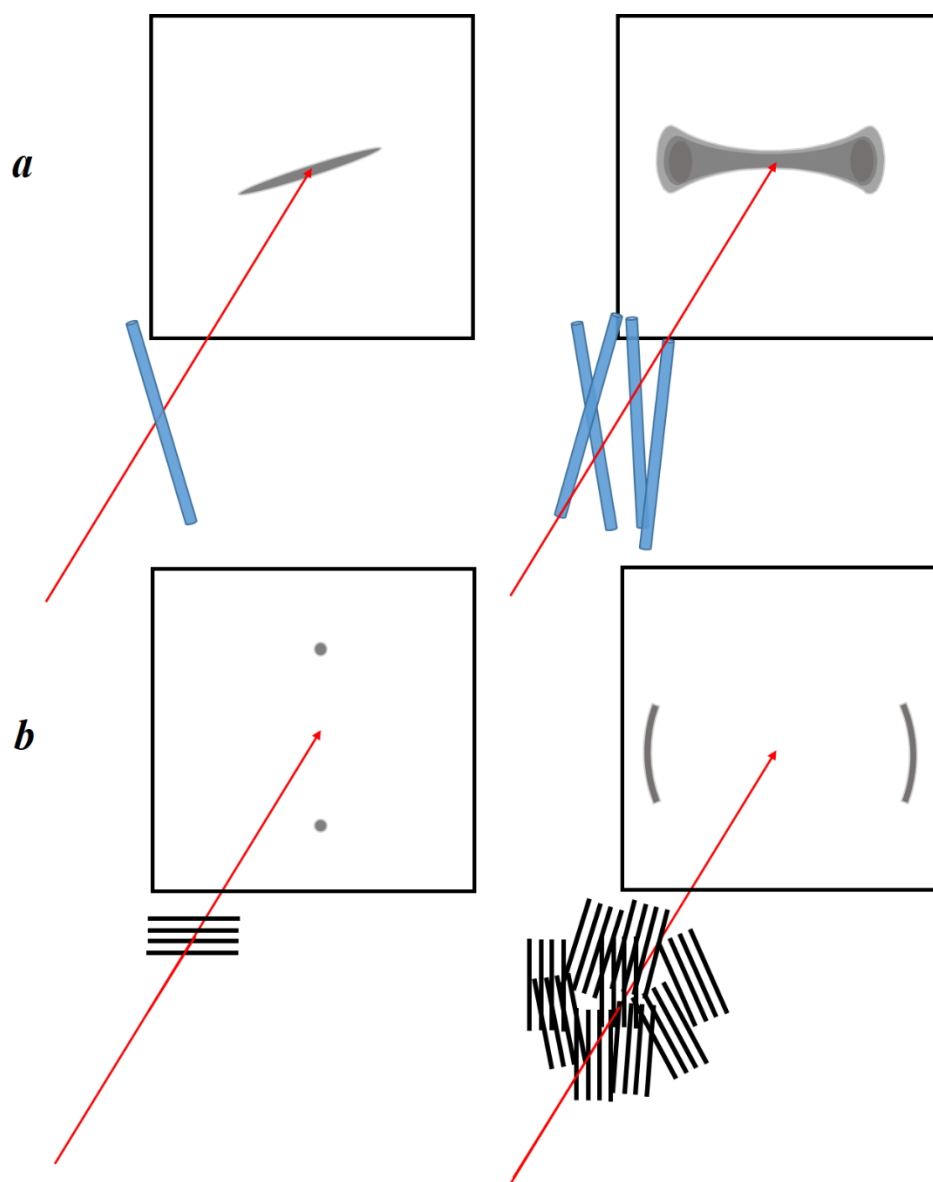


Figure 3.6 Scattering patterns from different anisotropic microstructures (a) rods (b) lamellar stacking

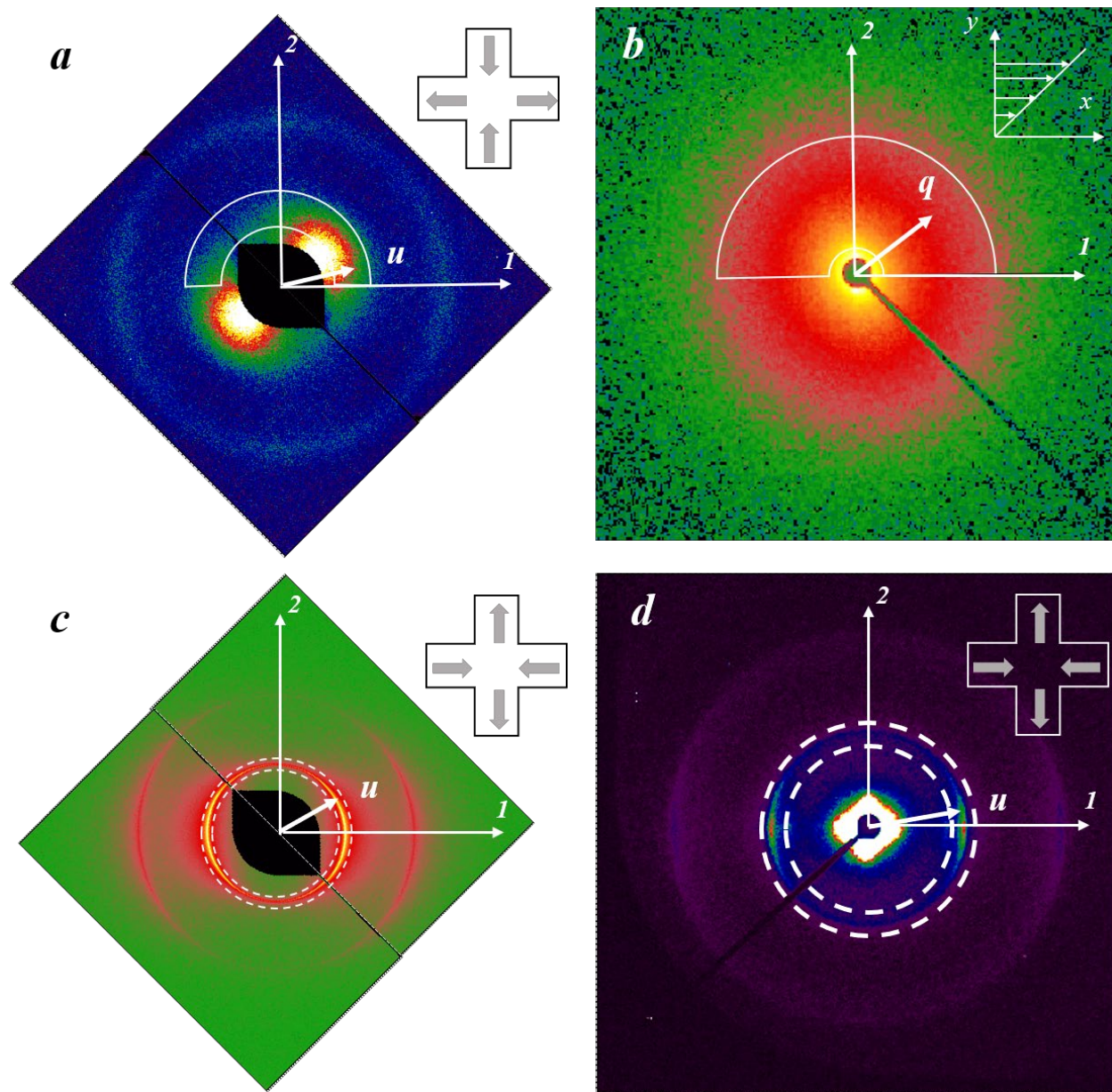


Figure 3.7 Selecting a q range on the scattering pattern for quantitative analysis. (a) 60 mM CTAB with 350 mM NaSal wormlike micelle solution (b) 0.05 wt% CNT suspension in EPON828 scattering under shear flow on SAXS detector (c) 17.4 wt% CTAC/ 20.0 wt% pentanol/ 62.6 wt% water lamellar surfactant (d) 60 mM DDAB lamellar surfactant. (a) and (c) are patched images obtained by rotating the MAXS pattern through 180° .

The microstructures' degree and direction of orientation may be quantified by characterizing the anisotropy of the scattering pattern. For a two-dimensional scattering pattern, two approaches have been used for work discussed in this thesis. The first approach begins by computing an azimuthal distribution of scattering intensity, $I(\phi)$, by averaging over a q -range encompassing the scattering feature of interest (Figure 3.7). Each location on the azimuthal scan may be represented by a unit vector, \mathbf{u} . An average of the dyadic product $\mathbf{u}\mathbf{u}$, weighted by $I(\phi)$, results in a second-moment tensor:

$$\langle \mathbf{u}\mathbf{u} \rangle = \begin{pmatrix} \langle u_1 u_1 \rangle & \langle u_1 u_2 \rangle \\ \langle u_1 u_2 \rangle & \langle u_2 u_2 \rangle \end{pmatrix} = \frac{\int \mathbf{u}\mathbf{u} I(\phi) d\phi}{\int I(\phi) d\phi} \quad (3.16)$$

The subscript 1 and 2 denotes coordinate axes in real and reciprocal space. In shear flow, “1” indicates the flow direction and “2” is the gradient direction. In planar extensional flow, “1” equates to “x” the horizontal direction and “2” equates to “y”, the vertical direction in real space (Figure 3.7). In this definition, the second moment tensor is normalized by the total scattered intensity to eliminate the effect of fluctuations of incident beam intensity.

In the second approach, a second moment tensor is computed directly from the measured intensity $I(\mathbf{q})$, without an intermediate calculation of $I(\phi)$. Specifically, the second moment tensor of scattering vector \mathbf{q} is computed through:

$$\langle \mathbf{q}\mathbf{q} \rangle = \begin{pmatrix} \langle q_1 q_1 \rangle & \langle q_1 q_2 \rangle \\ \langle q_1 q_2 \rangle & \langle q_2 q_2 \rangle \end{pmatrix} = \frac{\int \mathbf{q}\mathbf{q} I(\mathbf{q}) dq_1 dq_2}{\int q^2 I(\mathbf{q}) dq_1 dq_2} \quad (3.17)$$

These two approaches are closely related, and in fact become identical when scattering is concentrated into a diffraction peak at a particular value of q .

As is shown in Figure 3.7, the selection of scattering intensity range for quantitative analysis depends on the scattering characteristics of the sample. For blob scattering (Figure 3.7 *a* and *b*), the lower q limit is set by the beam stop; the upper q limit is set where scattered intensity decreases to near background levels. For well-defined Bragg diffraction peaks emerging at a specific scattering angle q^* in layered lamellar systems, the q -range is chosen as a narrow band close to the diffraction peak (Figure 3.7 *c* and *d*). Using Braggs' law, this q^* is related to the interlamellar spacing through

$$q^* = \frac{2\pi}{d} \quad (3.18)$$

Use of the second moment tensor to characterize orientation results in the loss of detailed information on the sample's orientation distribution function reflected in the full scattering pattern $I(\mathbf{q})$. Still, for patterns such as those found in Figure 3.6, displaying one dominant orientation direction and a smooth azimuthal intensity distribution, the second moment tensor captures the information of greatest interest.

The degree of orientation is quantified by an Anisotropy Factor AF , defined as the difference in the principal values of $\langle \mathbf{u}\mathbf{u} \rangle$ or $\langle \mathbf{q}\mathbf{q} \rangle$.¹¹¹

$$AF = \sqrt{(\langle u_1 u_1 \rangle - \langle u_2 u_2 \rangle)^2 + 4\langle u_1 u_2 \rangle^2} \quad (3.19a)$$

$$AF = \sqrt{(\langle q_1 q_1 \rangle - \langle q_2 q_2 \rangle)^2 + 4\langle q_1 q_2 \rangle^2} \quad (3.19b)$$

The value of AF can vary from 0 to 1, with 0 indicating an isotropic condition and 1 indicating a perfectly oriented situation in which scattered intensity is perfectly concentrated along a single

radial direction. In situations where symmetry dictates that anisotropy must lie along the 1 or 2 axis (such that $\langle q_1 q_2 \rangle = 0$ or $\langle u_1 u_2 \rangle = 0$), a simplified AF can prove advantageous:

$$sAF = \langle u_1 u_1 \rangle - \langle u_2 u_2 \rangle \quad (3.20a)$$

$$sAF = \langle q_1 q_1 \rangle - \langle q_2 q_2 \rangle \quad (3.20b)$$

The value of sAF can range from -1 to 1, corresponding to microstructures aligned from perfectly perpendicular to the flow, to perfectly along the flow.

AF can also be affected by background scattering. One source of background scattering is air surrounding the flow cell, windows in the flow cell, or windows in vacuum pipes upstream or downstream of the sample. In some cases, the sample of interest is a dilute solution or suspension, in which solvent can contribute an isotropic scattering background. The measured intensity is the sum from all such contributions. It is easy to anticipate that the presence of an additional isotropic background will reduce the value of AF , which should ideally describe the anisotropy of the sample scattering free from background effects. In Appendix B, we explore the quantitative impact from isotropic background scattering, and a way to correct it. More complex is the case of anisotropic background scattering, for instance, air scattering that has been projected through the cross-slot flow cell. A correction procedure suitable to this situation will be discussed later in connection with specific experimental results (Section 5.1.2.2).

The orientation angle χ , indicating an average direction of orientation may be determined from the principal directions of $\langle \mathbf{uu} \rangle$ or $\langle \mathbf{qq} \rangle$. In shearing flow, this is normally computed:

$$\chi = \frac{1}{2} \tan^{-1} \left(\frac{2\langle u_1 u_2 \rangle}{\langle u_1 u_1 \rangle - \langle u_2 u_2 \rangle} \right) \quad (3.21a)$$

$$\chi = \frac{1}{2} \tan^{-1} \left(\frac{2\langle q_1 q_2 \rangle}{\langle q_1 q_1 \rangle - \langle q_2 q_2 \rangle} \right) \quad (3.21b)$$

With this expression, the value of χ is constrained to range from -45° to 45° , consistent with the physical constraints of microstructure orientation in shear flow. For more general flows, an alternative equation may be used to compute χ :

$$\chi = \tan^{-1} \left(\frac{-\langle u_1 u_1 \rangle - \langle u_2 u_2 \rangle + \sqrt{(\langle u_1 u_1 \rangle - \langle u_2 u_2 \rangle)^2 + 4\langle u_1 u_2 \rangle^2}}{2\langle u_1 u_2 \rangle} \right) \quad (3.22a)$$

$$\chi = \tan^{-1} \left(\frac{-\langle q_1 q_1 \rangle - \langle q_2 q_2 \rangle + \sqrt{(\langle q_1 q_1 \rangle - \langle q_2 q_2 \rangle)^2 + 4\langle q_1 q_2 \rangle^2}}{2\langle q_1 q_2 \rangle} \right) \quad (3.22b)$$

With this definition, the value of χ may range from -90° to 90° . This version better suits cross-slot flow, where the orientation of microstructure is less constrained than in shear. Note that equation (3.21) can be derived from equation (3.22) using trigonometric identities. As shown in Figure 3.6, scattering features from anisotropic microstructures are typically oriented at right angles to the structure of interest (rod axis; lamellae). As a result, the angles computed from $\langle \mathbf{q}\mathbf{q} \rangle$ according to equation (3.21) or (3.22) will usually be adjusted by 90° in order to faithfully represent the orientation of the structure in physical space.

In addition to the AF and orientation angle described here, other quantities are often used in the literature to quantify anisotropic scattering patterns. One is the Herman's orientation parameter, defined as:

$$\langle P_2 \rangle = \frac{3\langle \cos^2 \phi \rangle - 1}{2} \quad (3.23)$$

When it is used, $\langle P_2 \rangle$ is intended to characterize an orientation distribution function of microstructure in a sample. Theoretically speaking, a complete orientation distribution can be represented as an eigenfunction expression using Legendre spherical harmonics as basis functions. The Herman's orientation parameter is the coefficient for the second order Legendre's polynomial in such an expansion. It describes the degree of orientation and is experimentally related to birefringence, dichroism and fluorescence.¹¹² Like AF , $\langle P_2 \rangle$ takes on values of 0 for a random distribution, and 1 for perfect orientation. However, computation of the average $\langle \cos^2 \phi \rangle$ from an azimuthal scattering intensity distribution, $I(\phi)$, requires that the orientation distribution function exhibit uniaxial symmetry, centered around $\phi = 0$.¹¹³ For the two-dimensional flows considered here, an assumption of uniaxial symmetry is not appropriate. For this reason, we rely on AF and orientation angle—which characterize scattering anisotropy without requiring additional assumption of symmetry—as the primary indicators of the degree and direction of microstructure in this work.

3.4 Two-dimensional scattering pattern analysis

Several software packages may be used to process 2-dimensional x-ray scattering patterns. An earlier practice within the group was to use “fit2d”.¹¹⁴ From the “sav” files attached with the scattering patterns, the x and y coordinates of the beam center, the pixel size of the detector, the sample-to-detector distance were extracted. These parameters were then used in the macro file which batch processed all the scattering image files. Specifically, the “cake” function in fit2d was used to extract intensity as a function of scattering vector q , azimuthal angle ϕ , or of both variables. In the “cake” function, the region for integral was defined by the start and end

azimuthal angles, inner and outer radii (pixel). The radial bin was set at 1 and the azimuthal bin 180 so that $I(\phi)$ was obtained, as introduced in Section 3.3.

As time progressed, we found that the detailed output of the fit2d “cake” function varied in unpredictable ways for different binning choices. Thus, over the course of my residence at Northwestern, we gradually shifted to using custom MATLAB scripts for data analysis and GSAS-II¹¹⁵ for image display.

We will take a SAXS image with 6×6 binning as an example. The SAXS detector provides full resolution 3840×3840 . With 6×6 binning, the file is a 640×640 integer array. The orientation of how the software reads the image file varies from one software package to another. In addition, we also have to keep track of the image file orientation with respect to the real-space orientation. If the observer is located at the sample position and faces the detector, which means the beam travels from the back of the observer to the front, the image file aligns with the pattern on the detector in this perspective. Remaining in this perspective, MATLAB® reads the image file from the upper left corner to the bottom right. We designate i as the row index and j as the column index. In MATLAB®, i and j are integer indices starting from 1 at the upper left corner. The integer coordinate (i, j) of the beam center is determined by surface plotting a sample image and manually examining the intensity near the given beam center in pixel.

Then we can take a sub-image from the whole pattern to reduce the data size for analysis. Normally the sub-image has a dimension of $(N+1) \times (2N+1)$ pixels, with the beam center located at the bottom middle of the sub-image. The N is chosen to be large enough to cover the q range desired for quantitative analysis. More importantly, this sub-image covers a full-range 180° of

data to compute anisotropy. Figure 3.8 illustrates a sub-image with $N = 7$. (In selecting the sub-image, $i = 1$ and $j = 1$ are redefined to correspond to the upper left most pixel in the image.)

We define coordinates x and y in pixels relative to the beam center, related to the intensity array indices i, j by:

$$\begin{aligned} x &= j - N - 1 \\ y &= -i + N + 1 \end{aligned} \quad (3.24)$$

The corresponding scattering vector q can be computed based on the geometry and small angle approximation:

$$\begin{aligned} q_x &= \frac{x \cdot 4\pi \cdot a}{2\lambda \cdot D} \\ q_y &= \frac{y \cdot 4\pi \cdot a}{2\lambda \cdot D} \end{aligned} \quad (3.25)$$

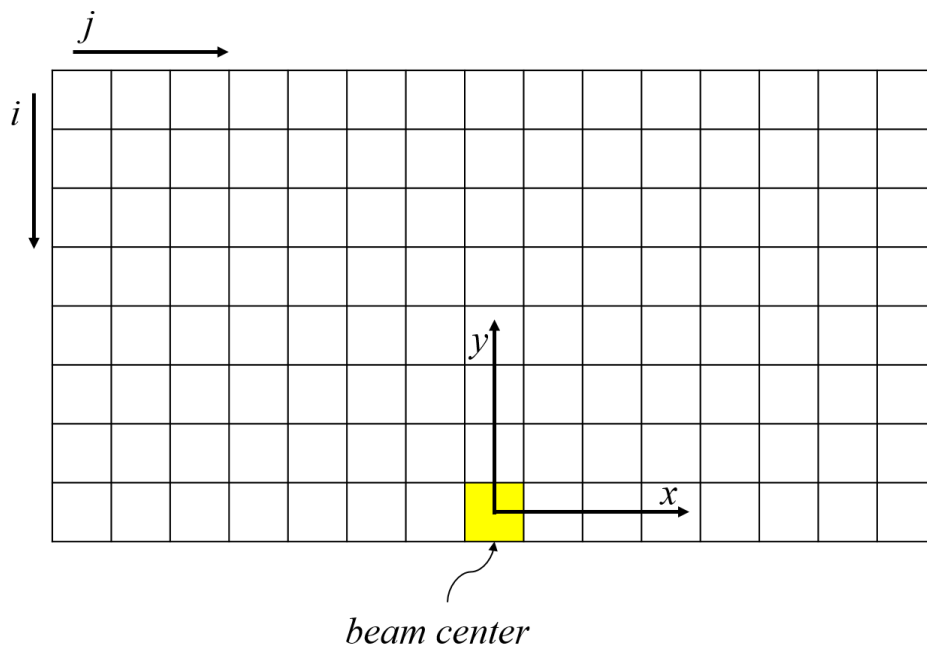


Figure 3.8 An illustration of sub-image of the 2-dimensional scattering pattern for quantitative analysis

Here a is the dimension of a pixel, D is the sample-to-detector distance, and λ is the wavelength of the x-ray beam.

With q_x and q_y determined for each pixel, the components of the second moment tensor can be computed based on the intensities of each pixel. We use a mask function $m(x, y)$ to signify if a particular pixel counts in the analysis. The default $m(x, y)$ equals to zero. If the equivalent q of the pixel (x, y) falls in between the lower and the upper q bounds selected for any particular sample's microstructure, then $m(x, y)$ equals to 1. Equivalently,

$$m(x, y) = 1 \text{ when } q_{lower} \leq \sqrt{q_x^2 + q_y^2} < q_{upper}, x \in [-N, N] \text{ and } y \in [0, N]$$

Thus the components of the second moment tensor can be computed by summing all the intensities on the sub-image, pixel by pixel,

$$\langle q_1 q_1 \rangle = \frac{\sum_{x \in [-N, N], y \in [0, N]} m(x, y) I(x, y) q_x^2}{\sum_{x \in [-N, N], y \in [0, N]} m(x, y) I(x, y) (q_x^2 + q_y^2)} \quad (3.26)$$

$$\langle q_2 q_2 \rangle = \frac{\sum_{x \in [-N, N], y \in [0, N]} m(x, y) I(x, y) q_y^2}{\sum_{x \in [-N, N], y \in [0, N]} m(x, y) I(x, y) (q_x^2 + q_y^2)} \quad (3.27)$$

$$\langle q_1 q_2 \rangle = \frac{\sum_{x \in [-N, N], y \in [0, N]} m(x, y) I(x, y) q_x q_y}{\sum_{x \in [-N, N], y \in [0, N]} m(x, y) I(x, y) (q_x^2 + q_y^2)} \quad (3.28)$$

The second moment tensor components computed by Equations (3.26) - (3.28) are then used to compute anisotropy factor and orientation angle.

Beyond analysis according to the second moment tensor procedure from Section 3.3, it is often helpful to extract 1- d scans of intensity as a function of scattering angle q or azimuthal angle ϕ . Simple algorithms to compute $I(q)$ and $I(\phi)$ from the 2-dimensional intensity array using MATLAB® are described here.

To compute $I(q)$, we usually set the q increment Δq in the mask function to be one pixel wide:

$$\Delta q = \frac{4\pi a}{2\lambda D} \quad (3.29)$$

Then the intensity at a particular scattering vector q is computed as the average of the intensities from all the pixels that satisfy the boundary conditions,

$$I(q) = \frac{\sum_{x \in [-N, N], y \in [0, N]} m(x, y) I(x, y)}{\sum_{x \in [-N, N], y \in [0, N]} m(x, y)} \quad (3.30)$$

Likewise, the intensity as a function of azimuthal angle ϕ can also be computed. The integral step $\Delta\phi$ is usually set at 1° . Again we designate the mask function $m(x, y)$ as the signal if a particular pixel (x, y) should be counted for $I(\phi)$, then

$$\begin{cases} m(x, y) = 1 & \text{when } q_{lower} \leq \sqrt{q_x^2 + q_y^2} < q_{upper} \text{ and } \cos \phi \geq \frac{q_x}{\sqrt{q_x^2 + q_y^2}} > \cos(\phi + \Delta\phi) \\ m(x, y) = 0 & \text{otherwise} \end{cases} \quad (3.31)$$

The intensity at a particular azimuthal angle ϕ can be computed by averaging all the qualified pixels:

$$I(\phi) = \frac{\sum_{x \in [-N, N], y \in [0, N]} m(x, y) I(x, y) (q_x^2 + q_y^2)}{\sum_{x \in [-N, N], y \in [0, N]} m(x, y)} \quad (3.32)$$

Chapter 4 Structural Dynamics of Carbon Nanotube Suspension under Homogeneous Shear and Planar Extensional Flow

4.1 Background

4.1.1 Introduction

Carbon nanotubes (CNTs) have received wide attention due to their exceptional thermal, mechanical and electrical properties, which offer promise for potential applications such as display screens and functional composites. Numerous investigations have been conducted to explore the shear^{116–120} and extensional^{43,121–124} rheology of CNT suspensions or composites through experiments and simulations.^{125–128} CNT dispersion¹²⁹ and flow-induced aggregation or disaggregation^{117,130–132} have been investigated. In addition, many researchers have studied the connection between the electrical properties of CNT suspensions with their rheological behavior,^{124,126,133–138} recognizing that the performance of CNT composite materials will be closely tied to their structure, which, in turn, will be influenced by flow fields encountered during processing. This chapter reports an investigation of CNT suspension microstructure under flow.

Although the behavior of CNTs in the dilute regime is the most basic and fundamental question regarding the dynamics of CNTs, the existing literature mostly emphasizes semi-dilute to concentrated CNT suspensions. Dilute samples produce weak signals, creating higher experimental demands. Studies under extensional flow are also scarce despite its stronger potential capacity to align CNTs and its relevance in material processing. A few studies have been reported with filament stretching¹²² and capillary thinning^{43,123,124} extensional rheometers.

However, these suspensions had to be in the semi-dilute or concentrated regime in order to form a stable liquid bridge, and no structural probe was used.

Many efforts have been made to investigate the impact of flow upon the orientation of CNT composites and suspensions. Fry *et al.*^{65,67,139} first measured anisotropy of CNT suspensions subjected to shear flow using birefringence and dichroism. Their measurements of semi-dilute CNT suspensions were made using parallel plates in the velocity-vorticity plane of shear flow, leading to a quantitative relationship between the degree of alignment and the Peclet number. They also found that the predicted alignment is much stronger than the experimental observation, due to polydispersity and tube deformation.⁶⁵ Pujari *et al.*^{95,97} investigated the orientation of CNT suspensions in both flow-gradient (1-2) and flow-vorticity (1-3) plane of shear flow in dilute and concentrated regimes using SAXS and WAXS. X-ray methods may be applied across a wide range of CNT concentrations, offering an advantage over optical techniques (birefringence, dichroism and light scattering) in these opaque materials. They found that orientation produced in 1-2 plane is higher than that in 1-3 plane, and orientation measured by WAXS is higher than orientation observed through SAXS. They also found a partial relaxation of orientation, despite the fact that the large CNTs used in their work should be non-Brownian. Tung *et al.*¹⁴⁰ studied the orientation of SWCNT nanocomposite, aligned by melt fiber spinning, using *ex situ* SANS and SAXS. Natale *et al.*⁶⁶ recently studied the shear dynamics of CNT suspensions from dilute to semi-dilute regime, in both 1-2 plane and 1-3 plane using dichroism. However, in the high Peclet number regime, the orientation angle relative to the flow direction was abnormally high, indicating that CNTs did not align close to flow

direction during strong shear. A semi-flexible model for representing CNTs was introduced to rationalize this observation.

In this chapter, we report a micro-structural study applying SAXS to investigate a dilute MWCNT/epoxy suspension reported in Natale *et al.*,⁶⁶ subjected to both shear and planar extensional flow. Shear flow is generated using a home-built cone and plate device⁹⁴ which offers accessibility to the orientational dynamics of CNTs in the 1-2 plane (Section 2.2), while planar extensional flow is generated using the cross-slot flow cell developed in this work (Section 2.1). Flow-induced CNT orientation is captured by small-angle x-ray scattering, which interrogates structure at length scales of tens of nanometers. For our samples, this is comparable to the diameter of the CNTs, but only a fraction of their contour length. Unlike the reports of Natale, our x-ray scattering data show an orientation angle within a few degrees of the flow direction at high Peclet number, suggesting relatively straightforward orientation dynamics. We thus also present comparisons between our data and an orientation model representing CNTs as rigid rods, including the hydrodynamic impact from flow and Brownian rotational diffusion.

4.1.2 Relaxation in Brownian systems

Brownian diffusion will cause flow-induced orientation to relax upon flow cessation. For monodisperse particles, this should follow a single-exponential relaxation process, where the relaxation time is inversely proportional to the rotational diffusivity of the particle. Due to the polydispersity of the CNT suspension studied here, a stretched exponential function is used to characterize the relaxation of anisotropy after flow, following the approach of our collaborators.

66,141

$$AF(t) = AF_0 e^{-(\alpha t)^\beta} \quad (4.1)$$

A stretched exponential function can describe global relaxation in a system containing many independently relaxation species, each of which decays exponentially with a specific fixed relaxation time. The parameter α has dimensions of inverse time, while β reflects the breadth of the relaxation time distribution. An average relaxation time is determined for the system as: ¹⁴¹

$$\tau = \int_0^{\infty} e^{-(\alpha t)^\beta} dt = \frac{1}{\alpha\beta} \Gamma\left(\frac{1}{\beta}\right) \quad (4.2)$$

The average relaxation time is related to rotational diffusivity by: ¹⁴²

$$D_r = (6\tau)^{-1} \quad (4.3)$$

Based on the measured rotational diffusivity, a Peclet number can be defined, which characterizes the competition between the orienting effect of shear or extensional flow and the randomizing influence of Brownian rotation:

$$Pe = \frac{\dot{\gamma}}{D_r} \quad \text{or} \quad Pe = \frac{\dot{\epsilon}_{nom}}{D_r} \quad (4.4)$$

Casting data in terms of the Peclet number allows comparison of results across samples prepared in different dispersing matrix, and across results measured by different methods.

4.2 Materials

MWCNT (multi-walled carbon nanotube)/epoxy suspensions have been widely used as model systems in previous research. ^{95,97,143–147} The samples studied here were provided by our collaborators Natale *et al.*, ⁶⁶ and the procedure for preparing CNT suspension can be found in their reports. The average length of the CNTs was 670 nm and the mean value of the outer diameter was 15 nm. The CNTs were polydisperse with an aspect ratio ranging from 4 to 314. ¹⁴⁴

The outer diameter falls within the length scales probed by small-angle x-ray scattering, while the average length is much larger. Perfectly aligned tubes should thus produce a narrow streak in a 2-dimensional SAXS pattern (Figure 3.5). Electron micrographs show that the CNTs used here are not perfectly straight, but are kinked and bent (Figure 4.1). Two epoxies were used as the dispersion matrix. EPON 815c has a viscosity of 0.56 Pa·s at 25 °C and EPON 828 has a

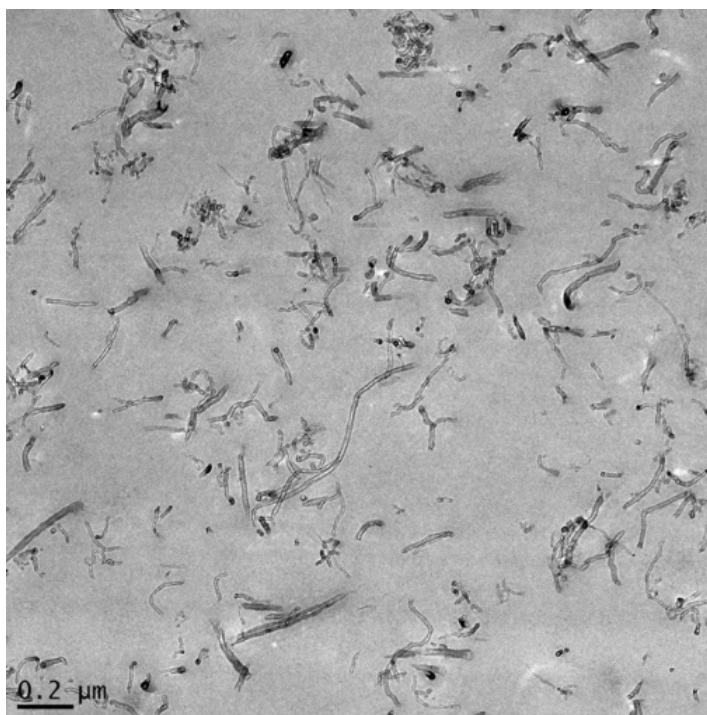


Figure 4.1 a TEM micrograph of 3 wt% CNT suspension (figure reprinted from [66]). The CNTs are long tubes with varying lengths and curvature or bending present.

viscosity of 12.5 Pa·s and a density of 1.16 g/ml at 25 °C. All the suspensions we studied are Newtonian, due to the low CNT concentration.

Natale's experiments utilized the more viscous EPON 828. With this epoxy, we studied CNT suspensions at a concentration of 0.05 wt%. The volume fraction of CNTs in this suspension was determined as 3.6×10^{-4} through the densities of carbon nanotubes and of the

dispersing agents. According to the dynamic concentration regimes defined by Doi and Edwards¹⁴⁸ and Larson,¹⁴⁹ our collaborator has determined⁶⁶ the upper limit of the CNT's volume fraction for the dilute regime is 3.8×10^{-4} and the upper limit for the semi-dilute regime is 1.74×10^{-2} . Thus, the 0.05 wt% suspension in EPON 828 is dilute. Based on the CNT's dimensions and matrix viscosity, this suspension should have an inverse of rotational diffusivity of 314 seconds.

To expand the range of experimentally accessible Peclet number, another set of CNT suspensions dispersed in a lower-viscosity epoxy (EPON 815c) was also prepared at the same concentrations of 0.05 wt % and 0.17 wt%. Based on the lower viscosity of this epoxy, the rotational diffusivity for the dilute 0.05 wt% dispersion is predicted to be 14.3 seconds at 25°C. The more concentrated 0.17 wt% suspension should be in the semi-dilute regime.

4.3 Methods

The CNT suspensions' behavior in shear flow and planar extensional flow was studied in the cone and plate shear cell, developed by Caputo *et al.*,⁹⁴ and the cross-slot flow cell introduced in Chapter 2. The shear flow cell can apply shear rates from 0.1 to 100 s⁻¹. This is the shear rate range used for the EPON 815c suspension. With the addition of a gear reducer, we studied the more viscous CNT suspension in EPON 828 with shear rates ranging from 0.002 to 100 s⁻¹. Using the 1-2 plane shear flow cell setup, we studied the dynamics of CNTs during shear inception, shear reversal, relaxation, and steady shear flow. In the cross-slot flow cell, the range of extensional flow rates was limited due to the large viscosity of the suspension matrix. Furthermore, a significant lag, usually over 15 seconds, exists between the time point when the syringe pump is set to stop and the time point when flow at the stagnation point of the cross-slot

cell ceases. This is attributed to compliance in the flow cell tubing and the high pressures generated with viscous samples. Therefore, cross-slot flow cell measurements were limited to steady state, taking care to assure that the flow is equilibrated at each condition prior to initiating data acquisition. The lower limit of the experimentally accessible flow rate is determined by the time duration for the flow in the cross-slot cell to reach the designated rate initiated by the syringe pump. The upper limit of the experimentally accessible flow rate is determined by the maximum force that a syringe can tolerate due to the pressure drop caused by the highly viscous matrix. For the experiments reported here, we applied flow rates between 0.09 ml/min and 9 ml/min, corresponding to nominal extensional rates of 0.3 to 30 s⁻¹ with the EPON 815c suspension, and flow rates from 0.0014 ml/min to 0.64 ml/min, corresponding to nominal extensional rates of 0.005 to 2 s⁻¹ with the EPON 828 suspension.

X-ray scattering experiments were conducted at APS Station 5 ID-D. The energy of the beam is 15 keV (wavelength 0.8265 Å). The incident beam size is 100 μm × 100 μm. The width of the beam is one tenth of the slot's width in the cross-slot cell. The SAXS detector was set with a 6 × 6 binning as a balance between image quality and data transfer rate.

After analyzing anisotropies and orientation angles of CNTs from initial experiments, we came to realize that beam exposure can strongly affect the anisotropy measured in CNTs under flow. Prolonged exposure to a particular region of the sample could significantly reduce the measured anisotropy (Figure 4.2), though the orientation angle was found to be less affected. The dip and rise of AF at $t = 100$ second and beyond is caused by the transit through the beam of a sample region that had been overexposed by repeated previous experiments. Then a “fresh” unexposed region is brought into the beam at $t = 120$ second, leading to a sharp rise in measured

anisotropy. The red line at $t = 130$ second indicates the reversal of shear flow. After the flow is reversed, the trend of AF looks almost like a mirror reflection of the AF before reversal, as the overexposed portion of the sample is swept back into the beam. Recognition of the potential for beam damage led us to establish protocols to reduce the cumulative exposure time, by spreading exposures more uniformly across all regions of the sample and limiting the number of experiments performed on each fresh sample loading.

The results presented in later sections are produced across several experimental runs. In June 2015, we tested CNT suspension in Epoxy 815c subjected to both homogenous shear and

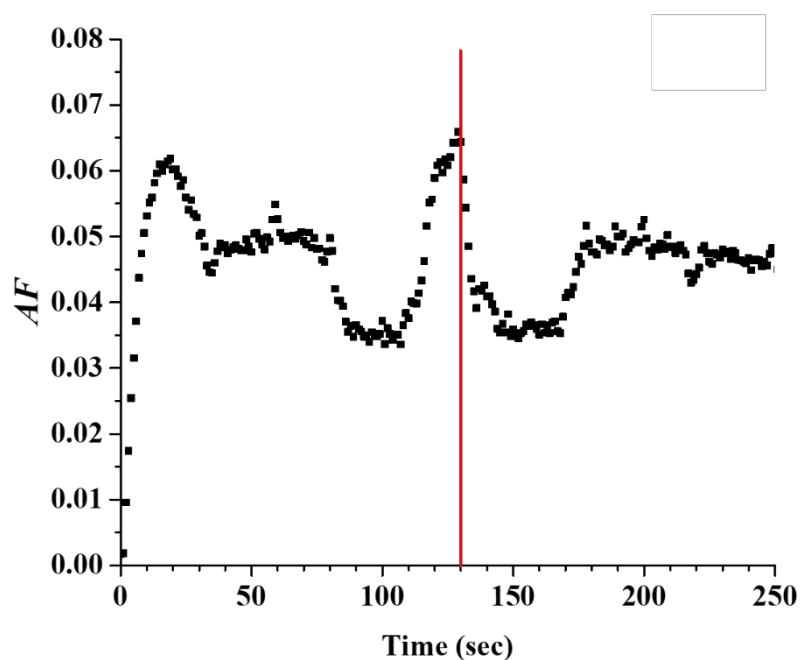


Figure 4.2 Time evolution of anisotropy factor measured in 0.05 wt% CNT suspension in EPON 828 using SAXS, subjected to a shear rate of 0.25 s^{-1} . Flow direction is reversed at $t = 130$ second. Data collected at an exposure time of 0.4 second and a frequency of 1 frame/second during experiments conducted in March 2015.

planar extensional flow. The exposure time was set at 1 second for planar extensional flow or 2 seconds for shear flow. In December 2015, we studied the 0.05 wt% dilute suspension in EPON 828 extensively, subjected to both shear and planar extensional flow. The exposure time was 0.8 second for all the experiments in shear flow and 1 second in planar extensional flow.

To determine the data collection frequency, we used a “non-overlapping exposure” guideline. In shear flow, the data collection frequency is 1 second/frame during shear inception and steady shear for rates above 0.1 s^{-1} . When shear rates were under 0.1 s^{-1} , the displacement of the sample became so small that the beam continued exposing the same region of the sample from one image to the next. Therefore, we reduced the collection frequency to 2, 4, 10 or 20 seconds per frame so that, prior to the next exposure, at least 80% of the originally exposed area has moved away from the beam spot. When the beam must be fixed at one spot to track relaxation, we separated the whole process into three stages to minimize beam exposure: during the first stage when rapid relaxation occurred the scattering patterns were collected at 1 second/frame. During the second stage when relaxation was still present but not as rapid as the first stage the scattering patterns were collected at 3 seconds/frame. During the final stage when the relaxation has mostly finished, scattering patterns were collected at 10 seconds/frame. In planar extension, scanning across different locations of the cross-slot cell was performed the opposite to the flow direction, so that measurements were performed on “fresh” suspension.

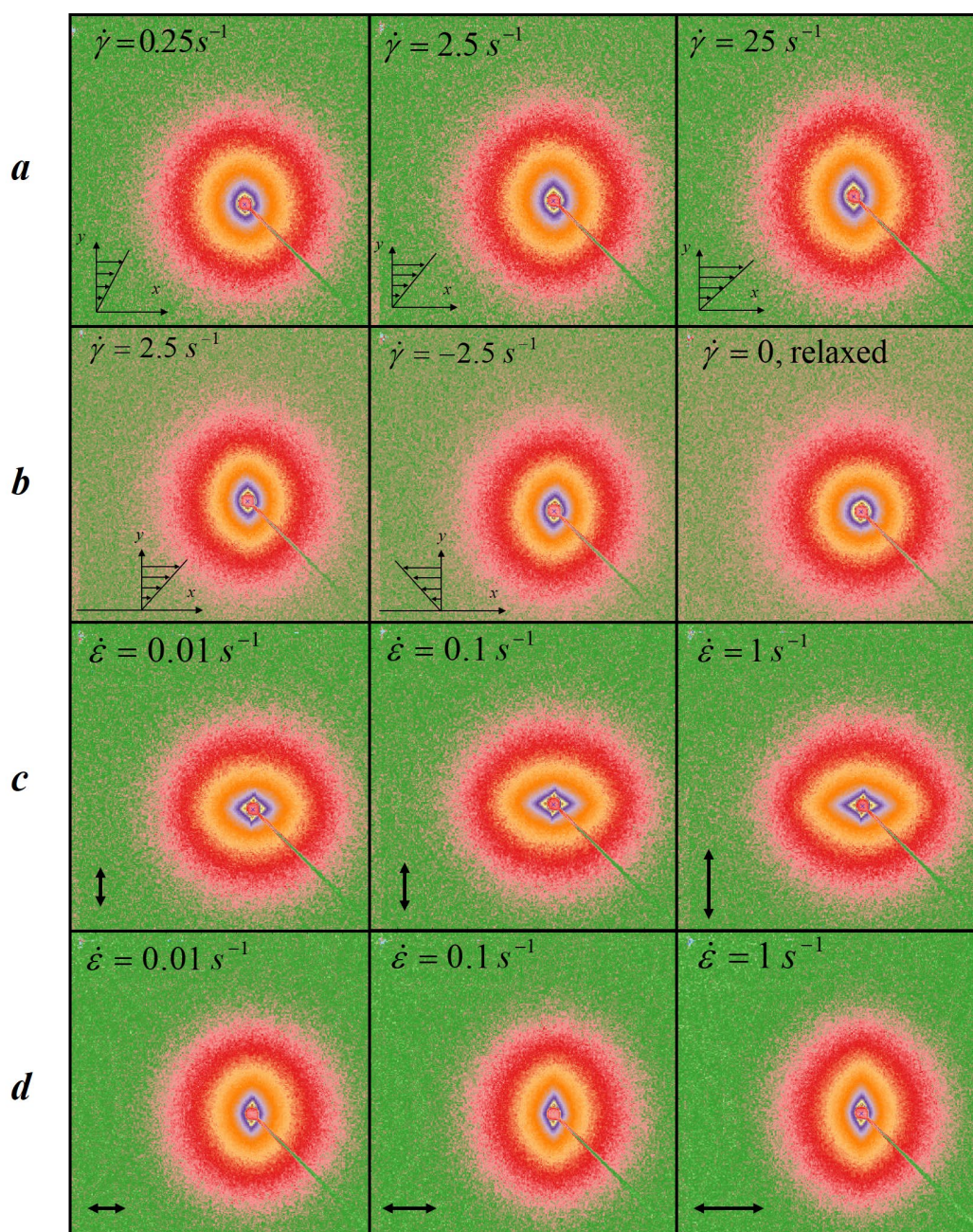


Figure 4.3 Representative SAXS patterns measured in 0.05 wt% CNT suspension in EPON 828 under flow (a) Homogeneous shear at different rates; (b) Shearing in opposite directions, and then after relaxation; (c) Planar extension along vertical direction at different rates; (d) Planar extension along horizontal direction at different rates

SAXS patterns illustrate anisotropy in CNT orientation induced by flow (Figure 4.3). SAXS patterns collected under homogeneous shear (Figure 4.3 *a*) become increasingly anisotropic as shear rate rises. At high rates, the anisotropy is oriented nearly vertically, indicating average CNT orientation is close to the horizontal flow direction. The axis of the elliptical pattern flips as the shear direction is reversed (Figure 4.3 *b*). After relaxation, the CNT suspension returns to an isotropic condition. SAXS patterns measured in planar extension (collected at the geometrical center of the cross-slot flow cell) show increasing anisotropy at higher extension rates (Figure 4.3 *c* and *d*). At comparable deformation rates, the planar extensional flow leads to a visibly higher degree of anisotropy than shear. For both flow directions, the scattering patterns deform perpendicularly to the extension direction, indicating CNT alignment along the stretching direction. To quantify the orientation dynamics of these suspensions, all scattering patterns are processed using the analysis methods introduced in Section 3.3 and 3.4 to compute anisotropy factor and orientation angle. The domain for such quantitative analysis was half of an annulus above the beam center with q ranging from 0.035 nm^{-1} to 0.23 nm^{-1} (Figure 3.7 *b*).

4.4 Results and discussion

4.4.1 Structural dynamics of 0.05 wt% dilute CNT suspension in EPON 828 during shear flow inception, reversal and relaxation

Though the shear flow cell can apply shear rates from 0.002 to 100 s^{-1} , the transient dynamics of CNT orientation was only accessible within a smaller flow rate range where the shear rate is high enough to induce significant structural response but not so high that the

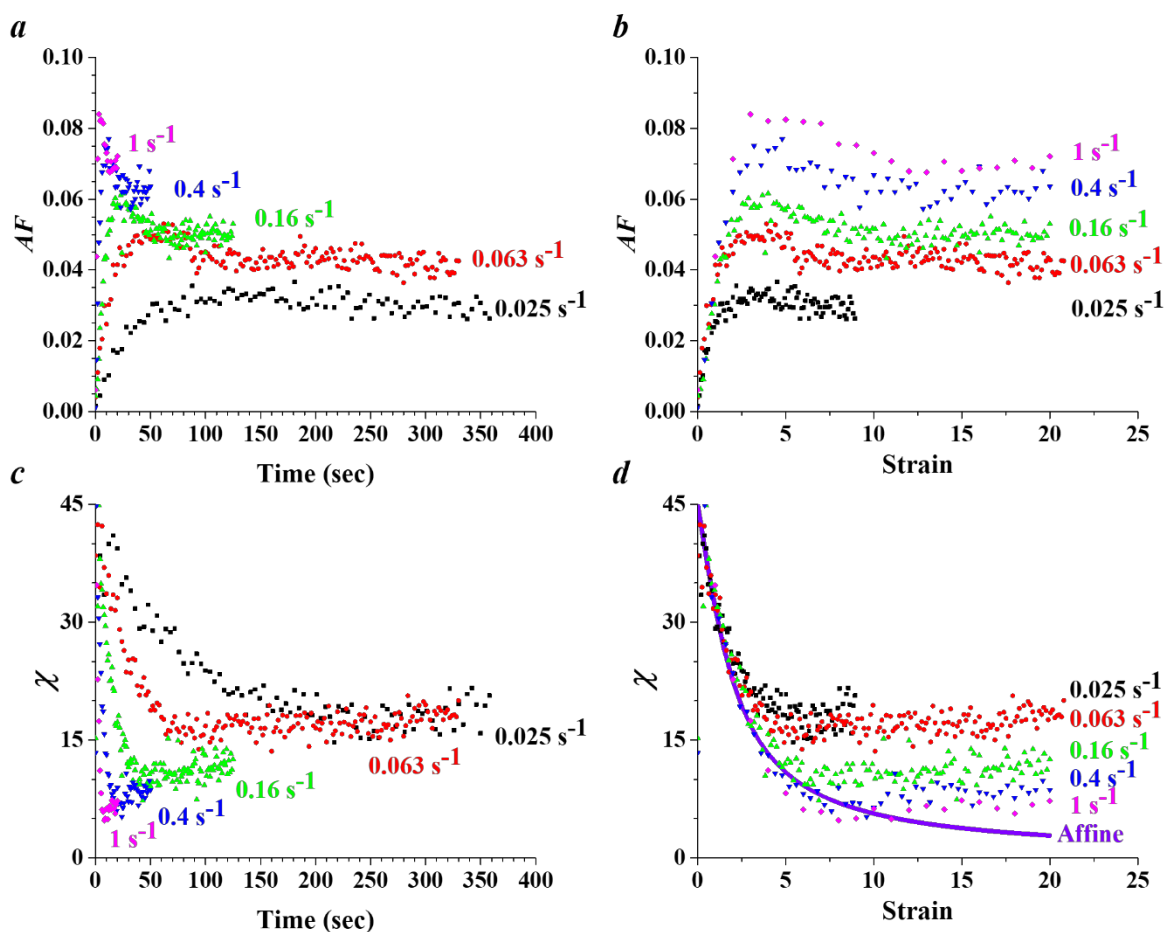


Figure 4.4 Transient evolution of AF and χ measured in 0.05 wt% CNT suspension in EPON 828 during shear flow inception at various shear rates, plotted against both time and strain.

dynamics is too fast to capture. An additional constraint is imposed by the reduction in data acquisition rate at low shear rates to avoid excessive sample exposure to the x-ray beam.

Figure 4.4 presents the transient evolution of AF and χ during flow inception, plotted against both time and strain. A total of 20 strain units were applied for shear rates above 0.063 s^{-1} . At low shear rates, flow was applied for 360 seconds, long enough to reach steady state conditions. At the lowest rate 0.025 s^{-1} , the AF rose as shear flow was initiated and later reached a steady state plateau and stabilized roughly at 0.03. With increasing shear rate, the steady-state AF increases, and the overshoot of AF become more pronounced. This resembles the stress overshoot phenomenon often observed in flexible polymers subjected to shear flow. Figure 4.4 *b* replots the AF data as a function of applied shear strain. The AF data overlap at small strains, indicating the initial development of CNT orientation is governed solely by the applied strain. Figure 4.4 *c* shows that the average orientation angle of CNTs always start at 45° with respect to the flow direction, and then rapidly decreases, as CNTs increasingly align along the flow direction. (An initial orientation angle of 45° is ubiquitous in the microstructure of complex fluids in shear flow, and follows directly from the principal axes of deformation in shear geometries.) Ultimately, the orientation angle stabilizes at a steady state value that decreases with increasing shear rate. Figure 4.4 *d* demonstrates again that the initial orientation dynamics are governed by the applied shear strain. This solid curve presents the orientation angle predicted for an affine orientation of microstructure in a shear deformation:

$$\chi = \frac{1}{2} \tan^{-1} \left(\frac{2}{\gamma} \right) \quad (4.5)$$

It is clear that CNTs initially experience affine reorientation upon the inception of shear flow.

However, the orienting influence of shear is balanced against rotational diffusion, which acts to randomize orientation. The steady state AF and χ are determined by a balance between these two

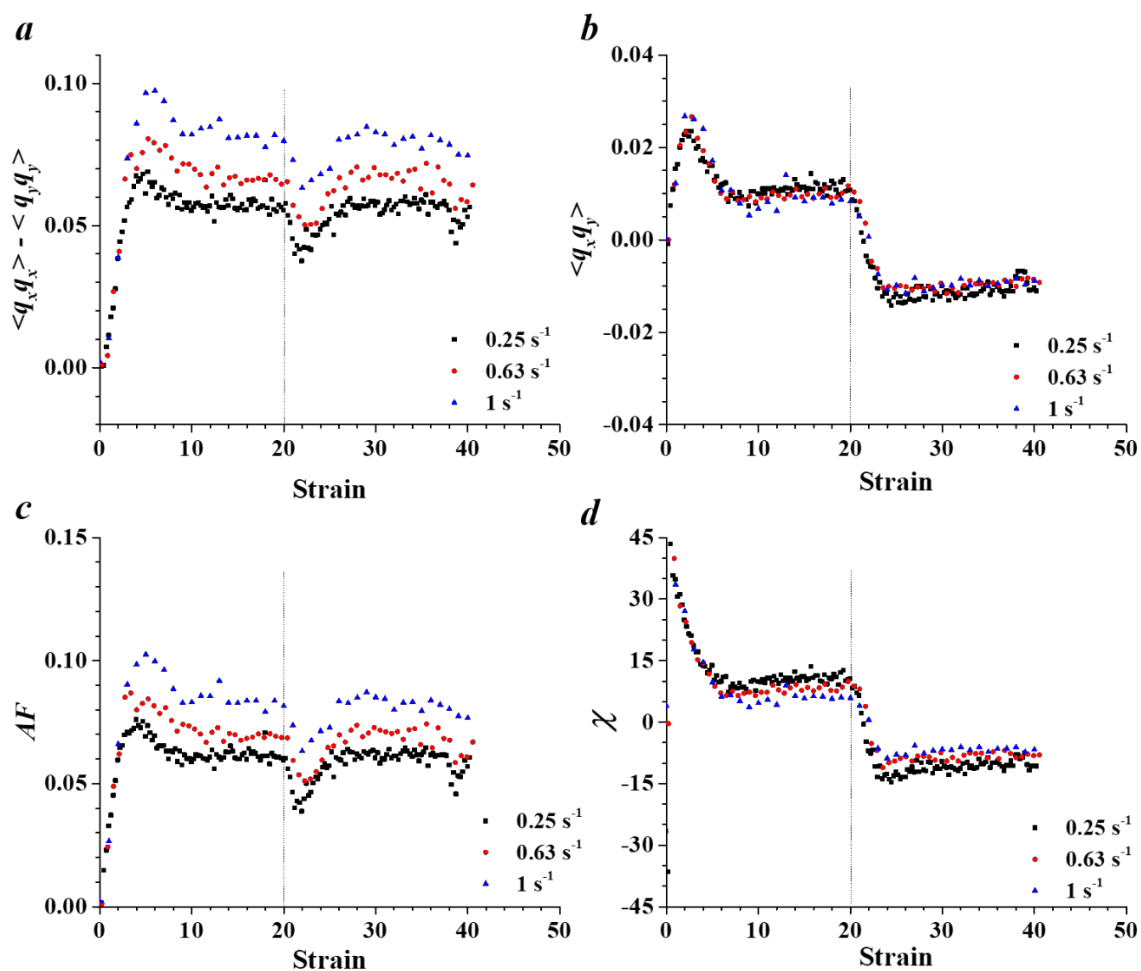


Figure 4.5 Transient evolution of the components of the second moment tensor, AF and orientation angle measured in 0.05 wt% CNT suspension in EPON 828, during shear reversal experiments.

processes. With increasing shear rate (Peclet number), the orienting influence of the flow increases in dominance, and the affine deformation prediction is more closely followed.

Figure 4.5 presents the dynamics of the CNT suspension subjected to shear reversal at different rates of 0.25, 0.63, and 1 s⁻¹. The suspension was first sheared for a total of 20 strain units to establish steady state, and then sheared at the same rate but in the opposite direction for another 20 strain units. The first 20 strain units of shearing again reveal orientation dynamics characteristic of shear inception. The components of second moment tensor and AF all grow from zero, and experience overshoots prior to reaching steady state. Over this limited shear rate range, $\langle q_x q_y \rangle$ shows no discernable shear rate dependence. Thus, the increasing steady state value of AF is driven by the increasing anisotropy in the normal components of $\langle \mathbf{q}\mathbf{q} \rangle$. Upon reversal of shear flow, CNTs reorient to the new flow condition. AF and $\langle q_x q_x \rangle - \langle q_y q_y \rangle$ both temporarily decrease and then return to the prior steady state values after roughly 6 strain units. The orientation angle χ and $\langle q_x q_y \rangle$ change signs, indicative of the reorientation observed in the scattering pattern (Figure 4.3 *b*). At steady state, the degree of orientation of CNTs is only affected by the strength of the shear flow. Switching the direction of shearing only alters the direction of orientation.

We investigated the relaxation of CNTs subjected to shear rates from 0.01 to 100 s⁻¹. The relaxation of AF is fit to a stretched exponential function. To achieve closer fits, we allowed a positive baseline in the equation:

$$AF(t) = AF_0 e^{-(\alpha t)^\beta} + b \quad (4.6)$$

Baseline values from fit were typically below 0.005. We attribute the need for these small baseline values to weak parasitic scattering that leads to small residual SAXS anisotropy.

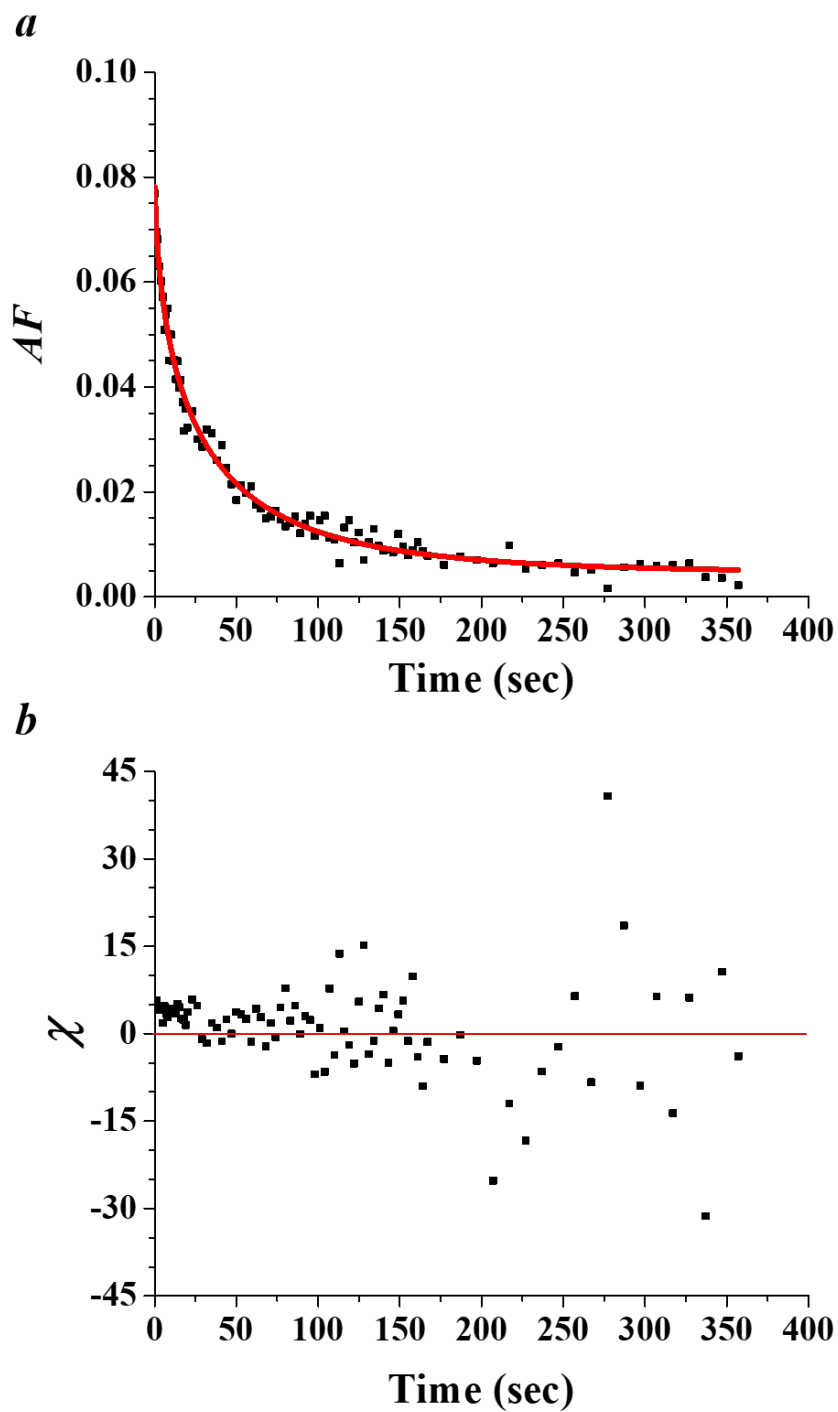


Figure 4.6 Representative data for anisotropy factor and orientation angle measured in 0.05 wt% CNT suspension in EPON 828 upon cessation of shear flow at a rate of 1.6 s^{-1} . Solid curve indicates stretched exponential fit of the data (Equation 4.6)

Figure 4.6 demonstrates representative relaxation data for anisotropy factor, and the stretched exponential fit, together with the relaxation of orientation angle. The orientation angle remains essentially constant during relaxation, although it exhibits increasingly large fluctuations due to the fact that χ becomes undefined as both the numerator and denominator in the right-hand side of Equation (3.22) tend towards zero during relaxation.

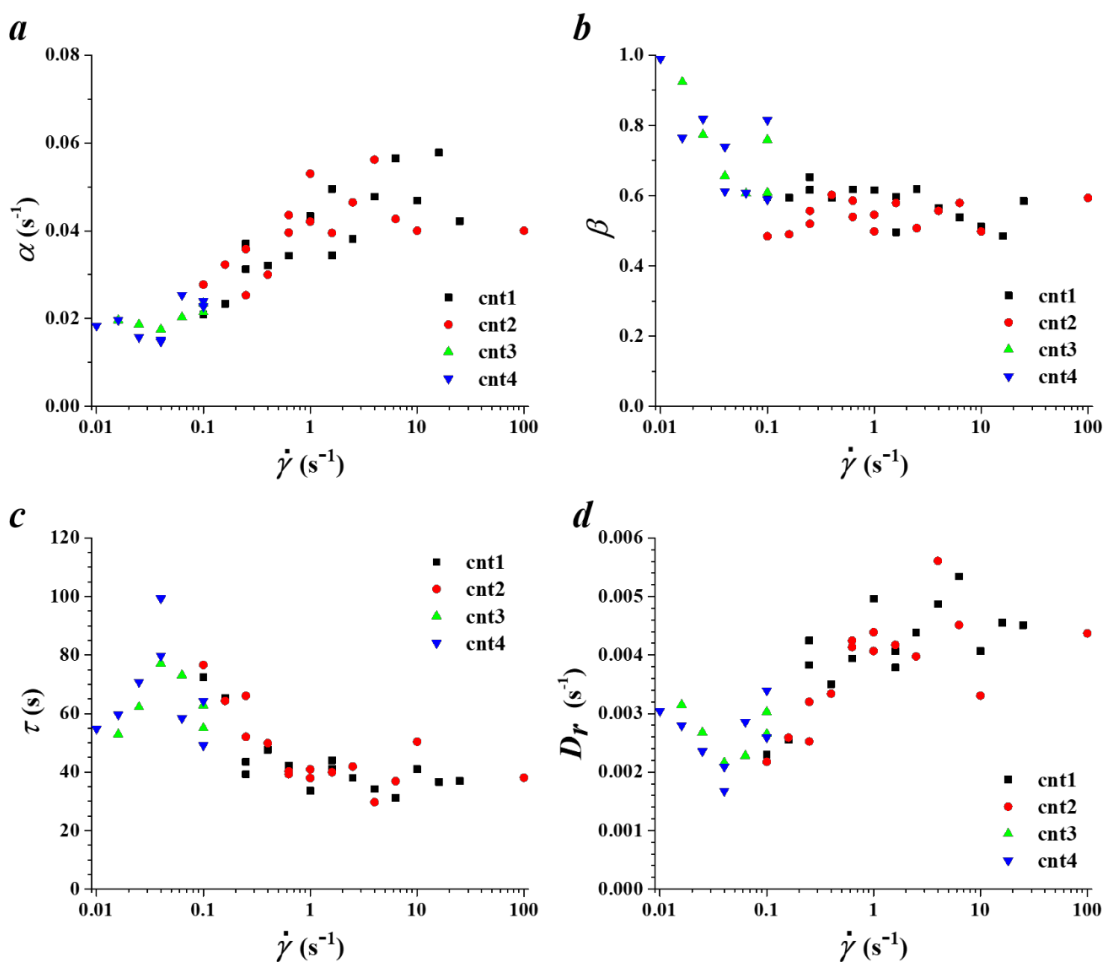


Figure 4.7 Fitting parameters α (a) and β (b), and the average relaxation time (c) and rotational diffusivity (d) determined from SAXS measurements on 0.05 wt% CNT suspension in EPON 828

Figure 4.7 *a* and *b* present the stretched exponential fitting parameters α and β defined by Equation 4.1. Given the fitting parameters α and β , the average relaxation time τ and the rotational diffusivity D_r could be computed according to Equation 4.2 and 4.3, plotted in Figure 4.7 *c* and *d*. The parameter α increases with shear rate, starting from roughly 0.02 at 0.01 s⁻¹ at low rates, and increasing to values around 0.05 s⁻¹. A naïve interpretation of α as the inverse of a relaxation time¹⁵⁰ suggests that the relaxation time decreases with increasing shear rate. The stretching exponent β is related to the distribution of relaxation times. When β approaches 1, Equation 4.1 reduces to single-mode exponential relaxation. As β decreases, the breadth in the relaxation time distribution relative to the characteristic relaxation time increases.¹⁴¹ The β we obtained from fitting the relaxation of *AF* starts close to 1 at low rates, then decreases to roughly 0.6 at higher rates. Based on the stretched exponential fitting parameters, the average relaxation time $\langle\tau\rangle$ shows a generally decreasing trend, settling into a value of around 40 seconds at shear rates of 1 s⁻¹ and above.

A monodisperse dispersion of rod-like particles should exhibit a single relaxation time, associated with the rotational diffusivity of the particles. We attributed the more complex behavior found in these fitting parameters to the polydispersity of the CNT dispersion. At low shear rates, only the longest CNTs in the system respond to the shear deformation and align with the flow, while shorter CNTs remain largely unoriented. Thus, the observed relaxation dynamics are biased towards the longer CNTs in the system, with a longer relaxation time and a narrower distribution of relaxation times (β close to 1). When shear rate increases, progressively smaller CNTs are aligned by the shear flow and contribute to the anisotropy of the whole system. Therefore, with increasing shear rate, the relaxation reflects a broader distribution of particle

sizes, leading to a decreasing value of β . This decrease of β should cease once the shear flow is strong enough to induce orientation for all the CNTs in the system. Thereafter β remains unchanged because increasing shear rate does not introduce new contributing population of CNTs. The β values determined from the stretched exponential fitting agreed with this proposition, dropping from near 1.0 to 0.6 as shear rate increases from 0.01 to 0.1 s^{-1} , and remaining relatively stable at higher rates. Under this proposition, the average relaxation time should decrease as shorter CNTs join the relaxation, and become constant at higher rates. These expectations are largely borne out in Figure 4.7 *c*.

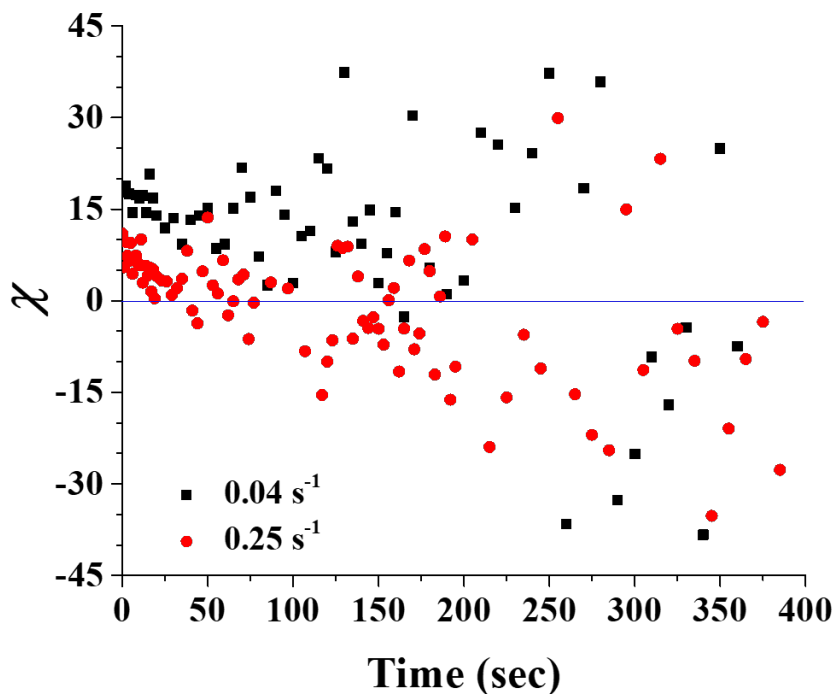


Figure 4.8 Relaxation of orientation angle data upon shear flow cessation at 0.04 and 0.25 s^{-1} , measured in 0.05 wt% CNT suspension in EPON 828

This complex relaxation behavior, attributed to the polydisperse CNTs in the suspension, is reinforced by the relaxation of orientation angle data at lower shear rates (Figure 4.8). At these weak flow conditions where CNTs are not thoroughly aligned, it is reasonable to speculate that the longer CNTs are better aligned at an angle closer to flow while the shorter CNTs are less oriented, at a relatively larger angle with respect to flow. Upon flow cessation, the shorter CNTs relax faster than the longer CNTs. Thus the orientation angle data experience a small decline at the initial stage of relaxation, as the orientation of shorter CNTs completely relax away while the longer CNTs still remain aligned, as the only contribution to the anisotropy of the whole system. As relaxation further progresses, the longer CNTs also lose their orientation. Thus the orientation angle data become noisy and undefined at long times.

To represent the average behavior of the full suspension, we take 40 seconds as the average relaxation time for our dilute CNT suspension in EPON 828. According to this value, the inverse of rotational diffusivity was 240 seconds. Our collaborators⁶⁶ studied the relaxation of orientation in the same CNT suspension using dichroism. For a shear rate of 10 s^{-1} , they reported $\alpha = 0.04 \text{ s}^{-1}$, $\beta = 0.54$, in good agreement with Figure 4.7. As discussed by Natale *et al.*, the value of rotational diffusivity associated with these values is consistent with predictions for dilute rod-like particles.¹⁴⁸

4.4.2 Spatial distribution of orientation of 0.05 wt% CNT suspension in EPON 828 measured in cross-slot flow

We now turn to the studies of this same CNT suspension in cross-slot flow. The degree and direction of orientation has been mapped throughout the cross-slot flow (Figure 4.9). A vector plot is used to illustrate the impact of flow on the distribution of particle orientation,

where the length of each vector is proportional to the magnitude of AF , and the direction of the vector illustrates the average orientation angle of CNTs. Under quiescent conditions, the AF is negligibly small (< 0.02) throughout the cell thus no orientation was present. For cross-slot flow with a nominal extensional rate of 1 s^{-1} along the horizontal direction (Figure 4.9 *b*), there is evidence of CNT alignment in the vertical slots along the incoming flow. This arises due to the shear in the plane Poiseuille flow in the slot. As fluid approaches the stagnation point, planar extension induces a realignment, promoting CNT orientation along the stretching direction. Horizontal alignment persists as fluid exits the cross-slot flow cell to the left and right. When the extension axis was changed to the vertical direction, a similar behavior pattern of CNTs is observed, simply flipped 90 degrees. (Figure 4.9 *c*).

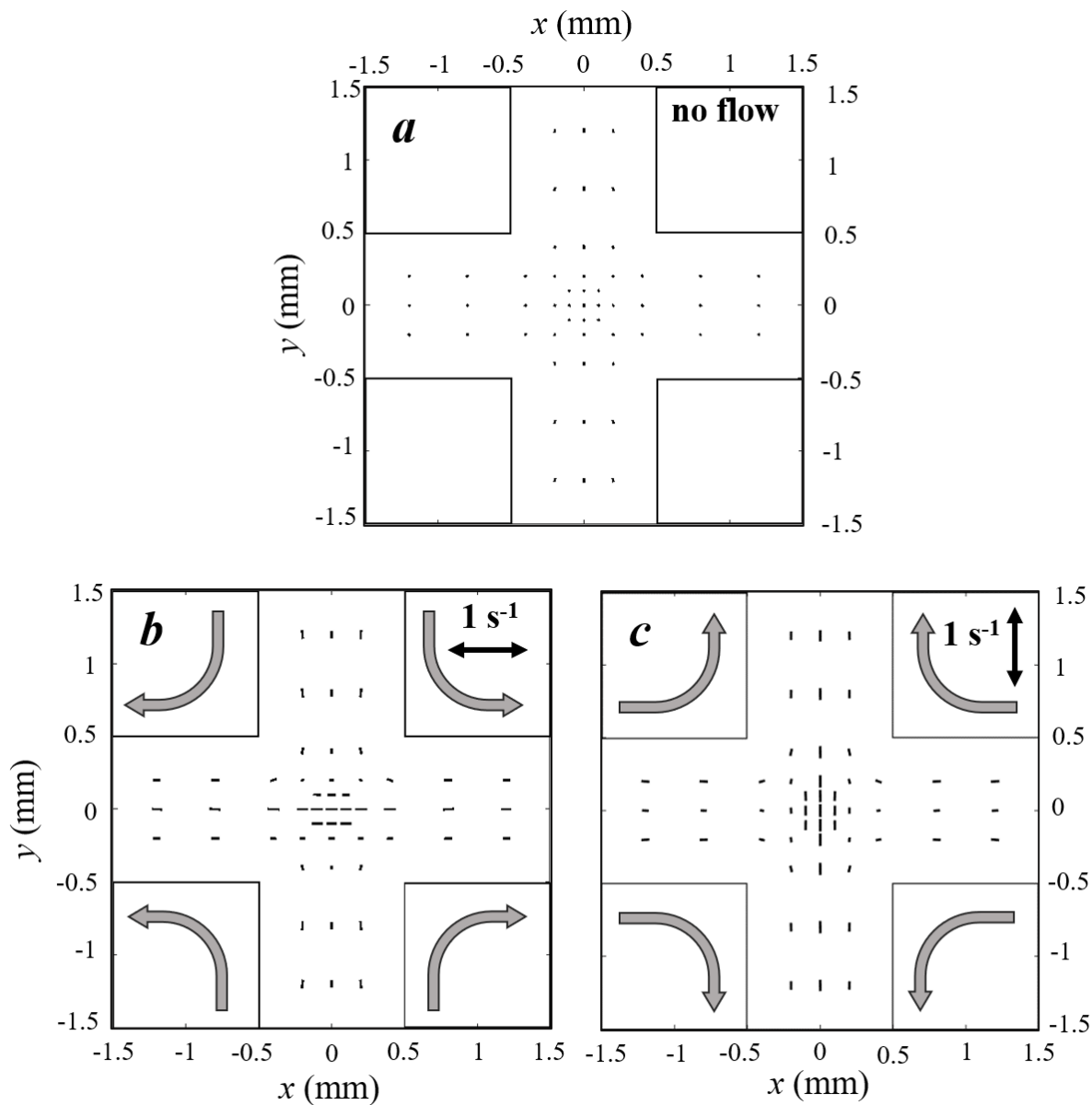


Figure 4.9 The degree and direction of orientation measured via SAXS in a 0.05 wt% CNT suspension in EPON 828 subjected to (a) no flow (b) planar extension along horizontal direction, and (c) planar extension along vertical direction

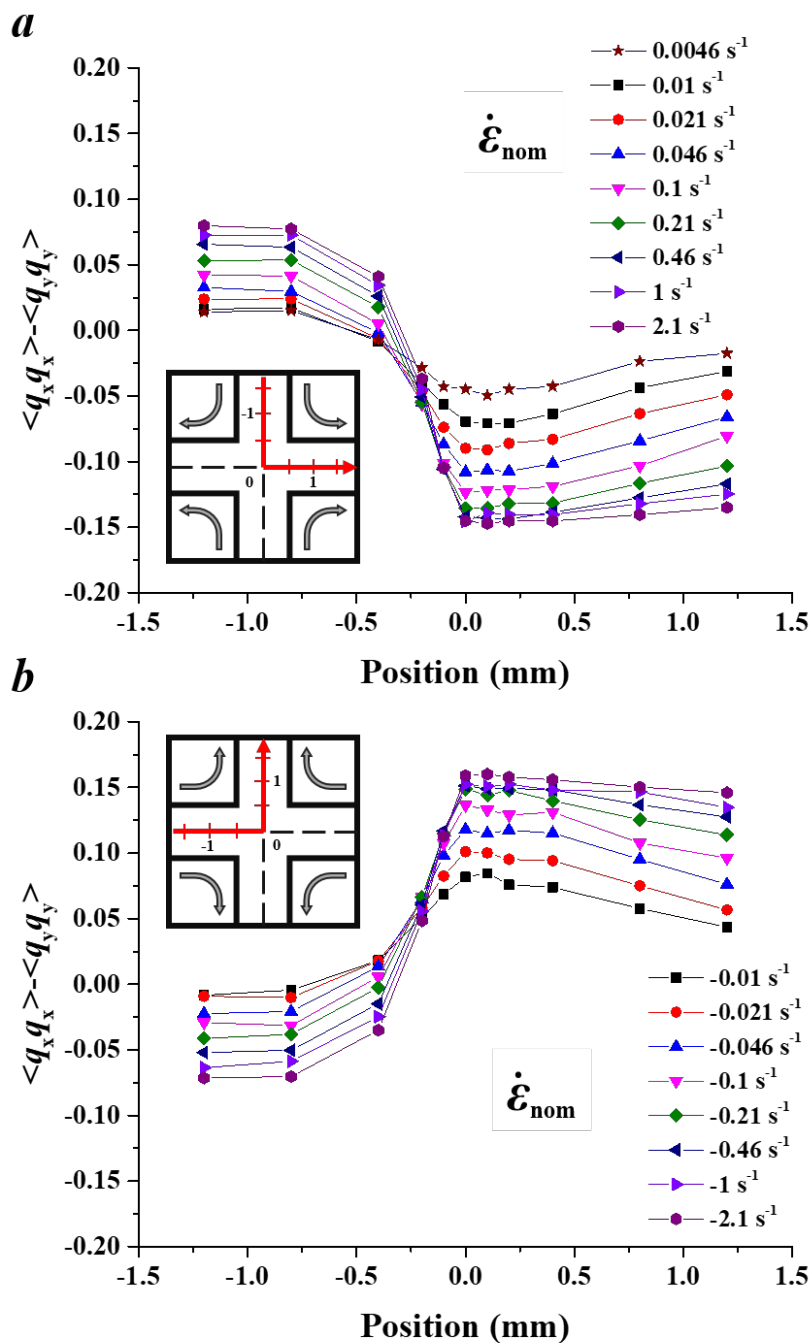


Figure 4.10 Evolution of simplified AF in 0.05 wt% CNT suspension in EPON 828, measured along the centerline of cross-slot flow. The origin is defined at the stagnation point. Negative positions correspond to distance upstream of the stagnation point, while positive positions are measured downstream of the stagnation point. (a) Stretching along horizontal direction, denoted by positive nominal extensional rates. (b) Stretching along vertical direction, denoted by negative nominal extensional rates.

Figure 4.10 examines the evolution of orientation in greater detail by plotting the anisotropy factor measured along the centerline. Due to flow symmetry, we use the simplified anisotropy factor defined in Equation 3.17. Here, positive values reflect CNT alignment along the vertical direction, while negative values reflect horizontal alignment. Upstream, before the suspension has entered the intersection, some degree of orientation is observed even though the Poiseuille flow in the slots should not present velocity gradient along the centerline. However, the finite width of the beam (1/10 of the channel width) means that some of the illuminated fluid is subjected to weak shearing away from the precise centerline. In addition, parasitic velocity gradients along the beam direction, produced by the presence of the Kapton® windows, can also induce some alignment. (The shearing flow in the upstream slots of the flow cell is discussed in detail in Section 4.4.3.2 below.) As the suspension enters the intersection, the orientation flips direction, reflected in the observed sign change of $\langle q_x q_x \rangle - \langle q_y q_y \rangle$, and reaches a maximum at the stagnation point. High CNT orientation is preserved while the suspension remains within the intersection of the cross slots. After the suspension exits the intersection, and enters the downstream slit flow, relaxation of flow-induced CNT orientation occurs. As extension rate increases, the extent of the observed relaxation decreases, owing to the shorter residence time in the downstream slits at higher flow rates.

4.4.3 Steady-state behavior of 0.05 wt % CNT suspension in EPON 828

This section considers steady state measurements of flow-induced orientation. We begin by comparing steady results from homogeneous shear flow to at the stagnation point of cross-slot flow, to directly compare the orienting capabilities of shear and extension. Next, we consider that steady shear flow data may, in principle, also be extracted from the fully-developed slit flow that

is present upstream of the intersection in the cross-slot flow cell. Finally, we compare our x-ray measurements of orientation against rheo-optical data previously published for this suspension by our collaborators.

4.4.3.1 Steady-state dynamics in shear versus planar extensional flow

For the 0.05 wt% CNT suspension in EPON 828, anisotropy in shear flow increases from nearly zero at low rates to values close to 0.1 at high rates (Figure 4.11 *a*). Correspondingly, the orientation angle decreases from 45° as $\dot{\gamma} \rightarrow 0$, to near 0° as $\dot{\gamma} \rightarrow \infty$; (Figure 4.11 *b*) The low rate limit of 45° reflects the fact that the first perturbations from isotropy are orientated along the principal stretching axes of shear flow. In planar extension, anisotropy increases strongly with increasing nominal extensional rate, greatly exceeding the anisotropy factor measured in shear at comparable deformation rates. The orientation angle in extension is near zero, as expected from the symmetry of planar extensional flow.

Flow-induced anisotropy is found to saturate at high rates in both shear and planar extension, suggesting that the Peclet number has grown large enough that the suspensions have achieved the maximum possible degree of flow-induced orientation. Figure 4.11 *a* shows that planar extension promotes higher anisotropy than shear. Although this fits the qualitative expectation that extension is more effective than shear at promoting microstructural alignment, this nonetheless requires further explanation, since rigid rods, are predicted to achieve *comparable* degree of alignment in both shear and extension at high Peclet number. In addition, the anisotropy factors measured in either shear or extension are not particularly large. As discussed below in Section 4.4.4, both observations may be rationalized in light of the crooked and bent nature of the tubes used here.

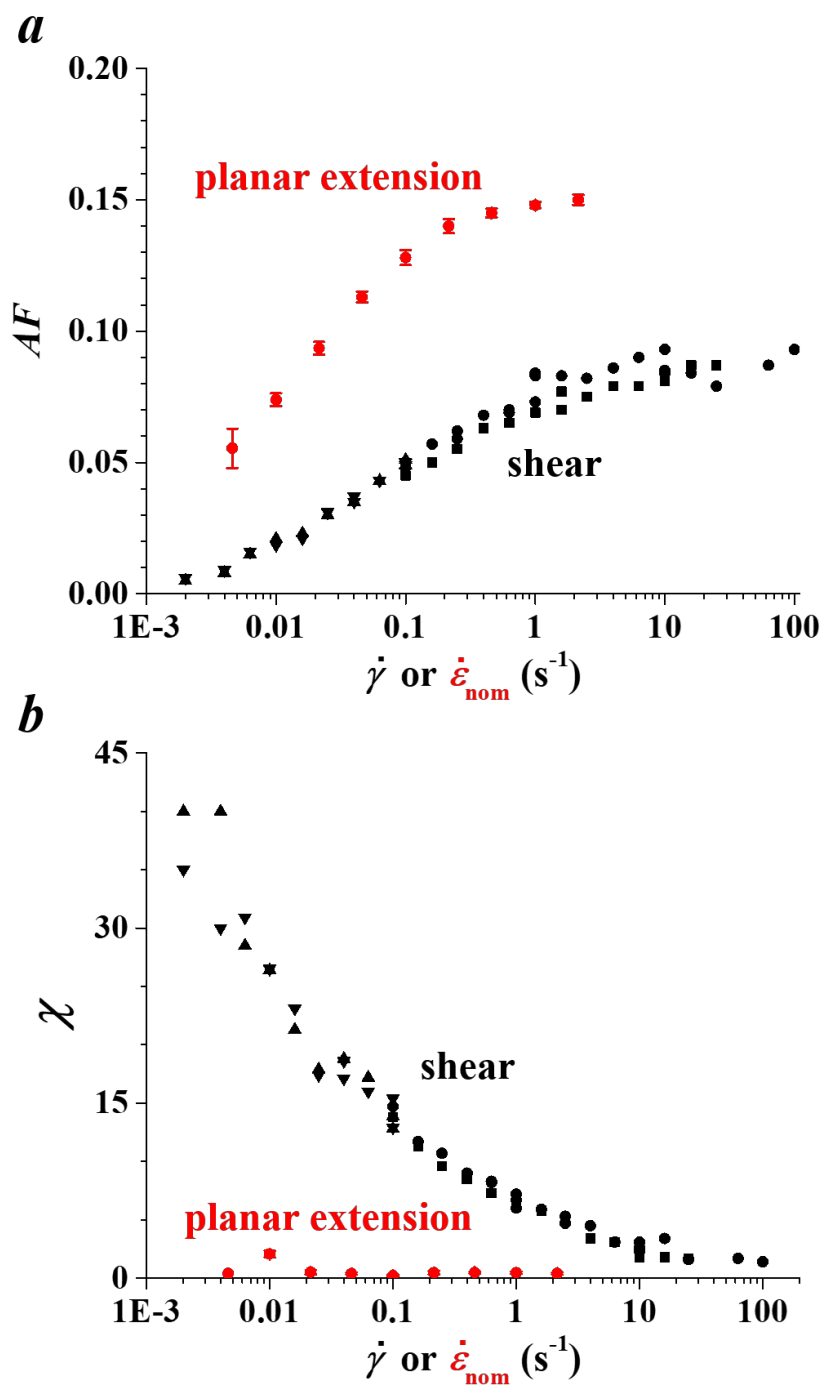


Figure 4.11 Steady state anisotropy factor and orientation angle measured in 0.05 wt% CNT suspension in EPON 828 in both homogeneous shear and planar extension. Different symbols in the shear flow data represent repeated measurements with different sample loadings.

4.4.3.2 Steady-state plane Poiseuille shear in upstream slots

The steady-state shear flow behavior of this CNT suspension has been measured directly using the cone and plate shear cell, but can also be examined in the upstream slots in the cross-slot flow cell. It is worthwhile to compare the steady-state behavior from these two scenarios, as this helps us to verify our assumption that the cross-slot flow cell has a sufficiently high aspect ratio to produce a quasi-two-dimensional planar extensional flow, and that the inlet channels are sufficiently long to produce fully-developed, steady flow conditions.

As discussed in Chapter 2, the aspect ratio (thickness/width) of the cross-slot flow cell is crucial measure of the fidelity of the cross-slot flow cell to the assumption of a two-dimensional flow (Figure 2.2). The aspect ratio for our flow cell is 5. The dilute CNT suspension in EPON 828 we studied is Newtonian across the flow rate regime probed. The Reynold numbers for different flow rates were computed and are all well below 1. As a result, the slot flow present upstream of the channel intersection should be a simple laminar, pressure-driven plane Poiseuille flow (Figure 4.12 *a*).

The shear rate in the upstream channels can be estimated by assuming a parabolic velocity profile (Figure 4.12 *a*) in the slots, neglecting the velocity variation along the beam path (flow cell depth):

$$v_x(y) = \frac{3Q}{4tb^3} (b^2 - y^2) \quad (4.7)$$

From this, the shear rate at some distance y away from the centerline is computed as:

$$\dot{\gamma}(y) = -\frac{3Q}{2tb^3} y \quad (4.8)$$

In these expressions, $b = \frac{1}{2}w = 0.5$ mm, while $t = 5$ mm.

In our cross-slot flow experiments, x-ray data were collected at locations 0.8 and 1.2 mm upstream of the stagnation point, and at $y = \pm 0.2$ mm relative to the centerline (Figure 4.12 *b*).

Orientation angle data extracted from x-ray measurements at these locations are adjusted to reflect the CNT orientation angle relative to the local shear flow direction.

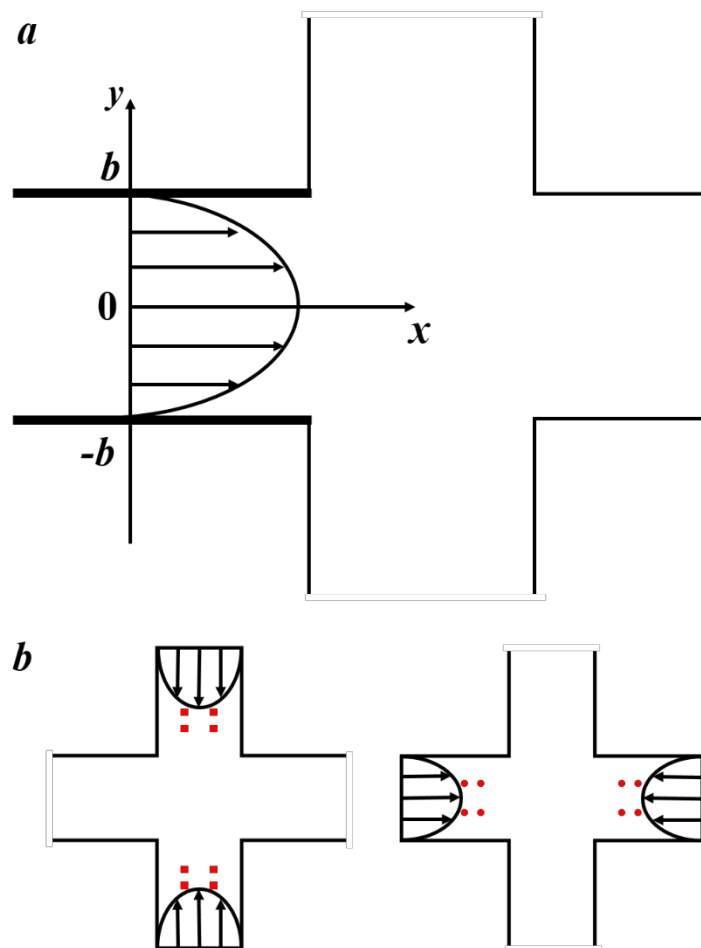


Figure 4.12 (a) Schematic of parabolic Poiseuille velocity profile expected in fully-developed slit flow upstream of the slot intersection. (b) Specific locations at which x-ray data collected in cross-slot flow are used to extract steady shear flow measurement of anisotropy and orientation angle

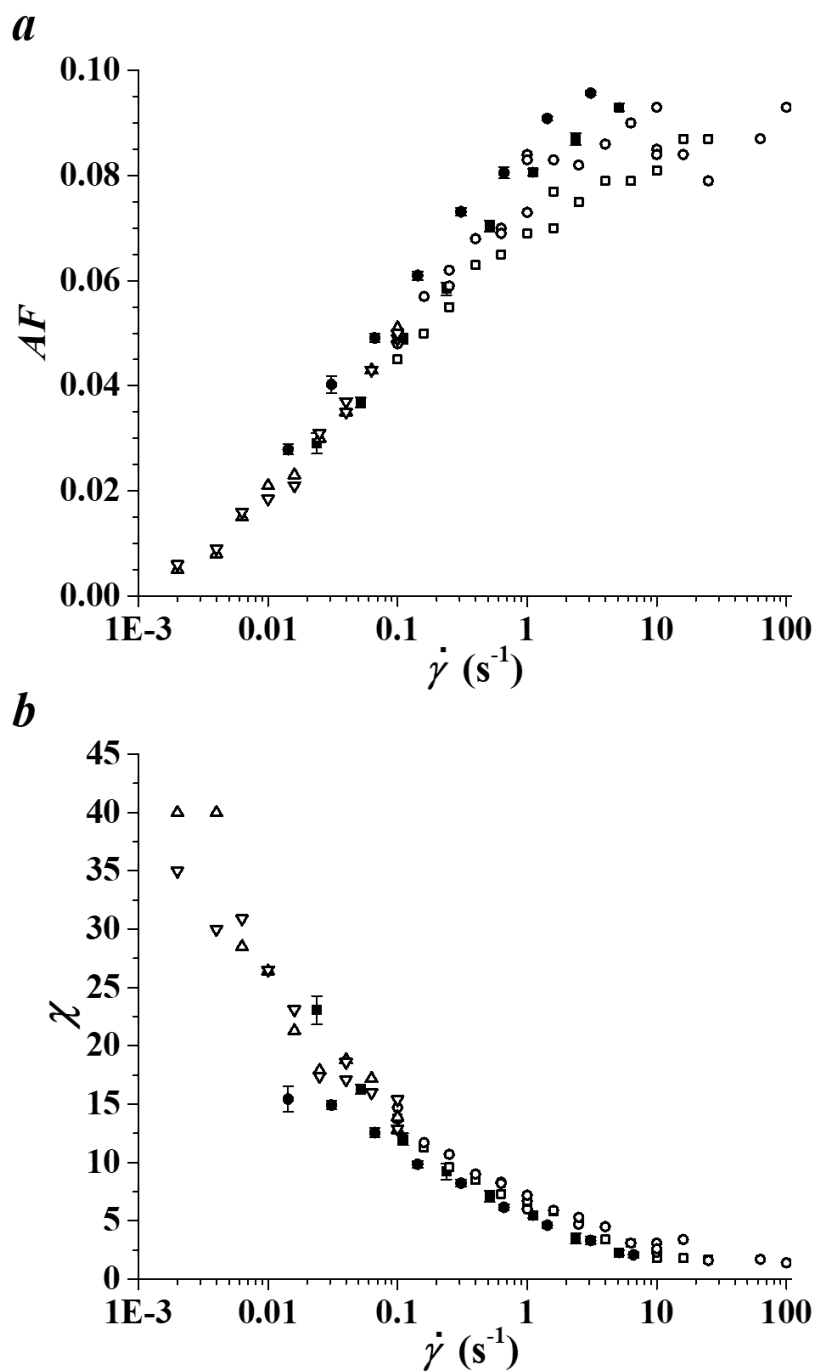


Figure 4.13 Shear flow-induced anisotropy factor (*a*) and orientation angle (*b*) in 0.05 wt% CNT suspension in EPON 828, measured in homogenous shear (open symbols) and in the upstream channels of the cross-slot flow cell (filled symbols)

Figure 4.13 compares steady shear flow orientation data obtained using the 1-2 plane cone and plate shear cell, and the upstream channels in cross-slot flow. Anisotropy factor and orientation angle data obtained using completely different flow geometries are generally consistent. This agreement provides powerful evidence of the reliability of these steady shear flow data. It also highlights that the larger anisotropy found in planar extension (Figure 4.11) is real, and not some artifact associated with differences between the cross-slot and cone-and-plate flow cells. Finally, this agreement confirms that an aspect ratio of 5 is sufficiently large to be able to treat the cross-slot flow as pseudo-two-dimensional, since this assumption is embedded in Equations 4.7 and 4.8.

4.4.3.3 Steady-state orientation measured by SAXS versus dichroism

In addition to x-ray scattering, the steady-state behavior of dilute CNT suspensions in EPON 828 was previously investigated by our collaborators using dichroism. They used an optical Couette cell to perform dichroism measurements in the flow-gradient (1-2) plane. To compare with their data, we have converted shear rate to Peclet number, using Equation 4.4 and a value of $D_r = 0.00417 \text{ s}^{-1}$, based on an average relaxation time $\tau = 40 \text{ sec}$ informed from high shear rate relaxation data (Figure 4.7). This mirrors their methods for characterizing D_r and computing Pe . After scaling, their dichroism data match with our x-ray data quite well, showing an expected trend of increasing orientation with increasing Pe . However, the orientation angle data differ significantly. At high Peclet number, the SAXS orientation angle approaches a value near zero degrees. Conversely, the orientation angle from dichroism experiments decrease, and remains above 15 degrees of the highest Peclet number studied, where SAXS data show an orientation angle of just 2 - 3°.

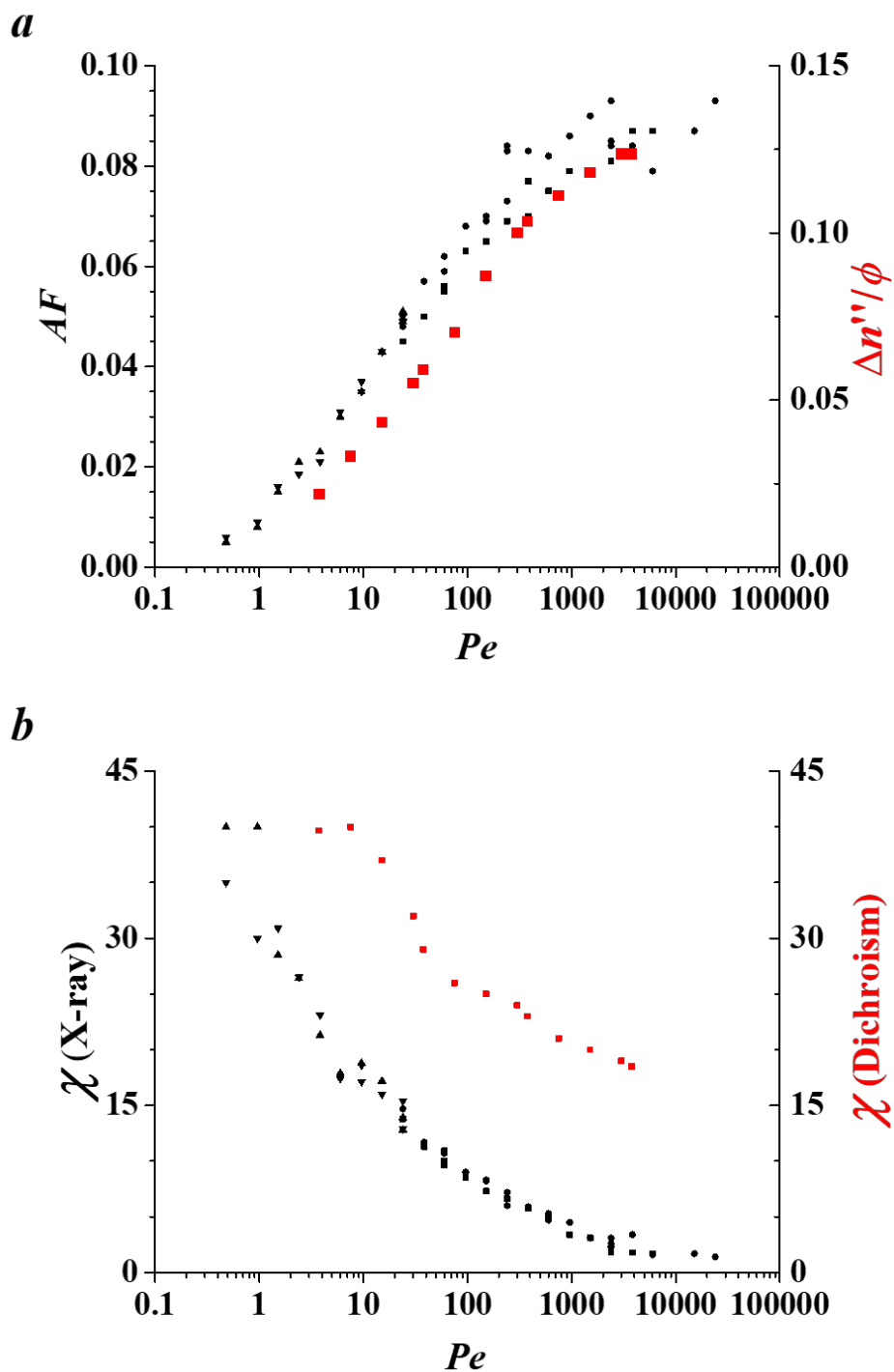


Figure 4.14 Comparison of (a) degree of orientation, and (b) orientation angle measured in dilute CNT suspensions in EPON 828, using SAXS (black) and optical dichroism (red) (dichroism data extracted from [66])

As will be seen in the following section, the pattern exhibited by the SAXS orientation angle data is completely consistent with expectations for Brownian rigid rod dynamics under shear flow. Specifically, rigid, anisotropic particles should, on average, approach an orientation angle of zero degrees at high Peclet number when the randomizing effects of Brownian motion are overwhelmed by the orienting influence of shear. Especially in light of the agreement in orientation angle in Figure 4.13, based on the completely independent shear flow experiments, we are confident that the x-ray data reflect the true orientation angle in this suspension during shear. In principle, the dichroism technique used by Natale *et al.* should yield comparable results, which was true for anisotropy. Indeed, as a purely geometrical measurement, the orientation angle would normally be expected to be particularly robust to differences in measurement techniques. We are not able to comment on what factors may be responsible for the discrepancy found in Figure 4.14 *b*.

4.4.4 Modeling of transient and steady-state orientation dynamics of rigid rods

Modeling has been an important tool for studying rheological,^{128,143,151–153} electrical,¹²⁶ and orientation behavior^{66,143} of CNT suspensions. Various approaches have been pursued, representing CNTs as rigid rods¹⁴³ or semi-flexible rods.^{66,152} Many efforts have been devoted to capturing tube-tube interactions,^{128,143,153–155} which are relevant in semi-dilute or concentrated suspensions. In this section, we explore modeling of transient and steady state data for our dilute CNT suspension, adopting a straightforward model that accounts for hydrodynamic forces that align CNTs under flow, and rotational diffusion driven by Brownian forces randomizing the orientation of CNTs.

Based on the rigid dumbbell dynamics,¹⁵⁶ the unit vector \mathbf{u} that describes the orientation of a rigid rod responds to a flow or deformation through affine rotation with no stretching:

$$\dot{\mathbf{u}} = \mathbf{u} \cdot \nabla \mathbf{v} - \mathbf{u}\mathbf{u} : \mathbf{D} \quad (4.9)$$

$\nabla \mathbf{v}$ is the velocity gradient tensor, and \mathbf{D} is the rate of deformation tensor, $\frac{1}{2}[(\nabla \mathbf{v}) + (\nabla \mathbf{v})^T]$. The first term describes affine deformation, while the second term subtracts any stretching, such that \mathbf{u} remains a unit vector. Modeling calculations in this section were performed by our collaborators using Brownian dynamics methods, where an ensemble of individual rod trajectories is simulated according to the dynamics of Equation 4.9, to which stochastic terms are added to represent the effects of Brownian motion. The simulated orientation may be represented using a second moment tensor $\langle \mathbf{u}\mathbf{u} \rangle$, where the angled brackets represent an average over the simulated ensemble of rod orientations. By analogy with Equations 3.19, 3.21 and 3.22, the differences in principal values and the principal directions of $\langle \mathbf{u}\mathbf{u} \rangle$ may be computed as anisotropy factor and orientation angle, allowing direct comparison to our experimental data. In both shear and extensional flow, Equation 4.9 predicts that rods eventually align along the flow direction.

Figure 4.15 shows the modeling of transient dynamics under various shear rates compared with data. At high shear rates (high Peclet number), the rigid-rod model of Equation 4.9 will predict essentially perfect orientation with an anisotropy factor = 1. This greatly exceeds what is observed experimentally. However, after scaling the modeled AF with 0.1, the simulation agrees with data rather well, capturing the transient overshoot in orientation prior to reaching steady state. The orientation angle from modeling also agrees well with experimental data.

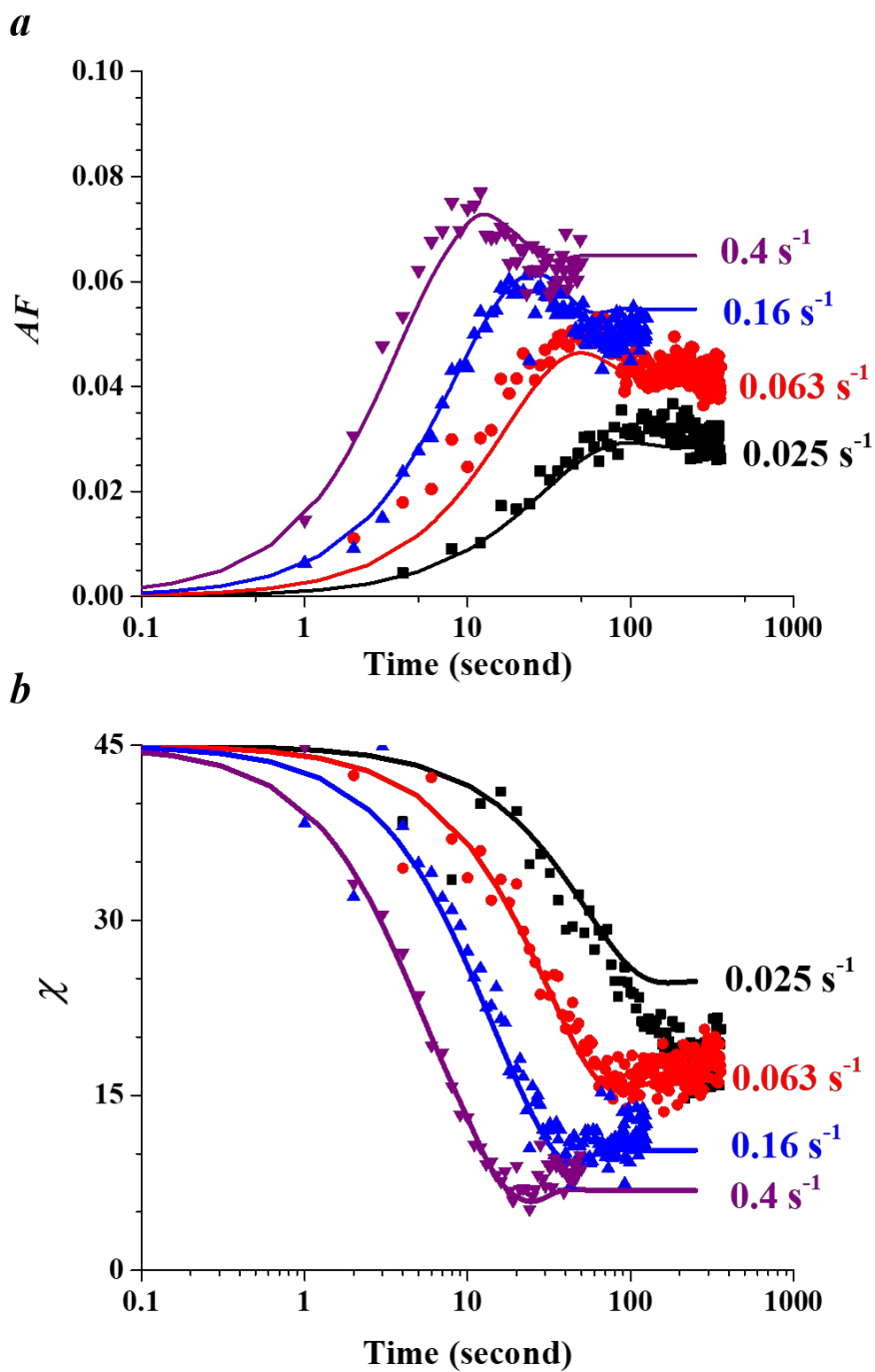


Figure 4.15 Transient anisotropy factor (*a*) and orientation angle (*b*) data measured upon flow inception of 0.05 wt% CNT suspension in EPON 828. Solid lines represent predictions of a rigid rod orientation model, with AF values scaled by a factor of 0.1.

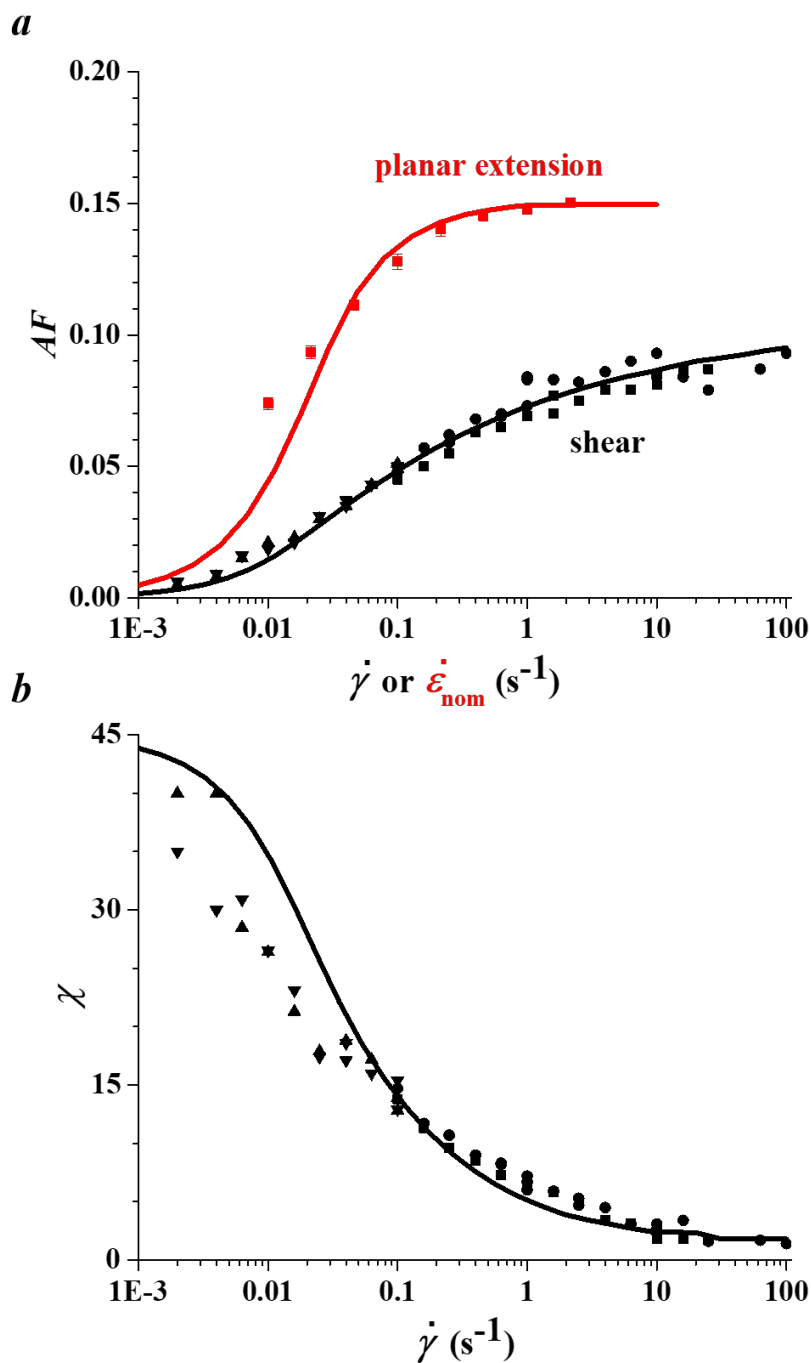


Figure 4.16 Modeling of rigid rods dynamics in steady-state shear or planar extension (curves) compared with experimental data (symbols) for 0.05 wt% CNT suspension in EPON 828 (a) anisotropy factors, the model AF for planar extension is scaled by 0.15 and the model AF for steady shear is scaled by 0.1 (b) orientation angle in shear

Figure 4.16 shows the steady state dynamics under shear and planar extensional flow. Here the modeled AF under shear is scaled with 0.1, while modeled AF under planar extension is scaled with 0.15. With these scalings, the AF s match well between the x-ray scattering data and the model. Figure 4.16 *b* shows the prediction for orientation angle in steady shear. The success of this simple model in capturing the orientation behavior of our suspension in both shear and planar extension confirms that, in this dilute sample, the observed orientation behavior reflects a simple competition between flow and rotational diffusion.

While the agreement in Figure 4.16 is satisfying, it requires application of *different* scaling factors for AF in shear and extensional flow. The model itself predicts that $AF \rightarrow 1$ at high Peclet number in both shear and extensional flow. Thus, if CNTs truly behaved as rigid rods, the experimentally measured AF should asymptote to the same value at high deformation rates. However, we find *higher* orientation in planar extension. This suggests that the rigid rod model is too simplistic. In particular, we speculate that the bent and crooked nature of the tubes used here account for this difference.

As shown in Figure 4.17, a bent/crooked rod may be thought of as an elongated object with finite aspect ratio. Critically, this means that it will always experience a hydrodynamic torque, regardless of its orientation in a shear flow, resulting in tumbling motions known as Jeffrey orbits. Conversely, infinite aspect ratio rods simply line up along the flow direction. To explore the impact of aspect ratio on orientation behavior, Equation 4.9 may be replaced with the following equation, which describes the orientation behavior of ellipsoidal particles:¹⁵⁶

$$\dot{\mathbf{u}} = \mathbf{u} \cdot \boldsymbol{\omega} + \left(\frac{r^2 - 1}{r^2 + 1} \right) (\mathbf{u} \cdot \mathbf{D} - \mathbf{u}\mathbf{u} : \mathbf{D}) \quad (4.10)$$

Here r is the aspect ratio of the ellipsoidal particle, and $\boldsymbol{\omega}$ is the vorticity tensor. When the aspect ratio goes to infinity, this equation is reduced to Equation 4.9. Conversely, when $r = 1$ (spherical particles), Equation 4.10 predicts that the particles simply rotate with the vorticity of the flow.

The geometric quantity $\left(\frac{r^2-1}{r^2+1}\right)$ is often denoted by the variable λ .

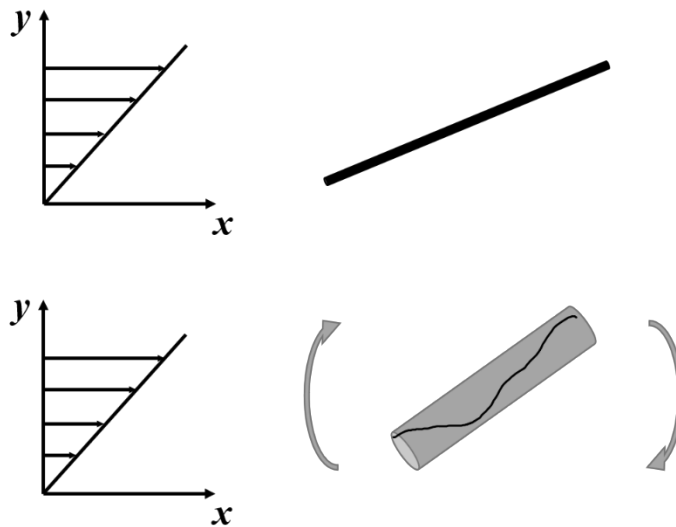


Figure 4.17 Tumbling motion of finite aspect-ratio particle

Figure 4.18 demonstrates the dynamics of particles with different aspect ratios in steady shear versus planar extension. In planar extensional flow, the aspect ratio does not significantly impact the anisotropy factor. With no vorticity, particles continue to align perfectly along the flow direction regardless of their aspect ratio. In steady shear, however, the high Peclet number limit of anisotropy factor is significantly lower with particles of finite aspect ratios, due to the tumbling motion present in shear. As the aspect ratio drops from infinity to 2, AF at high Peclet number regime decreases from approximately 1 to around 0.3. Referring back to the experimental data in Figure 4.16, then, we hypothesize that the lower AF observed in shear

relative to extension reflects consequences of tumbling of dilute CNTs in shear flow. This, in turn, is caused by a low effective aspect ratio associated with the bent/kinked structure of the CNTs used here.

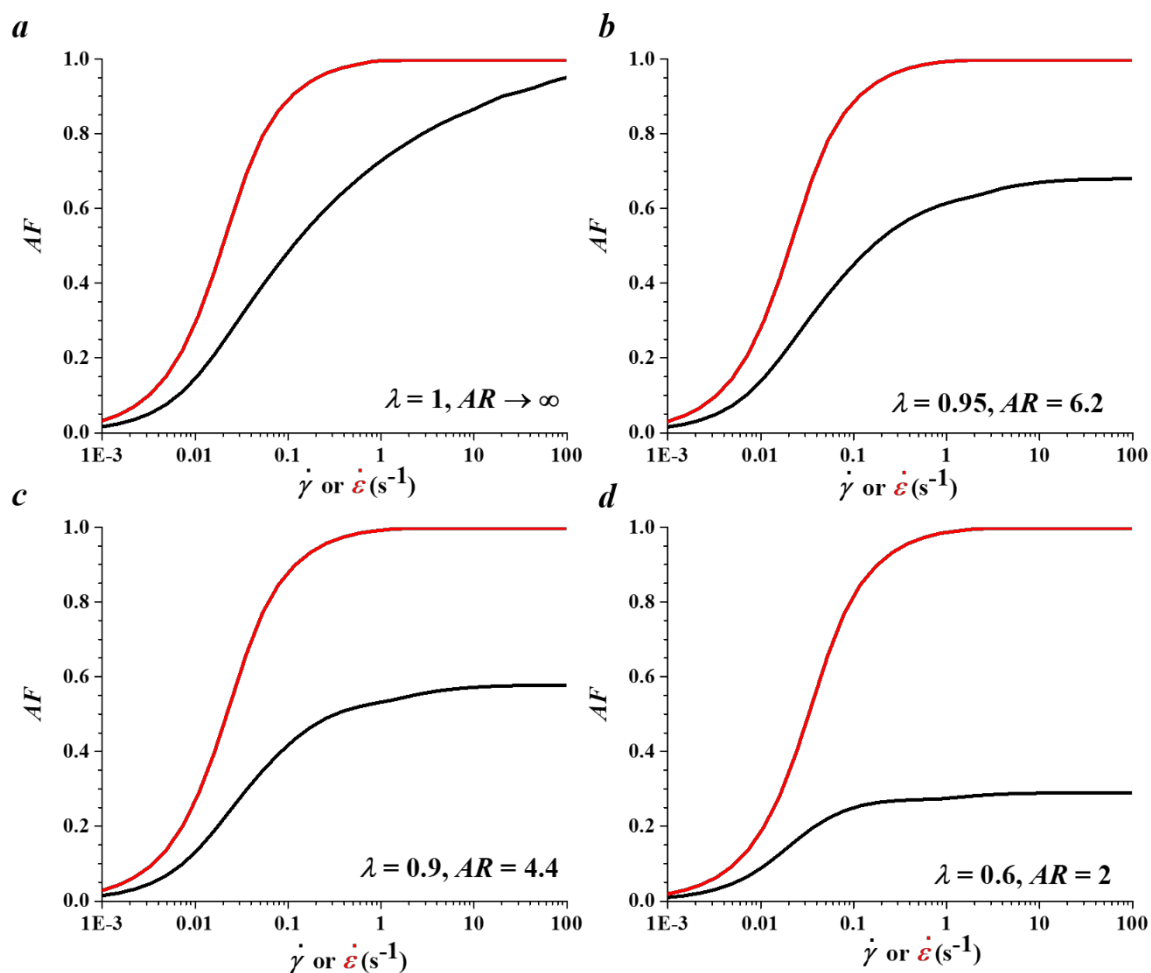


Figure 4.18 Simulated anisotropy factor of particles with changing particle aspect ratios in steady shear and planar extension

As seen in Figure 4.19, the steady state orientation behavior of our sample in both shear and extension may be self-consistently predicted by these simulations using an effective aspect

ratio of 4.4. With this value, a scale factor of 0.15 must be applied to the simulated anisotropy factor; the experimentally observed anisotropy factor measured using scattering is only a fraction of the AF predicted by the simulation. We explored the possibility that isotropic background scattering from the epoxy matrix might contribute to the total intensity, diluting the anisotropic scattering from the CNTs (mathematical details discussed in Appendix B). However, scattering experiments on pure epoxy showed that the scattered intensity from the matrix was two orders-of-magnitude smaller than the CNT scattering. Other researchers have observed smaller than expected anisotropy in experiments. Fan and Advani¹⁵⁷ characterized orientation of CNTs using second moment tensor through direction visualization of CNTs subjected to shear. They designated one direction for each tube and summed over all the tubes. The resulting AF s from direct visualization were still far away from the perfect alignment. Similar observations have been noted by Fry *et al.*,⁶⁵ with predicted alignment being much stronger than their optical measurements.

With bent and crooked rods, 2- d scattering patterns will always be “smeared” relative to the ideal scattering from aligned rod-like objects as illustrated in Figure 4.20. Thus, even perfect alignment of imperfect tubes will yield experimental AF values less than unity. It appears that $AF = 0.15$ observed at high Pe in planar extensional flow may be the maximum possible value obtainable in these particular CNTs.

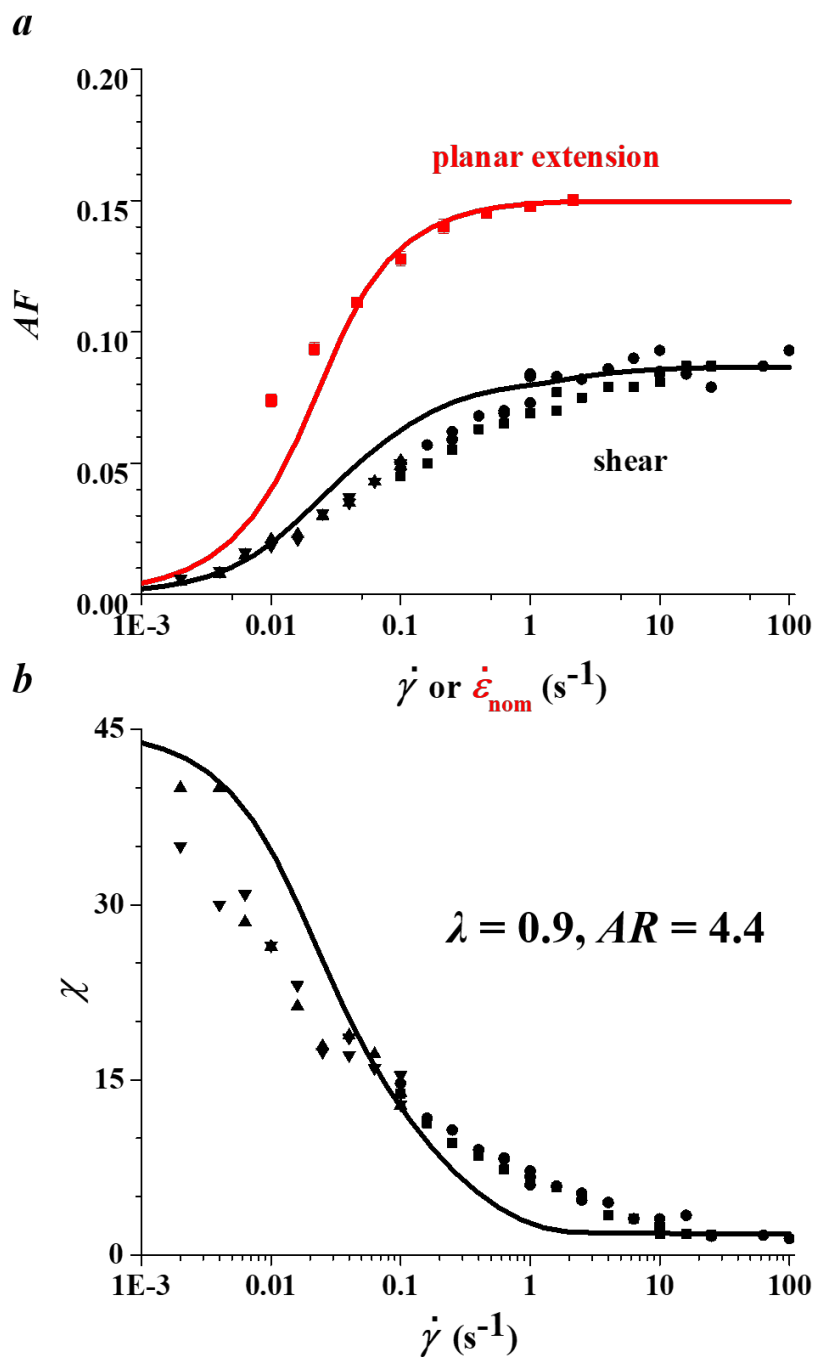


Figure 4.19 (a) Modeling rigid rods dynamics with an aspect ratio of $\lambda = 0.9$ (solid curves) plotted with experimental data (symbols) obtained from 0.05 wt% CNT suspension in EPON 828; Model AF in both planar extensional and shear flow is scaled by 0.15; (b) Model orientation angle in shear

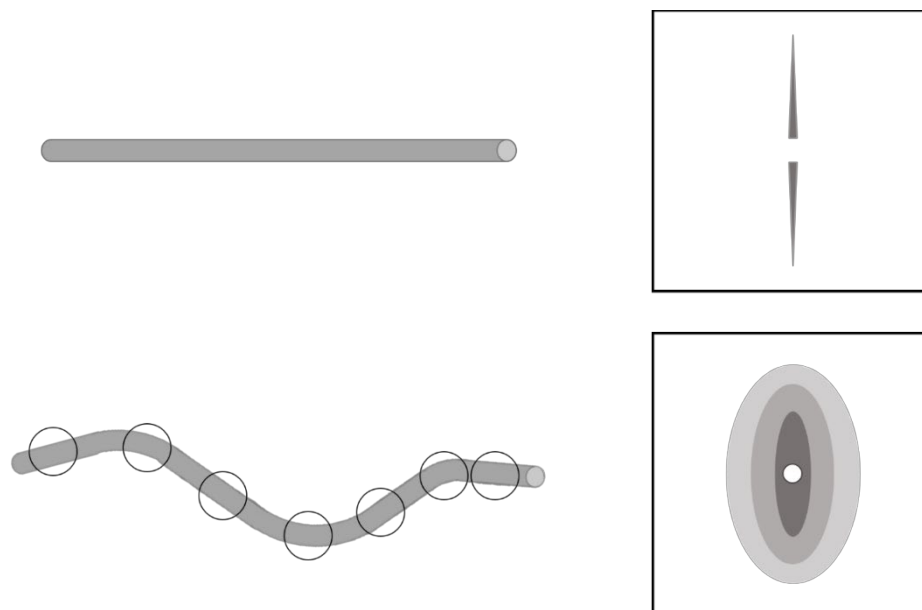


Figure 4.20 Schematic scattering patterns for perfectly aligned straight rods versus oriented but bent and crooked tubes

4.4.5 Suspensions in low-viscosity matrix

In addition to the comprehensive studies in shear and extension of the single suspension discussed above, we also studied suspensions in a lower viscosity epoxy. This was motivated by a desire to increase the rotational diffusivity, and thus facilitate measurement over a wider range of Peclet number. However, as discussed in this section, all experiments on suspensions in the lower-viscosity matrix displayed surprisingly low degrees of orientation. Due to the weak anisotropy and faster dynamics, no reliable transient data could be obtained; this section focuses exclusively on steady-state anisotropy and orientation angle.

4.4.5.1 Dilute CNT suspension subjected to both shear and planar extension

We measured the steady state CNT orientation in 0.05 wt % (dilute) CNT suspensions in two Newtonian matrices EPON 815c (0.56 Pa·s) and EPON 828 (12.5 Pa·s), subjected to both

shear and planar extensional flow. Data for the EPON 828 suspension were presented earlier in Figure 4.11; results for the lower-viscosity EPON 815c are shown in Figure 4.21. Planar extensional flow data were collected at the stagnation point of the flow cell. In EPON 815c, the AF s gradually increase from around 0.002 to somewhere close to 0.01 as shear rate is intensified from 0.1 to 100 s^{-1} . In planar extension, the AF s rise from 0.012 to roughly 0.027 as nominal extensional rates increase from 0.3 to 30 s^{-1} . As reflected by these small AF values, the scattering patterns from this suspension were nearly isotropic and showed no visually discernable differences between frames. Quantitatively, planar extension still demonstrates a stronger capacity for orienting CNTs than the shear flow. The AF s generated by planar extension are roughly five times of the AF s induced by shear. The orientation angles in shear flow fluctuated significantly. Equation 3.22 for orientation angle becomes indeterminate as anisotropy approaches zero. Still, there was an observable trend of decrease in orientation angle from roughly 25° to about 10° as shear flow was raised from 0.1 to 100 s^{-1} . The orientation angles induced by planar extension were all near zero, consistent with the symmetry of planar extensional flow. A small but consistent deviation is found, in which the infuse mode often produced small positive deviations in orientation angle while withdraw mode typically displayed negative deviations. This could be due to either a small asymmetry in the flow system, or imperfectly corrected background scattering that could systematically bias the measured orientation angle under conditions where anisotropy in the CNT scattering is so weak.

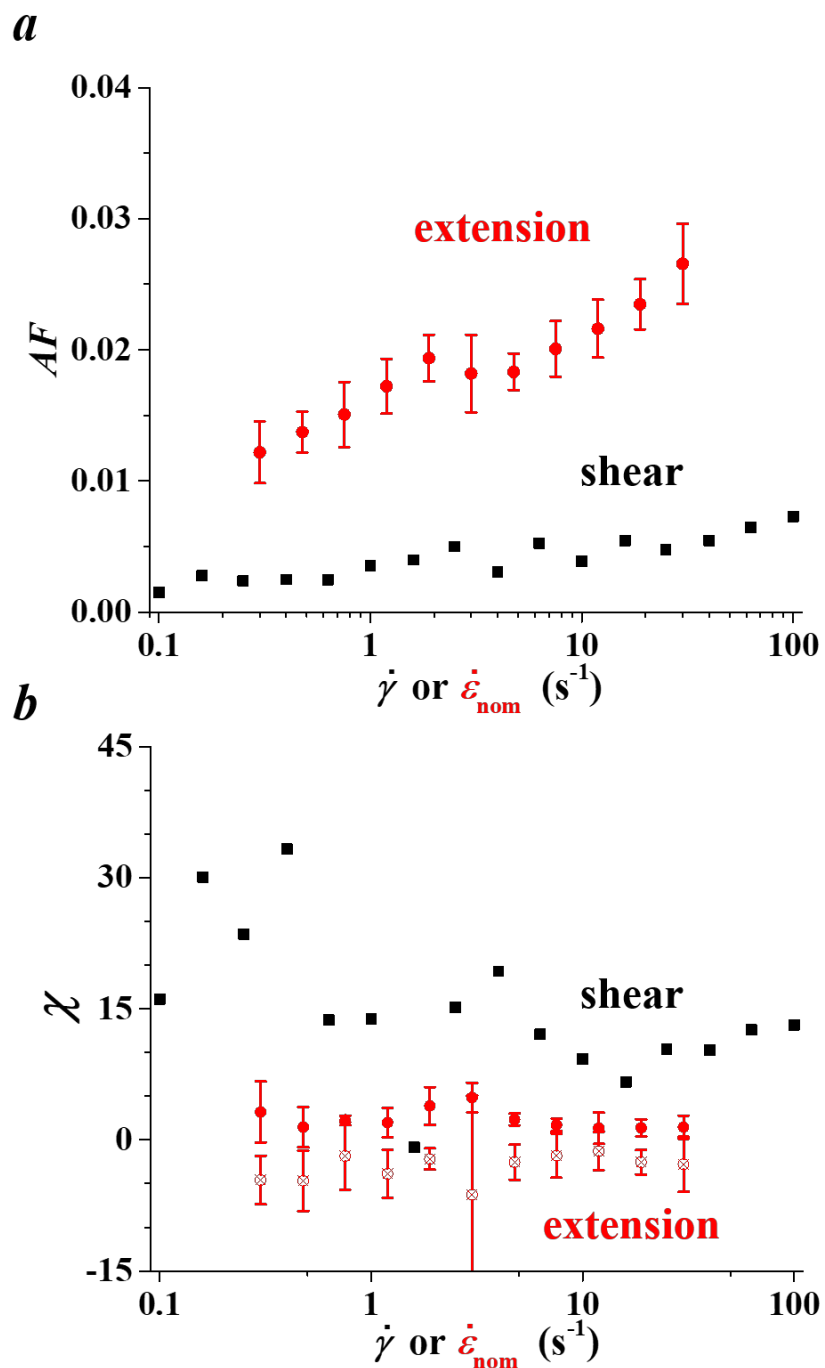


Figure 4.21 Steady-state anisotropy factor (a) and orientation angle (b) measured in 0.05 wt% CNT suspension in EPON 815c

To compare data obtained from the CNT suspension in EPON 828 versus the CNT suspension in EPON 815c, data for both suspensions may be expressed in terms Peclet number (Figure 4.22), using the ratio of matrix viscosity of EPON 815c over EPON 828, since matrix viscosity is inversely proportional to the CNT rotational diffusivity.¹⁴⁸ When comparing the two suspensions at the same Peclet number, we find that the CNTs in the more viscous matrix EPON 828 exhibited much higher orientation in both shear and planar extensional flow. In the present case, it is hard to understand the origin of this discrepancy. Both suspensions use the same CNTs, dispersed using similar methods. Results from earlier in this Chapter demonstrate that the orientation dynamics in the 0.05 wt% CNT suspension in EPON 828 are well described by a straightforward competition between flow and Brownian diffusion. Under such circumstances, one expects identical CNT orientation under flow when Peclet number is matched. Fry *et al.*^{65,67} studied semi-dilute CNT suspensions in matrices of different viscosities (comparable to EPON 828 and EPON 815c used here), where birefringence and dichroism data were successfully scaled to a master power-law relationship with respect to Peclet number. This makes the substantial contrast (an order-of-magnitude difference in AF between the suspension in EPON 828 versus the suspension in EPON 815c) illustrated in Figure 4.22 *a* even more bewildering. An early study towards the orientation behavior of single fiber and semi-dilute fiber suspensions in matrices of varying elasticity by Iso *et al.*¹⁵⁸ tells that solvent elasticity can enhance flow alignment. However, it is merely a speculation at this point.

In the 1-2 plane, AF is predicted to be proportional to Pe for small Pe .¹⁴⁸ The dependence has been observed experimentally with the 0.05 wt% CNT suspension in EPON 828 (Figure 4.22 *a*).

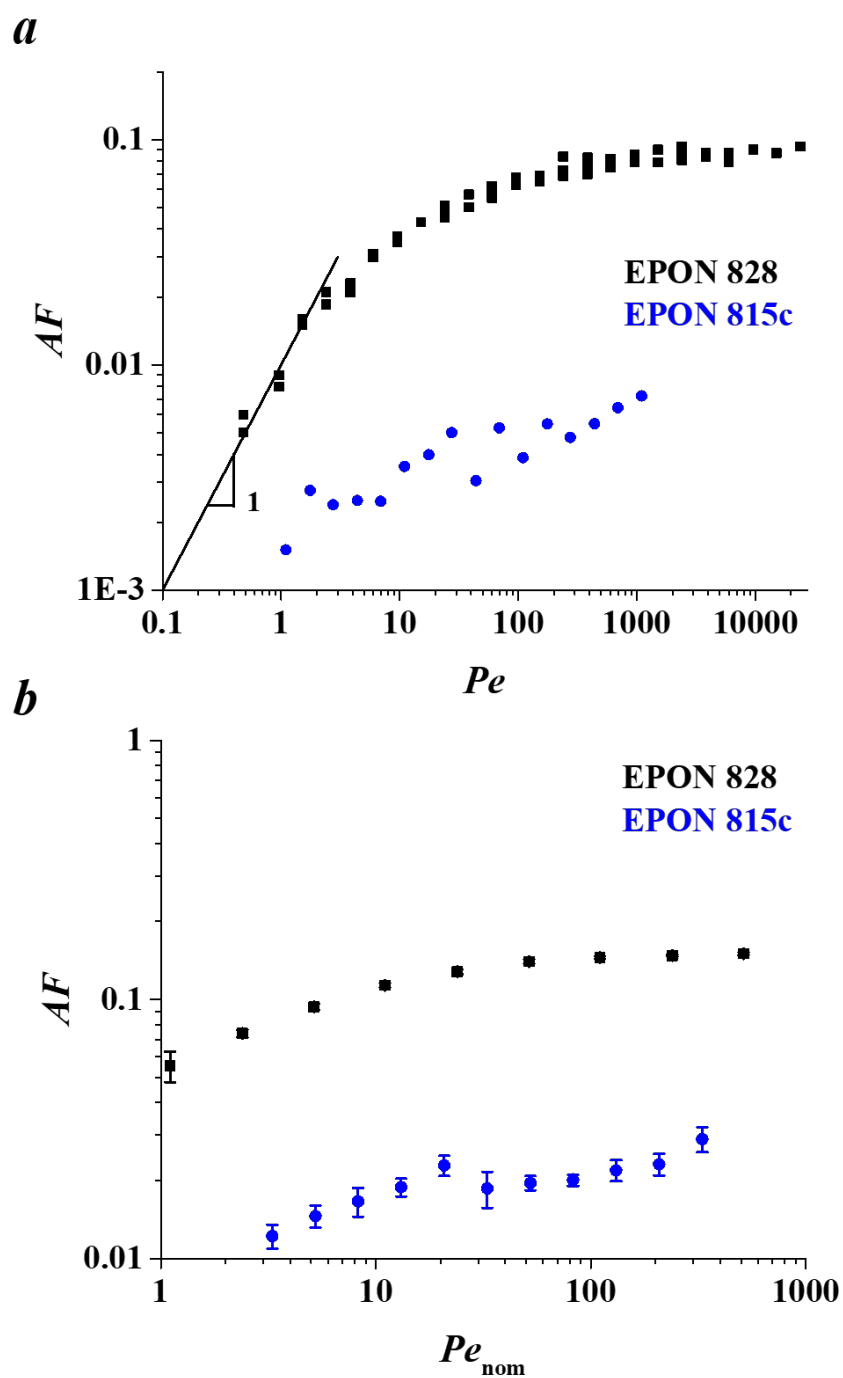


Figure 4.22 Anisotropy factor of CNT suspended in EPON 828 and EPON 815c subjected to homogeneous shear (a) and planar extension (b) scaled to Peclet number using rotational diffusivity

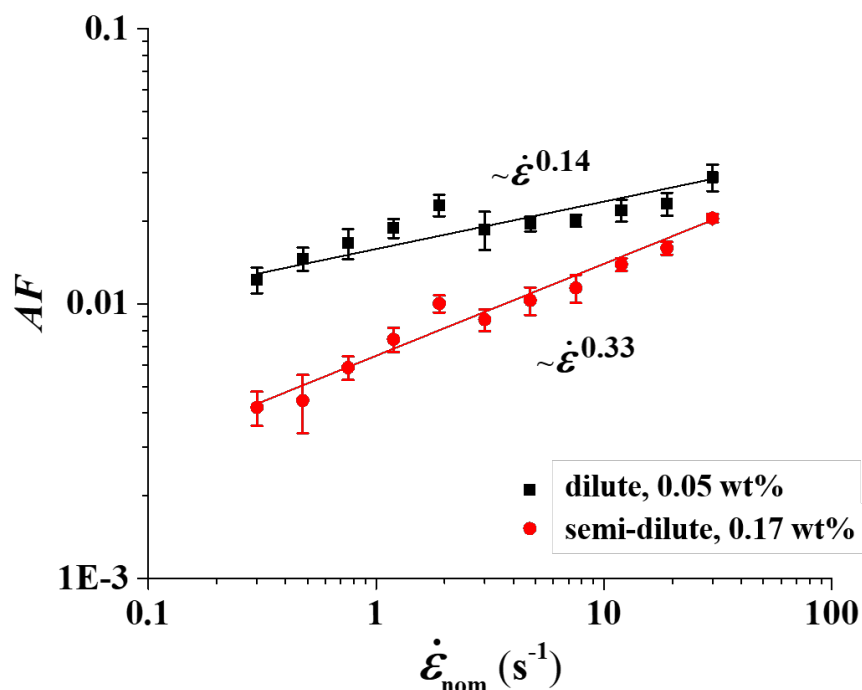


Figure 4.23 0.05 wt% (dilute) and 0.17 wt% (semi-dilute) CNT suspension in EPON 815c, subjected to planar extension

4.4.5.2 The effect of concentration: dilute versus semi-dilute CNT suspension

We compared 0.05 wt % (dilute) and 0.17 wt % (semi-dilute) CNT suspensions in EPON 815c subjected to planar extensional flow. Figure 4.23 shows that the dilute suspension exhibits higher AF s than the semi-dilute suspension at comparable flow rates. Since these data were collected in the low viscosity matrix, all AF values are small. Over this range of flow rates, the data follow a power law with a stronger dependence in the semi-dilute sample, although the absolute magnitude of AF is smaller. Our collaborators⁶⁶ also observed slightly smaller degree of orientation (scaled dichroism with CNT volume fraction) in semi-dilute suspension than a dilute suspension at the 1-3 plane of shear flow in parallel plates. Judging by the power law

indices, we found that the extensional flow had a stronger impact towards the semi dilute suspension than the dilute one. This stronger rate dependence might reflect the combined processes of flow induced orientation and disentanglement in the semi-dilute suspension.

4.4.6 The state of dispersion reflected by the absolute scattering intensity as a function of scattering vector q

In the literature describing the microstructure of CNTs in suspension, considerable attention is paid to the impact of dispersion techniques on the structure. White *et al.*¹⁴⁷ argued that “majority of experimental results reflected properties dominated by the clusters”. Our collaborators⁶⁶ also executed a pre-shearing protocol to erase the flow history of the CNT suspensions. In semi-dilute suspension, there is ample evidence that clustering under flow, and flow-induced cluster breakdown, can influence orientation measurements.^{97,139} In sufficiently dilute samples, such as the suspension featured in this chapter, particles should be orienting independently; the qualitative success of simple models of Brownian rods in Section 4.4 suggests that this outlook is appropriate. However, given the modest degree of scattering anisotropy produced under the most favorable conditions, here we consider whether equilibrium scattering can offer us insights into the structure of our suspensions.

Scattering models for randomly oriented ideal rigid rods (length = L , radius = R) predict three regimes of behavior. For $q < 1/L$, scattered intensity is predicted to reach a constant value, determined by the particle size, concentration and scattering contrast. (Given the average tube length of 670 nm for the tubes used here, this regime is inaccessible for SAXS.) At intermediate q regime where $1/L < q < 1/R$, intensity is predicted to decrease as $I \sim q^{-1}$, a classic scattering signature for rod-like objects. Finally, when $q > 1/R$, scattering is predicted to decrease more

rapidly, $I \sim q^{-4}$, as predicted by Porod's law (the high- q limit of small-angle scattering), which holds for particles of any shape.

Figure 4.24 presents $I(q)$ data measured in the dilute CNT suspension in EPON 828 under quiescent conditions. These results were consistent from the beginning to the end of the whole beam time run, indicating the stability of our suspension. Arrows indicate the point at which $q = 1/R$, using the average tube radius of the CNTs used here. The data in fact show a transition in this region. The broad crossover transition regime may be due to the polydispersity in tube diameter. At smaller q , the data show a power-law index of 1.6 in shear and 1.7 in planar extension, while at higher q , a stronger q dependence is observed with a slope of 4. The q dependence at the smaller q disagree somewhat with the expectations for ideal rods, while the q dependence at higher q meets Porod's prediction. The larger exponent found at smaller q most likely reflects the crooked/bent nature of the tubes (Figure 4.1), which would push the scattering characteristics in the direction of more flexible structures like polymer chains, which exhibit a steeper q -dependence.¹⁵⁹ More generally, the fact that a pronounced change of slope is found in the q -range expected based on the independently measured average tube radius suggests that the nanotubes in this sample are well dispersed and scatter as independent objects.

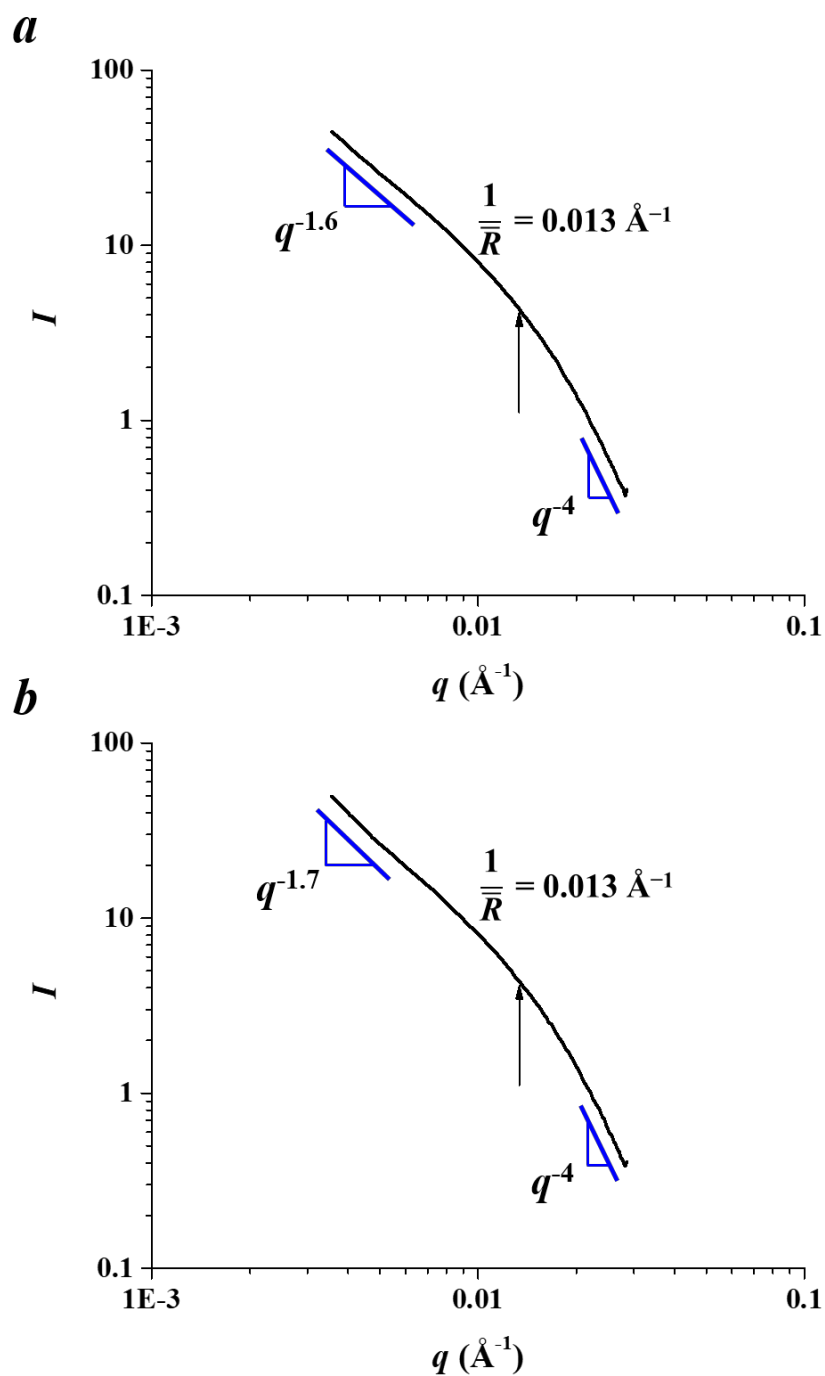


Figure 4.24 Scattered intensity of 0.05 wt% CNT suspension in EPON 828 versus scattering vector q (\AA^{-1}) in (a) homogeneous shear and (b) planar extensional flow

4.5 Conclusion

We probed the dynamics of MWCNT suspensions subjected to homogeneous shear and planar extensional flow using SAXS, under both transient and steady-state flow conditions. In transient experiments, CNT dynamics in a dilute suspension during shear inception, reversal, and relaxation show classic signatures expected for Brownian rod-like particles. Parameters obtained from fitting the relaxation behavior to a stretched exponential function suggest that polydispersity affects the relaxation behavior. Specifically, at intermediate shear rates, the orientation is dominated by longer particles, that relax more slowly. The relaxation behavior revealed by SAXS was consistent with independent measurements, by our collaborators using optical dichroism. Under the steady-state conditions, higher shear rates lead to higher orientation and smaller orientation angle relative to the flow direction. Good consistency was found between shear flow data extracted from the upstream channels in the cross-slot flow cell, and data collected using a dedicated homogeneous shear flow cell. This demonstrates that the aspect ratio of the cross-slot flow cell suffices to allow the flow field to be treated as two-dimensional. Planar extensional flow was more effective at aligning CNTs than shear at comparable flow rates. Simulations of orientation in dilute Brownian rods capture most aspects of the orientation behavior, but use of a finite particle aspect ratio is required to rationalize the difference in degree of orientation seen in extension versus shear. We also found that a semi-dilute suspension exhibits weaker orientation compared to a dilute suspension but was more susceptible to flow.

Chapter 5 Structural Dynamics of Self-assembled Surfactants in Planar Extensional Flow

Surfactants are amphiphilic molecules that contain a hydrophilic head and a hydrophobic tail. Above the critical micelle concentration (CMC), surfactants can self-assemble into aggregates of various shapes. Depending on the size and shape of the head and the tail group, spherical, cylindrical, and lamellar micelles can form. Surfactants have attracted much attention due to their ubiquitous industrial applications, including additives to reduce turbulent drag forces and to enhance oil recovery, pesticides, district heating systems, home and personal care products.^{110,160} Moreover, they have attracted enormous academic interest due to their complexity and diverse behavior. Significant efforts have been undertaken to uncover their properties such as morphology, phase diagram, shear and extensional rheology. As with most complex fluids, however, structural studies of surfactants subjected to extensional flow have been quite limited. Here we present x-ray scattering studies of two classes of surfactant aggregates subjected to planar extensional flow: wormlike micelles and lamellar surfactants.

5.1 Wormlike-micelle solution

5.1.1 Introduction

Above a critical concentration and under proper conditions of salt concentration and temperature, cylindrical micelles can grow to great lengths and form entangled wormlike micelle (WLM) solutions. The transient network formed by the elongated, flexible and entangled micelle threads renders such solutions highly viscoelastic, similar to polymer solutions and melts. Unlike

a covalently bonded polymer backbone, micelles are in a state of thermodynamic equilibrium with the solvent and are continuously broken and reformed under Brownian fluctuations. Hence WLMs are sometimes referred to “living polymers”. This leads to a broad equilibrium distribution of micelle lengths which can change under an imposed shear or extensional flow. Lots of work has been conducted and summarized on WLM’s applications, rheology and microstructures.^{110,161,162} Here we focus on the impact of flow upon WLMs.

In the linear viscoelastic regime, many WLMs exhibit nearly single-exponential relaxation such that storage and loss moduli (G' and G'') are described by the classic Maxwell model.^{163,164} This behavior is a consequence of a combined reptation/scission mechanism. The Maxwell relaxation time τ , is the geometric mean of the breaking and reptation time scales, $\tau = \sqrt{\tau_{break} \cdot \tau_{rep}}$. In steady shearing experiments, WLMs generally shear thin in the nonlinear regime due to micellar alignment under flow.^{165–168}

Some WLM formulations shear thin sufficiently to exhibit a stress plateau, where the stress does not change with shear rate over a certain shear rate range.²² This is often ascribed to a fundamentally non-monotonic constitutive relation between stress and shear rates. When the macroscopic shear rate is between two critical rates, the original homogeneous flow field is unstable and splits into two separate bands of different velocity gradient, micelle concentrations, and microstructure, a phenomenon, known as “shear banding”.^{68,169–172} Conversely, some dilute cationic surfactants demonstrate shear thickening behavior.²² This phenomenon has been associated with the formation of shear-induced structures, under selective conditions involving critical shear rate and surfactant and salt concentrations,^{173,174} where shorter rod-like micelles

further aggregate to wormlike micelles, aligned in the flow.¹⁷⁰ Many researchers have studied this structural shift using light scattering,^{175,176} SANS,^{85,177} and birefringence.^{70,105}

The extensional rheology of WLM is less well studied compared to shear, due to the scarcity of extensional rheometers. Early investigations were made with opposed-jets, including Prud'homme *et al.*,¹⁷⁸ Walker *et al.*,¹² Chen *et al.*,⁴⁷ and Muller *et al.*¹⁶⁵ In these studies, the apparent extensional viscosities generally remain constant at small rates, rise to a maximum at a critical strain rate and then decrease afterwards. The increase was first interpreted as micelles being extended and aligned in the elongational flow field,^{12,178} but was later attributed to the inertial effects in the flow field itself produced by opposed jets.¹⁶⁵ The drop of apparent extensional viscosity occurring at larger strain rates is understood as micelle scission caused by the strong extension. This disruptive effect of extensional flow is confirmed by the work of Chen *et al.*,⁴⁷ which demonstrated a concurrent decrease in micelle radius of gyration measured using light scattering and apparent extensional viscosity measured with opposed-jets. The strength of the extensional flow is also confirmed by the study from Muller *et al.*,¹⁶⁵ where their wormlike micelle sample thickens in shear, suggesting flow-induced structure buildup, but thins in extensional flow, attributed to degradation of micelles.

More recently, the extensional rheology of WLMs has been probed with filament stretching (FiSER) and capillary breaking (CaBER) extensional rheometers. In these studies performed with FiSER^{38,179} and CaBER,^{11,180} strain-hardening behavior is generally observed across a range of samples, including model systems like CTAB/NaSal and CPyCl/NaSal, regardless of whether the solutions exhibit shear-banding or not. Also, according to the filament stretching experiments, the maximum extensional viscosity achieved before filament rupture decreases with increasing extensional rate, thus qualitatively consistent with observations made

with opposed-jets. Nonetheless, Bhardwaj *et al.*¹⁷⁹ found that at comparable nominal extensional rates, the results from FiSER do not agree with that of CaBER. Kim *et al.*⁴² reported that the apparent extensional viscosity measured by CaBER is influenced by experimental parameters such as radius of the endplates and the initial strain imposed.

In addition to direct measurements of extensional viscosities in an elongational flow field, Kato *et al.*¹⁸¹ measured 0.03 M CTAB/ 0.23 M NaSal wormlike micelle solution in a four-roll mill using birefringence and observed elongational thinning behavior. However, the validity of stress-optical rule, particularly under a strong flow regime, was not addressed. Haward *et al.*⁶² measured the excess pressure drop induced by the extensional flow in a cross-slot cell, using data from cone-and-plate rheometry to correct for the shear contribution. However, this quantity is highly convoluted since the sample experiences different strain rates and flow histories in different parts of the cross-slot cell. Further, the flow field within a cross-slot cell is likely to be affected by the viscoelastic property of the wormlike micelle solution itself. The complexity makes such pressure drop measurements hard to be compared with studies using other techniques, as the authors discuss, making reference to the contrasts between birefringence and pressure drop.

Additional factors have been found to impact the dynamics and hence the extensional rheology of wormlike micelles. Fischer and Fuller¹³ found distinctly different behavior of branched micelles in opposed jets, compared to linear micelles. Similarly, Chellamuthu *et al.*¹⁸² found that branched micelles exhibit little strain hardening behavior in FiSER and CaBER experiments, in contrast to linear entangled micelles. The concentration of surfactant solutions can also play a significant role. Bhardwaj *et al.*¹⁷⁹ reported filaments of more concentrated solutions do not rupture below a critical extensional rate, whereas generally filaments fail

through a dramatic rupture at midplane. Sachsenheimer *et al.*⁴¹ discovered that at lower surfactant concentrations, the observed filament lifetime in CaBER is much longer than expected from zero-shear viscosity, suggesting elongation-induced structure. Bhardwaj *et al.*¹⁴ identified that pre-shearing impacted FiSER and CaBER differently: it delays the onset of strain hardening in FiSER but accelerates strain hardening in CaBER. All the complexities demonstrated by wormlike micelles in extensional flow point to the desirability of direct structural studies of WLM in extensional flow, though to date such investigations are rare compared to studies made in shear.

The earliest structural observation for wormlike micelles in extensional flow was made by Wheeler *et al.*¹⁸³ using light scattering, demonstrating strong alignment effect of extensional flow compared to shear in a four-roll mill for a semi-dilute WLM solution. Their work is followed by Chen and Warr,⁴⁷ who presented a concurrent trend between a decrease in micelle radius of gyration and the onset of extensional viscosity thinning, for a dilute WLM solution in a four-roll mill as well.

Over the past two decades, flow birefringence has been a common structural probe for wormlike micelles. Kato *et al.*¹⁸¹ first used birefringence to infer planar extensional viscosity in a four-roll mill, assuming validity of the stress-optical rule. Rothstein³⁸ investigated the flow-induced birefringence at the midplane of concentrated and entangled WLM filaments and found that birefringence signal grows rapidly at short times and later exponentially with time. More recently, many studies have employed birefringence measurements combined with cross-slot flow cells producing planar extensional flow fields,^{55,58,62} to advance understanding of the viscoelastic properties of wormlike micelles and the fluid dynamics of wormlike micelles within cross-slot flow cells. These studies mostly targeted classic semi-dilute, entangled WLM recipes

such as CTAB/NaSal and CPyCl/NaSal of various concentrations, though Dubash *et al.*⁵⁵ included a shear-thickening formulation. Generally, a streak of birefringence indicating micelle alignment along the outflow direction is first observed. As flow is strengthened, bifurcation appears due to complex fluid dynamics in cross-slot cells with sharp corners. Time-dependent flow may be observed if the flow rate is further increased.

Neutron scattering is a versatile technique and has been used widely to study the equilibrium microstructure of wormlike micelles (persistent length, entanglement, contour length *etc.*),^{69,82,83,161} and their microstructural response in shear.^{92,184} In extensional flow, the only contribution is from Penfold *et al.*,⁶⁰ who studied the alignment of wormlike micelles in a cross-slot flow cell and observed that WLMs show a weaker coupling to the flow pattern compared to lamellar surfactants. Due to multiple scattering concerns, the thickness of the cross-slot flow cell they employed for SANS was limited and hence so was the aspect ratio. Penfold's device has an aspect ratio of 0.5. This then impacted the fluid dynamics of the cell and made shear a dominant component of the deformation. The opportunities provided by x-ray scattering to extend similar methods to a high aspect ratio flow cell provide strong motivation for studying the structural response of wormlike micelles using the device developed in this thesis.

The cetyltrimethylammonium bromide/sodium salicylate (CTAB/NaSal) system is a well-researched wormlike micelle recipe. In the dilute regime, shear thickening is generally observed, ascribed to the formation of shear-induced structure.^{70,105,173–175,185,186} In the semi-dilute regime, when the salt concentration is relatively low, shear banding is often observed.^{180,187–189} In the semi-dilute regime with higher salt concentration, the viscoelastic properties of wormlike micelles can be described by the Maxwell model with a single characteristic relaxation time, while solutions generally shear thin without evidence of shear-banding.^{160,166,168,183,190} The

solution studied here (60 mM CTAB / 350 mM NaSal) falls into this higher salt regime, and is believed not to exhibit more complex behavior such as shear banding or flow-induced phase transition, according to Fischer *et al.*¹⁶⁸ We also found that the rheology of this system varies little between 20 and 30 °C, near ambient conditions. Considering that our cross-slot flow cell does not have active control over temperature, this characteristic of 60 mM CTAB/ 350 mM NaSal solution is also desirable.

5.1.2 Material and methods

5.1.2.1 Materials and rheological characterization

To prepare the wormlike micelle solution [60 mM cetyltrimethylammonium bromide (CTAB) and 350 mM sodium salicylate (NaSal)],¹⁶⁸ 2.187 grams of CTAB, 5.604 grams of NaSal, and 92.2 grams of deionized water were weighed and sealed inside a glass bottle. It was vigorously shaken upside and down by hand for at least 5 minutes. Finally, it was left in an oven and equilibrated at 25 °C for 3 days. Rheological characterization of the WLM solution included small-amplitude oscillatory shear and steady shear experiments (Figure 5.1), using an Anton Paar MCR 302 stress-controlled rheometer and cone-and-plate geometry of 50 mm diameter and 2° cone angle. Small-amplitude oscillatory data could be fitted to a single-mode Maxwell model with a modulus of 19.4 Pa and relaxation time of 0.310 seconds. The steady-shear viscosity began shear thinning around 4 s^{-1} , consistent with the SAOS relaxation time. The steady shear stress does not exhibit a plateau in the shear-thinning regime, confirming that this WLM solution does not shear band.

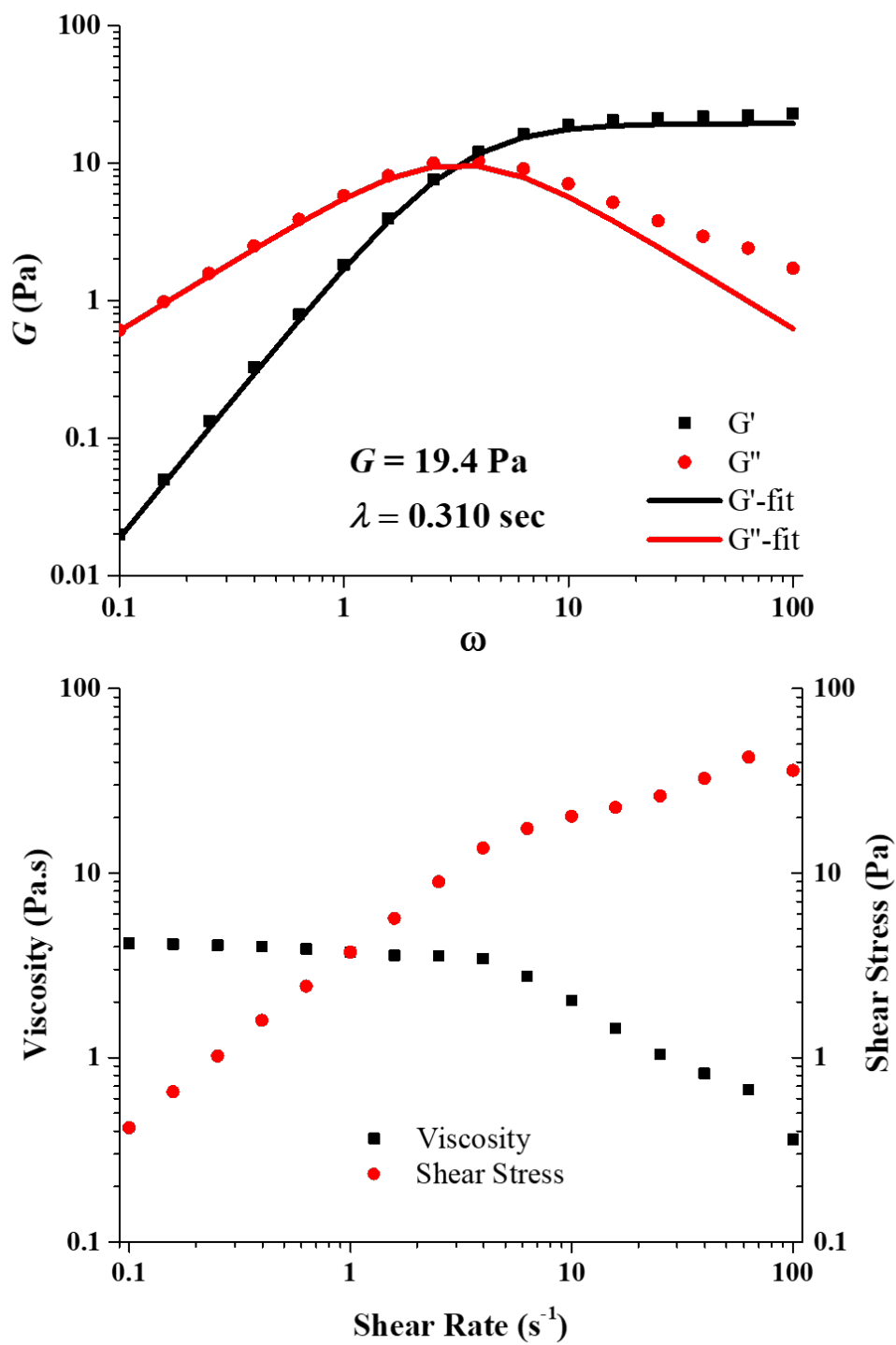


Figure 5.1 Small-amplitude oscillatory shear and steady shear viscosity for wormlike micelle solution 60 mM CTAB /350 mM NaSal measured at 25 °C

Based on the relaxation time extracted from SAOS and the nominal extensional rate extracted from the volumetric flow rate and the flow cell dimensions, we characterize the strength of planar extensional flow using a Weissenberg number:

$$Wi_{nom} = \dot{\epsilon}_{nom} \cdot \lambda = \frac{Q}{w^2 t} \cdot \lambda \quad (5.1)$$

Here Q is the volumetric flow rate within one slot, w is the width of the cross-slot flow cell, and t is the thickness of the flow cell along the beam path. We studied volumetric flow rates ranging from 0.113 to 11.3 ml/min, corresponding to nominal extensional rates ranging from 0.377 to 37.7 s⁻¹, or, equivalently, nominal Weissenberg number of 0.117 to 11.7.

5.1.2.2 Scattering methods and data analysis

The *in situ* synchrotron x-ray scattering experiments were performed at APS 5-ID-D. The incident beam energy was set at 15 keV, corresponding to a wavelength at 0.8266 Å. The exposure time was 10 seconds for each frame. The medium-angle detector was used (Rayonix LX170HS), with a detector-to-sample distance of 1013.2 mm. The detector binning was set at 4 by 4.

Before each measurement, 1.5 ml solution was pumped through the flow cell to make sure that the flow was fully developed. Then we scanned through different locations within the flow cell. Due to the relatively weak scattering for this sample, background subtractions were important. For this reason, data were also collected at each flow cell position with the empty flow cell. We attempted to pursue complementary studies of structural dynamics of this WLM solution under homogeneous shear with our cone-and-plate shear flow cell.⁹⁴ However, the

experiment was unsuccessful because the solution was driven out of the flow cell through the center by normal stresses.

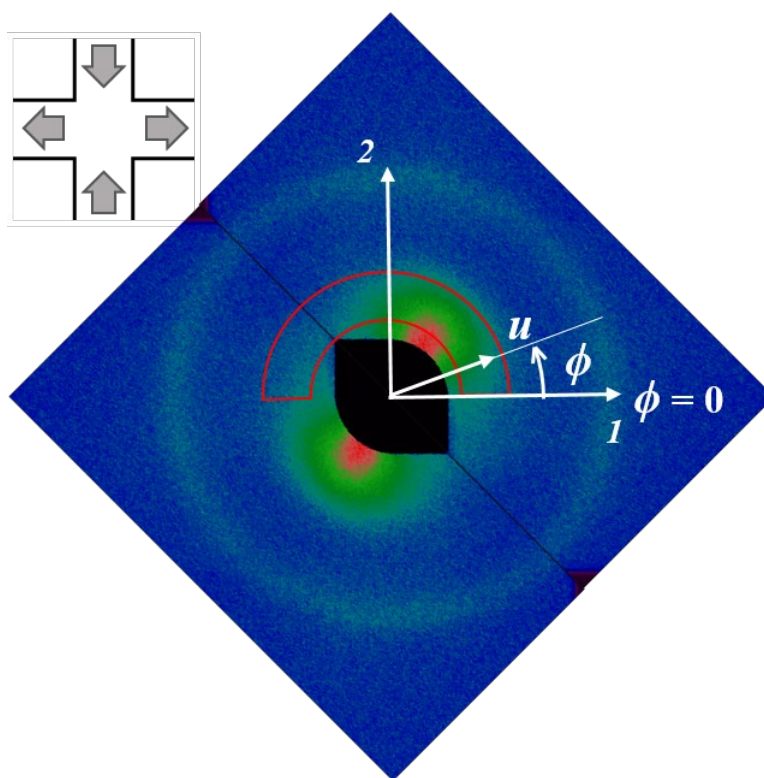


Figure 5.2 Representative medium-angle scattering pattern measured on the 60 mM CTAB/ 350 mM NaSal WLM solution.

Figure 5.2 is a representative 2-*d* scattering pattern, collected at $x = 0, y = 0$, from the WLM solution when subjected a nominal Wi of 4.64 with extension along horizontal direction. As illustrated in Figure 3.4, the medium-angle detector only covers a data range of 180° , with the detector's real-space orientation offset to 45° . The raw image was duplicated and rotated by 180° to produce a composite image spanning a full azimuthal range. This is justified in light of the symmetry properties of scattering in reciprocal space. The dark shade at the center of Figure 5.2 comes from the notch of the medium detector to allow small-angle scattering to pass. Scattering from CTAB/NaSal wormlike micelles produces the bright "blob" observed in this pattern. The

azimuthal intensity distribution and orientation of this blob varies with flow condition, as well as with measurement position in the flow cell. To quantify the impact of planar extensional flow, an azimuthal angle of intensity is defined starting from the direction of extension, which is horizontal for this representative image. An annular range of intensity is selected, highlighted by the red semi-annular ring, to cover the characteristic scattering features of wormlike micelles and yet avoid the tip of the notch. The 2-*d* scattering patterns are processed with FIT2D software, to extract an intensity profile as a function of azimuthal angle ϕ , as discussed in the beginning of Section 3.4. The azimuthal intensity distribution $I(\phi)$ is then used to compute the average of second moment tensor $\langle \mathbf{u}\mathbf{u} \rangle$, as defined by 3.16. The second moment tensor gives the two major quantitative measurements of our focus, anisotropy factor AF and orientation angle χ , as defined by Equation 3.19a and 3.22a.

Figure 5.2 also displays an anisotropic diffuse scattering ring close to the image edge, with slightly stronger intensity showing up along horizontal and vertical ends extending from the center of the image. This is due to scattering from the Kapton® windows, and air scattering projected through the cross-slot flow cell. Figure 5.3 presents a scattering pattern collected using an empty flow cell, illustrating these features. To account for the impact of flow cell background scattering, an intensity correction procedure has been developed and applied before computing $\langle \mathbf{u}\mathbf{u} \rangle$. An identical q and ϕ range is used for both the WLM scattering image and the empty cell scattering at each flow cell location to compute $I_{raw}(\phi)$ and $I_{bkgd}(\phi)$. The background scattering is then adjusted based on Equation 5.2.

$$I(\phi) = \frac{I_{raw}(\phi)}{I_0} - \frac{I_{bkgd}(\phi)}{(I_0)_{bkgd}} \cdot \frac{A_{sample}}{A_{emptycell}} \quad (5.2)$$

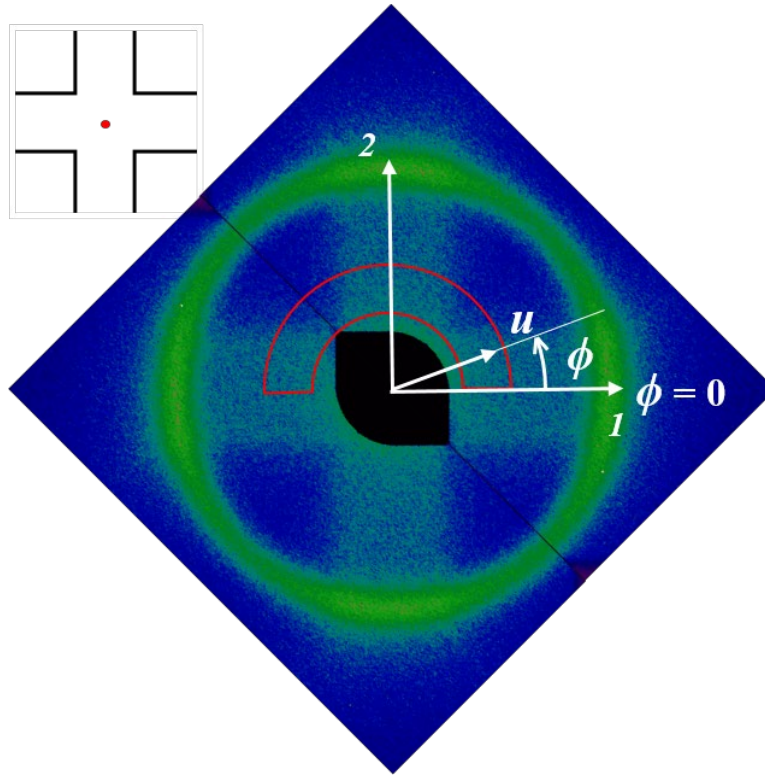


Figure 5.3 A 2-*d* scattering pattern collected with an empty cell

Here, $I_{raw}(\phi)$ is the intensity extracted from WLM scattering. I_0 is the incident beam intensity for that image. $I_{bgd}(\phi)$ is the intensity extracted from the empty cell scattering at the same location of the cross-slot flow cell. $(I_0)_{bgd}$ is the incident beam intensity of that empty cell scattering. The ratio of the absorbance of WLM sample A_{sample} over that of the empty cell $A_{emptycell}$ is computed by dividing the ratio of transmitted over incident beam intensity $\frac{I_t}{I_0}$ with the ratio for empty cell $\left(\frac{I_t}{I_0}\right)_{bgd}$. This is to account for the fact that absorption by the sample will attenuate the contribution of background scattering when the flow cell is filled. An illustration of this procedure is shown in Figure 5.4. The red data are scattering extracted from the raw image corrected with the incident beam intensity. The blue data are extracted from empty cell scattering

at the same location of the flow cell, corrected with incident beam intensity and the ratio of absorbance of sample over empty cell. The black data shows the result of corrected intensity as a function of azimuthal angle ϕ . The crevice at $\phi = 135^\circ$ comes from patching data from two edges of the detector due to its orientation in real space.

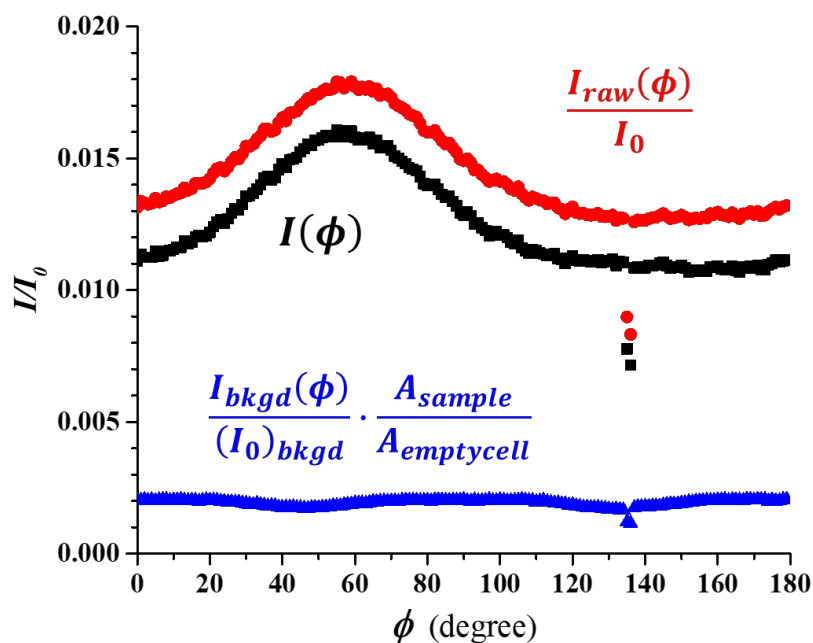


Figure 5.4 A sample background correction for scattering data on the medium angle

5.1.3 Structural dynamics of WLMs in cross-slot flow

In this section, the steady-state structural behavior of wormlike micelles in cross-slot flow under various flow conditions will be examined. First, the degree and direction of orientation of wormlike micelles throughout the cross-slot flow under four representative flow rates are mapped out by a series of vector plots. Second, the anisotropy factor measured along centerlines of extension and contraction axes will be inspected. Third, the degree and direction of

orientation at the stagnation point of the cross-slot flow cell is considered in detail. Finally, the anisotropy factors of wormlike micelles produced by cross-slot flow will be compared to the structural dynamics in Poiseuille flow, using data extracted at the upstream of incoming channels.

5.1.3.1 Orientation maps throughout cross-slot flow cell

Figures 5.5 to 5.8 present a series of vector plots showing degree and direction of orientation in the CTAB/NaSal solution during cross-slot flow at various Weissenberg number. The length of each vector is proportional to the magnitude of anisotropy factor, while the direction of the vector represents the average orientation direction of wormlike micelles. The plots on the left show flow coming through vertical slots and exiting in horizontal slots (designated extension along horizontal direction) while the plots on the right show flow coming through horizontal slots and exiting in vertical slots (designated extension along vertical direction).

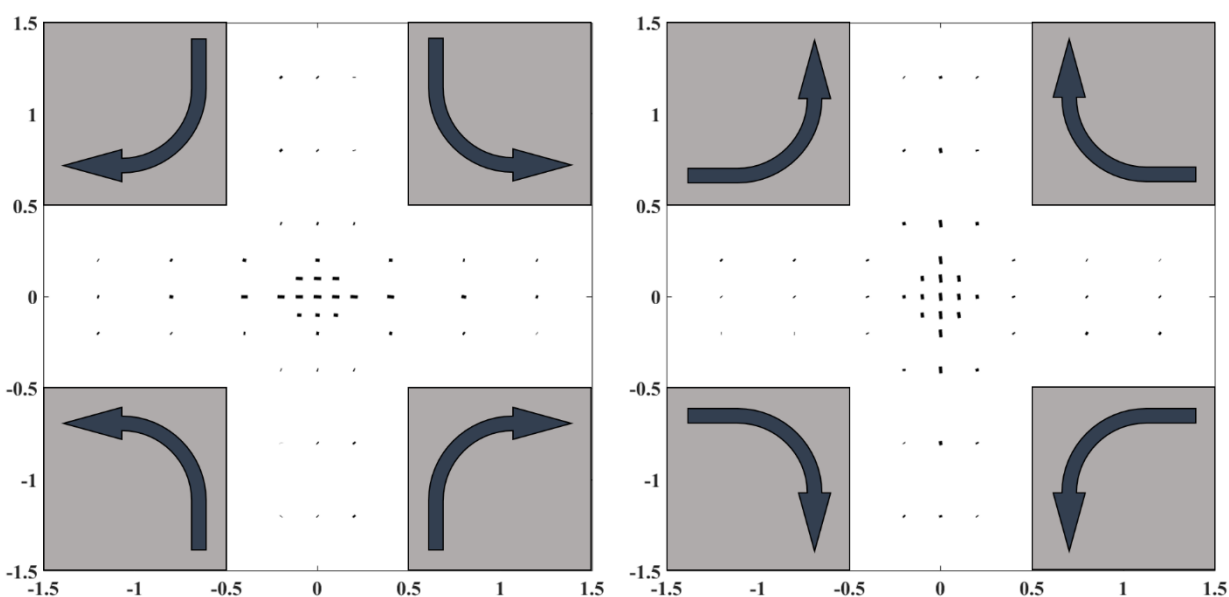


Figure 5.5 Vector plot representing anisotropy factor and orientation angle throughout the cross-slot flow cell, for 60 mM CTAB/ 350 mM NaSal solution subjected to a flow rate of 0.283 ml/min (Nominal Wi : 0.293)

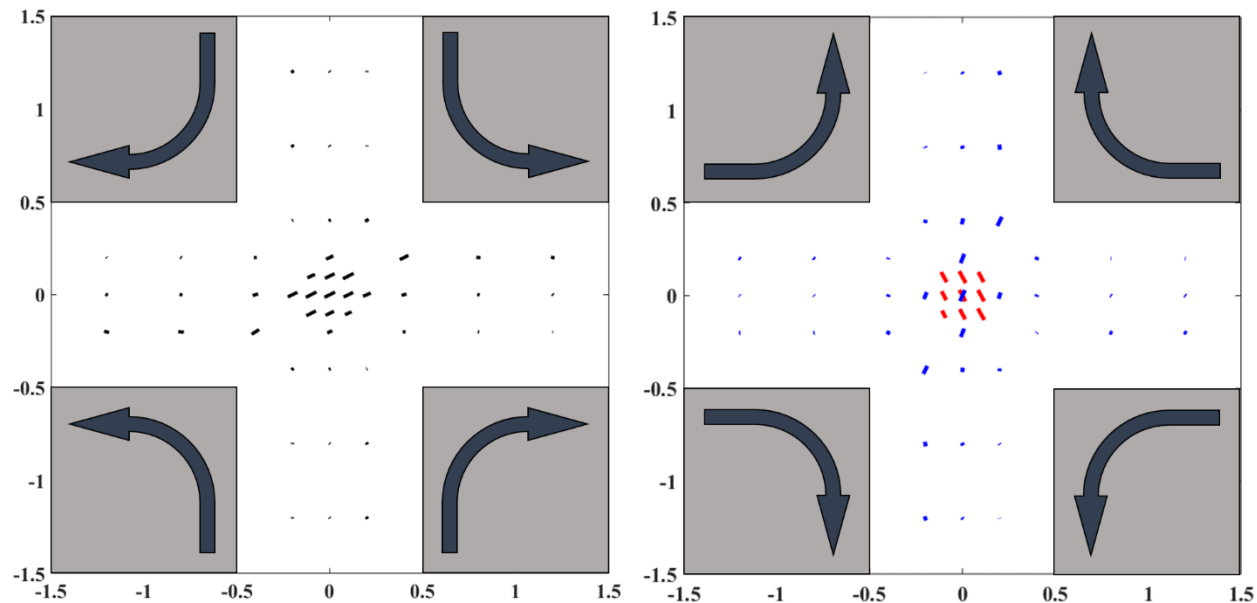


Figure 5.6 Vector plot representing anisotropy factor and orientation angle throughout the cross-slot flow cell, for 60 mM CTAB/350 mM NaSal solution subjected to a flow rate of 0.712 ml/min (Nominal Wi : 0.736)

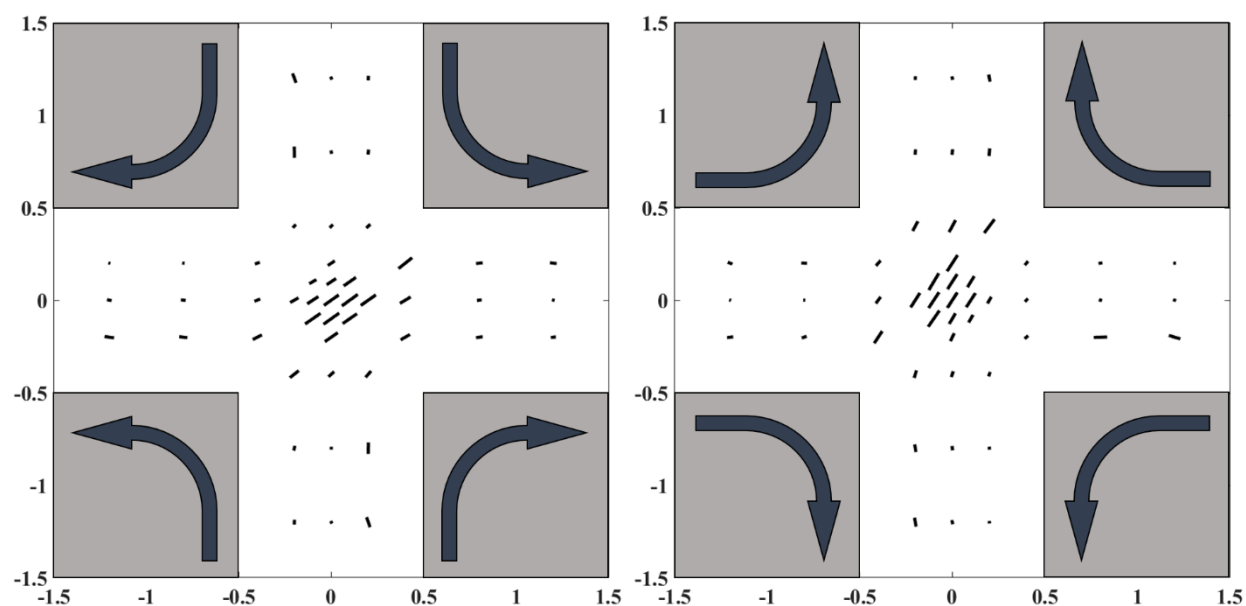


Figure 5.7 Vector plot representing anisotropy factor and orientation angle throughout the cross-slot flow cell, for 60 mM CTAB/350 mM NaSal solution subjected to a flow rate of 1.78 ml/min (Nominal Wi : 1.84)

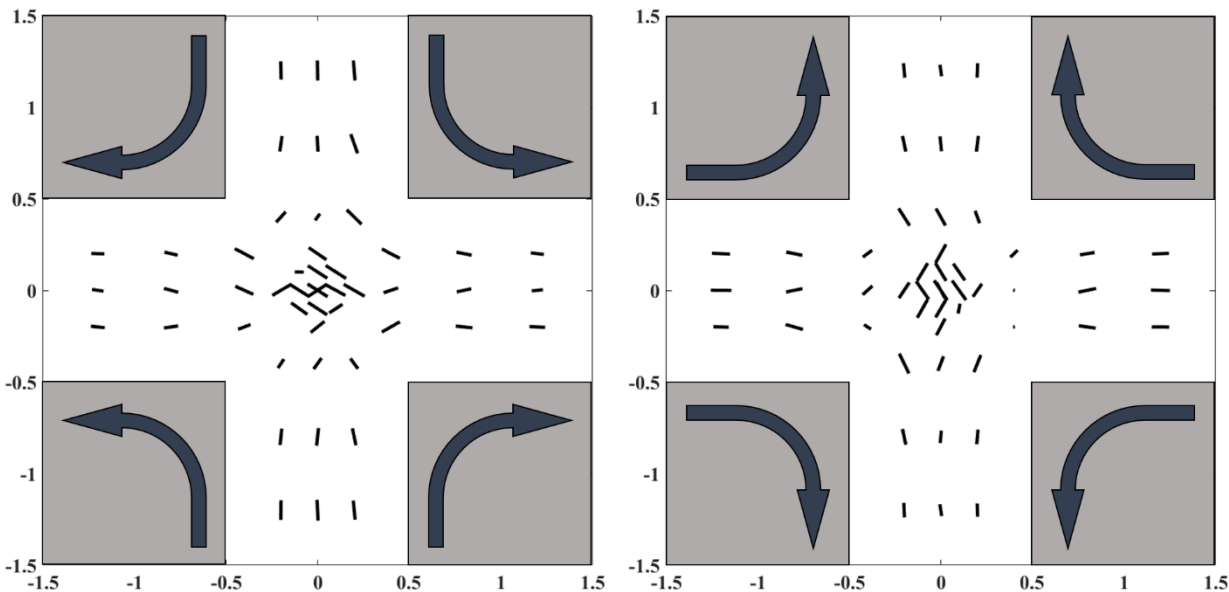


Figure 5.8 Vector plot representing anisotropy factor and orientation angle throughout the cross-slot flow cell, for 60 mM CTAB/350 mM NaSal solution subjected to a flow rate of 4.49 ml/min (Nominal Wi : 4.64)

When the flow is weak (nominal $Wi = 0.293$) (Figure 5.5), negligible orientation is observed in the upstream slit flow region. However, there is clear flow-induced alignment in the cross-slot region, with micellar orientation along the stretching direction: horizontal for infusion and vertical for withdrawal. As the solution moves through the intersection, orientation is maintained within the cross-slot region and gradually decays as fluid moves into the straight slit flow regions downstream. This provides direct evidence that under a nominal Wi of 0.293, the shear flow in the slots does not induce orientation, and that the planar extensional flow in the stagnation region is solely responsible for the observed micellar alignment. When the flow direction is switched to produce extension along vertical axis, the micellar orientation also shifts by 90 degrees. The strongest alignment along the extension axis was found along the centerline. This indicates that the orienting effect of planar extension was strongest at the stagnation point. The off-center region produced weaker orientation, both because the planar extension flow is

weaker, and the residence time along those paths is shorter, meaning micelles experience weaker extensional flow for a shorter period.

When the flow rate is increased to a slightly higher rate (nominal $Wi = 0.736$) as shown by Figure 5.6, the orientation becomes stronger in the cross-slot region, compared to the orientation at the nominal Wi of 0.293 (Figure 5.5). More strikingly, the angle of orientation deviates away from the flow cell axes, indicating that the actual flow pattern departs from our assumed symmetric pattern. This break of symmetry is believed to be induced by an uneven split among the incoming wormlike micelle solution to the outgoing channels.^{55,56,58,62,191} As illustrated in Figure 5.9, the major stream can flow to either outgoing slot, left or right, to produce the asymmetric pattern. As discussed earlier in Section 2.1.3.3, the volume in the syringe is limited, restricting the amount of data that can be collected before the solution in the syringe is all used up and the flow needs to be reversed. Thus, multiple scans are necessary to collect orientation dynamics throughout the whole cell, particularly for experiments with strong flow conditions. These two factors can explain the orientation angle observed in the stagnation region of the right-side plot in Figure 5.6. Two separate experimental runs (color coded in red and blue respectively), necessary to complete this orientation map, yielded two distinct orientation angles at the stagnation point, symmetrically oriented with respect to the vertical direction. More generally, this orientation map may be thought of as juxtapositions of two orientation distributions similar to what is observed in the left panel, except that the symmetry breaking was different in the two runs. Further discussion of this bifurcation will be given at the end of this section.

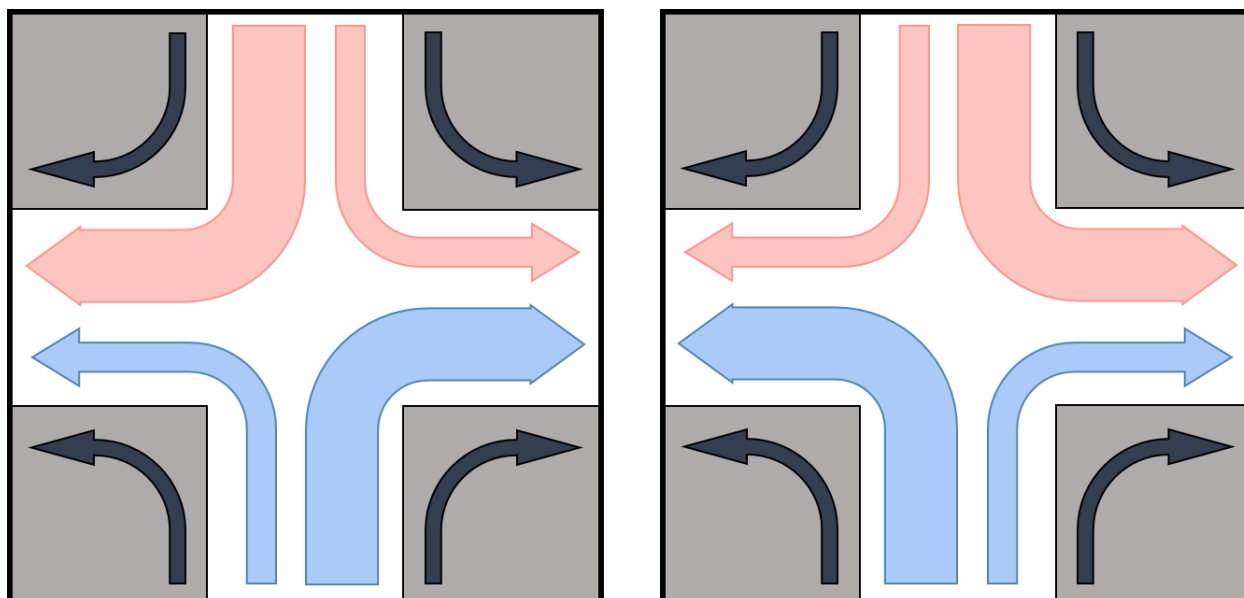


Figure 5.9 An illustration of bifurcation, incoming wormlike micelle solution unevenly splitting to the outgoing channels

At a higher nominal Wi of 1.84 shown in Figure 5.7, the bifurcation in the stagnation region persists, and the observed orientation fails to align along the nominal stretching direction. Additionally, appreciable micellar orientation begins to occur in the slot, both upstream and downstream. Notably, the orientation in the slot is visibly stronger at one side than the other, indicating that the velocity field in the slots is not a symmetric profile that one would normally associate with pressure-driven slit flow. Dubash *et al.*⁵⁵ observed such asymmetric velocity profiles in the slots when studying a shear-banding CTAB/NaSal solution in a low-aspect-ratio cross-slot flow cell.

At a still higher nominal Wi of 4.64, shown in Figure 5.8, a high degree of micellar orientation is observed both in the stagnation region and the slots. Unlike the data in Figure 5.7, there is less asymmetry in AF across the slot. However, here there is evidence of high orientation along the centerline in the slot. Usually, symmetry in slit flow would lead to zero velocity

gradients and no orientation along the slot centerlines away from the contraction. Of course, here the flow bifurcation renders the flow field much more complex. The orientation angles in the cross-slot region are particularly chaotic. At such high rates, multiple reversals of flow are necessary to scan the entire flow cell. At this flow rate, fifteen reversals of flow direction in total were executed to produce the vector plots for both infusion and withdrawal modes. As the flow randomly bifurcates to either direction, the orientation angles appear rather irregular when data from different experiments are combined to produce these vector plots.

This phenomenon of unequal bifurcation in the cross-slot flows has been observed for a while, with the flow pattern generally progressing from symmetrical steady flow, to asymmetrical steady flow, and finally to time-dependent flow. Early studies were made with high molecular-weight polymer in Newtonian solvent. James *et al.*³³ argued that a drawback of using the stagnation-point flow technique to produce extensional flow is this bifurcation, driven by a significant reduction in the stress levels compared with the stress levels in the presumed flow pattern. Arratia *et al.*⁵⁶ demonstrated that within a medium range of Deborah numbers (between 4.5 and 12.5), the flow pattern in the cross-slot turns to be a steady asymmetric one. They also suggested that the flow instabilities may be introduced by the stretching of polymer molecules near the hyperbolic point.

More recently, studies have focused on wormlike micelle solutions. Haward *et al.*⁶² and Dubash *et al.*⁵⁵ both researched shear-banding solutions in microfluidic cross-slots. Haward *et al.* observed bifurcation for Weissenberg number between 1 and 200 and stagnant regions near re-entrant corners. Hence, they attributed the asymmetric pattern to shear localization at the sharp re-entrant corners. Dubash *et al.* identified boundaries on a $Wi-Re$ map for when the steady asymmetric pattern appears and when lip vortices are observed. These two phenomena overlap

significantly, but the critical conditions do not exactly overlap. Pathak and Hudson⁵⁸ studied two WLM solutions, one shear banding and the other not. They observed similar bifurcations for both solutions, but the non-shear-banding CTAB/NaSal solution has an earlier onset of bifurcation than the shear-banding CPyCl/NaSal solution. The curves of how orientation angle changes with Wi are different for the two solutions, while possible reasons remain unclear.

Finally, viscoelastic flow simulations of cross-slot flow with classic models has provided further insights into this bifurcation. Using the upper-convected Maxwell model, Poole *et al.*¹⁹¹ demonstrated that the bifurcation is purely elastic, and that inertia stabilizes the flow pattern. Reduction of stress was believed to drive the bifurcation. Simulations with the more realistic “FENE” model¹⁹² revealed that the extensional properties, or the level of extensibility, strongly influence the bifurcation. On the other hand, they found that the roundness of corners only had a marginal influence on triggering the bifurcation, especially if the corner is changed from a perfectly sharp corner to a round shape of small radius of curvature.

With all these documentations on symmetry-breaking bifurcation in cross-slot flows of other WLM solutions, it is tempting to quantitatively compare all the studies. However, differences in precise formulation and flow cell geometry complicate direct comparisons. Pathak and Hudson studied a more dilute CTAB solutions, but which has a high salt to surfactant ratio. (30 mM CTAB/ 240 mM NaSal). They report a bifurcation at $Wi_{crit} = 1.24$, higher than our value. However, their reported Wi_{crit} is based on measured extension rate at the midplane rather than the nominal extension rate used here. Cast in terms of a nominal Weissenberg number, their critical value 0.33, in remarkable agreement with our observation (0.3, Figure 5.13). This agreement may be fortuitous, since their flow geometry is very different: aspect ratio of 0.53 compared to the high aspect ratio of 5 used here. Our data may also be cast onto the $Wi-Re$ map generated by

Dubash for CTAB solutions with much lower salt concentration, which renders them shear-banding. Dubash's results would suggest a much higher critical Wi (4) than what is observed here (0.3). Dubash's study also employed a low aspect ratio cross-slot geometry, so that there are significant differences in both the nature of the WLM solution and the geometry. In this light, significant differences in critical flow conditions are not too surprising. The simulation by Poole *et al.*¹⁹¹ also reported a critical De of 0.31. Considering the rudimentary nature of upper-convected Maxwell model and the unrealistic 2- d flow field in the absence of inertia, plus the complexities illustrated by comparing our results to all the other documentations on critical conditions, it is hard to judge whether this coincidence is merely out of luck or such a simple setup is enough to capture the essence of bifurcation.

A noticeable distinction among our observations is the relationship between the onset of bifurcation and a saturation of orientation. Pathak and Hudson observed a small Wi regime before the critical Wi for bifurcation where birefringence essentially saturates. This saturation was interpreted as wormlike micelle chains being nearly fully extended and aligned. Similar saturations of birefringence signals were also found in Pathak and Hudson's other shear-banding sample 100 mM CPyCl/ 60 mM NaSal solution, as well as the study by Haward *et al.*⁶² using the same sample. Contrarily, the degree of alignment of WLMs before bifurcation in our study shows no sign of saturation at all. In fact, the increase in micellar alignment after bifurcation is rather considerable compared to the growth before bifurcation. Because each of our studies are all different from each other, either the properties of wormlike micelles or the cross-slot flow cell geometries, it is impossible to precisely identify the source of such unusual behavior.

Finally, we found that our value of critical Wi for bifurcation at 0.3, produced in our "macrofluidic" cross-slot flow cell, is not far away from the results from birefringence

measurements in microfluidic cross-slot flow cells by Pathak and Hudson, Haward, Dubash *et al.* The cross-slot cells employed in birefringence measurement often have dimensions less than 1 mm. In Haward's experiment, the Re for symmetric and bifurcated flow conditions were all below 10^{-5} , while our Re ranges from 9.4×10^{-5} to 0.094. Poole *et al.*¹⁹¹ suggested that inertia will delay the onset of bifurcation and reduce the magnitude of asymmetry. Comparing the results from our SAXS data versus others' birefringence measurements, it appears that inertia may just play a limited role in this phenomenon.

5.1.3.2 Anisotropy factor measured along extension and compression axes at various rates

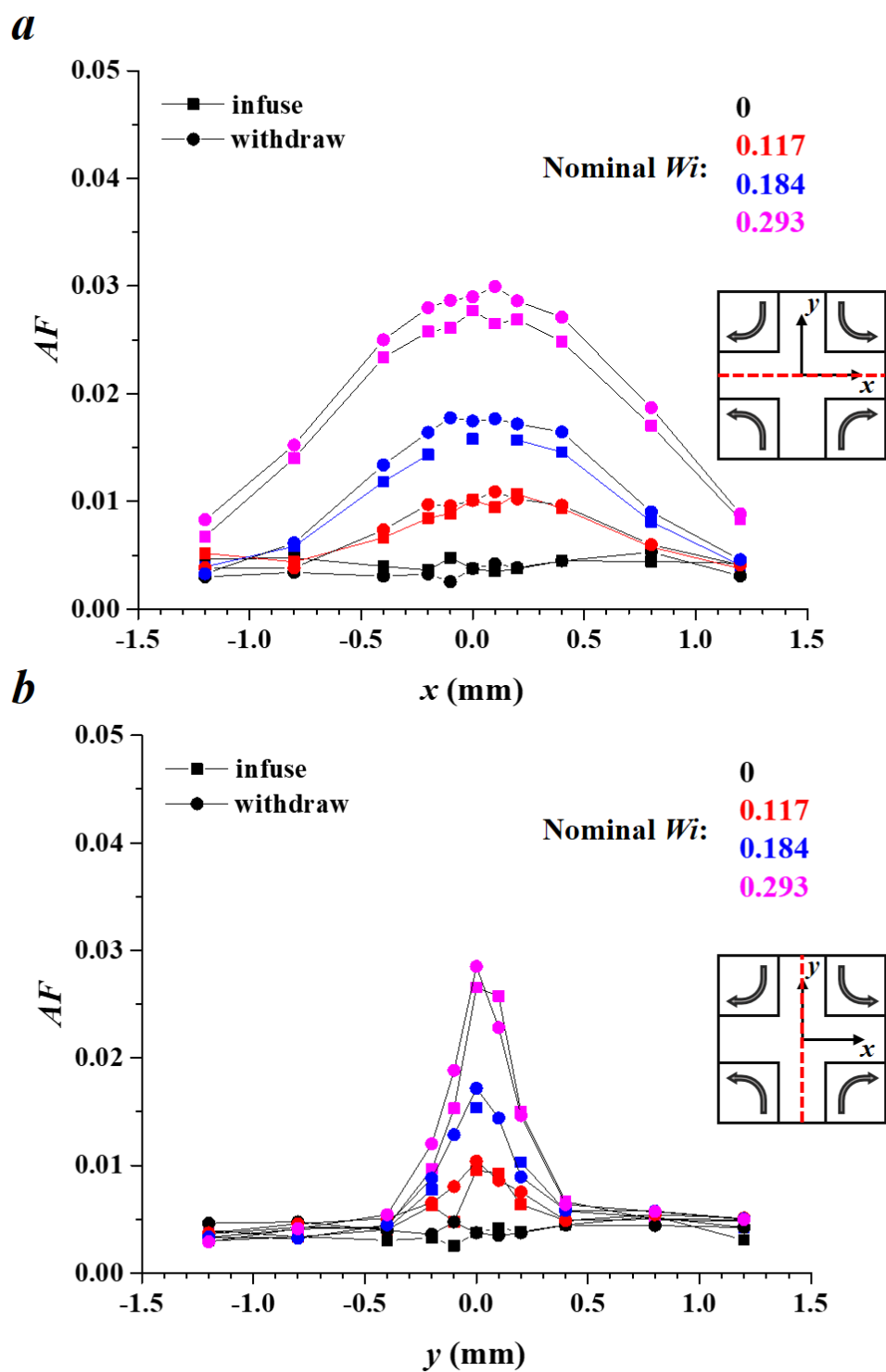
The anisotropy factors along the extension axis x and compression axis y under various flow conditions are plotted in Figure 5.10 to Figure 5.12. The coordinate $(x, y) = (0, 0)$ represents the stagnation point. Since a complete orientation map was collected for both infusion and withdrawal pump flow, each flow condition results in two sets of data. In these figures, coordinates are adjusted to reflect the actual stretching and compression axes. We consider results with flow rates divided into three groups.

In the relatively small flow rate regime (Figure 5.10), as nominal Wi increases from 0 to 0.29, anisotropy factor data are consistent for both infusion and withdrawal, along both extension and compression axes. Along the compression axis, significant anisotropy only appears for $-0.5 < y < 0.5$, while AFs along the extension axis extend to 1.0 mm away from the stagnation point. Since these flow conditions do not induce orientation in the upstream channels (along the compression axis), the planar extensional flow in the stagnation region is responsible for this orientation, which relaxes as the WLM solution is driven into the downstream slots (along

extension axis). The orientation persists beyond the stagnation region, but eventually relaxes as the deformation rate along the centerline is zero in the downstream slit flow.

At a medium range of flow rate (nominal Wi from 0.464 to 1.84; Figure 5.11), anisotropy factor data have less consistency between infusion and withdrawal, compared to the small rate regime. The AF s also do not exhibit symmetry with respect to $x = 0$ or $y = 0$. Both observations are attributable to the flow bifurcation as discussed earlier in relation to Figure 5.6. Still, under these conditions the overall behavior pattern retains some similarity to Figure 5.10, with orientation more highly confined along the compression axis, and low centerline orientation in both up- and downstream channels.

As flow increases to the strongest regime at nominal Wi ranging from 1.84 to 11.7 (Figure 5.12), the behavior pattern changes dramatically. Between Wi of 1.84 and 2.93, the anisotropy measured along the centerline in the upstream slots jumps to large values, and exhibits erratic behavior. Since a symmetric slit flow is not expected to produce *any* orientation, this suggests that complexities associated with the flow bifurcation are affecting behavior upstream of the stagnation zone. Remarkably, orientation in the upstream slots is on par with that in the cross-slot region. A pronounced dip in anisotropy factor is observed along the compression axis y near the edge of the cross-slot intersection ($y = \pm 0.5$) for the largest three rates. This may be attributed to the reorientation that wormlike micelles undergo near the border between the upstream slots and the cross-slot region as the direction of flow is drastically altered in the asymmetric, bifurcated flow field.



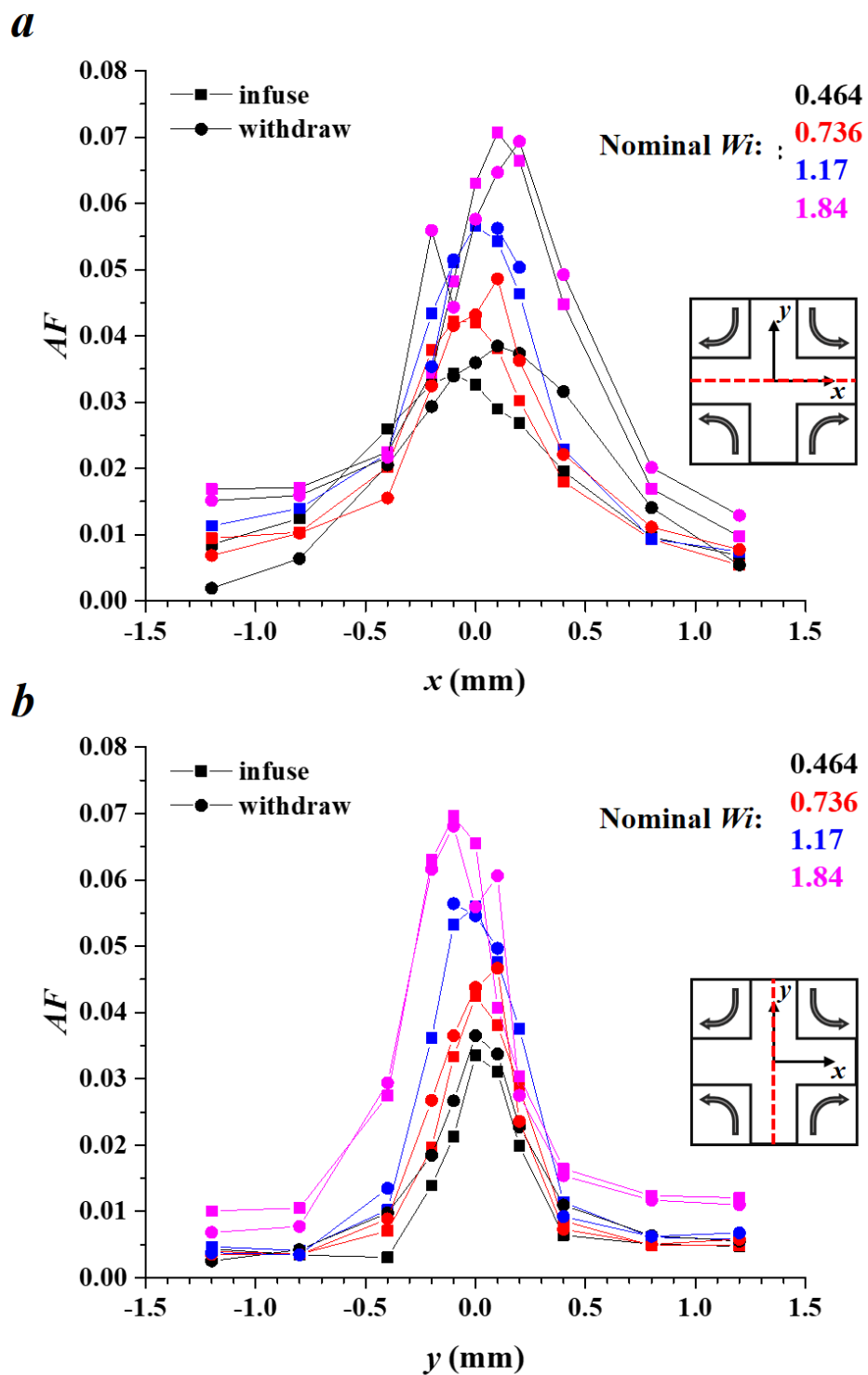


Figure 5.11 Anisotropy factor data measured along (a) extension axis x and (b) compression axis y for 60mM CTAB/ 350 mM NaSal solution in cross-slot flow

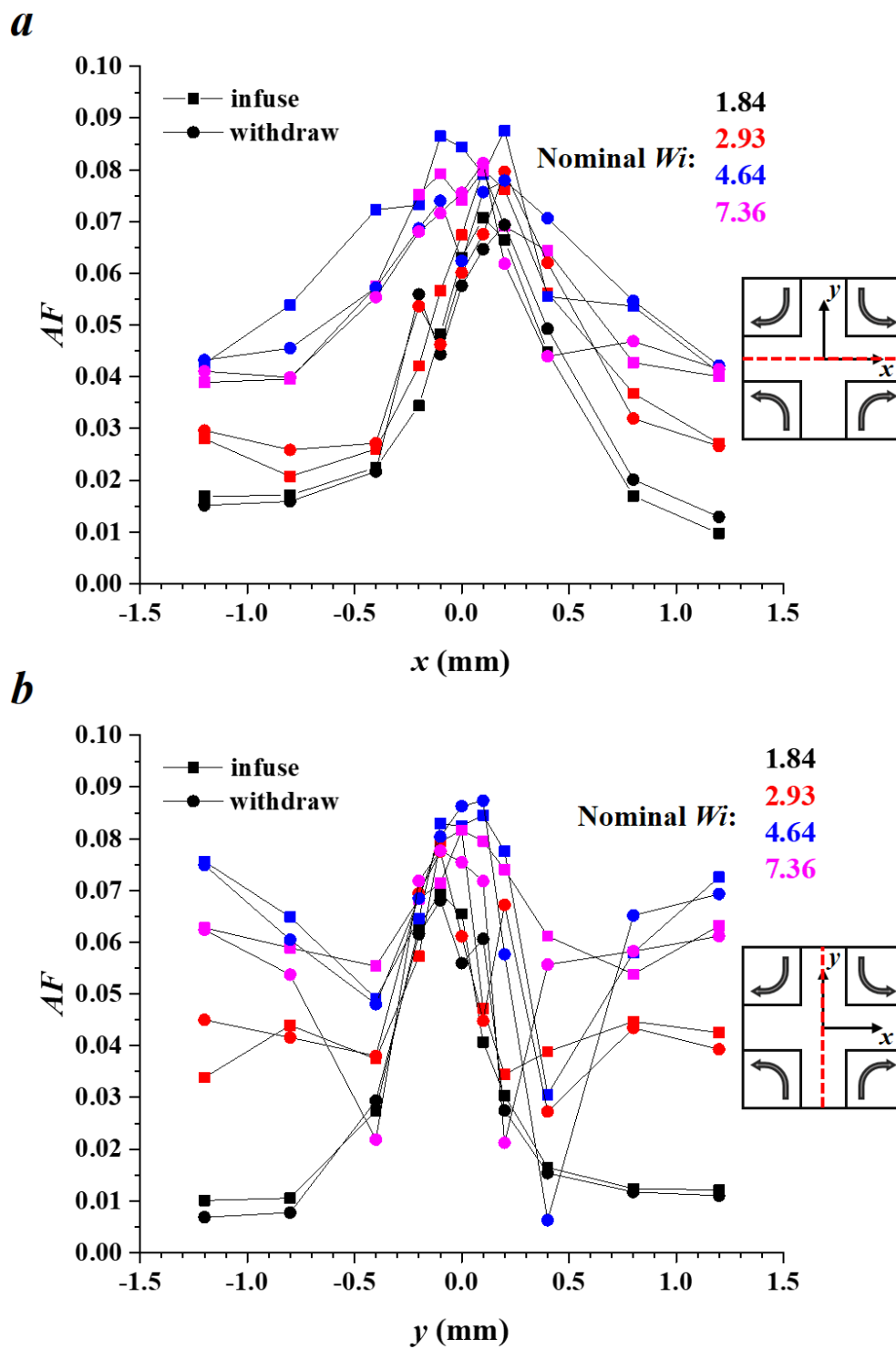


Figure 5.12 Anisotropy factor data measured along (a) extension axis x and (b) compression axis y for 60mM CTAB/ 350 mM NaSal solution in cross-slot flow

5.1.3.3 Degree and direction of orientation at stagnation point

Figure 5.13 presents the anisotropy factor and orientation angle measured at the stagnation point as a function of nominal Weissenberg number. For the smallest three rates at nominal Wi of 0.117, 0.184, and 0.293, AF grows from 0.01 to 0.03. This trend that stronger flow induces larger micellar orientation is expected, and is also reflected in birefringence studies on similar WLM systems.^{55,62} In contrast to studies of coil-stretch transitions in dilute polymer solutions,^{54,59} a critical extensional rate associated with dramatically enhanced orientation is not observed. At these lowest rates, the average orientation angles are near zero, indicating that wormlike micelles align along the expected stretching axis of the planar extensional flow. A slight deviation from the symmetry axis is observed, however. According to Equation 3.22, the orientation angle becomes undefined at low rates as both the numerator and denominator in the argument of the inverse tangent go to zero. The nonzero orientation angle at low Wi can be attributed to some systematic bias in the data, such as imperfection in background subtraction, that affects the orientation angle results as the anisotropy in the sample itself tends towards zero.

At intermediate flow conditions, the alignment of wormlike micelles continues to grow. However, the flow (or elastic) instability intervenes, and the orientation angle bifurcates into two paths, symmetrical with respect to stretching direction. As discussed in Section 5.1.3.1, multiple passes of flow in both directions are necessary to collect the entire orientation map, and, in a given run, the flow instability can result in the major stream exiting either outflow slot, stochastically. Thus both positive and negative orientation angles are observed, for both infusion and withdrawal modes. Because of the flow bifurcation, the increasing anisotropy in this regime cannot be attributed solely to an increasing planar extension rate since the flow profile at the geometrical center (presumed stagnation point) is rendered more complex.

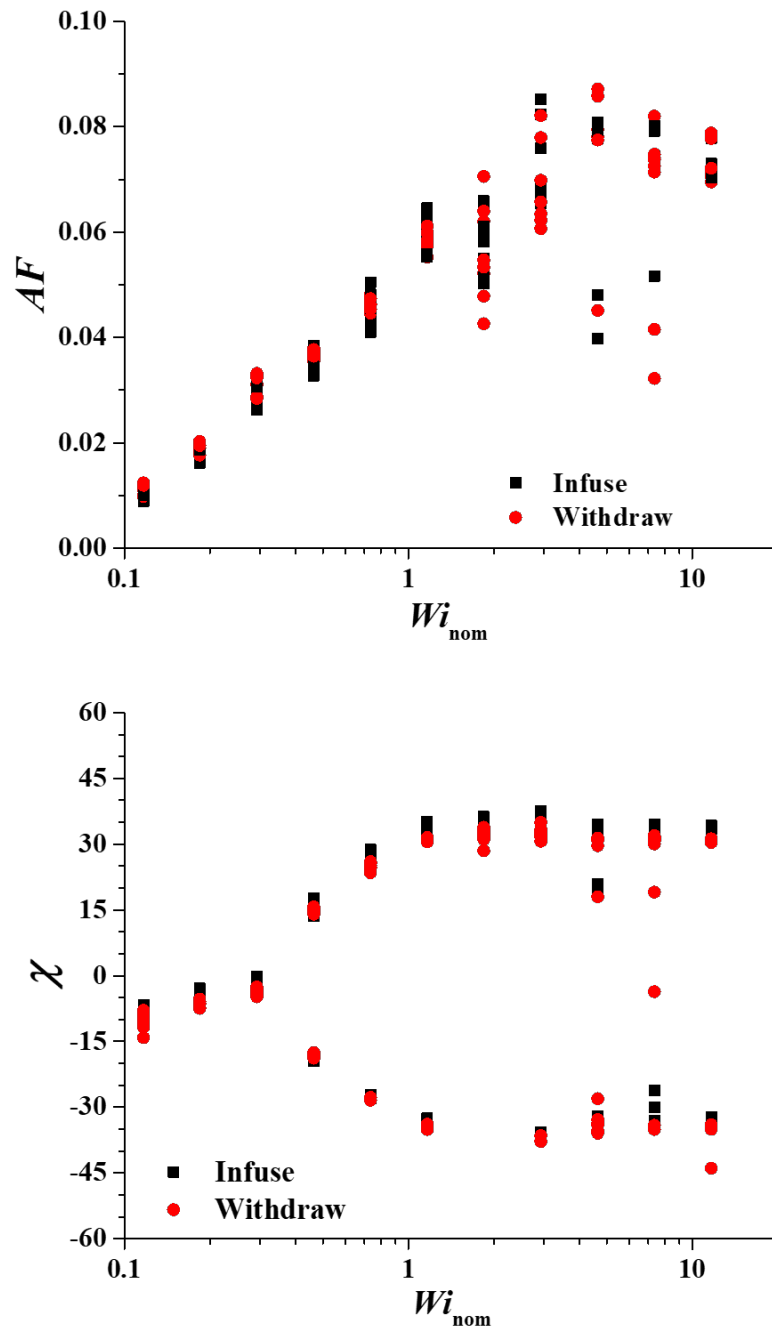


Figure 5.13 Anisotropy factors and orientation angles of WLMs at stagnation point as a function of nominal Weissenberg number.

At higher Wi of 1.84 and above, the AF data becomes erratic, fluctuating from 0.04 to 0.09, as the instability continues and the flow profile in the cross-slot intersection presumably becomes more complex. Except for a few outliers, the orientation angle at high flow rates seems to saturate around $\pm 35^\circ$. This disagrees with the square root relationship described by Pathak and Hudson⁵⁸ with the 30 mM CTAB / 240 mM NaSal solution. Due to the weak scattering from this WLM sample and associated long exposure time, it is impossible to tell whether or not a time-dependent flow emerges at these high flow rates. However, this is a commonly observed phenomenon in other studies, and could explain the increasingly erratic data found here.

5.1.3.4 Comparison of anisotropy measured in shear and planar extension

We attempted studies of our CTAB/NaSal solution in homogeneous shear, but due to its viscoelastic properties, the solution was expelled from our 1-2 plane cone-and-plate cell. As an alternative, as in Section 4.4.3.2, we examined orientation data in the upstream slots to gain some insights into the impact of shear on micellar orientation. The data collected at the farthest ends in the upstream slots are used. Specifically, the AF data measured at (-0.2, 1.2), (0.2, 1.2), (-0.2, -1.2), and (0.2, -1.2) are averaged for infusion mode, while AF data measured at (-1.2, -0.2), (-1.2, 0.2), (1.2, -0.2), and (1.2, 0.2) are averaged for withdrawal mode.

The MWCNT suspension studied in Chapter 4 was Newtonian, and hence the relevant shear rate could be readily computed from the slit flow dimensions and volumetric flow rate. This is complicated by the shear-thinning viscosity of the WLM solution. Fitting the viscosity to a shear-thinning constitutive equation (*e.g.*, the Ellis model) can allow an analogous analysis. However, the orientation maps in Figures 5.6 and 5.7 illustrate asymmetries in the flow field, which call into question the validity of any detailed analysis. Rather, since estimates of

characteristic shear rate (Equation 2.2) and characteristic extension rate (Equation 2.1) are identical for high aspect-ratio cross-slot flow, we simply plot both stagnation point (extension) and slit flow (shear) data against nominal Weissenberg number, in order to gain qualitative insights into the relative impact of shear and extension on micellar orientation (Figure 5.14).

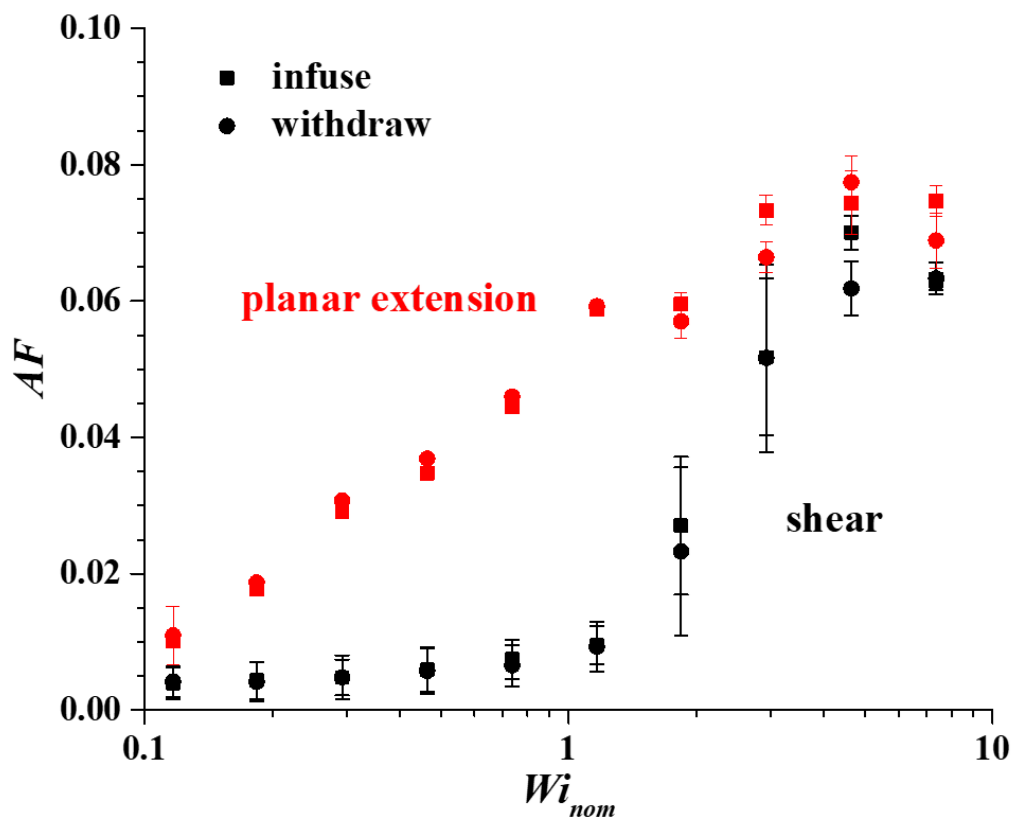


Figure 5.14 AF measured in upstream slots and at stagnation point of cross-slot flow cell

For all flow conditions at $Wi_{nom} \lesssim 1$, anisotropy measured at the stagnation point shows an increasing trend, and is significantly higher than what is found in upstream slots. This is consistent with the general expectation that planar extension should produce stronger alignment

effect. This also resembles observations in Pathak's work where birefringence induced at the (Note that this trend extends to intermediate Wi , where the orientation fields illustrate symmetry breaking in both the cross-slot region as well as in the upstream slit flow.) As nominal Wi grows beyond 1, the flow in the cross-slot intersection becomes erratic, and the anisotropy found in the slots dramatically grows, reaching values comparable to what is measured in the stagnation region. This sudden increase in AF in the upstream channels mirrors the growth in AF measured along the upstream centerline at the highest flow rates (Figure 5.12 *b*).

5.2 Lamellar surfactants

Lamellar phases, constituted by stacking of self-assembled surfactant bilayers, constitute another class of surfactant solutions that have attracted a great deal of research. Such phases appear in additives in many detergents, cosmetics, pharmaceutical and other commercial products. Unlike WLMs, which are disordered liquids, lamellar phases possess long range order in one direction which leads to more complex rheology. The small-amplitude oscillatory shear of lamellar surfactants often displays almost constant G' across the frequency domain and order-of-magnitude smaller G'' .^{60,193} The steady-state viscosity usually shear thins, attributed to the alignment of lamellae upon flow.^{60,194} When subjected to shear flow, the viscosity of lamellar phases may gradually build up¹⁹⁴ as a result of a structural transformation to form multilayer vesicles, often referred to as "onion phase". This phenomenon has been probed by various techniques such as microscopy,¹⁹⁴ light,¹⁹⁵ x-ray^{102,196} and neutron scattering.⁶⁰ The impact of flow conditions (rate, strain, and stress) upon onion size, orientation, long range ordering,^{194,195,197} and defects in the lamellar packing¹⁹⁸ have been explored, while the connection

between microstructures and the macroscopic rheology has been stressed by several articles.^{177,194,198,199}

The extensional rheology of lamellar surfactants has rarely been investigated. Most existing research has employed scattering techniques to explore microstructural changes under extensional flow, where orientation of lamellar stacking, domain size, and intermembrane spacing can be affected.^{60,102,196} However, due to experimental constraints discussed earlier (Section 2.1.1), the devices used in these studies produced flows in which the desired extensional flow is conflated with stronger shear gradients through most of the flow cell. Hence, using the newly-built high aspect ratio cross-slot flow cell, the studies described here provide a cleaner opportunity to explore the impact of extensional flow on lamellar surfactant phases. Diffraction from periodically stacked lamellae can produce strong scattering intensities, facilitating such measurements. We report studies on two surfactant systems reported in the literature to show lamellar ordering. The first recipe consists of 17.4 wt% cetyltrimethylammonium chloride (CTAC), 20 wt% 1-pentanol and 62.6 wt% millipore water from Martin *et al.*¹⁹⁶ The second is a 60 mM solution of didodecyldimethylammonium bromide (DDAB) in deionized water.^{86,193,200}

5.2.1 CTAC/Pentanol/ Water

5.2.1.1 Materials and Methods

This recipe was reported by Martin *et al.*,¹⁹⁶ The solution studied here, consisting of 17.4 wt% CTAC, 20 wt% 1-pentanol and 62.6 wt% water, shows strong x-ray diffraction peak at $q \sim 0.1 \text{ \AA}^{-1}$, corresponding to a d -spacing about 63 Å, and the orientation of lamellar microstructure has been shown to change depending on flow conditions. Chemicals were purchased from Sigma-Aldrich and used as received. All the ingredients were sealed inside a glass bottle and

then shaken vigorously for at least 10 minutes by hand. The sample was then kept in a thermostat at 25 Celsius for a week. Finally, we centrifuged the solution to remove air bubbles.

The CTAC/Pentanol/Water sample exhibits significant solid-like character in its rheology (Figure 5.15). The storage modulus G' is nearly constant across the frequency range studied, and is much larger than G'' . No terminal relaxation regime is observed, indicating a lack of relaxation processes on the time scales probed in the oscillatory experiments. Both observations result from the ordered, layered structure present in this material. In steady shear, the viscosity shows strong shear thinning with no indications of a zero-shear plateau, behavior that is characteristic of soft solid-like samples that are forced to yield. Figure 5.15 *b* also shows the magnitude of the complex viscosity, $|\eta^*|$, derived from oscillatory shear data, which is found to be substantially larger than the shear viscosity. Failure of the empirical Cox-Merz rule (which postulates equivalence between $\eta(\dot{\gamma})$ and $|\eta^*(\omega)|$ when evaluated at $\omega = \dot{\gamma}$) is not surprising for ordered complex fluids. The fact that the steady shear viscosity is much smaller than $|\eta^*|$ suggests the possibility that shear-induced alignment of lamellae reduces the samples resistance to deformation during continuous flow. (An alternative explanation is that the steady shear data are affected by slip at the fixture surfaces, a frequent artifact in the rheological testing of soft solid-like samples.)

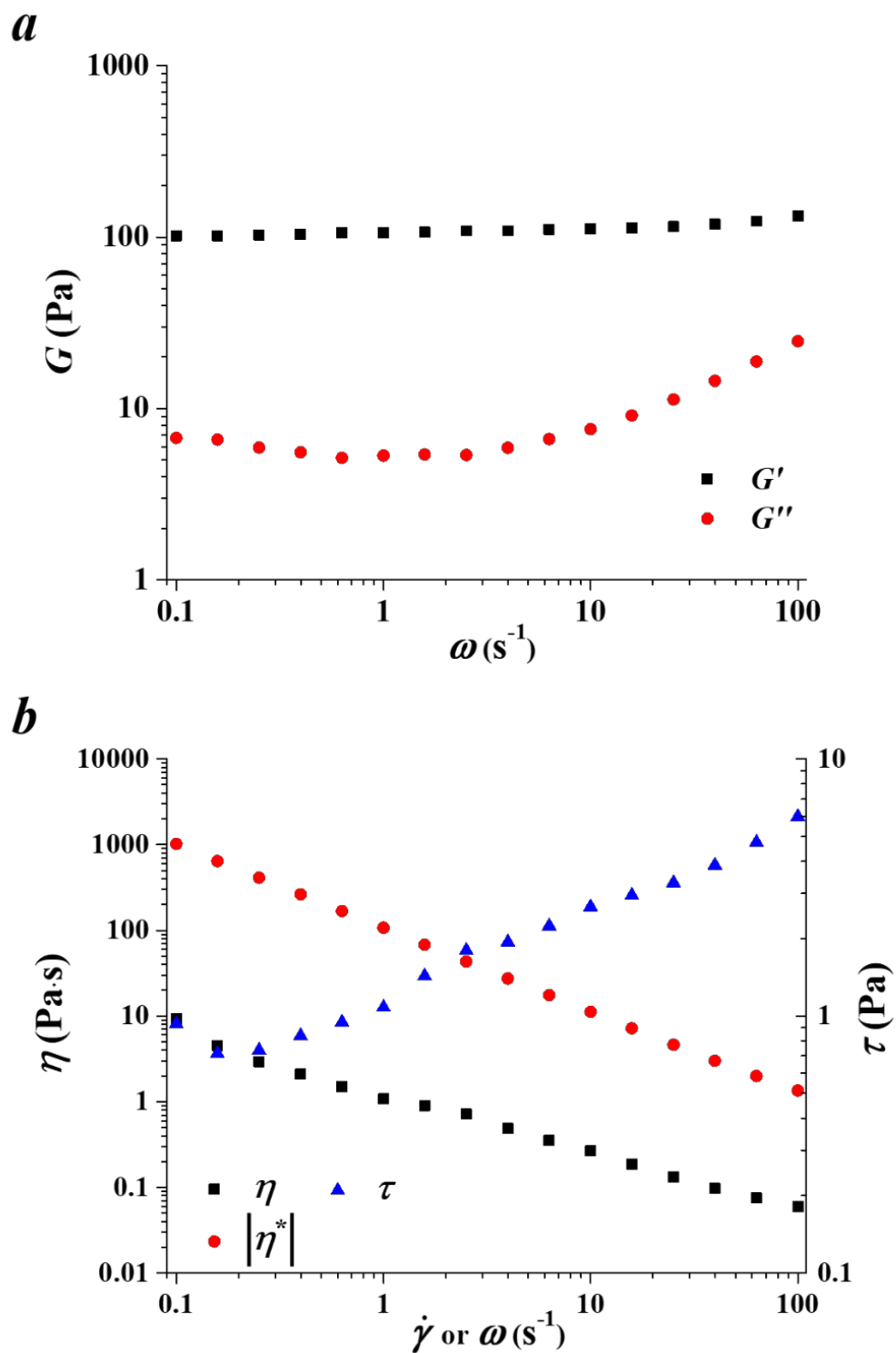


Figure 5.15 Shear rheology of CTAC/Pentanol/Water lamellar surfactant solution in (a) small-amplitude oscillatory shear, and (b) steady shear

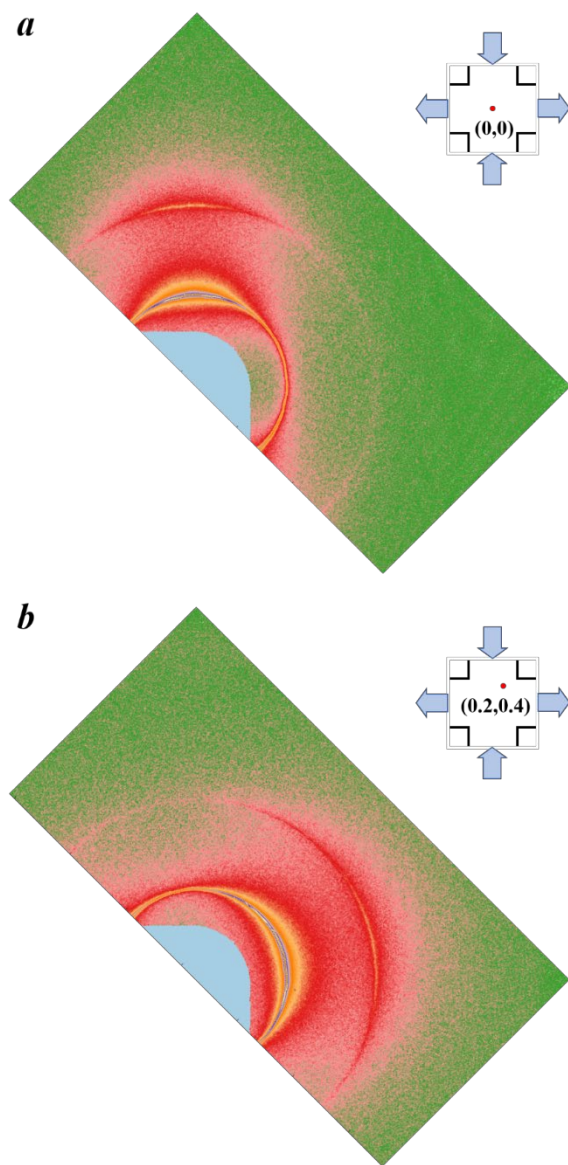


Figure 5.16 Representative scattering patterns from CTAC/Pentanol/Water solution at two locations in the cross-slot flow cell, during flow at a nominal extension rate of 1 s^{-1}

The high modulus (relative to the CTAB/NaSal WLM system) created difficulty for the syringe pump and cross-slot flow cell. Specifically, we could only apply flow along one direction to this lamellar surfactant recipe, since attempts to alternate between infuse and withdraw modes led to excessive entrainment of air bubbles. This limited the range of flow rates that could be

studied to what could be supplied by in one pass supplied by filled syringes, and restricted the flow to a single direction. We chose to feed in the solution along vertical channels and hence produced extension along the horizontal axis.

The x-ray scattering experiments were carried out at the APS 5-ID-D station at Argonne National Laboratory. The energy of the incident beam is 9.4 keV, equivalently with a wavelength of 1.32 Ångström. The exposure time was 3 seconds for each frame. The scattering patterns were collected with the medium angle detector Rayonix LX170HS. The binning of the detector was set at 4 by 4.

5.2.1.2 Structural dynamics of CTAC/Pentanol/Water subjected to planar extension

Flow-induced orientation of lamellar orientation in the CTAC/Pentanol/Water solution varies strongly with position in cross-slot flow (Figure 5.16). A strong primary diffraction peak, as well as a weaker secondary diffraction peak both lie in the q -range covered by the medium angle detector. The secondary peak is found at twice the scattering vector associated with the primary peak, confirming 1-dimensional lamellar ordering. The scattering pattern collected at the stagnation point shows concentration of diffracted intensity in the vertical direction, indicating that lamellae align along the horizontal flow direction. An image collected at a different location in the cross-slot flow cell shows strong differences in both the direction and degree of lamellar alignment compared to the intensity profile collected at the stagnation point.

Vector plots representing the spatial distribution of measured anisotropy factor and orientation angle indicate that strong lamellar orientation is found throughout the cross-slot flow cell at all flow rates studied (Figure 5.17). At the smallest flow rate (nominal extensional rate of 0.01 s^{-1}), the distribution of orientation is somewhat non-symmetrical. This reflects the

orientation state induced during the original filling process of the lamellar sample into the flow cell. Experiments at the lowest flow rates were the first performed after filling and mounting the flow cell, and it appears that flow at these low rates was insufficiently strong to ‘wash out’ the

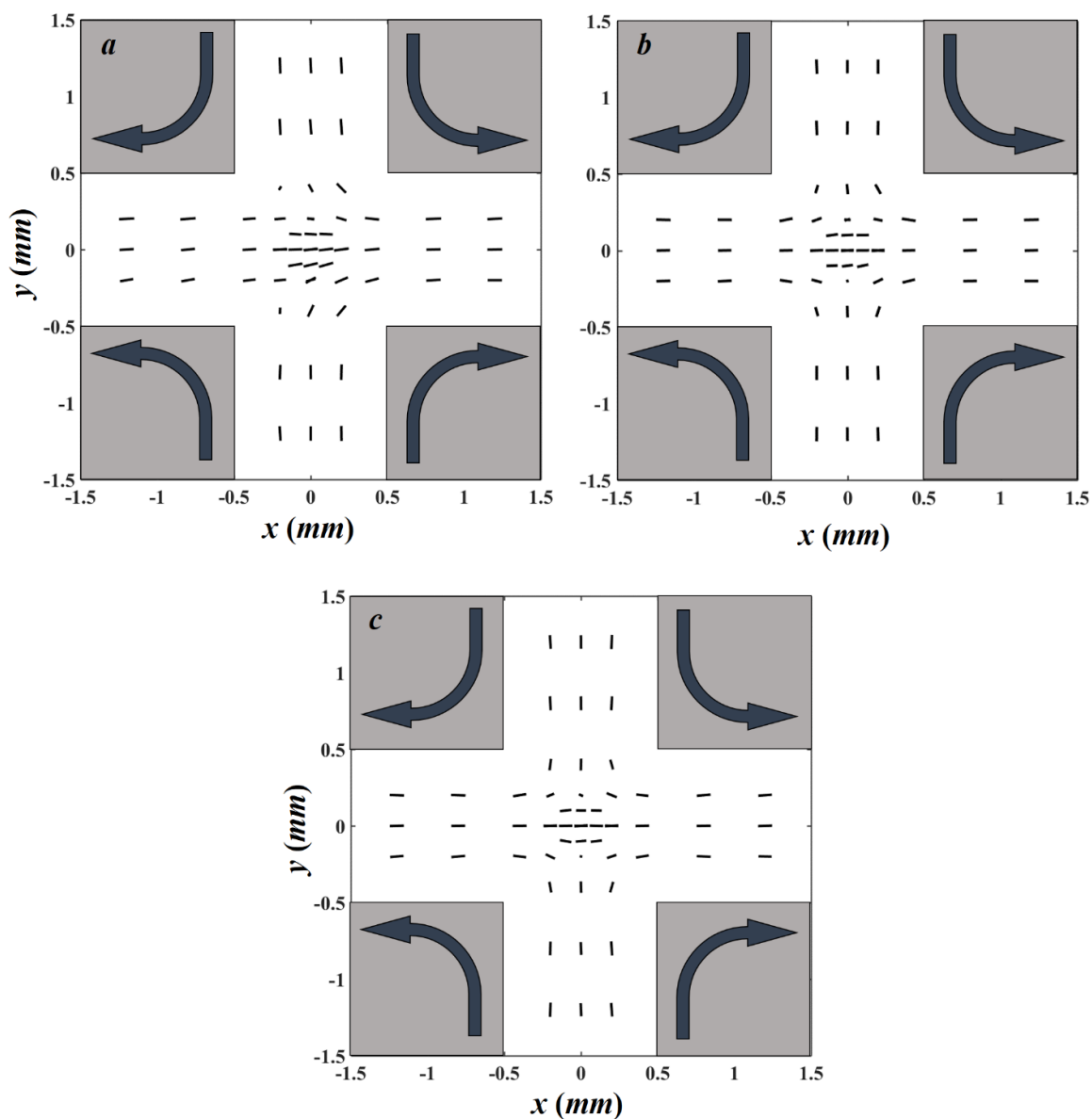


Figure 5.17 Vector plots representing orientation state measured in lamellar surfactant CTAC/Pentanol/Water in cross-slot flow at nominal extensional rates of (a) 0.01, (b) 0.1, and (c) 1 s⁻¹.

pre-existing orientation. With continued flow at progressively increasing rates, the lamellar orientation distribution became symmetric, as is expected for planar extensional flow, although the degree of orientation is nearly independent of flow. For instance, the vector plots representing the distribution of lamellar orientation at nominal extension rates of 0.1 and 1.0 s^{-1} are nearly identical.

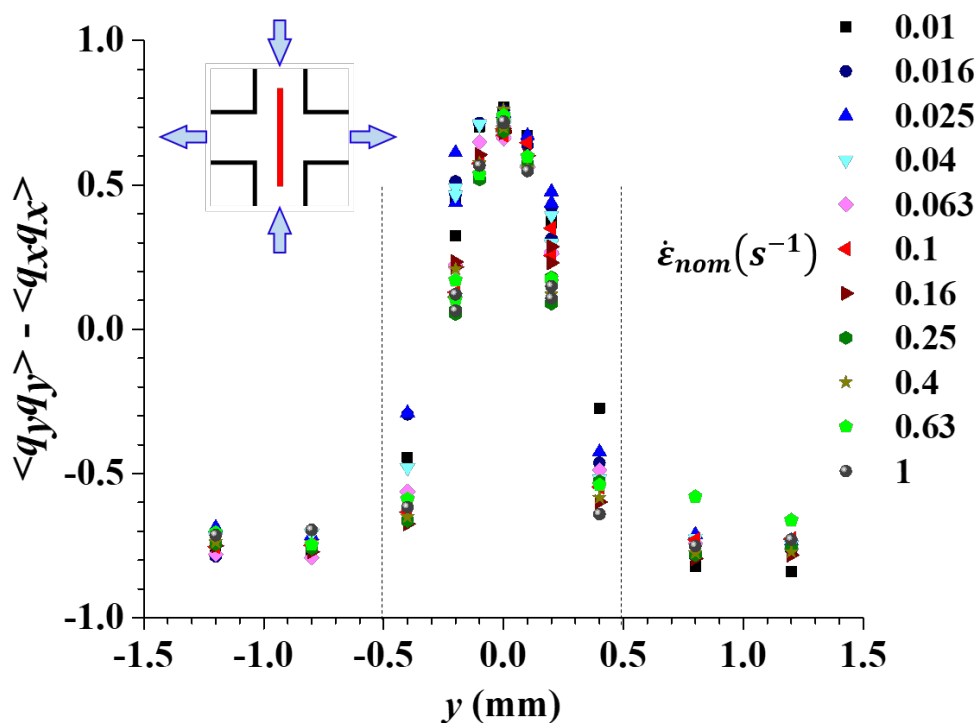


Figure 5.18 Distribution of simplified $AF \langle q_y q_y \rangle - \langle q_x q_x \rangle$ measured in CTAC/Pentanol/Water along the vertical centerline axis of cross-slot flow cell ($x = 0$) at indicated nominal extension rates

Lamellae are well oriented along the flow direction by shearing in the straight sections of pressure-driven flow upstream and downstream of the cross-slot region. Indeed, the primary effect of the extension-dominated flow in the cross-slot is to flip the direction of lamellar

alignment to horizontal at the stagnation point. This may be demonstrated by plotting the simplified AF along the vertical centerline axis of the flow ($x = 0$); that is, along the incoming channels as fluid approaches the stagnation point from above and below (Figure 5.18). The shift from vertical alignment of lamellae in the upstream slots to horizontal alignment in the stagnation region is characterized by the localized change in sign of the simplified anisotropy factor from roughly -0.8 to $+0.8$, for all flow rates. The lack of any significant rate-dependence to the measured anisotropy is further reinforced by Figure 5.19, which presents steady state AF measured at the stagnation point.

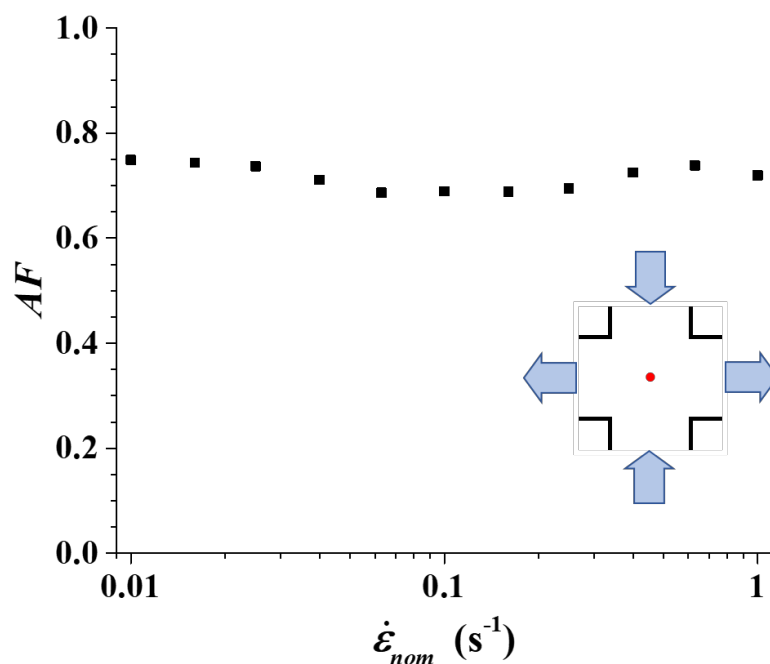


Figure 5.19 Steady-state anisotropy factor measured in CTAC/Pentanol/Water at stagnation point in cross-slot flow, as a function of nominal extension rate.

Upon flow cessation, negligible relaxation of flow-induced orientation is found (Figure 5.20). Azimuthal intensity scans show some weakening of the strength of the peaks observed

perpendicular to the flow direction, which is manifested quantitatively in a slight decrease in the

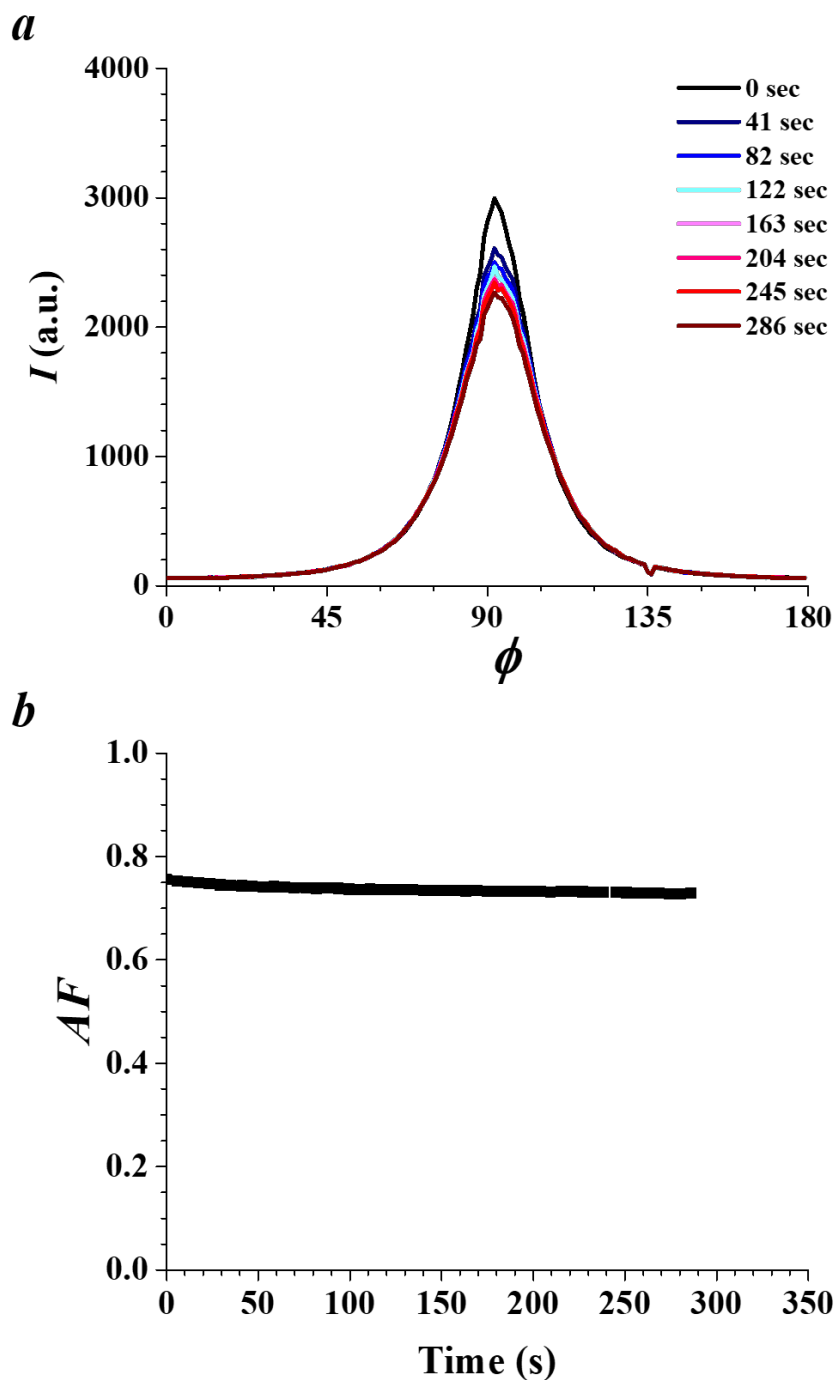


Figure 5.20 Relaxation of lamellar orientation in CTAC/Pentanol/Water measured at stagnation point of cross-slot flow cell, after cessation of planar extensional flow at a nominal extension rate of 1.0 s^{-1} . (a) Series of azimuthal intensity scans measured at time intervals of 41 seconds. (b) AF vs time.

associated AF value. All data in the CTAC/Pentanol/Water solution thus consistently show a high degree of lamellar alignment whose direction is strongly influenced by the velocity field in the cross-slot flow, but which otherwise is not responsive to changes in flow conditions, including flow cessation.

5.2.2 Aqueous DDAB

The second recipe we studied was 60 mM didodecyldimethylammonium bromide (DDAB) in water. Dubois *et al.*²⁰⁰ reported the phase diagram for aqueous DDAB solutions, suggesting that a pure lamellar liquid crystal phase exists at concentrations from around 3 wt% to 25 wt%. Yang *et al.*²⁰¹ confirmed the lamellar structure through freeze-fracture-TEM image. X-ray scattering from DDAB solutions has been explored by Li *et al.*⁸⁶ The stability of lamellar structure and the rheology of DDAB solutions have been tested by Soltero *et al.*¹⁹³ as a function of temperature and concentration.

5.2.2.1 Materials and Methods

DDAB was purchased from Sigma-Aldrich. To produce a 60 mM solution, 2.77 grams of DDAB were mixed with 97.2 ml deionized water. The solution was sealed and shaken vigorously for at least 10 minutes. The solution then sat at 25°C for at least one week to equilibrate. Finally, the solution was centrifuged to remove air bubbles for future use. The diffraction peak associated with lamellar ordering in the DDAB solution (Figure 3.7 *d*) occurs around $q = 0.0094 \text{ \AA}^{-1}$, corresponding to a d -spacing of 67 nm. This is considerably larger than the d -spacing of the CTAC/Pentanol/Water solution considered above, which makes sense in so far as the surfactant concentration is lower in this DDAB solution, leading to a wider separation of hydrophobic bilayer structures.

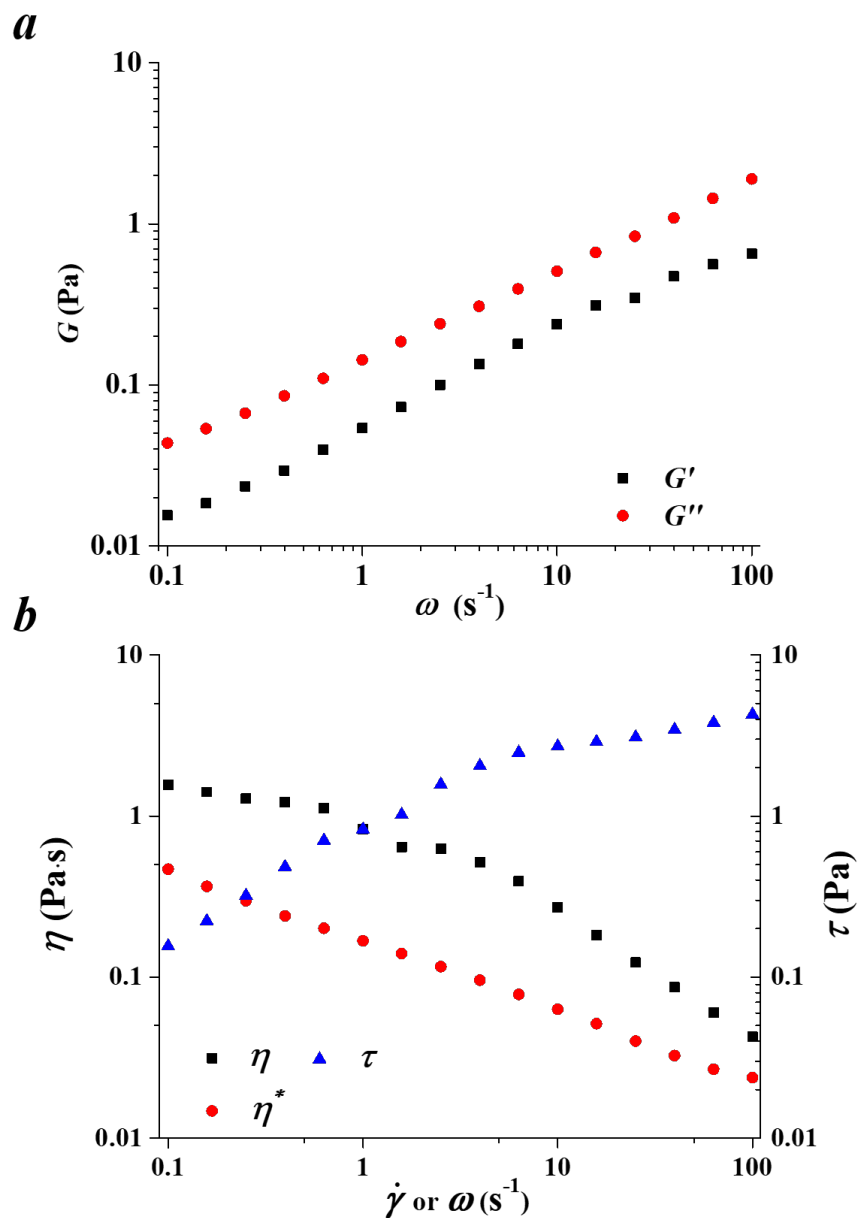


Figure 5.21 Shear rheology of aqueous DDAB lamellar surfactant solution in (a) small-amplitude oscillatory shear, and (b) steady shear flow

Likely owing to its lower concentration, the DDAB solution exhibits much weaker elastic character than CTAC/Pentanol/Water (Figure 5.21). Instead of a pronounced solid-like plateau in storage modulus, in this case G' and G'' both exhibit roughly power-law behavior over the

measured frequency range. Power-law relaxation is frequently found in samples such as critical gels¹⁴⁹ that are at the edge between liquid-like and solid-like behavior. Here, it may reflect that this more dilute lamellar system has less robust long-range ordering than CTAC/Pentanol/Water. Steady shear rheology also shows an interesting contrast between the two systems. In DDAB, the viscosity again shows shear thinning, but in this case, the shear viscosity is *higher* than the complex viscosity when evaluated at $\omega = \dot{\gamma}$. This is consistent with literature reports in other lamellar systems indicating an increase in viscosity during unidirectional shearing.¹⁹⁴

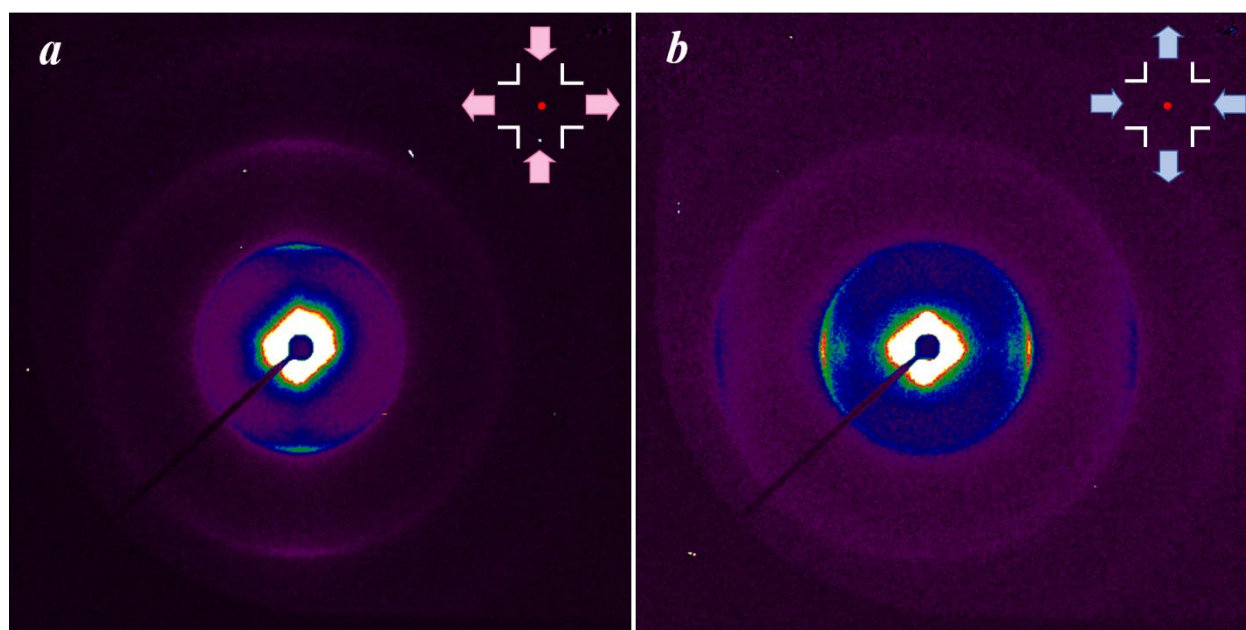


Figure 5.22 Representative scattering patterns from 60 mM DDAB solution, measured at the stagnation point in cross-slot flow at a nominal extension rate of 3.33 s^{-1} . Flow direction is indicated

In situ x-ray scattering studies were performed at APS beamline 5-ID-D. The energy of the incident beam was set at 9.4 keV, corresponding to a wavelength of 1.32 Å. Due to the larger *d*-spacing of the DDAB sample, the scattering features of interest lie at smaller *q*, and two-dimensional patterns were collected using the small angle detector: Rayonix MX170HS. The

detector-to-sample distance was 7500 mm. The detector binning was set at 4 by 4. The exposure time for each frame was 30 seconds. Due to the longer required exposure time, data were collected only at positions within the intersection of the cross-slot flow cell.

5.2.2.2 Structural dynamics of aqueous DDAB subjected to planar extension

Small-angle scattering patterns show both primary diffraction peaks and a weaker secondary reflection, consistent with the 1-*d* lamellar ordering expected in this system based on literature reports (Figure 5.22). The scattering was not as strong as in the CTAC/Pentanol/Water solution (Figure 5.16), and its azimuthal distribution is not a highly anisotropic. The concentration of intensity perpendicular to the stretching direction for both infusing and withdrawal flow directions shows that lamellae align along the flow, as expected.

Vector plots representing the spatial distribution of orientation (Figure 5.23) show that as the lamellar sample enters the cross-slot region from the upstream, their orientation direction is already flipped to lie along the principle stretching direction, although the anisotropy is weak. As fluid approaches the center near the stagnation point, anisotropy increases. This higher orientation produced by planar extension at the stagnation point is maintained as fluid is swept towards the downstream channels. Anisotropy factor is at most weakly dependent on flow rate over the range of nominal extensional rates studied (0.01 to 10 s⁻¹; Figure 5.24). As quantified by *AF*, the degree of orientation found in DDAB is significantly lower than seen above in CTAC/Pentanol/Water (Figure 5.19). Measured orientation angles were generally close to zero as expected given the symmetry of the flow, although strong deviations were found at a nominal extension rate of 0.16 s⁻¹, for reasons that are not clear.

We studied the relaxation of DDAB lamellar orientation after cessation of flow at a nominal extensional rate of 3.3 s^{-1} for 30 minutes (Figure 5.25). Unlike CTAC/Pentanol/Water which showed negligible relaxation, DDAB lamellar orientation relaxed to a nearly isotropic condition. The relaxation of AF could be described by a single-mode exponential decay with a characteristic relaxation time at 157 seconds. The fact that flow-induced lamellar orientation relaxes upon flow cessation is consistent with the higher degree of fluidity manifested in the linear viscoelasticity of DDAB relative to CTAC/Pentanol/Water (Figure 5.21 *a* vs Figure 5.15 *a*).

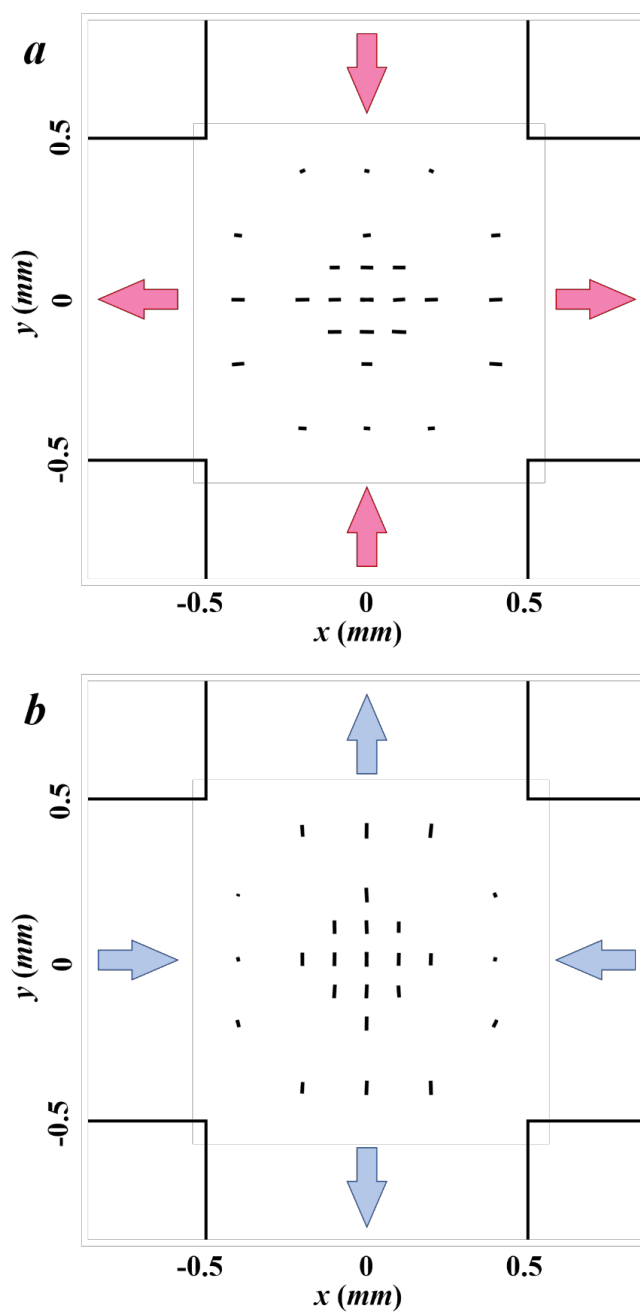


Figure 5.23 Vector plots representing orientation state measured in aqueous DDAB in cross-slot flow at a nominal extensional rate of 0.1 s^{-1} . (a) extension along horizontal axis; (b) extension along vertical axis.

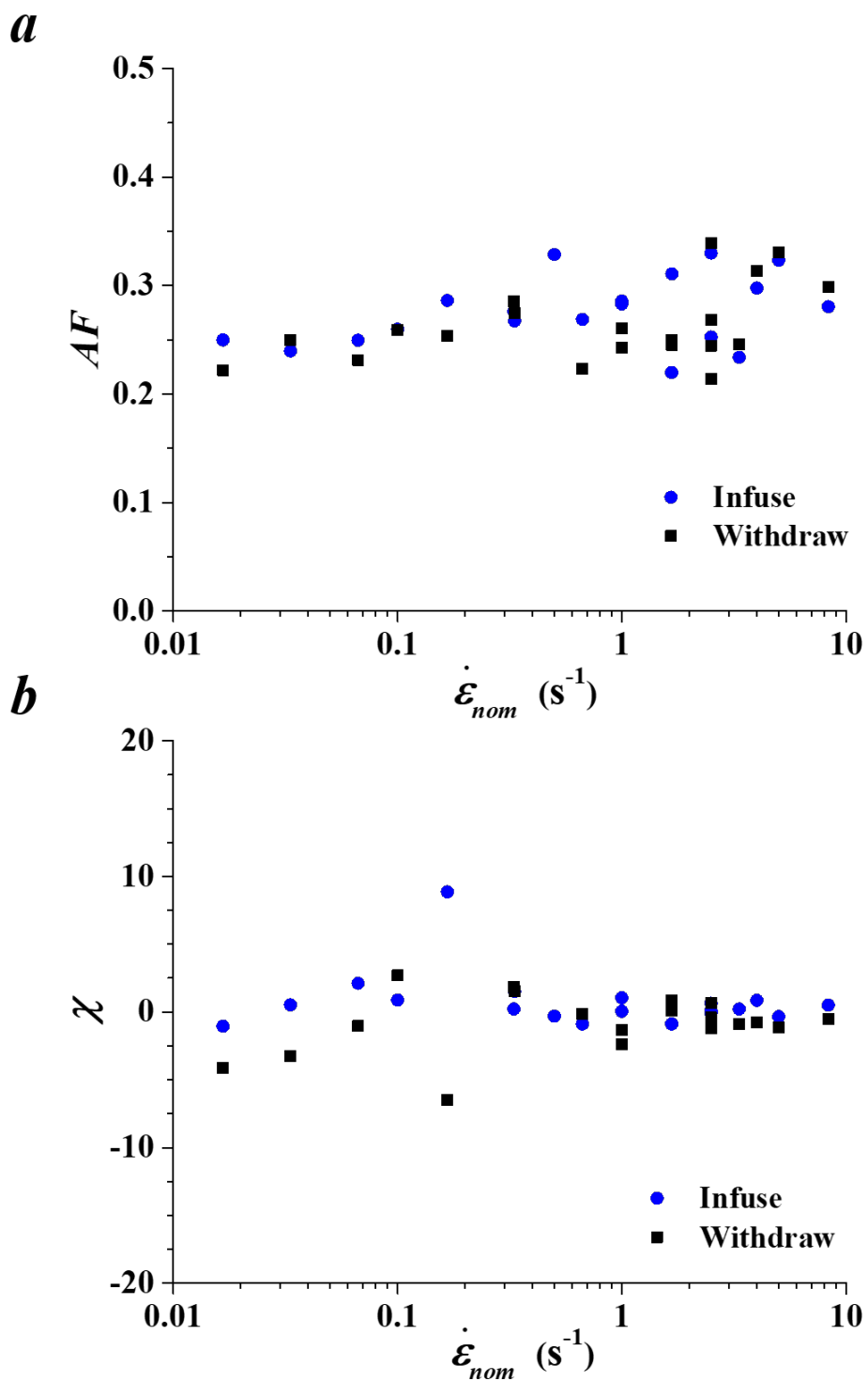


Figure 5.24 Steady-state (a) anisotropy factor and (b) orientation angle measured in 60 mM DDAB at stagnation point in cross-slot flow, as a function of nominal extension rate.

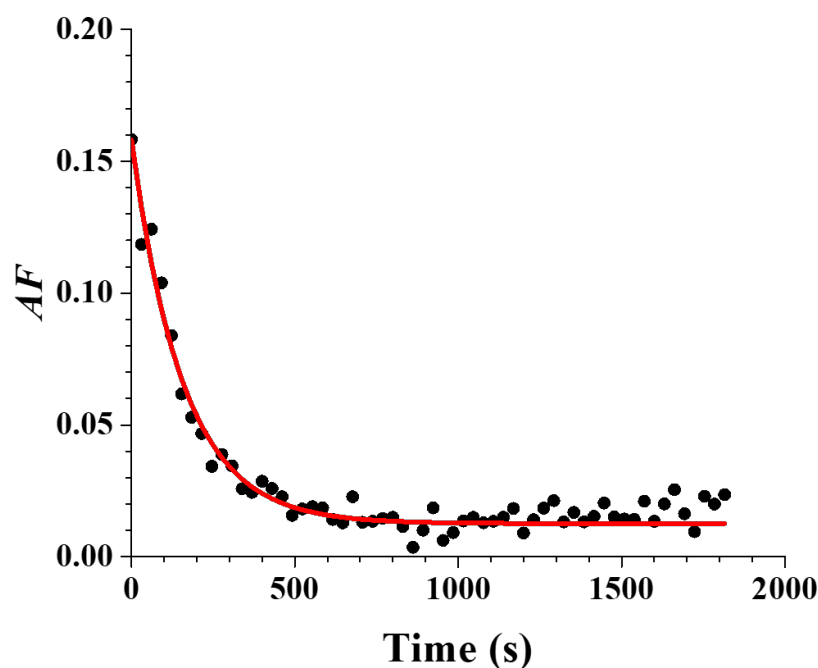


Figure 5.25 Relaxation of AF in the 60 mM DDAB solution fitted to a single-mode exponential decay

Motivated by the study of Idziak *et al.*,¹⁰² we also examined at the scattering intensity as a function of scattering vector q . We found no pattern of variation of lamellar spacing, domain size or absolute scattered intensity as a function of nominal extensional rate over the range studied. This contrasted with the study by Idziak *et al.*, who reported decreases in both domain size and d -spacing with increasing extensional rates. Our studies differed in multiple respects. In terms of methods, they used a low-aspect ratio cross-slot flow cell where shear gradients experienced in the slit flow sections may have played a dominant role, considering their cell dimensions. Their experiments spanned 6 decades of flow rate, while our experiments only covered 3 decades. Finally, the inherent dynamics of the lamellae aggregates could determine

their interaction with the flow. Thus, this difference may simply reflect the different lamellar surfactant system employed in their study.

5.3 Summary

We have characterized the structural response of wormlike micelles and lamellar surfactants to planar extensional flow. At modest Weissenberg number, wormlike micelles demonstrate increasing orientation as extension rate grows. Beyond a critical flow rate, however, a bifurcation in flow field was found, similar to viscoelastic flow instabilities documented in other work on stagnation flow of WLM systems. X-ray scattering data show that the micellar structure provides a robust indicator of the broken symmetry of the flow pattern, as orientation angle bifurcated into two branches showing significant misalignment relative to the simple alignment along the nominal stretching direction expected in cross-slot flow. The two lamellar surfactants studied here exhibited different inherent ordering, manifested by differences in their viscoelastic properties, and in the degree of lamellar orientation generated by flow. Most significantly, one of the lamellar systems (DDAB) showed relaxation of flow-induced orientation, while the other (CTAC/Pentanol/Water) exhibited negligible relaxation. In both cases, however, planar extensional flow at the stagnation point of the cross-slot flow cell led to alignment of lamellae along the stretching direction, with little change in the spatial distribution or degree of lamellar orientation with changes in flow rate.

Chapter 6 Conclusions and Future Directions

In this work, we presented studies on the *in situ* structural dynamics of complex fluids in planar extensional flow using synchrotron x-ray scattering. This was achieved by first building a high-aspect-ratio cross-slot flow cell for applying planar extensional flow upon low-viscosity complex fluids and integrating the flow cell to the x-ray data acquisition system at the synchrotron. The custom-built platform was then employed for studies on two categories of complex fluids: dilute MWCNT suspensions and surfactant solutions.

In Chapter 4, transient and steady-state orientational dynamics of a dilute MWCNT suspension were reported. During shear inception and reversal, the MWCNTs follow the classic behavior of Brownian rod-like particles. The relaxation of the polydisperse MWCNT suspension can be described using the stretched exponential function. The fitting parameters measured using SAXS demonstrate that as shear rate increases, shorter CNTs become aligned and participate in relaxation in the polydisperse CNT suspension. These fitting parameters are consistent with those obtained using optical dichroism by our collaborators.⁶⁶ The polydispersity of the sample is also reflected in specific experiments under intermediate shear rates, where the orientation angle decreases during initial relaxation and then becomes undefined later, in that longer CNTs dominate the overall orientation which also relax more slowly.

Under steady state planar extensional flow, the spatial variation of orientation state within the cross-slot flow cell indicates that the flow field produced, as expected, is symmetrical with the strongest orienting impact at the stagnation point. Orientation data extracted from the

shearing flow in upstream channels agree with the data collected using a dedicated homogeneous shear flow cell. This consistency demonstrates that the aspect ratio of the cross-slot flow cell suffices to allow the flow field to be treated as two-dimensional.

Under steady state shear, increasing deformation rates produce higher degree of nanotube orientation and smaller orientation angle relative to the flow direction. Comparing anisotropy generated at the stagnation point by planar extension versus that by shear flow at equivalent rates, planar extension is more effective at aligning CNTs. At large deformation rates, the anisotropy factor in planar extension saturates at around 0.15 while the anisotropy factor in shear reaches a plateau near 0.1. Simulation of Brownian rigid rods captures both transient and steady state orientation behavior, except that a scale factor is needed to bridge the gap of AF values between experiments and simulation, which is tentatively attributed to smearing of the scattering patterns of even highly aligned nanotubes due to the crooked nature of the CNTs used in this study. The difference in plateau AF values between shear versus planar extension can be rationalized using simulation of particles with a finite aspect ratio. Specifically, tumbling motions of finite aspect particles in shear reduce the maximum possible degree of alignment relative to extensional flow.

The orientation behavior measured using SAXS is qualitatively consistent with our collaborators' measurements using optical dichroism, although there is an unresolved difference in orientation angle at high shear rates. We also discovered that a semi-dilute suspension exhibits smaller anisotropy than the dilute suspension, but is more susceptible to flow. Finally, the q dependence of the scattered intensity confirms that the crooked and bent morphology of CNTs, in the length scale range used for quantitative data analysis.

In Chapter 5, two categories of surfactant solutions were studied under planar extensional flow: wormlike-micelle solutions and lamellar surfactant solutions. The wormlike micelles demonstrate stronger orientation with increasing extension rate at modest Weissenberg numbers. Beyond a critical Weissenberg number, a flow bifurcation occurs where the symmetry flow field breaks due to the viscoelasticity of WLMs. A detailed comparison of our observation with the flow instabilities in cross-slot flow reported by others was given. Although there are differences in choice of WLM samples and flow cell geometry (*e.g.*, low versus high aspect ratio), the onset of bifurcation in our experiment is in a range similar to others' work. We also observed that once bifurcation starts, even the flow field in the upstream channels is strongly affected.

The two lamellar surfactant solutions exhibit many differences. Under planar extension, both solutions aligned along the flow direction in the cross-slot cell and the degree of alignment is little affected by the strength of flow. However, the anisotropy values differ a great deal: the CTAC/Pentanol/Water solution, in which storage modulus is significantly higher than loss modulus, demonstrates high degree of orientation everywhere and shows minimal relaxation following flow cessation; the DDAB/Water solution, in which loss modulus is larger than storage modulus, exhibits relatively smaller degree of orientation, and anisotropy decays nearly entirely during relaxation.

Future work can be developed in a number of directions. One possible improvement would be to adapt the cross-slot flow cell to additional optical techniques. During the studies reported here, we have tried to look into the possibility of using birefringence. This failed due to the highly birefringent Kapton® windows, and lack of other suitable thin materials that would be compatible with the current flow cell design. A possible approach would be to use custom-cut

optical glass windows, which fits the dimensions of the aluminum cross-slot cell, with the silicone adhesive. Adapting the cross-slot flow cell to accommodate optical techniques such as light scattering and birefringence will expand the length scale range of microstructure beyond the range accessed by synchrotron x-ray scattering. It will also allow us to visualize the fluid mechanics of cross-slot flow cell in greater detail, by optically focusing on different depths. Cross-slot flows have frequently been employed in conjunction with optical techniques,^{58,62} but have often employed low or moderate aspect ratios, with associated drawbacks.

Another improvement that can be made to the flow cell is temperature control. At present, the device operates at room temperature and samples are specifically chosen whose rheological properties vary little as temperature drifts between 20 to 25 °C. Water circulation path can be added near the cross slots and a series of syringe warmers and other accessories are available.²⁰² It can be anticipated that temperature control in such a system will be a complicated task as the sample fluid is distributed among the flow cell, tubing, and syringes, each with different thermal characteristics. But equipping the flow cell with the ability to control temperature would be rewarding as it not only ensures a consistent temperature for measurement, thus enabling studying complex fluids that are sensitive to temperature, but also permits us to manipulate the relaxation time of the sample, consequently expanding the range of Weissenberg or Peclet number that can be reached. It could also facilitate erasing the alignment introduced during loading.

As discussed in Chapter 4, an advantage of x-ray scattering over optical techniques is that it can be applied to a wide range of CNT concentrations, while birefringence and dichroism are inadequate due to the opaqueness. Therefore, extending the study of CNT dynamics under planar

extensional flow into semi-dilute and concentrated regimes would be a straightforward goal to pursue. The study in Chapter 4 tells that in our dilute MWCNT suspension, CNTs can be described by rigid-rod Brownian dynamics. Previous work conducted with higher concentration CNT suspensions in shear flow^{95,128} has suggested the existence of aggregated clusters or entangled network, and the impacts of flow upon these suspensions are not only orienting the tubes or clusters, but also dis-associating the aggregates. It is intriguing to compare the behavior of semi-dilute and concentrated CNT suspensions in planar extensional flow versus in shear flow as extensional flow is considered a “strong” flow and much more effective in orientation and disaggregation. It can be speculated that as the concentration of suspension increases, the CNTs will contribute to the viscosity, which generally makes the suspension shear-thinning and introduces new complexities compared to the Newtonian suspension we studied. If in the future, a reliable measurement of steady-state extensional viscosity can be established for semi-dilute and concentrated CNT suspensions, that may be paired with the structural dynamics to understand the structure-property relationship. X-ray scattering might offer additional insights upon microstructure through the dependence of intensity on scattering vector. The dilute CNT suspension we studied in this work had a consistent power-law index of 1.6 to 1.7 throughout the entire experiment, reflecting the bent and crooked nature of the tubes. At higher concentrations, the microstructure will be more complex, even become hierarchical. The $I(q)$ behavior may be more illuminating, regarding flow-induced changes in network structure.

In addition to expanding the concentration regime, another potential direction is to explore the impact of CNTs themselves. The suspension we studied is constituted of polydisperse CNTs, which is also manifested in the stretched exponential relaxation behavior

(Figure 4.7) discussed in Section 4.4.1. Systematic variation of the length distribution would allow more quantitative tests of these concepts. Further, our results suggest that straighter tubes should show smaller differences between alignment in shear versus extension, a prediction that could be tested using tubes produced by other techniques that are intrinsically straighter.

Surfactant solutions vary significantly in behavior depending on details of their formulation (choice of surfactant and salt, composition, *etc.*). Thus, a great deal of future work can be conducted just by varying the specific formula. Based on our work as well as others', two solutions of immediate interest are CPyCl/NaSal solution and water/SDS/pentanol/dodecane solution. The CPyCl/NaSal solution is a classic shear-banding WLM solution that has been frequently studied in cross-slot flow cell. Since previous work⁵⁸ is limited by aspect ratio of the flow cell, it would be worthwhile to study a representative shear-banding solution with our flow cell, whose aspect ratio has been confirmed to be sufficient to produce quasi-2-dimensional planar extensional flow (at least prior to flow bifurcation). The quaternary water/SDS/pentanol/dodecane mixture is a lamellar surfactant solution used by Idziak *et al.*¹⁰² They reported that flow rate changes the direction of orientation, domain size, and intermembrane spacing. Since the aspect ratio of their cross-slot cell is only 0.225, it is intuitive to speculate whether these variations are truly induced by the planar extensional flow, or rather by the mix of shear and planar extension produced in such a low-aspect-ratio flow cell.

Moving beyond the types of samples studied here, measurements of the coil deformation of dilute polymeric solutions would be a challenging future direction. As is briefly discussed in Chapter 1, the coil-stretch transition of dilute DNA solutions have been directly observed in cross-slot flow using fluorescence microscopy where the extension ratio of DNA molecules

exceeds 3 for the ensemble average.⁶⁴ At the same time, the polymer coil sizes measured using light scattering in shear⁷⁵ and extensional⁵² flow shows only 1.2 and 1.4 for extension ratio in shear and extensional flow, respectively. This variation can be caused by the nature of the molecule itself, as DNA is a stiff polyelectrolyte and has an order-of-magnitude larger number of persistence lengths per molecule. The polymer coils studied in the light scattering, on the other hand, is much more flexible. Another possible reason proposed by Lee and Muller is the relative size of the polymer segment to that of the solvent. It may also due to the resolution, *i.e.*, the size of the incident beam relative to that flow field, as extensional flow is often highly localized in these stagnation flow fields. In any case, this variation and the contrast between experimental observation and model prediction invite an investigation of the coil deformation of polymeric solutions using our high-aspect-ratio cross-slot flow cell and synchrotron x-ray scattering. The result hopefully will add a piece to the whole picture of coil deformation as x-ray scattering would most naturally be suitable for coils much smaller than those studied in light scattering. It can also provide another comparison of the efficacy of shear versus extensional flow in orienting and stretching flexible molecules.

The suitable dilute polymeric solutions should have an electron density contrast between the solute and the solvent to observe the scattering. It will also be convenient to start with Boger fluids, *i.e.*, of high constant viscosity but with elastic solutes, because the open space in the cone-and-plate shear cell requires a constant viscosity to avoid flow instabilities and the cross-slot flow cell produces planar extensional flow of higher confidence with constant-viscosity fluids. Preliminary work has been conducted to measure the coil size of polystyrene dissolved in toluene, measured using synchrotron x-ray scattering and a thin capillary tube to hold the

solution. Such measurements were complicated by the accumulation of x-ray beam damage. This was also an issue with the CNT suspensions discussed in Chapter 4 as well. If a careful plan can be executed so that the sample at a specific region is limited to a small amount of total exposure and scanning routes are designed so that the incident beam always hits fresh samples in the cross-slot cell, the impact of overexposure and burning may be controlled.

Finally, this work has mostly focused on the quantitative dynamics at the stagnation point. If more properties of the kinematics in our cross-slot cell could be known, the data collected at the off-center locations may reveal additional knowledge on the behavior of complex fluids. Such studies would provide a useful test bed for broader simulations of both the cross-slot flow field and the associated fluid microstructure.

Appendix A (Previous Research): *In situ* SAXS/WAXD studies of shear-induced crystallization of poly(1-butene) in shear flow

A1. Introduction

Nowadays, polymers have almost touched every aspect of human life, from water bottles, grocery bags, textile fibers, to tires. The total production of plastics in North America has reached over 50 million tons in 2017.²⁰³ As polymer melts experience complex thermal conditions, pressure change and deformation during processing, and are finally molded into plastic products, crystallization often concurs, in the most commonly seen polymer commodities such as polyethylene and polypropylene. The microstructure formed during the crystallization will ultimately determine the properties of final products, such as mechanical strength and durability. Thus, the phenomenon of polymer crystallization is of high practical concern.

In the crystallization of polymers at temperatures below the melting point, chains align and fold to form lamellae, which further stack into spherulites (Figure A1).^{204–206} Usually, the regular stacking of polymeric chains will not be perfect and the crystallinity varies from 10% to 80%.²⁰⁷ From the perspective of phase separation, this process can also be regarded as the original polymer melt dividing itself into two regions: amorphous and crystalline phases (Figure A2).²⁰⁸

Polymer crystallization itself is already an intricate problem. Applied flow further complicates this process, exerting influence on multiple aspects. In the initial nucleation stage,

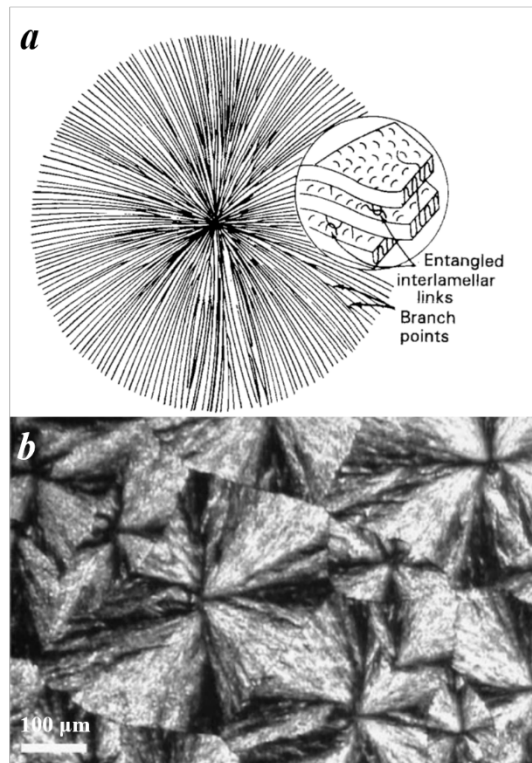


Figure A1 (a) An schematic illustration of chains folding into lamellae, which further piled to formulate the spherulite (figure reprinted from [205]) (b) spherulites from peptide crystallization visualized by polarized light microscopy (figure reprinted from [206])

flow can enhance the number density of “activated” nuclei, as well as changing their shape, producing oblong-shaped nuclei.²⁰⁹ In the chain folding stage, flow may orient and stretch chain segments, or even affect the conformational order.²¹⁰ As a result, the kinetics of crystallization is further accelerated. Under strong flow conditions where chains are significantly stretched, a shish-kebab structure (Figure A3) can be formed where the lamellae kebab is organized vertically around a long shish, which aligns along the flow direction.^{211,212} Here the crystalline phase is highly anisotropic compared to the spherulite morphology found under quiescent conditions. Finally, flow may also cause disruption as it disentangles long chains and occasionally breaks temporary bridges.²⁰⁹ In short, the impacts of flow upon polymer

crystallization is multifaceted, from the kinetics of growth, to the morphology of microstructures at various length scales.

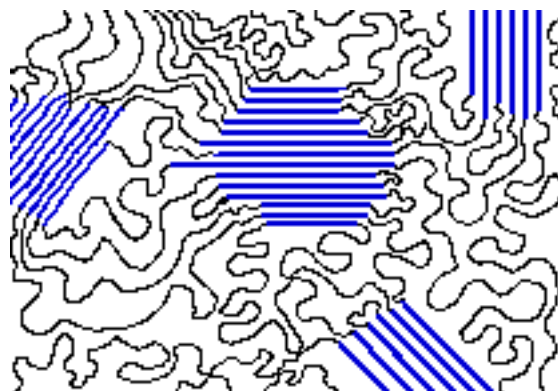


Figure A2 An illustrations of crystalline (blue) and amorphous phases in semi-crystalline polymer (figure reprinted from [208])

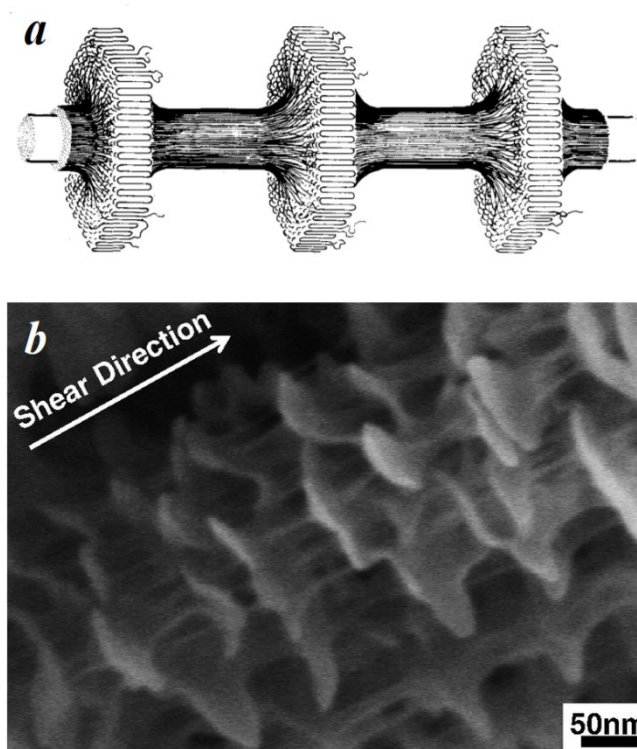


Figure A3 “Shish-kebab” morphology of semi-crystalline polymers (a) a schematic illustration (figure reprinted from [211]) (b) an SEM image of shish-kebab crystallites of ultrahigh-molecular-weight polyethylene (figure reprinted from [212])

Many techniques have been employed, targeting various stages or different microstructures during flow-induced crystallization. Fourier-transform infrared spectroscopy (FT-IR) and Raman spectroscopy have been often used to study the early-stage conformational change of chain segments.^{213–215} Birefringence has also been used to track the early-stage orientation of chain during flow and shortly after.^{216,217} Small-angle light scattering has also been used to monitor the growth and orientation of isotactic polypropylene (iPP)^{218,219} and polyethylene (PE).²²⁰ Other techniques used include differential scanning calorimetry (for quiescent crystallization or *ex situ* characterization of crystallinity),^{219,221,222} turbidity,^{217,219,223} and rheology.^{219,224–227}

X-ray scattering, as a powerful tool to probe structures at tens to hundreds of nanometers length scales, has been a standard technique for studying polymer crystallization for decades. In Chapter 3, Equation 3.9, 3.10, 3.14, and 3.15 illustrate that scattered intensity rise from the electron density contrast within the illuminated sample. During polymer crystallization where an emerging crystalline phase has a different density than the amorphous phase, the growth of the invariant (total scattered intensity) can be used to measure the growth of crystalline phase. The synchrotron facility (Section 3.2) provides a highly-collimated incident beam that allows for following the transient growth of crystallization, as well as simultaneous *in situ* scattering data collection at both small and wide angles. The simultaneous SAXS and WAXD data collection offers insights for microstructural changes at multiple length scales, namely, the lamellar stacking which has the length scale around tens of nanometers and will be accessible through the small-angle detector (Figure A4 *a*), as well as the unit cell structure (Figure A4 *b*), which usually has the lattice constants around several to tens of Ångströms and thus will be visible on the wide-

angle detector. For isotactic poly-1-butene crystallization, the kinetically favored Form II crystal, which is also the crystal lattice we observed on the WAXD pattern, has a tetragonal lattice. There are three major peaks: ²²⁸ the (200), (220), and (301) peaks. If the c-axis is perfectly aligned along the flow and the crystallites formed is uniaxially symmetric about the c-axis, the (200) and (220) peaks appear perpendicular to the flow direction on the WAXD patterns, and the (301) peak at a tilted angle. As discussed in Chapter 3, both small- and wide-angle features become smeared azimuthally as the degree of orientation decreases.

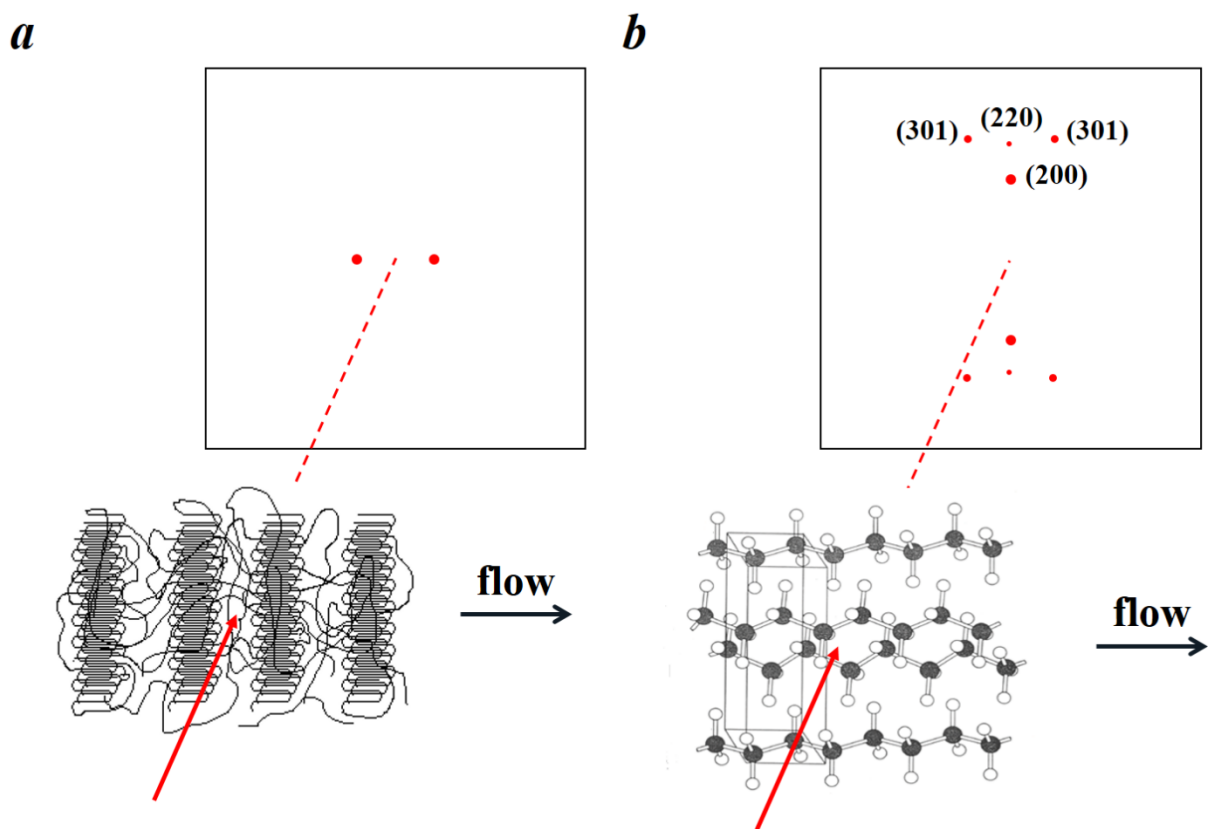


Figure A4 Illustrations of (a) lamellae and its scattering (SAXS); (b) unit cell and its x-ray scattering (WAXD)

Flow-induced crystallization is an intricate process involving a wide range of variables, including temperature (sub-cooling relative to the equilibrium melting point), flow (the type of flow, rate of deformation, strain, and flow history), and the relaxation spectrum of the polymer itself.^{216,223,224} This appendix reports a study of the shear-induced crystallization of poly-1-butene (PB-1) at a fixed temperature, subjected to varying shear rates and strains, using simultaneous *in situ* SAXS and WAXD technique. Poly-1-butene is a commodity polymer possessing unique properties such as stiffness, puncture resistance in films, and low creep at high pressure.²²⁸ These advantageous features recommend PB-1 to be employed in pressure piping, flexible packaging, *etc.* However, studies of flow-induced crystallization of PB-1 are relatively rare compared to other commercial polymers such as polypropylene or polyethylene. The crystallization temperature will be chosen such that quiescent crystallization costs significantly longer time than when flow is applied, even under relatively weak flow conditions compared to industrial processing conditions. Shear flow is applied using a rotating parallel-plate flow cell, modified for x-ray scattering previously in our lab.²²⁹

With this study, we develop analysis methods for 2-*d* x-ray scattering patterns, to quantitatively measure the kinetics of growth of lamellae (from SAXS) and unit cell structure (from WAXD), and their orientation states during crystallization. The results will hopefully reveal the influence of shear flow upon crystallization, on both the kinetics and the orientation state of lamellae and unit cells. The analysis methods established may pave a way for others in the group to develop new analyses for extension-induced crystallization, where such strong deformation may induce more complicated shift such as morphological change from spherulites

to shish-kebab. Finally, the x-ray scattering technique will also be compared to turbidity and rheological measurements that are also sensitive to development of crystallinity.

A2. SAXS/WAXD data analysis background

Many researchers have used SAXS and/or WAXD to measure the growth of crystallization and orientation state. However, data analysis methods vary considerably among the different published work. For example, some used SAXS intensity enclosed in an angular range in meridional or equatorial region to characterize the growth of lamellae,^{217,226,230,231} while others employed an full-azimuthal-range integration of intensity within a designated q range.^{232,233} To quantify the growth of unit cells, generally an integrated peak area is utilized.^{217,233,234} With respect to orientation, Hermans' orientation parameter is often used.²³⁵ Besides, Somani *et al.* have deconvoluted the isotropic and oriented contribution from the total SAXS intensity²³⁶ to characterize the anisotropy induced by flow. In this section, we describe a data analysis protocol, for 2- d x-ray scattering patterns, to quantitatively measure the kinetics of growth for lamellae stacking and unit cells, as well as the orientation states for both microstructures.

As Figure 3.3 illustrates, the 2- d scattered pattern is a projection from many intersecting circles of Ewald sphere and the sphere of position (consisting of all the scattering vector of the same magnitude). To account for the 3- d growth of crystallites from a 2- d scattering pattern, a uniaxial symmetry with respect to the flow axis is assumed. The uniaxial symmetry is more relevant to uniaxial extensional flow and is unlikely to stand in shear flow field. But considering the fact that some kind of symmetry must be assumed if a 3- d account of crystallization is to be constructed based on 2- d scattering patterns, this assumption is a reasonable starting point.

A2.1 Kinetics of Crystallization

A2.1.1 Growth of lamellae

Figure A4 *a* illustrated that the scattering of lamellae will appear along the normal of the lamellae stacking. The interlamellar spacing renders the scattered intensity appearing on the SAXS detector. Figure A5 shows a sequence of SAXS patterns collected during crystallization. The parasitic scattering features in the left part of the SAXS pattern may be caused by some misalignments and will be excluded from quantitative data analysis. As time progresses, intensity grows in the horizontal direction in SAXS patterns, which indicates the emergence and growth of lamellar stacking. The intensity is congregated along the flow direction, suggesting that lamellae are preferably aligned perpendicular to the flow.

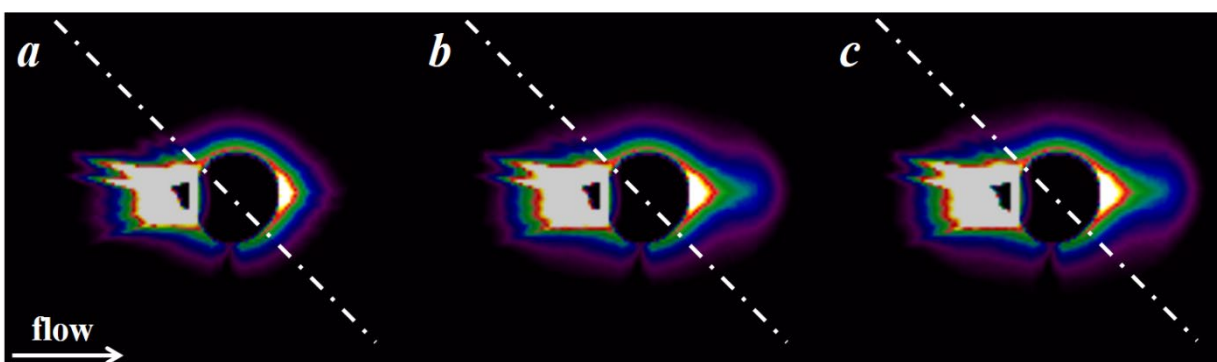


Figure A5 A sequence of SAXS patterns collected during shear-induced crystallization, subjected to a shear rate of 4 s^{-1} and a strain of 12, at (a) $t = 0 \text{ min}$ (at the time when flow was applied) (b) $t = 20 \text{ min}$ (c) $t = 40 \text{ min}$

In Chapter 3, Equations 3.14 and 3.15 illustrate that the observable scattered intensity is related to the self-correlation of the fluctuation from the average scattering length density and the scattering invariant Q , an integral of intensity with respect to the whole reciprocal space, is a product of the illuminated volume and the average of the squared relative scattering length. For

semi-crystalline polymers, crystalline and amorphous phases each have their own scattering length density, ρ_1 and ρ_2 respectively. Then, the average scattering length density can be written as

$$\langle \rho \rangle = \rho_1 \phi_1 + \rho_2 \phi_2 \quad (\text{A1})$$

Here ϕ_1 and ϕ_2 are the volume fractions of crystalline and amorphous phases respectively. If the difference of ρ_1 and ρ_2 is $\Delta\rho$,

$$\Delta\rho = \rho_1 - \rho_2 \quad (\text{A2})$$

then the invariant Q can be written as: ¹⁰⁸

$$\begin{aligned} Q &= V(\eta_1^2 \phi_1 + \eta_2^2 \phi_2) = V[(\rho_1 - \langle \rho \rangle)^2 \phi_1 + (\rho_2 - \langle \rho \rangle)^2 \phi_2] \\ &= V[(\Delta\rho \phi_2)^2 \phi_1 + (-\Delta\rho \phi_1)^2 \phi_2] = V(\Delta\rho)^2 \phi_1 \phi_2 \end{aligned} \quad (\text{A3})$$

This illustrates that the SAXS invariant will increase as crystallization progresses (ϕ_1 increases and ϕ_2 decreases). Therefore, it is a robust indicator of the growth of crystalline lamellae.

A2.1.2 Growth of unit cell structure

As Figure A4 *b* illustrates, the crystal lattice formed by the polymer chains produces discrete scattering peaks on the WAXD pattern. Figure A6 shows a sequence of WAXD patterns collected simultaneously with the SAXS patterns in Figure A5. At the beginning of crystallization, the scattered intensity is visibly stronger in the perpendicular region than the parallel region relative to flow direction, indicative of preferred chain alignment along the flow direction when flow was applied. As crystallization progresses, well-defined crystalline peaks emerge on the amorphous background scattering. The innermost crystalline peak on the WAXD

patterns is the (200) reflection, which also happens to be brightest peak and will be used for quantitative measure of crystallization. The weaker peak (a thin red arc on the meridional panel) at a larger scattering angle is the (220) reflection. These two crystalline peaks exhibit stronger intensity perpendicular to the flow direction rather than parallel, indicating that the chain axis of the unit cell is preferably oriented along the flow direction. The outermost peak where the strongest intensity appear at a tilted angle is the (301) reflection. Here the wide-angle diffraction

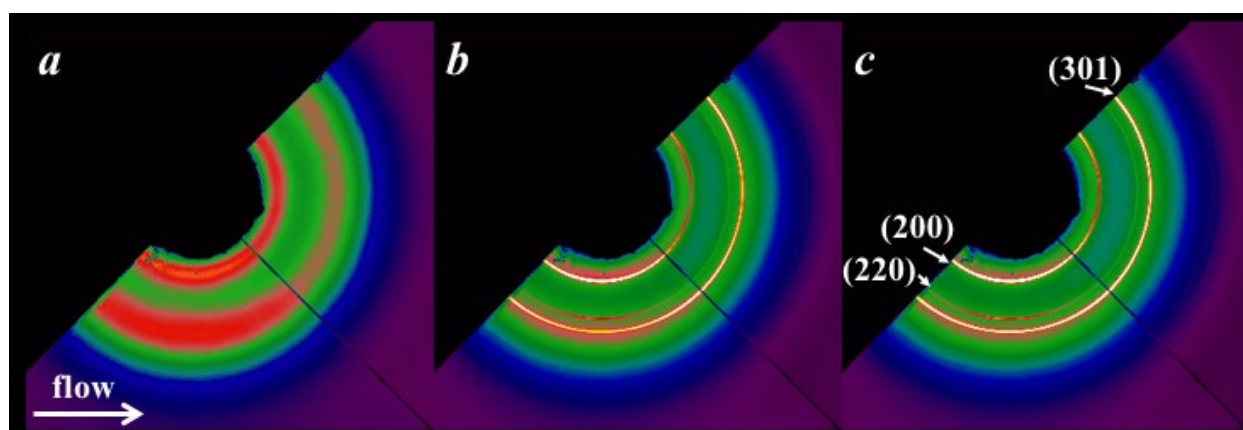


Figure A6 A sequence of WAXD patterns collected during shear-induced crystallization, subjected to a shear rate of 4 s^{-1} and a strain of 12, at (a) $t = 0 \text{ min}$ (at the time when flow was applied) (b) $t = 20 \text{ min}$ (c) $t = 40 \text{ min}$

observed as arcs (Figure A6) rather than the discrete peaks (Figure A4 b) demonstrates that the chain axis is not perfectly aligned along the flow direction.

A2.2 Orientation of microstructures

As demonstrated by Figure A5 and A6, both lamellae and unit cells exhibit preferred orientation due to the influence of flow. To compare the degree of orientation of various microstructures, a single number indicator is desirable. For a system with uniaxial symmetry, the Hermans orientation parameter²³⁷ has widely been used.^{108,235} The definition of the orientation

parameter has been given in Equation 3.23. For perfect orientation along the flow axis, the orientation parameter equals 1. For randomly oriented systems, the orientation parameter equals 0. For perfect orientation perpendicular to the flow axis, the orientation parameter is -0.5.

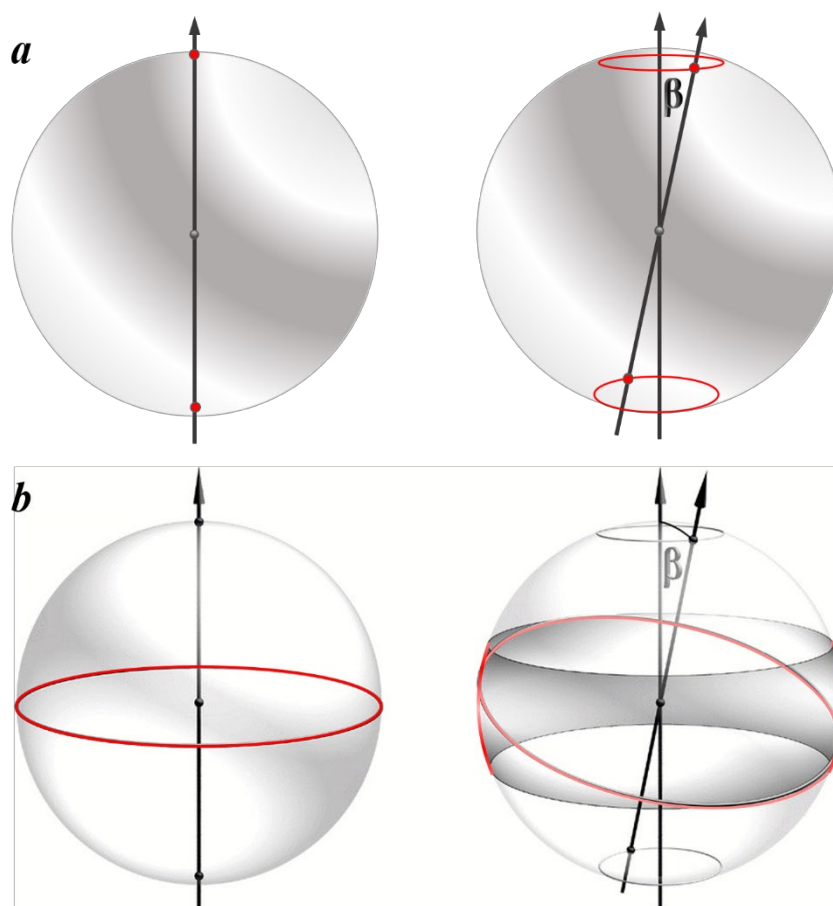


Figure A7 (a) scattering of lamellae perfectly aligned perpendicular to the flow axis versus uniaxially symmetrically aligned with a tilted angle β (b) scattering of unit cells perfectly aligned along the flow axis versus uniaxially symmetrically aligned with a tilted angle β (figure adapted from [239])

Figure A7 demonstrates that due to the nature of the repetitive structural units and scattering, the scattered intensity does not reflect the orientation of the structural units straightforwardly. For the scattered intensity of lamellae (Figure A7 a), the intensity appears

along the normal of the lamellae. When the lamellae is tilted by an angle β , the scattered intensity is also tilted with an angle β . Hence, the orientation of lamellae is directly revealed by the scattered intensity. However, for the scattering of unit cells with fiber (uniaxial) symmetry (Figure A7 b), the scattered intensity for many diffraction peaks, such as the (200) peak of interest here, is an equatorial ring normal to the chain axis. When the chain axis is tilted by an angle β uniaxially symmetric with respect to the flow axis, the scattered intensity becomes an equatorial band of varying intensities at different polar angles. Therefore, the angular distribution of scattered intensity does *not* reflect the orientation distribution of unit cells. Hermans' orientation parameter is the second order Legendre's polynomials. Using the orthogonality of the spherical harmonics and the convolution theorem,^{238,239} the coefficient of the total orientation (scattered intensity with respect to the flow axis) can be written as the product of the coefficients of the orientation of the scattered intensity with respect to the chain axis and the orientation of the chain axis with respect to the flow axis:

$$\langle P_2(\cos \phi) \rangle_{intensity-flow} = \langle P_2(\cos \phi) \rangle_{intensity-chain} \cdot \langle P_2(\cos \phi) \rangle_{chain-flow} \quad (A4)$$

For (200) peak, the scattered intensity is always normal to the polymer chain axis. Therefore,

$$\langle P_2(\cos \phi) \rangle_{intensity-chain} = -0.5 \quad (A5)$$

Hence the Hermans orientation parameter of unit cell (chain axis) to flow is related to the Hermans orientation parameter of intensity with respect to flow by:

$$\langle P_2(\cos \phi) \rangle_{chain-flow} = -2 \cdot \langle P_2(\cos \phi) \rangle_{intensity-flow} \quad (A6)$$

A3. Experimental methods

A3.1 Materials

The poly-1-butene sample was obtained from LyondellBasell (PB 0300 M). It is a semi-crystalline isotactic polymer, which has a relatively slow kinetics of crystallization under quiescent conditions. When crystallized from the melt state at atmospheric pressure, a tetragonal form II crystal is obtained. The Form II crystal is unstable and will gradually transform to a hexagonal Form I crystal after several days under ambient conditions. Form I is more stable and has a higher density, melting temperature, and stiffness than Form II.²⁴⁰ The melting onset temperature is reported to be 127 °C for Form I and 116 °C for Form II crystals, based on the report from LyondellBasell. The linear viscoelasticity of PB 0300 M melt (Figure A8) shows that the sample is a polydisperse polymer melt with a broad distribution of relaxation times.

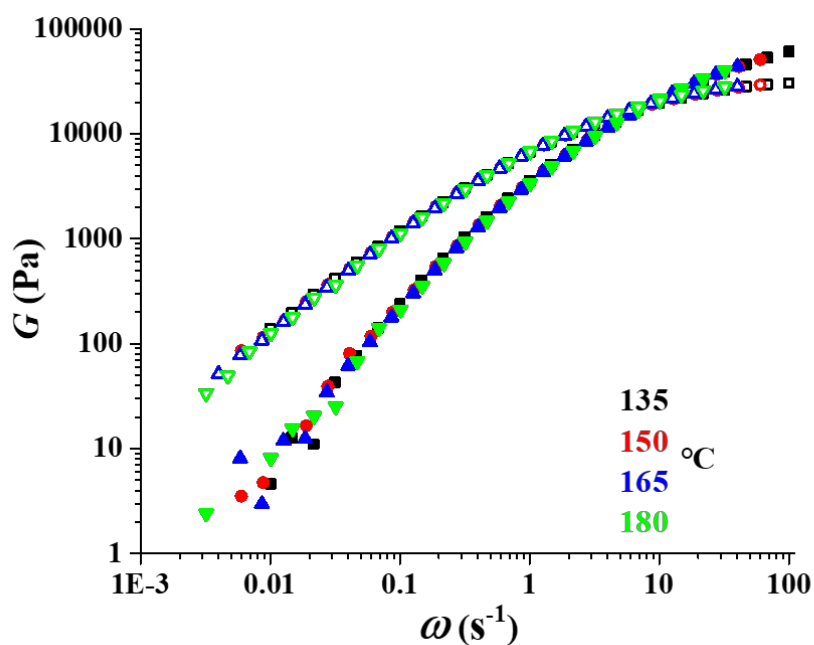


Figure A8 G' (filled) and G'' (open) of PB 0300M, measured at 135, 150, 165, and 180 °C, shifted to a reference temperature at 135 °C

A3.2 Shear flow device

A Linkam CSS-450 high temperature shearing stage modified for x-ray scattering, developed earlier in this group,²²⁹ was used for this work (Figure A9 *a*). This device applies shear flow in a rotating parallel-plate geometry. A pair of stainless steel inserts (Figure A9 *b*)

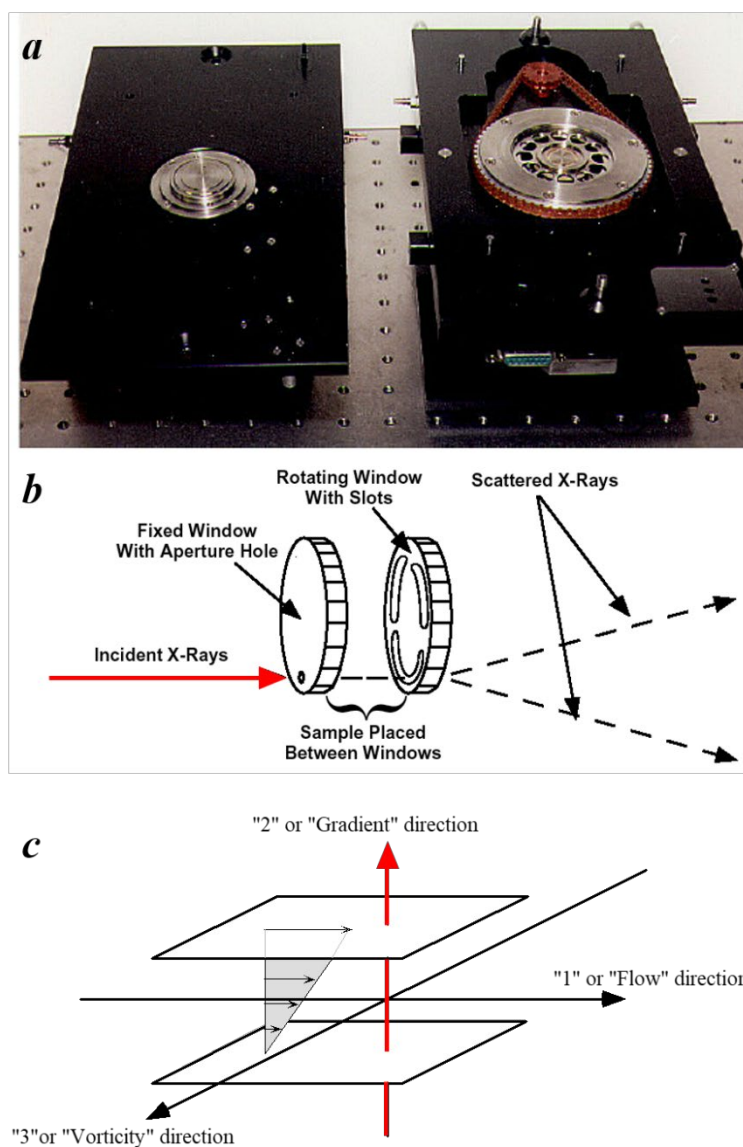


Figure A9 (a) the Linkam CSS-450 high temperature shearing stage (b) an illustration of the beam path through parallel-plate geometry of the shearing stage (c) an illustration of beam path in the shear flow field

was used for containing samples, with Kapton® windows glued on each insert for x-ray scattering. Figure A9 *b* also demonstrates that the incident beam travels through the aperture hole of the fixed window, with the scattered beam transmitted through the three curved slits of the rotating window. Therefore, the x-ray beam investigates the structural range at the plane of velocity and vorticity (1-3 plane), or along the shear gradient direction (Figure A9 *c*).

A3.3 Temperature and flow protocols

A testing protocol developed by Janeschitz-Kriegl²⁴¹ was employed here (Figure A10), where a short-term shear flow is applied below the melting temperature. With such short

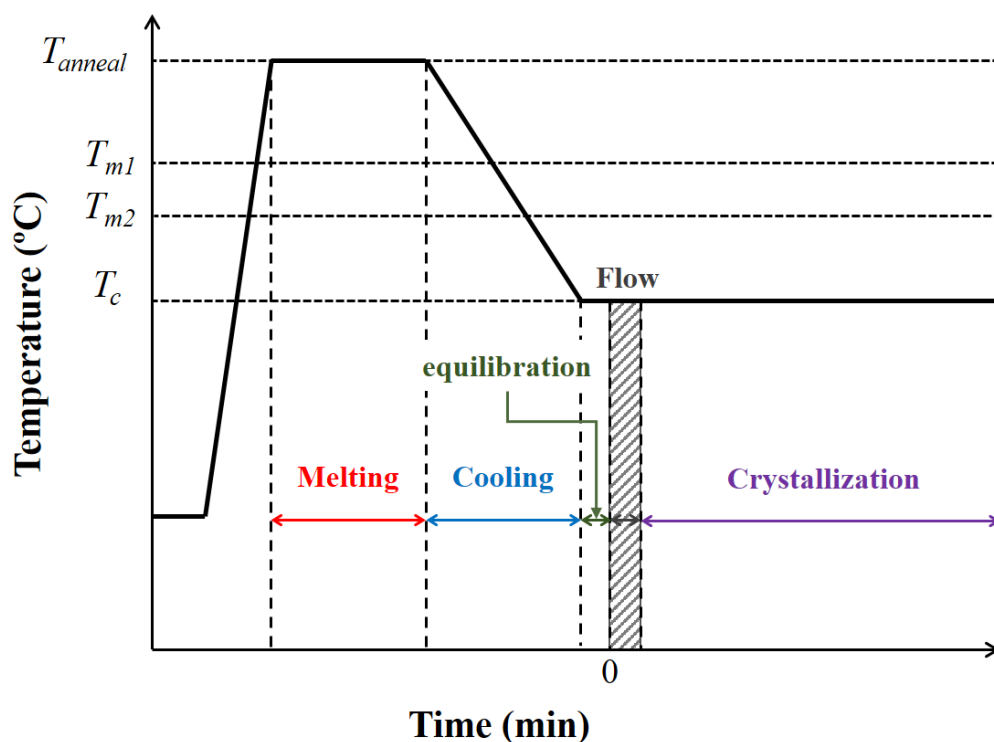


Figure A10 Temperature and flow protocol

duration of flow at moderate rates, the nucleation and growth processes are separated. This protocol is thus a good starting point to probe the impact of shear flow upon crystallization.

The poly-1-butene sample was first heated to an elevated temperature (180°C) well above the melting point to erase any thermal history, and then cooled down to the crystallization temperature 106°C at a rate of 20°C/min. The crystallization temperature was determined from previous crystallization experiments conducted in the lab using differential scanning calorimetry and turbidity measurements, such that at this temperature, the quiescent crystallization would take hours to occur while, when shear flow is applied, crystallization is observable within 45 minutes. After reaching the crystallization temperature, the sample was left for 1 min for equilibration before application of a short-term shear flow. The specific x-ray frame when flow was applied was regarded as $t = 0$ for data analysis. We probed two series of flow conditions: varying strain units (4, 8, and 12) at a fixed shear rate (4 s⁻¹), and varying shear rates (1, 2, and 4 s⁻¹) at a fixed strain unit (12).

A3.4 Synchrotron x-ray scattering

The two-dimensional SAXS and WAXD patterns were collected in the Sector 5ID-D, Advanced Photon Source, Argonne National Laboratory. The energy of the x-ray beam was set at 17 keV (wavelength equals 0.729 Å). A simultaneous collection of 2-*d* SAXS and WAXD patterns was set up. The exposure time was 1 second for each frame and the data collection frequency was 8 seconds (between the start of each frame) for both SAXS and WAXD. The small-angle detector used was a MarCCD detector with a pixel dimension of 1024 × 1024 (161.8mm × 161.8 mm). The sample-to-detector distance was 4569 mm. The WAXD detector consisted of a pair of CCD cameras (670 × 650 in pixel, 105.86 mm × 102.7 mm) from Roper

Scientific, patched together to cover a full 180° range. The wide-angle detector was placed at a distance of 233 mm away from the sample. The x-ray scattering data collection was initiated 1 minute after the cooling was started (when the sample had been cooled to around 160°C). Thereafter, the data collection continued for another 50 minutes (375 frames in total).

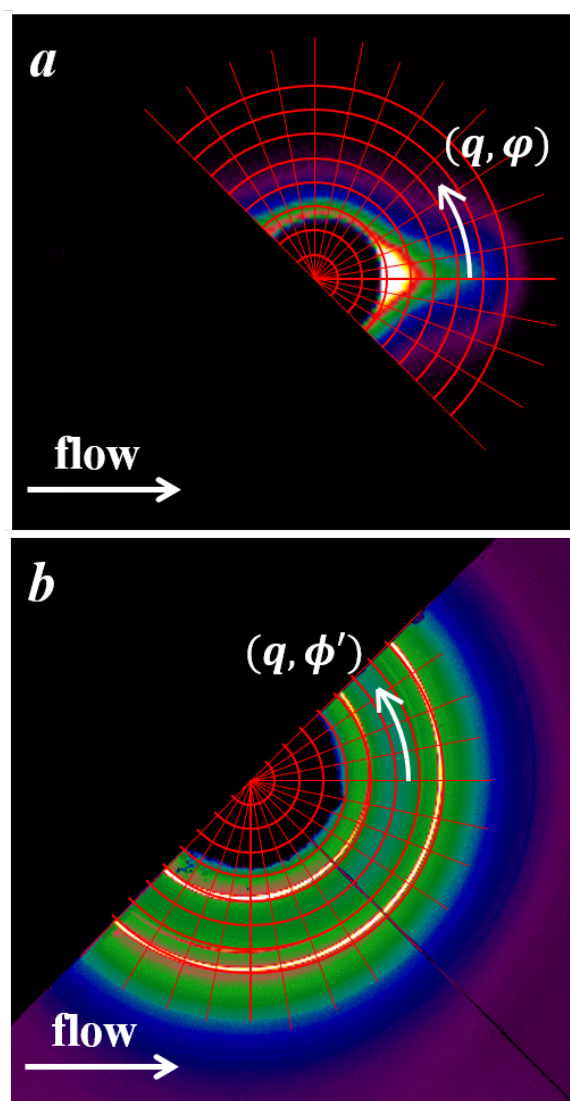


Figure A11 An illustration of the grid for extracting the intensity profile as a function of scattering angle and azimuthal angle with respect to the flow axis (a) on SAXS patterns (b) on WAXD patterns

A3.5 X-ray scattering data analysis

The scattering patterns were processed using fit2d software as described at the beginning of Section 3.4 (Figure A11), to obtain a scattered intensity profile as a function of scattering angle and azimuthal angle, as $I(q, \varphi)$ for SAXS intensity or $I(q, \phi')$ for WAXD intensity.¹¹⁴ (A much finer grid than demonstrated in Figure A11 was used for analysis.)

In Chapter 3, Section 3.1 discusses the difference between the azimuthal angle (ϕ') measured on the 2- d scattering pattern with respect to the flow axis and the true angle (ϕ) with respect to the symmetry axis (illustrated in the Figure 3.3 as the blue and red arc respectively). The two angles are related using the scattering angle 2θ through Equation 3.12. In SAXS, the scattering angle is rather small ($2\theta < 1^\circ$) and so $\cos \theta$ is nearly 1. In WAXD, this correction is numerically significant. The corrected intensity profile, $I(q, \varphi)$ for SAXS or $I(q, \phi)$ for WAXD was then to be calibrated into absolute units based on glassy carbon standard, using Equation 3.13.

A3.5.1 Characterization of lamellae growth

Section 3.3 introduced the quantity scattering invariant is related to the growth of lamellae. Under uniaxial symmetry, $I(\mathbf{q})$ can be fully described with $I(q, \varphi)$. Thus, the 3- d integration across the whole reciprocal space can be written as:

$$Q = \frac{1}{(2\pi)^3} \iiint I(\mathbf{q}) d\mathbf{q} = \frac{1}{(2\pi)^3} \iiint I(q, \varphi) q^2 \sin \varphi dq d\varphi d\Phi = \frac{1}{(2\pi)^2} \iint I(q, \varphi) q^2 \sin \varphi dq d\varphi \quad (\text{A7})$$

When calculating the invariant, trace noise in scattered intensity at the large q , when weighted with q^2 , became an overwhelming contribution to the invariant.²³³ Also, at the small

angle end, the parasitic scattering features (Figure A5) presented additional interferences. To reduce these impacts, the invariant was integrated over the q range between 0.00819 \AA^{-1} and 0.04007 \AA^{-1} . Due again to the parasitic scattering, the azimuthal range for integration was from $-\pi/4$ to $3\pi/4$. Figure A12 *a* demonstrates a series of intensity integrated azimuthally using:

$$\bar{I}(q) = \int_{-\frac{\pi}{4}}^{\frac{3\pi}{4}} I(q, \varphi) |\sin \varphi| d\varphi \quad (\text{A8})$$

The evolution of $\bar{I}(q)$ shows a clear growth in the region of q around 0.012 \AA^{-1} , indicative of the growth of lamellae and the average lamellar spacing. Figure A12 *b* shows the background corrected intensity profile during crystallization, using the scattering pattern collected while flow was being applied as a baseline. Finally, an integration of $\bar{I}(q)$ over the chosen q range generates the invariant as a function of time.

$$Q = \int [\bar{I}(q) - \bar{I}_{flow}(q)] q^2 dq \quad (\text{A9})$$

The growth of invariant as a function of time illustrates the progress of crystallization as the volume fraction of crystalline phase increases and the volume fraction of amorphous phase decreases (Equation A3).

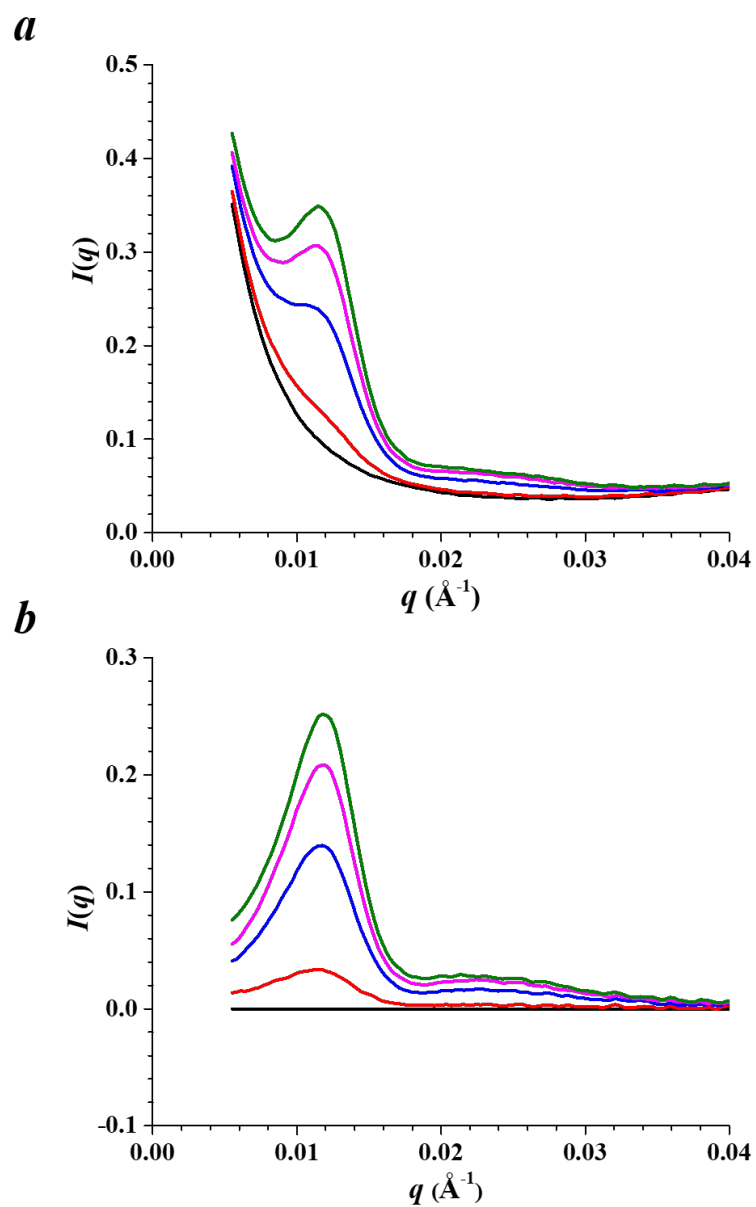


Figure A12 An illustration of calculation of lamellae growth induced by shear flow at a rate of 4 s^{-1} and a strain of 12 units, collected at $t = 0$ (black), 4 (red), 12 (blue), 20 (magenta), 40 (olive) min (a) the azimuthally integrated intensity as crystallization progresses (b) subtracted intensity profile using the intensity profile while flow was applied as the background

A3.5.2 Calculation of unit cell growth

Figure A6 demonstrates that for the WAXD patterns, distinct scattering peaks emerge as the crystallization progresses and polymer chains are packed into unit cells. The integrated peak area was used to quantify the amount of unit cell structure formed during crystallization. Figure A6 *c* shows that at the end of crystallization, multiple scattering peaks appear on the WAXD pattern. In this study, the strongest (200) reflection at $q = 0.823 \text{ \AA}^{-1}$ (Figure A13) was chosen for quantitative analysis.

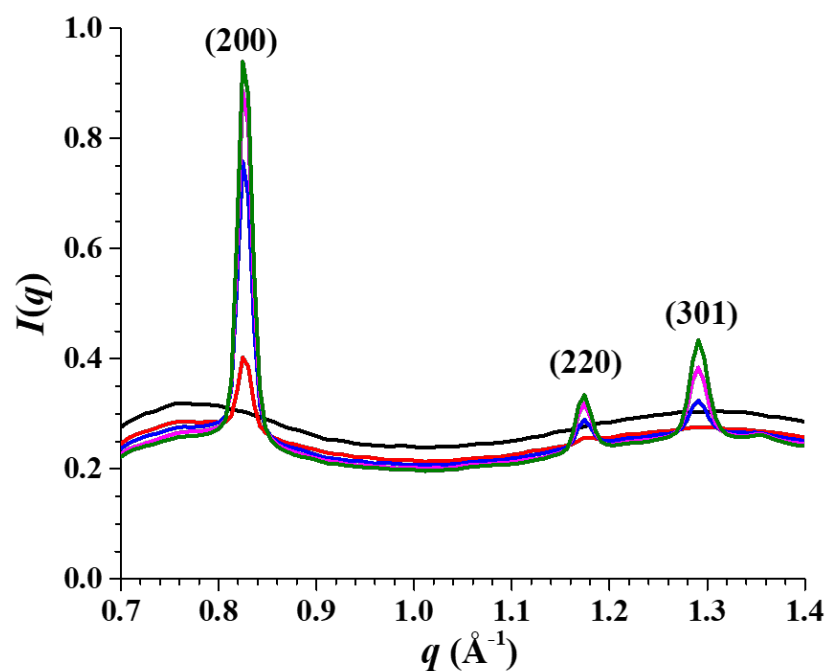


Figure A13 WAXD intensity as a function of q measured perpendicular to the flow direction

As shown in Figure A11 *b*, the WAXD patterns were processed using FIT2D to obtain $I(q, \phi')$ and then the intensity was calibrated to absolute units. Figure A14 shows an exemplary

calculation of integrated peak area. First, the intensities adjacent to the crystalline peak at both sides were extracted, and fitted to a fourth-order polynomial. Then the polynomial function generates the amorphous baseline at the peak, shown as the black dash in Figure A14. Finally, the integrated peak area at a particular azimuthal angle was calculated as the area in between the amorphous baseline and crystalline peak:

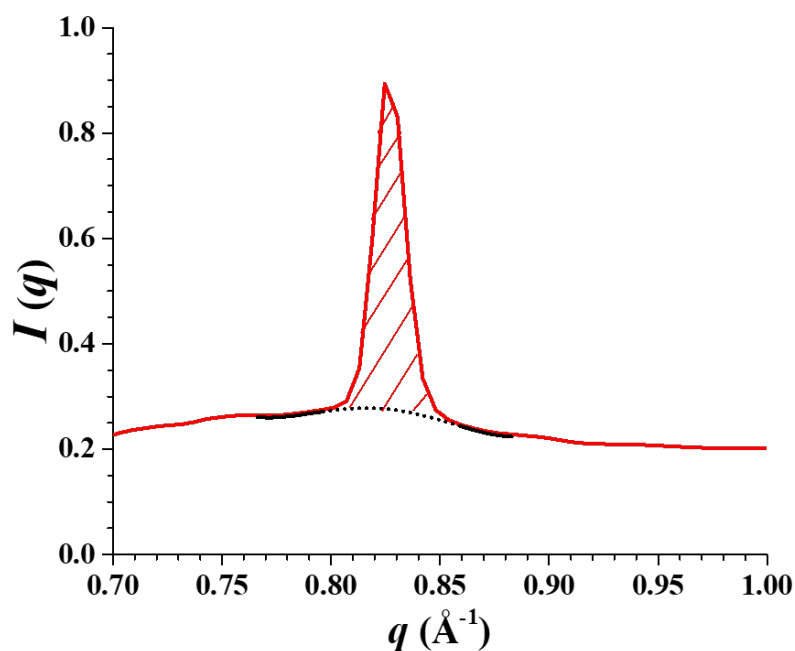


Figure A14 A demonstration of the calculation of integrated peak area, for the experiment when flow was applied at a shear rate of 4 s^{-1} and a strain of 12 units, intensity collected at $t = 40 \text{ min}$.

$$A'(\phi') = \int_{peak} [I_{crys}(q, \phi') - I_{amor}(q, \phi')] dq \quad (\text{A10})$$

This integration was performed at each azimuthal angle. Then the apparent azimuthal angle was corrected to the true angle with respect to the flow axis (Figure 3.3) using Equation 3.12 (Figure A15).

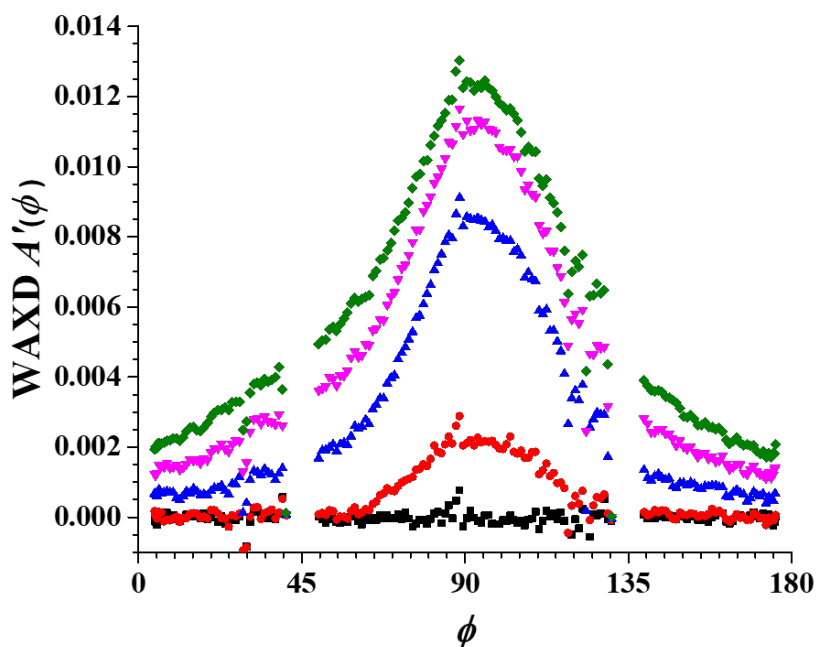


Figure A15 WAXD integrated peak area as a function of ϕ , the corrected azimuthal angle according to the curvature of Ewald sphere, collected in the experiment where flow was at a shear rate of 4 s^{-1} and a strain of 12 units, collected at $t = 0$ (black), 4 (red), 12 (blue), 20 (magenta), 40 (olive) min

Figure A15 exhibits multiple gaps. The gap at 45° and 135° were introduced by the edges of the two panels of the WAXD detector. The gaps at 0° and 180° were caused by the Ewald sphere curvature correction. The integrated peak area was averaged with respect to the axis $\phi = 90^\circ$, and a double Gaussian function was used to fit the data (Figure A16). Finally, the total integrated area was obtained by integrating azimuthally:

$$A = \int_0^{\frac{\pi}{2}} A'_{fit}(\phi) \sin \phi \, d\phi \quad (\text{A11})$$

The evolution of WAXD integrated peak area offers a perspective upon crystallization through the growth of unit cells.

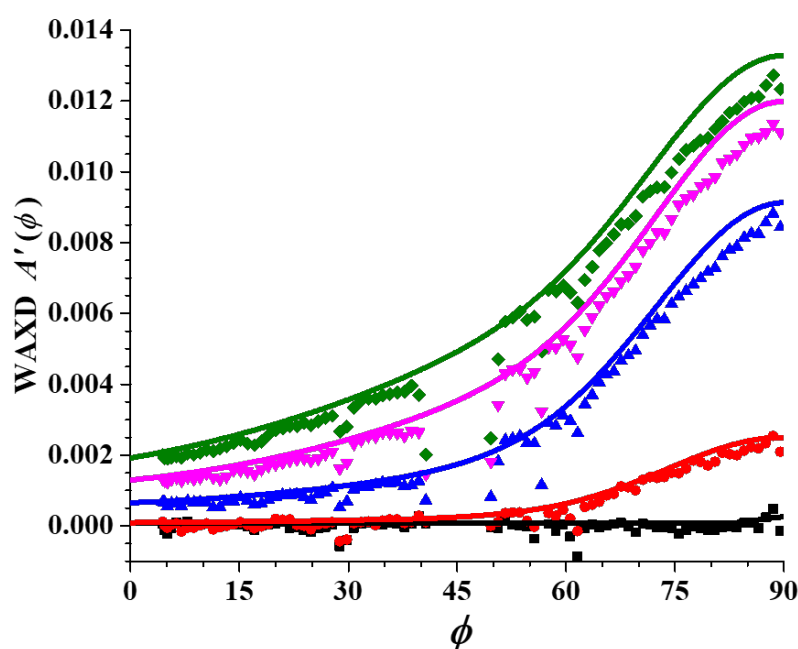


Figure A16 WAXD integrated peak area fitted to a double Gaussian function, collected in the experiment of a shear rate of 4 s^{-1} and a strain of 12 units, collected at $t = 0$ (black), 4 (red), 12 (blue), 20 (magenta), 40 (olive) min

A3.5.3 Calculation of orientation parameter for lamellae and unit cells

At the end of crystallization experiment, both the SAXS and WAXD scattering patterns (Figure A5 and A6 respectively) show a preferred direction of orientation. Section A2.2 have introduced the Hermans' orientation parameter for quantitatively measure the degree of orientation.

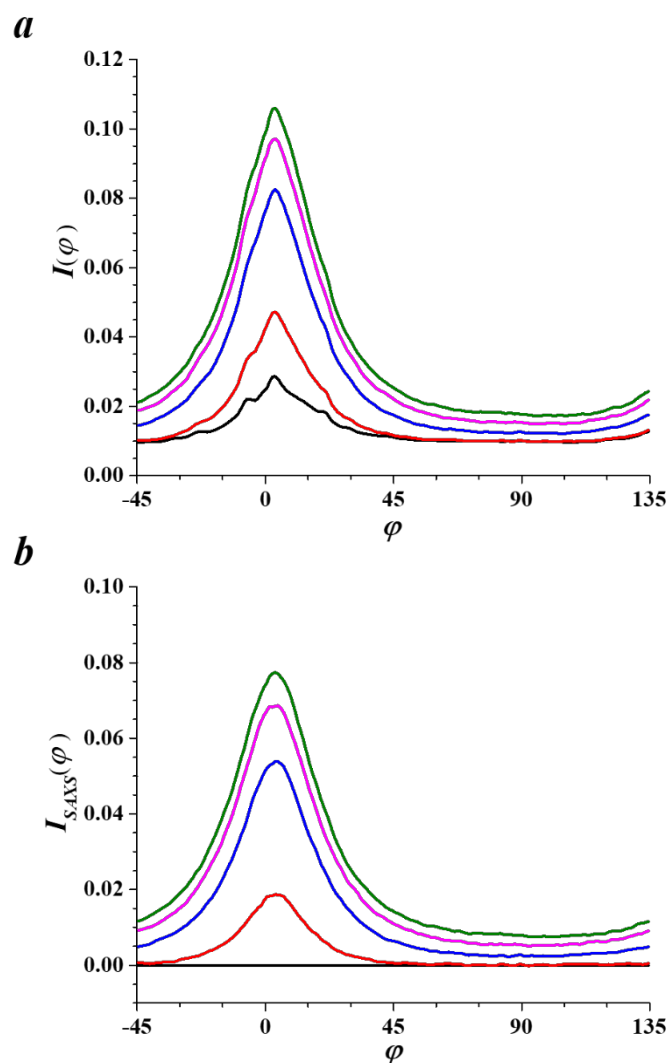


Figure A17 (a) $I(\varphi)$ obtained by integrated $I(q, \varphi)$ over the q range of 0.00819 \AA^{-1} and 0.0143 \AA^{-1} (b) background subtracted $I_{SAXS}(\varphi)$ using $I_{flow}(\varphi)$, integrated from the scattering pattern subjected to a shear rate of 4 s^{-1} and a strain of 12 units, collected at $t = 0$ (black), 4 (red), 12 (blue), 20 (magenta), 40 (olive) min

As shown by Figure A7 a, the scattered intensity from lamellae is a direct indicator of the orientation of lamellae. To compute the Hermans' orientation parameter for lamellae (Equation 3.23), first the intensity profile $I(q, \varphi)$ was integrated over q to obtain $I(\varphi)$. Here a narrower

range of q where the major growth of intensity occurred was used for the degree of orientation, compared to the broader range of q for invariant calculation.

$$I(\varphi) = \int_{q'}^{q''} I(q, \varphi) q^2 dq \quad (\text{A12})$$

Then the integrated $I(\varphi)$ (Figure A17 *a*) were all corrected with the background $I_{flow}(\varphi)$, integrated from the scattering pattern when the shear flow as applied. Figure A17 *b* demonstrates the background corrected $I(\varphi)$: at the start of crystallization, almost all the lamellae are oriented towards the flow direction ($t = 4$ min); Between 4 to 12 min after shear flow being applied, the growth of intensity is highly concentrated along the flow direction. Beyond 12 min, the intensity rises at all azimuthal angles.

From the partially integrated and background subtracted intensity profile $I_{SAXS}(\varphi)$, the average of $\cos^2 \varphi$ can be computed as:

$$\langle \cos^2 \phi \rangle = \frac{\int_{-\frac{3\pi}{4}}^{\frac{3\pi}{4}} I_{SAXS}(\varphi) \cos^2 \varphi |\sin \varphi| d\varphi}{\int_{-\frac{3\pi}{4}}^{\frac{3\pi}{4}} I_{SAXS}(\varphi) |\sin \varphi| d\varphi} \quad (\text{A13})$$

Using the average $\langle \cos^2 \varphi \rangle$, the Hermans' orientation parameter can be calculated using Equation 3.23.

The orientation parameter of unit cells was computed from the fitted WAXD integrated area $A'_{fit}(\phi)$, numerically. In addition, the calculated $\langle P_2 \rangle$ was multiplied by -2 to account for

the perpendicular relationship between chain axis and WAXD intensity, as discussed in Section A2.2.

A3.6 Turbidity measurements

As the amorphous polymer solidifies, it gradually becomes opaque. Thus turbidity can be a gauge for the progress of crystallization. A He-Ne laser ($\lambda = 633 \text{ nm}$) was used as the light source for measuring turbidity. The same Linkam shear flow cell introduced in Section A3.2 was used to turbidity studies except that the original quartz optical windows were employed instead of the customized stainless steel inserts. A photodiode detector was used to measure the transmitted light intensity. Figure A18 demonstrates the experimental setup.

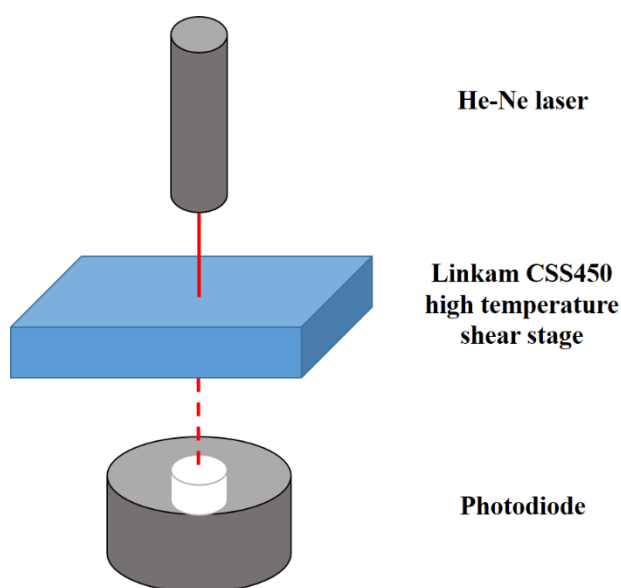


Figure A18 Setup for turbidity measurements of shear-induced crystallization

A3.7 Linear viscoelasticity

Rheological measurements have been widely used to probe the crystallization of semi-crystalline polymers, including pressure drop in a slit,²²⁶ or steady shear viscosity upshoot.²²⁴

Here the storage modulus measured in small-amplitude oscillatory shear is employed as an indicator of the extent of crystallization. An ARES rotational rheometer from TA Instruments was used for measuring linear viscoelasticity during crystallization, with an 8-mm-cone-and-plate geometry. The same temperature and flow protocol was applied. Instead of monitoring crystallization with x-ray or laser, a small amplitude oscillatory time sweep was set up to measure the storage modulus for 60 minutes after shear flow was applied. For the small-amplitude oscillatory time sweep, the frequency was set at 10 rad/s and the initial strain was set at 1%. As crystallization progressed and the storage modulus increased, the applied strain was automatically adjusted to a smaller value based on a preset critical torque threshold. The small fixtures were chosen to avoid excessive sample stiffness, which induces errors due to the compliance of the torque transducer.

A4 Results and discussion

A4.1 X-ray scattering results and discussion

Figure A19 *a* and *b* demonstrate the kinetics of crystallization when the shear rate is fixed at 4 s^{-1} and the applied strains are increased from 4 to 12 units, through the perspective of SAXS invariant and WAXD integrated peak area. As the applied strain is increased from 4 to 8 units, a moderate increase of the extent of crystallization was observed in both the SAXS invariant and WAXD integrated peak area. When the applied strain is increased to 12 units, both SAXS invariant and WAXD integrated peak area increase by a considerable amount at the end of crystallization. The onset of crystallization (upturn of the curve) is earlier than the onset observed in the smaller strains experiments and the speed of crystallization is considerably faster in the early stage. Using a scale factor, the SAXS invariant and WAXD integrated peak area

curves qualitatively resemble each other (Figure A19 *c*). We also notice that the onset of crystallization reflected by SAXS invariant versus WAXD integrated peak area appear to be about the same, indicating that the growth of lamellae is roughly on the same pace with the development of unit cells. This is contrary to previous work with polypropylene^{232,233} and

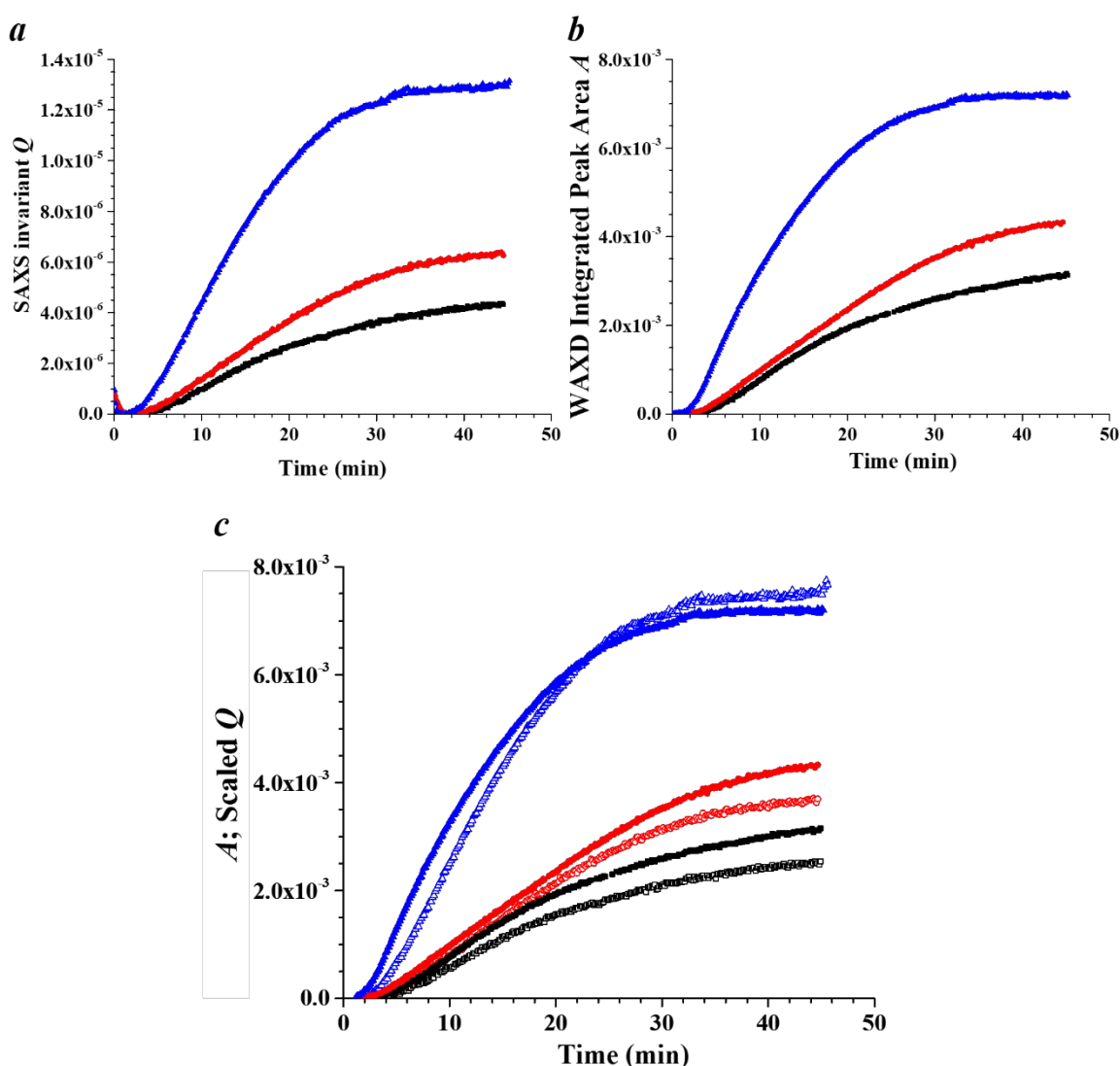


Figure A19 Kinetics for shear-induced crystallization with the shear rate fixed at 4 s^{-1} and the applied strain is varied at 4 (black), 8 (red), and 12 (blue) units (a) the evolution of SAXS invariant, indicative of lamellae growth (b) the growth of WAXD integrated peak area, representative of unit cell growth (c) scaled SAXS invariant Q (open) plotted together with WAXD integrated peak area A (filled)

polyethylene,²³⁰ where the appearance of crystalline peaks in WAXD patterns always lag behind the appearance of SAXS intensity, attributed to that long-range density fluctuations occur before 3-*d* crystalline ordering.

Figure A20 *a* and *b* show the evolution of orientation parameter for lamellae and unit cells respectively. Both structural features show the highest orientation parameters at the initial stage and decreasing degrees of orientation as crystallization progresses. This coincides with the observation of intensity growth (Figures A15 and A16), that the scattered intensity is highly concentrated at a certain direction at the beginning of crystallization and appears more diffused at later stage. As the applied strain is increased from 4 to 8 units, the initial orientation parameter is enhanced, but the final stage $\langle P_2 \rangle$ is unaffected. As the applied strain is increased to 12 units, the alignment for both lamellae and unit cells become much stronger at both initial and final stages. An all-encompassing plot of orientation parameters for both structural features (Figure A19 *c*) shows that the degree of orientation in unit cells is higher than that observed in lamellae.

Figures A21 and A22 illustrate the kinetics and degree of orientation for shear-induced crystallization when the applied strain is fixed at 12 and shear rate is varied at 1, 2, and 4 s⁻¹. The data for the shear rate of 1 s⁻¹ ends at 24 min because of a computer memory glitch occurred while this experiment was conducted. Nonetheless, similar to the trend observed in shear-induced crystallization at a fixed shear rate and increasing strains, both SAXS invariant and WAXD integrated peak area rise with increasing shear rates. The same synchronized emergence of SAXS invariant and WAXD integrated peak is observed, as well as the higher degree of orientation in unit cell than that in the lamellae. The orientation parameter collected at the shear rate of 1 s⁻¹ has higher orientation than that observed at the shear rate of 2 s⁻¹, on par with the

orientation parameter observed at the shear rate of 4 s^{-1} . Unfortunately, data at a longer time scale is missing and whether this high degree of orientation will remain high or be lowered as crystallization progresses is unknown, so as the possible causes for such unusual behavior.

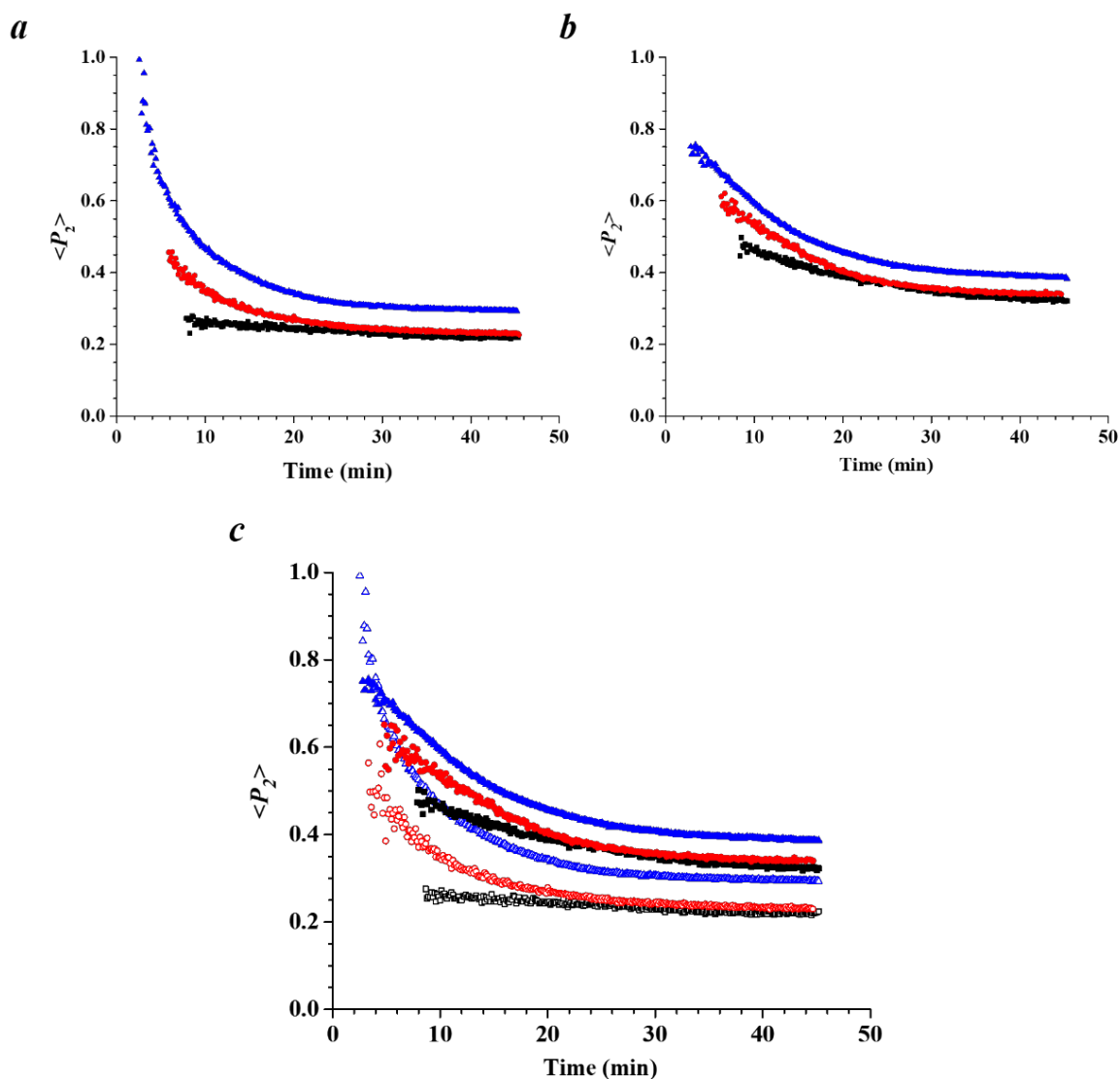


Figure A20 Evolution of Hermans' orientation parameter for (a) lamellae (b) unit cells (c) both structural features with unit cell (filled) and lamellae (open) when the shear rate is fixed at 4 s^{-1} and the applied is varied at 4 (black), 8 (red), and 12 (blue) units

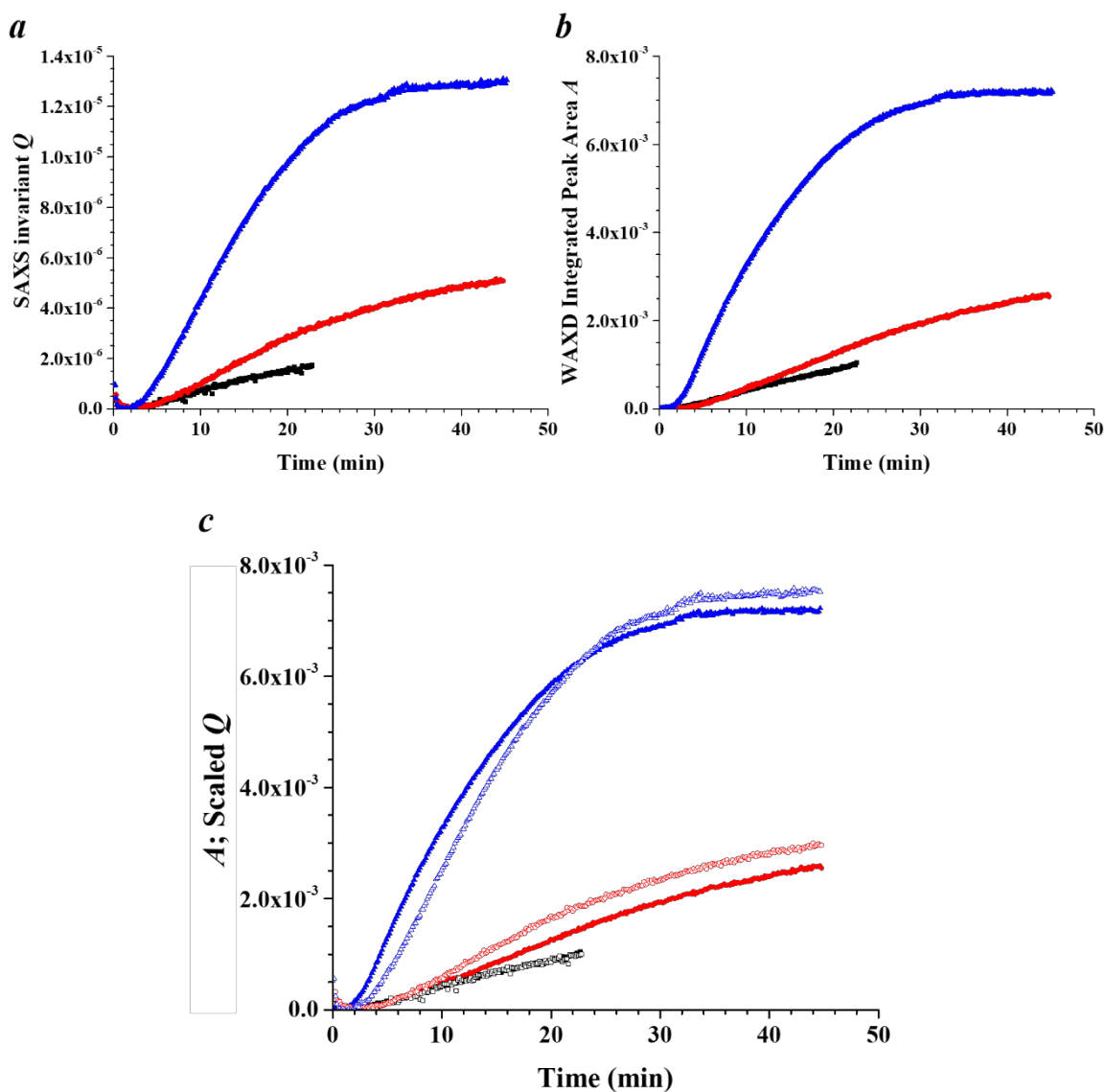


Figure A21 Kinetics for shear-induced crystallization with flow of a fixed strain and varying shear rates at 1 (black), 2 (red), and 4 (blue) s⁻¹ (a) the evolution of SAXS invariant, indicative of lamellae growth (b) the growth of WAXD integrated peak area, representative of unit cell growth (c) scaled SAXS invariant Q (open) plotted together with WAXD integrated peak area A (filled)

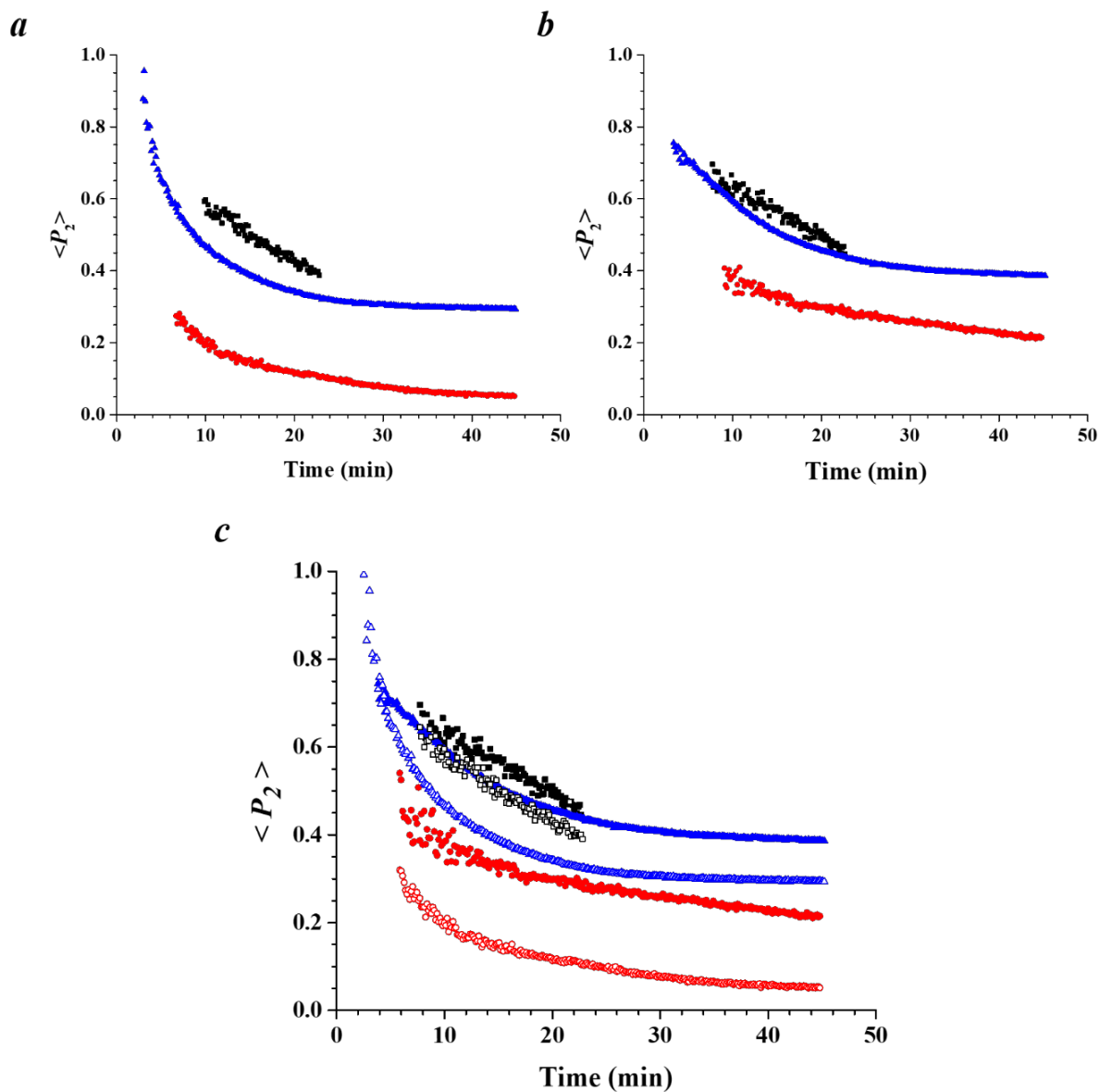


Figure A22 Hermans' orientation parameters (a) lamellae (b) unit cells (c) both lamellae (open) and unit cells (filled) for shear-induced crystallization when the applied strain is fixed at 12 units and the shear rate is varied at 1 (black), 2 (red), and 4 (blue) s^{-1}

A4.2 Turbidity measurements versus x-ray scattering

Figure A23 *a* and *b* demonstrate the kinetics of crystallization (scaled SAXS invariant and WAXD integrated peak area) and the evolution of turbidity respectively, for shear-induced crystallization when the applied strain is fixed at 8 units and the shear rate is varied from 0.5, 1, 4, and 8 s⁻¹, as well as the quiescent crystallization at the same temperature. Compared to x-ray scattering, the turbidity measurements demonstrate the onset of crystallization signal at a much shorter time scale, and reach a saturation of turbidity rather quickly and for all flow conditions. In turbidity measurements, the quiescent crystallization has little growth while all the other flow conditions significantly accelerate crystallization. In the x-ray scattering data, only under shear rates of 4 or 8 s⁻¹ exhibits significant growth of crystallization while under the shear rates of 0.5 and 1 s⁻¹, the extent of crystallization appears to be similar to quiescent crystallization, *i.e.*, little crystallization occurs. The comparison between the two techniques demonstrate that turbidity is better at distinguishing the influence of flow when the flow conditions are weak and the amount of crystallization is relatively small, while x-ray scattering is more suitable and responsive at stronger flow conditions and greater extent of crystallization.

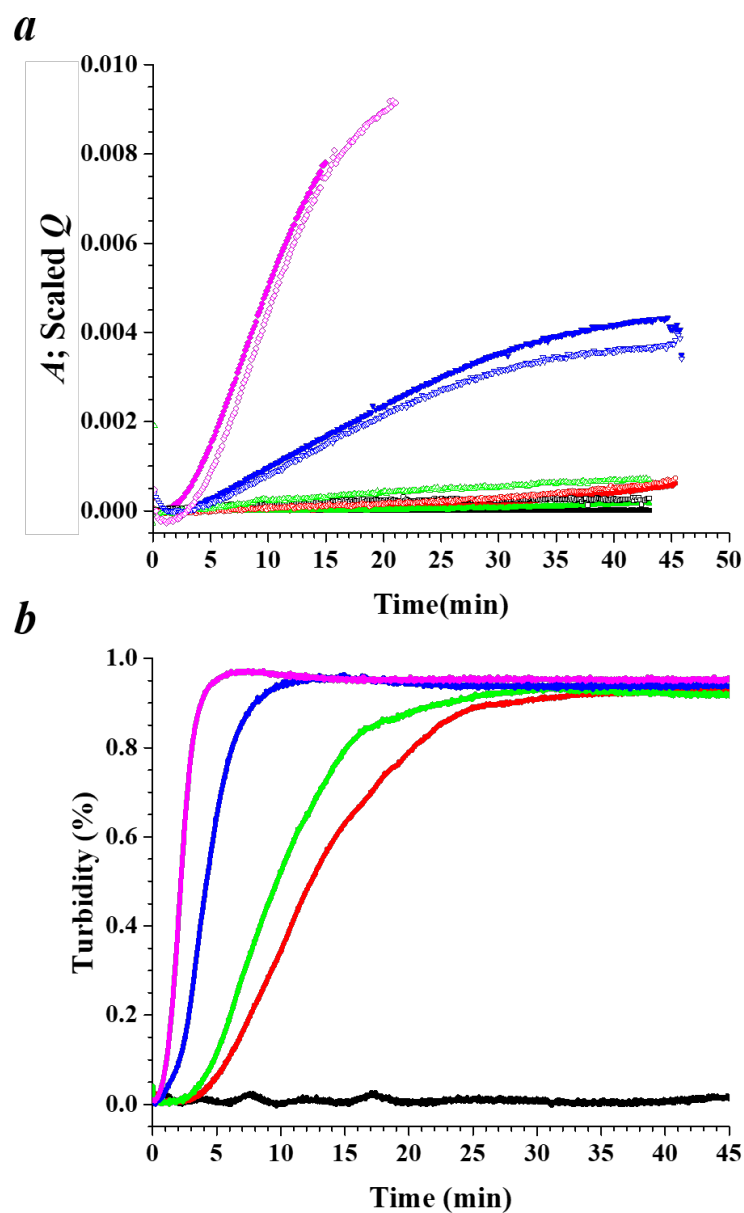


Figure A23 Quiescent crystallization from PB-1 melt (black) as well as shear-induced crystallization at a fixed strain of 8 units and shear rates are varied from 0.5 (red), 1 (green), 4 (blue), and 8 (magenta) s^{-1} , measured using (a) WAXD integrated peak area A (filled) and scaled SAXS invariant Q (open) (b) turbidity

A4.3 Linear viscoelasticity versus x-ray scattering

Figures A24 and A25 present the parallel studies of shear-induced crystallization under the shear flow when the applied strain is fixed at 12 units and shear rates are varied from 1, 2, to 4 s⁻¹, and when the shear rate is fixed at 4 s⁻¹ while the strain is varied from 4, 8, to 12 units, measured using simultaneous SAXS/WAXD versus linear viscoelasticity. In both sets of comparisons, the onset of crystallization measured by linear viscoelasticity occur considerably later than the onset indicated by x-ray scattering. This may be interpreted as that in LVE measurement, the crystalline phase needs to grow to a substantial volume fraction to induce a measurable change in the mechanical stress. At the final stage of crystallization, The G' under various flow conditions all achieve roughly the same mechanical strength around 10⁷ Pa. However, the extent of crystallization measured using x-ray differ from one another under various flow conditions. In the LVE measurements, we observed that at the end of data collection, the fixture connecting the torque transducer was vibrating. This may be attributed to the substantially crystallized poly-1-butene sample connecting the two pieces of cone-and-plate fixture together like an adhesive. After a certain extent of crystallization, the upper fixture experienced the oscillatory shear strain as it was connected to the lower fixture but rather performed stress measurements. This suggests that the rheological measurement has an upper limit on distinguishing the extent of crystallization. In all, compared to LVE, x-ray scattering is responsive at a wider range of the extent of crystallization.

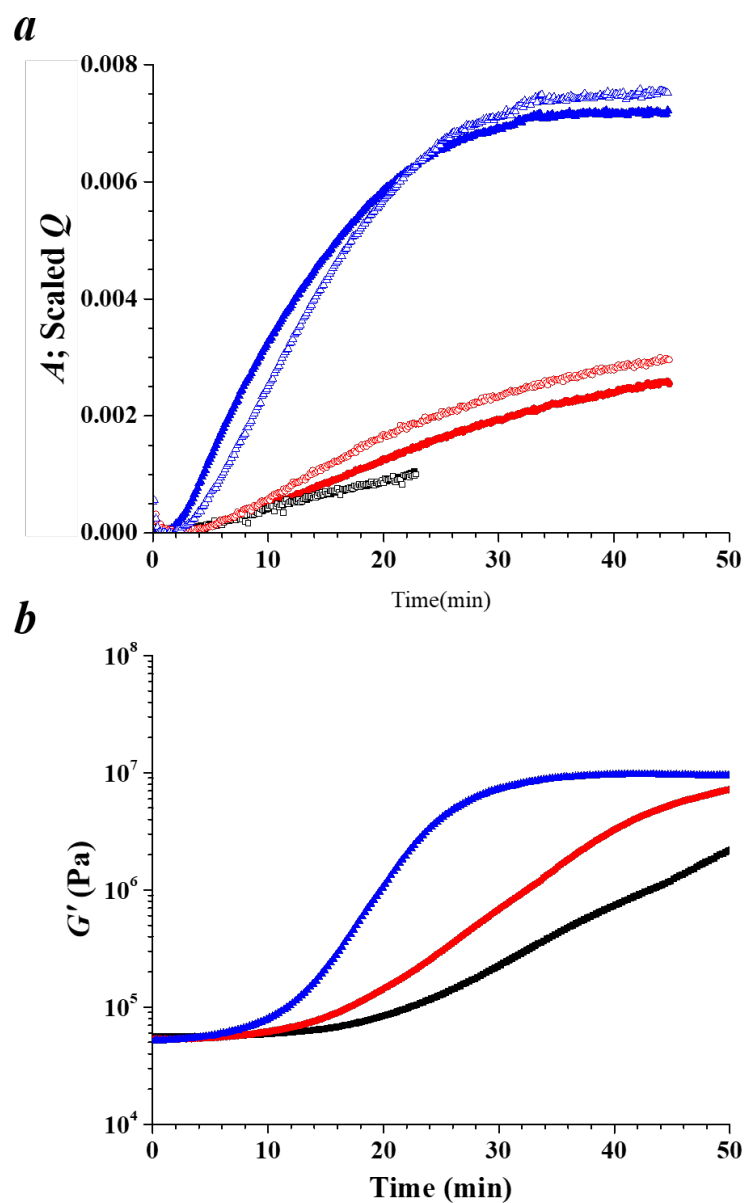


Figure A24 Kinetics of shear-induced crystallization under a strain of 12 units and shear rates of 1 (black), 2 (red), and 4 (blue) s^{-1} measured using (a) WAXD integrated peak area A (filled) and scaled SAXS invariant Q (open) (b) small-amplitude oscillatory shear

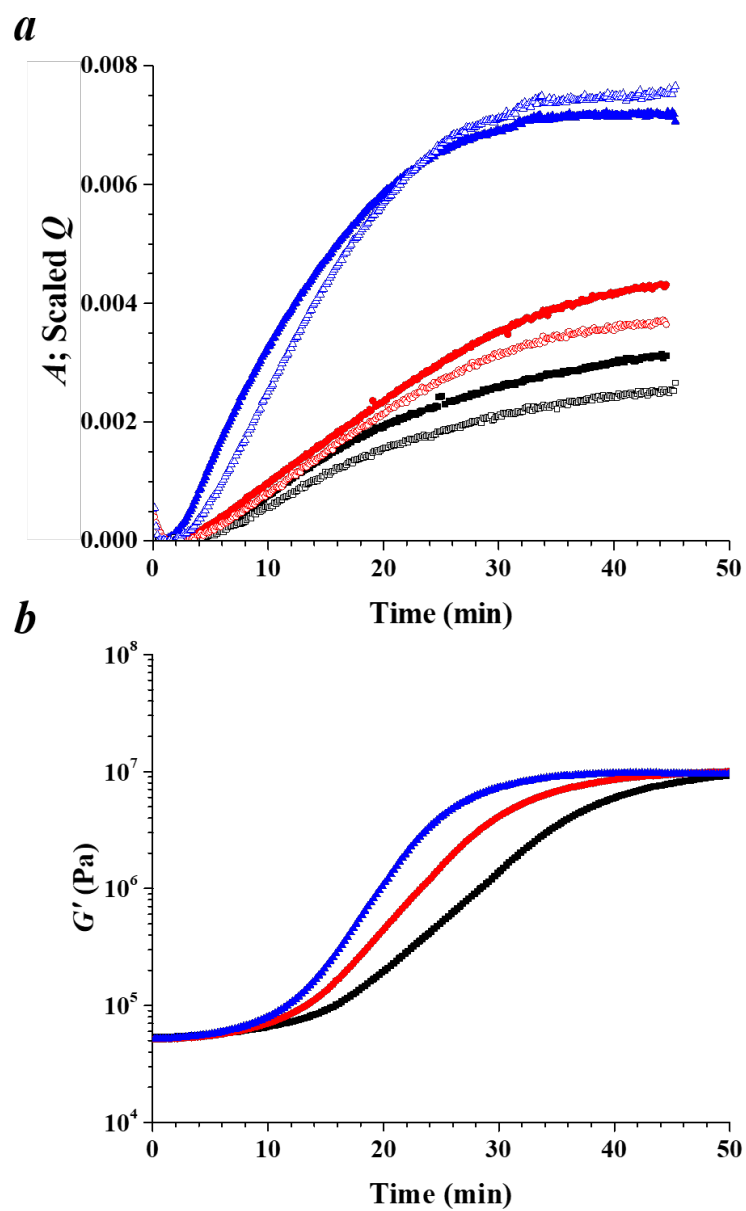


Figure A25 Kinetics of shear-induced crystallization under a shear rate of 4 s^{-1} and varied strain of 4 (black), 8 (red), and 12 (blue) units, measured using (a) WAXD integrated peak area A (filled) and scaled SAXS invariant Q (open) (b) small-amplitude oscillatory shear

A5 Conclusions

Shear-induced crystallization of poly-1-butene has been studied using simultaneous SAXS/WAXD techniques. Quantitative analysis methods have been developed and employed to extract the kinetics of crystallization as well as the orientation state of structural features at multiple length scales.

The x-ray scattering results suggest that generally stronger flow conditions induce greater extent of crystallization and higher degree of orientation. The orientation states of both lamellae and unit cells tend to be higher at the early stage of crystallization and then gradually decrease as crystallization progresses. In addition, the orientation of the unit cells at the shorter length scale (observed in SAXS) is always higher than the orientation of lamellae at the longer length scale (reflected by WAXD). The extent of crystallization indicated by lamellae growth from SAXS invariant and the unit cell growth based on the WAXD integrated peak area can generally be scaled together. We also observed that the onset of crystallization indicated by SAXS is on the same pace with the onset of WAXD integrated peak area. This is in contrast to x-ray scattering studies conducted with other semi-crystalline polymers where SAXS often demonstrate density fluctuations before WAXD crystalline peaks emerge.

We also compared x-ray scattering with other techniques (turbidity and linear viscoelasticity) and found that in addition to offer orientation state of various structural features, x-ray scattering has a wide “responsive range” on the extent of crystallization. The preliminary data analysis methods developed in this study hopefully may support future studies with extensional flow as such strong flow will likely be a more sophisticated process at various dimensions such as kinetics, orientation state, and morphologies.

Appendix B: Quantitative Impact from Isotropic Background Scattering and Correction

As briefly discussed in Section 3.3, the presence of an isotropic scattering background will reduce the value of AF , because the scattering from the isotropic background is counted in the calculation of anisotropy factor and thus decreases the anisotropy from the true value, which should be computed solely based on the scattering intensity from the anisotropic sample. This effort is motivated by Section 4.4.4, as we were speculating possible causes for the large discrepancy of AF predicted by simulation versus experimental observation for carbon nanotube dispersions. In this appendix, we consider a mathematical analysis of the impact of an isotropic background scattering and a possible correction to account for this effect, provided that the isotropic scattering background can be measured separately.

The measured total (apparent) scattered intensity can be separated into the contributions from an anisotropic scattering from the sample (of interest), and the isotropic scattering intensity from the background:

$$I_{app}(q) = I_s(q) + I_{bkgd}(q) \quad (B1)$$

To uncover the impact of the isotropic background scattering on the AF and the orientation angle, we can first look at its influence upon the second moment tensor. Based on equation (B1), the computed or apparent components of the second moment tensor can be written as:

$$\langle \mathbf{q}\mathbf{q} \rangle_{app} = \begin{pmatrix} \langle q_1 q_1 \rangle & \langle q_1 q_2 \rangle \\ \langle q_1 q_2 \rangle & \langle q_2 q_2 \rangle \end{pmatrix} = \frac{\iint \mathbf{q}\mathbf{q} \left(I_s(\mathbf{q}) + I_{bkgd}(\mathbf{q}) \right) dq_1 dq_2}{\iint q^2 \left(I_s(\mathbf{q}) + I_{bkgd}(\mathbf{q}) \right) dq_1 dq_2} \quad (\text{B2})$$

The desired true components of the second moment tensor should be computed solely based on the anisotropic contribution $I_s(\mathbf{q})$.

Thus,

$$\langle \mathbf{q}\mathbf{q} \rangle = \frac{\iint \mathbf{q}\mathbf{q} I_s(\mathbf{q}) dq_1 dq_2}{\iint q^2 I_s(\mathbf{q}) dq_1 dq_2} \quad (\text{B3})$$

Since the background scattering is isotropic, the components of the second moment tensor follow:

$$\iint q_1 q_1 I_{bkgd}(\mathbf{q}) dq_1 dq_2 = \iint q_2 q_2 I_{bkgd}(\mathbf{q}) dq_1 dq_2 \quad (\text{B4})$$

$$\iint q_1 q_2 I_{bkgd}(\mathbf{q}) dq_1 dq_2 = 0 \quad (\text{B5})$$

Using equation (B1), the apparent anisotropy factor computed from the apparent second moment tensor using the measured scattering intensity can be written as:

$$\begin{aligned}
AF_{app} &= \sqrt{(\langle q_1 q_1 \rangle_{app} - \langle q_2 q_2 \rangle_{app})^2 + 4\langle q_1 q_2 \rangle_{app}^2} \\
&= \sqrt{\left[\frac{\iint q_1 q_1 (I_s(\mathbf{q}) + I_{bkga}(\mathbf{q})) dq_1 dq_2}{\iint q^2 (I_s(\mathbf{q}) + I_{bkga}(\mathbf{q})) dq_1 dq_2} - \frac{\iint q_2 q_2 (I_s(\mathbf{q}) + I_{bkga}(\mathbf{q})) dq_1 dq_2}{\iint q^2 (I_s(\mathbf{q}) + I_{bkga}(\mathbf{q})) dq_1 dq_2} \right]^2 + 4 \cdot \left[\frac{\iint q_1 q_2 (I_s(\mathbf{q}) + I_{bkga}(\mathbf{q})) dq_1 dq_2}{\iint q^2 (I_s(\mathbf{q}) + I_{bkga}(\mathbf{q})) dq_1 dq_2} \right]^2}
\end{aligned} \tag{B6}$$

Canceling out the terms from isotropic background scattering, Equation B6 is rearranged as:

$$\begin{aligned}
AF_{app} &= \sqrt{(\langle q_1 q_1 \rangle_{app} - \langle q_2 q_2 \rangle_{app})^2 + 4\langle q_1 q_2 \rangle_{app}^2} \\
&= \sqrt{\left[\frac{\iint q_1 q_1 I_s(\mathbf{q}) dq_1 dq_2}{\iint q^2 (I_s(\mathbf{q}) + I_{bkga}(\mathbf{q})) dq_1 dq_2} - \frac{\iint q_2 q_2 I_s(\mathbf{q}) dq_1 dq_2}{\iint q^2 (I_s(\mathbf{q}) + I_{bkga}(\mathbf{q})) dq_1 dq_2} \right]^2 + 4 \cdot \left[\frac{\iint q_1 q_2 I_s(\mathbf{q}) dq_1 dq_2}{\iint q^2 (I_s(\mathbf{q}) + I_{bkga}(\mathbf{q})) dq_1 dq_2} \right]^2} \\
&= \frac{\sqrt{(\iint q_1 q_1 I_s(\mathbf{q}) dq_1 dq_2 - \iint q_2 q_2 I_s(\mathbf{q}) dq_1 dq_2)^2 + 4 \cdot (\iint q_1 q_2 I_s(\mathbf{q}) dq_1 dq_2)^2}}{\iint q^2 (I_s(\mathbf{q}) + I_{bkga}(\mathbf{q})) dq_1 dq_2} \\
&= \frac{\sqrt{(\iint q_1 q_1 I_s(\mathbf{q}) dq_1 dq_2 - \iint q_2 q_2 I_s(\mathbf{q}) dq_1 dq_2)^2 + 4 \cdot (\iint q_1 q_2 I_s(\mathbf{q}) dq_1 dq_2)^2}}{\iint q^2 I_s(\mathbf{q}) dq_1 dq_2} \cdot \frac{\iint q^2 I_s(\mathbf{q}) dq_1 dq_2}{\iint q^2 (I_s(\mathbf{q}) + I_{bkga}(\mathbf{q})) dq_1 dq_2}
\end{aligned} \tag{B7}$$

The first term is the true AF of interest based solely on the sample scattering (Equation B3). If the ratio between the “invariant” of background scattering over that of the sample is defined as β :

$$\beta = \frac{\iint q^2 I_{bkgd}(\mathbf{q}) dq_1 dq_2}{\iint q^2 I_s(\mathbf{q}) dq_1 dq_2} \quad (\text{B8})$$

Then the true AF is related to the apparent AF through:

$$AF_{app} = AF \cdot \frac{1}{1 + \beta} \quad (\text{B9})$$

This tells us that the isotropic background scattering simply dilutes the true anisotropy of the sample by inflating the denominator with its scattered intensity “invariant”. If the total isotropic background scattering intensity can be collected separately, the true anisotropy of the sample can be corrected from the apparent anisotropy factor if the intensity contribution from both the sample and the isotropic background can be determined:

$$AF = AF_{app} \cdot (1 + \beta) \quad (\text{B10})$$

Likewise, we can prove that the true orientation angle χ is equal to the apparent orientation angle χ_{app} , using Equations B4 and B5.

$$\begin{aligned}
\chi_{app} &= \tan^{-1} \left(\frac{-\langle q_1 q_1 \rangle_{app} - \langle q_2 q_2 \rangle_{app} + \sqrt{(\langle q_1 q_1 \rangle_{app} - \langle q_2 q_2 \rangle_{app})^2 + 4 \cdot \langle q_1 q_2 \rangle_{app}^2}}{2 \langle q_1 q_2 \rangle_{app}} \right) \\
&= \tan^{-1} \left(\frac{-\iint (q_1 q_1 - q_2 q_2) (I_s(\mathbf{q}) + I_{bkga}(\mathbf{q})) dq_1 dq_2 + \sqrt{\left(\iint (q_1 q_1 - q_2 q_2) (I_s(\mathbf{q}) + I_{bkga}(\mathbf{q})) dq_1 dq_2\right)^2 + 4 \cdot \left(\iint q_1 q_2 (I_s(\mathbf{q}) + I_{bkga}(\mathbf{q})) dq_1 dq_2\right)^2}}{2 \iint q_1 q_2 (I_s(\mathbf{q}) + I_{bkga}(\mathbf{q})) dq_1 dq_2} \right) \\
&= \tan^{-1} \left(\frac{-\iint (q_1 q_1 - q_2 q_2) I_s(\mathbf{q}) dq_1 dq_2 + \sqrt{\left(\iint (q_1 q_1 - q_2 q_2) I_s(\mathbf{q}) dq_1 dq_2\right)^2 + 4 \cdot \left(\iint q_1 q_2 I_s(\mathbf{q}) dq_1 dq_2\right)^2}}{2 \iint q_1 q_2 I_s(\mathbf{q}) dq_1 dq_2} \right) = \chi
\end{aligned}
\tag{B11}$$

Therefore, orientation angle is unaffected by isotropic background scattering.

The Hermans' orientation parameter can also be corrected using a similar method. The main goal is to connect the apparent $\langle \cos^2 \phi \rangle_{app}$ to the true $\langle \cos^2 \phi \rangle$ of the sample:

$$\begin{aligned}
\langle \cos^2 \phi \rangle_{app} &= \frac{\int \cos^2 \phi (I_s(\phi) + I_{bkga}(\phi)) \sin \phi d\phi}{\int (I_s(\phi) + I_{bkga}(\phi)) \sin \phi d\phi} = \frac{\int \cos^2 \phi I_s(\phi) \sin \phi d\phi}{\int (I_s(\phi) + I_{bkga}(\phi)) \sin \phi d\phi} + \frac{\int \cos^2 \phi I_{bkga}(\phi) \sin \phi d\phi}{\int (I_s(\phi) + I_{bkga}(\phi)) \sin \phi d\phi} \\
&= \frac{\int \cos^2 \phi I_s(\phi) \sin \phi d\phi}{\int I_s(\phi) \sin \phi d\phi} \cdot \frac{\int I_s(\phi) \sin \phi d\phi}{\int (I_s(\phi) + I_{bkga}(\phi)) \sin \phi d\phi} + \frac{\int \cos^2 \phi I_{bkga}(\phi) \sin \phi d\phi}{\int I_{bkga}(\phi) \sin \phi d\phi} \cdot \frac{\int I_{bkga}(\phi) \sin \phi d\phi}{\int (I_s(\phi) + I_{bkga}(\phi)) \sin \phi d\phi}
\end{aligned}
\tag{B12}$$

If the ratio of the integrated intensity from the isotropic background over that of the sample is defined as α :

$$\alpha = \frac{\int I_{bkgd}(\phi) \sin \phi \, d\phi}{\int I_s(\phi) \sin \phi \, d\phi} \quad (\text{B13})$$

Together with the isotropic nature of background scattering:

$$\frac{\int \cos^2 \phi I_{bkgd}(\phi) \sin \phi \, d\phi}{\int I_{bkgd}(\phi) \sin \phi \, d\phi} = \frac{1}{3} \quad (\text{B14})$$

Equation B12 can be rewritten as:

$$\langle \cos^2 \phi \rangle_{app} = \langle \cos^2 \phi \rangle \cdot \frac{1}{1 + \alpha} + \frac{1}{3} \cdot \frac{\alpha}{1 + \alpha} \quad (\text{B15})$$

Thus, the $\langle \cos^2 \phi \rangle$ of the sample is related to the

$$\langle \cos^2 \phi \rangle = \langle \cos^2 \phi \rangle_{app} (1 + \alpha) - \frac{\alpha}{3} \quad (\text{B16})$$

Finally, the true $\langle P_2 \rangle$ is related to the apparent $\langle P_2 \rangle_{app}$ by:

$$\begin{aligned}
\langle P_2 \rangle &= \frac{3}{2} \langle \cos^2 \phi \rangle - \frac{1}{2} = \frac{3}{2} \left[\langle \cos^2 \phi \rangle_{app} (1 + \alpha) - \frac{\alpha}{3} \right] - \frac{1}{2} \\
&= \frac{3}{2} \langle \cos^2 \phi \rangle_{app} (1 + \alpha) - \frac{1}{2} (1 + \alpha) = \langle P_2 \rangle_{app} (1 + \alpha)
\end{aligned}
\tag{B17}$$

The influence of the presence of an isotropic background scattering upon the Hermans' orientation parameter is exactly the same as the influence upon the anisotropy factor.

Reference

1. Trouton, F. T. On the Coefficient of Viscous Traction and Its Relation to that of Viscosity. *Proc. R. Soc. A Math. Phys. Eng. Sci.* **77**, 426–440 (1906).
2. Petrie, C. J. S. *Elongational Flows: Aspects of the Behaviour of Model Elastoviscous Fluids*. (Pitman Publishing, 1979).
3. Tanner, R. I. Stresses in Dilute Solutions of Bead-Nonlinear-Spring Macromolecules. III. Friction Coefficient Varying with Dumbbell Extension. *Trans. Soc. Rheol.* **19**, 557–582 (1975).
4. Meissner, J. Rheometry of Polymer Melts. *Annu. Rev. Fluid Mech.* **17**, 45–64 (1985).
5. Meissner, J. & Hostettler, J. A New Elongational Rheometer for Polymer Melts and Other Highly Viscoelastic Liquids. *Rheol. Acta* **33**, 1–21 (1994).
6. Münstedt, H. Viscoelasticity of polystyrene melts in tensile creep experiments. *Rheol. Acta* **14**, 1077–1088 (1975).
7. Laun, H. M. & Münstedt, H. Elongational behaviour of a low density polyethylene melt. *Rheol. Acta* **17**, 415–425 (1978).
8. Laun, H. M. & Münstedt, H. Comparison of the elongational behaviour of a polyethylene melt at constant stress and constant strain rate. *Rheol. Acta* **15**, 517–524 (1976).
9. Sridhar, T., Nguyen, D. . & Fuller, G. . Birefringence and stress growth in uniaxial extension of polymer solutions. *J. Nonnewton. Fluid Mech.* **90**, 299–315 (2000).
10. Rothstein, J. P. & McKinley, G. H. A comparison of the stress and birefringence growth of dilute, semi-dilute and concentrated polymer solutions in uniaxial extensional flows. *J. Nonnewton. Fluid Mech.* **108**, 275–290 (2002).
11. Yesilata, B., Clasen, C. & McKinley, G. H. Nonlinear shear and extensional flow dynamics of wormlike surfactant solutions. *J. Nonnewton. Fluid Mech.* **133**, 73–90 (2006).
12. Walker, L. M., Moldenaers, P. & Berret, J.-F. F. Macroscopic response of wormlike micelles to elongational flow. *Langmuir* **12**, 6309–6314 (1996).
13. Fischer, P., Fuller, G. G. & Lin, Z. Branched viscoelastic surfactant solutions and their response to elongational flow. *Rheol. Acta* **36**, 632–638 (1997).
14. Bhardwaj, A., Richter, D., Chellamuthu, M. & Rothstein, J. P. The effect of pre-shear on the extensional rheology of wormlike micelle solutions. *Rheol. Acta* **46**, 861–875 (2007).
15. Chellamuthu, M., Arndt, E. M. & Rothstein, J. P. Extensional rheology of shear-

- thickening nanoparticle suspensions. *Soft Matter* **5**, 2117 (2009).
16. Alexandrou, A. N., Bazilevskii, A. V., Entov, V. M., Rozhkov, A. N. & Sharaf, A. Breakup of a capillary bridge of suspensions. *Fluid Dyn.* **45**, 952–964 (2010).
 17. Bischoff White, E. E., Chellamuthu, M. & Rothstein, J. P. Extensional rheology of a shear-thickening cornstarch and water suspension. *Rheol. Acta* **49**, 119–129 (2010).
 18. Gelbart, W. M. & Ben-Shaul, A. The “New” Science of “Complex Fluids”. *J. Phys. Chem.* **100**, 13169–13189 (1996).
 19. Jeffery, G. B. The Motion of Ellipsoidal Particles Immersed in a Viscous Fluid. *Proc. R. Soc. A Math. Phys. Eng. Sci.* **102**, 161–179 (1922).
 20. Caputo, F. E., Burghardt, W. R. & Berret, J.-F. Tumbling dynamics in a nematic surfactant solution in transient shear flows. *J. Rheol. (N. Y. N. Y.)* **43**, 765 (1999).
 21. Larson, R. G. The rheology of dilute solutions of flexible polymers: Progress and problems. *J. Rheol. (N. Y. N. Y.)* **49**, 1–70 (2005).
 22. Lerouge, S. & Berret, J.-F. *Polymer Characterization. POLYMER CHARACTERIZATION: RHEOLOGY, LASER INTERFEROMETRY, ELECTROOPTICS* **230**, (Springer Berlin Heidelberg, 2010).
 23. Macosko, C. *Rheology: principles, measurements, and applications*. (VCH, 1994).
 24. Binding, D. M. in *Techniques in Rheological Measurement* 1–32 (Springer Netherlands, 1993). doi:10.1007/978-94-011-2114-9_1
 25. Gibson, A. G. Converging Dies.
 26. Meissner, J. Development of a Universal Extensional Rheometer for the Uniaxial Extension of Polymer Melts. *J. Rheol. (N. Y. N. Y.)* **16**, 405 (1972).
 27. Meissner, J., Raible, T. & Stephenson, S. E. Rotary Clamp in Uniaxial and Biaxial Extensional Rheometry of Polymer Melts. *J. Rheol. (N. Y. N. Y.)* **25**, 1–28 (1981).
 28. Hachmann, P. & Meissner, J. Rheometer for equibiaxial and planar elongations of polymer melts. *J. Rheol. (N. Y. N. Y.)* **47**, 989–1010 (2003).
 29. Münstedt, H. New Universal Extensional Rheometer for Polymer Melts. Measurements on a Polystyrene Sample. *J. Rheol. (N. Y. N. Y.)* **23**, 421 (1979).
 30. Sentmanat, M., Wang, B. N. & McKinley, G. H. Measuring the transient extensional rheology of polyethylene melts using the SER universal testing platform. *J. Rheol. (N. Y. N. Y.)* **49**, 585 (2005).
 31. McCready, E. M. & Burghardt, W. R. In Situ SAXS Studies of Structural Relaxation of an Ordered Block Copolymer Melt Following Cessation of Uniaxial Extensional Flow. *Macromolecules* **48**, 264–271 (2015).
 32. McCready, E. M. & Burghardt, W. R. Structural response of a prealigned cylindrical

- block copolymer melt to extensional flow. *J. Rheol. (N. Y. N. Y.)* **59**, 935–956 (2015).
33. James, D. F. & Walters, K. in *Techniques in Rheological Measurement* 33–53 (Springer Netherlands, 1993). doi:10.1007/978-94-011-2114-9_2
 34. McKinley, G. H. & Sridhar, T. Filament-stretching rheometry of complex fluids. *Annu. Rev. Fluid Mech.* **34**, 375–415 (2002).
 35. Anna, S. L. *et al.* An interlaboratory comparison of measurements from filament-stretching rheometers using common test fluids. *J. Rheol. (N. Y. N. Y.)* **45**, 83–114 (2001).
 36. McKinley, G. H. & Tripathi, A. How to extract the Newtonian viscosity from capillary breakup measurements in a filament rheometer. *J. Rheol. (N. Y. N. Y.)* **44**, 653–670 (2000).
 37. Mckinley, G. H. VISCO-ELASTO-CAPILLARY THINNING AND BREAK-UP OF COMPLEX FLUIDS. *Rheol. Rev.* 1–48 (2005). at <<http://www.bsr.org.uk>>
 38. Rothstein, J. P. Transient extensional rheology of wormlike micelle solutions. *J. Rheol. (N. Y. N. Y.)* **47**, 1227–1247 (2003).
 39. Clasen, C. *et al.* How dilute are dilute solutions in extensional flows? *J. Rheol. (N. Y. N. Y.)* **50**, 849–881 (2006).
 40. Arnolds, O., Buggisch, H., Sachsenheimer, D. & Willenbacher, N. Capillary breakup extensional rheometry (CaBER) on semi-dilute and concentrated polyethyleneoxide (PEO) solutions. *Rheol. Acta* **49**, 1207–1217 (2010).
 41. Sachsenheimer, D. *et al.* Elongational deformation of wormlike micellar solutions. *J. Rheol. (N. Y. N. Y.)* **58**, 2017–2042 (2014).
 42. Kim, N. J., Pipe, C. J., Ahn, K. H., Lee, S. J. & McKinley, G. H. Capillary breakup extensional rheometry of a wormlike micellar solution. *Korea Aust. Rheol. J.* (2010).
 43. Tsentalovich, D. E. *et al.* Relationship of Extensional Viscosity and Liquid Crystalline Transition to Length Distribution in Carbon Nanotube Solutions. *Macromolecules* **49**, 681–689 (2016).
 44. Haward, S. J., Sharma, V., Butts, C. P., McKinley, G. H. & Rahatekar, S. S. Shear and Extensional Rheology of Cellulose/Ionic Liquid Solutions. *Biomacromolecules* **13**, 1688–1699 (2012).
 45. Cathey, C. A. & Fuller, G. G. The optical and mechanical response of flexible polymer solutions to extensional flow. *J. Nonnewton. Fluid Mech.* **34**, 63–88 (1990).
 46. Menasveta, M. J. & Hoagland, D. A. Light scattering from dilute poly(styrene) solutions in uniaxial elongational flow. *Macromolecules* **24**, 3427–3433 (1991).
 47. Chen, C.-M. & Warr, G. G. Light Scattering from Wormlike Micelles in an Elongational Field. *Langmuir* **13**, 1374–1376 (1997).

48. Carrington, S. P., Tatham, J. P., Odell, J. A. & Sáez, A. E. Macromolecular dynamics in extensional flows: 1. Birefringence and viscometry. *Polymer (Guildf)*. **38**, 4151–4164 (1997).
49. Crowley, D. G., Frank, F. C., Mackley, M. R. & Stephenson, R. G. Localized flow birefringence of polyethylene oxide solutions in a four roll mill. *J. Polym. Sci. Polym. Phys. Ed.* **14**, 1111–1119 (1976).
50. Pope, D. P. & Keller, A. Alignment of macromolecules in solution by elongational flow: a study of the effect of pure shear in a four roll mill. *Colloid Polym. Sci* **255**, 633–643 (1977).
51. Dunlap, P. N. & Leal, L. G. Dilute polystyrene solutions in extensional flows: Birefringence and flow modification. *J. Nonnewton. Fluid Mech.* **23**, 5–48 (1987).
52. Lee, E. C. & Muller, S. J. Flow light scattering studies of polymer coil conformation in solutions in extensional flow. *Macromolecules* **32**, 3295–3305 (1999).
53. Odell, J. A. & Carrington, S. P. Extensional flow oscillatory rheometry. *J. Nonnewton. Fluid Mech.* **137**, 110–120 (2006).
54. Perkins, T. T., Smith, D. E. & Chu, S. Single polymer dynamics in an elongational flow. *Science (80-.)*. **276**, 2016–2021 (1997).
55. Dubash, N., Cheung, P. & Shen, A. Q. Elastic instabilities in a microfluidic cross-slot flow of wormlike micellar solutions. *Soft Matter* **8**, 5847–5856 (2012).
56. Arratia, P. E., Thomas, C. C., Diorio, J. & Gollub, J. P. Elastic Instabilities of Polymer Solutions in Cross-Channel Flow. *Phys. Rev. Lett.* **96**, 144502 (2006).
57. Farinato, R. S. Elongational flow birefringence of poly(styrene sulphonate). *Polymer (Guildf)*. **29**, 160–167 (1988).
58. Pathak, J. A. & Hudson, S. D. Rheo-optics of Equilibrium Polymer Solutions: Wormlike Micelles in Elongational Flow in a Microfluidic Cross-Slot. *Macromolecules* **39**, 8782–8792 (2006).
59. Stone, P. A. *et al.* Dynamics of Wormlike Micelles in Elongational Flows. *Macromolecules* **39**, 7144–7148 (2006).
60. Penfold, J. *et al.* Elongational flow induced ordering in surfactant micelles and mesophases. *J. Phys. Chem. B* **110**, 1073–1082 (2006).
61. Haward, S. J., Odell, J. A., Li, Z. & Yuan, X.-F. F. Extensional rheology of dilute polymer solutions in oscillatory cross-slot flow: the transient behaviour of birefringent strands. *Rheol. Acta* **49**, 633–645 (2010).
62. Haward, S. J., Ober, T. J., Oliveira, M. S. N., Alves, M. A. & McKinley, G. H. Extensional rheology and elastic instabilities of a wormlike micellar solution in a microfluidic cross-slot device. *Soft Matter* **8**, 536–555 (2012).

63. Dylla-Spears, R., Townsend, J. E., Jen-Jacobson, L., Sohn, L. L. & Muller, S. J. Single-molecule sequence detection via microfluidic planar extensional flow at a stagnation point. *Lab Chip* **10**, 1543–9 (2010).
64. Smith, D. E. & Chu, S. Response of flexible polymers to a sudden elongational flow. *Science* (80-.). **281**, 1335–1340 (1998).
65. Fry, D. *et al.* Rheo-optical studies of carbon nanotube suspensions. *J. Chem. Phys.* **124**, 054703 (2006).
66. Natale, G. *et al.* Rheo-optical response of carbon nanotube suspensions. *J. Rheol. (N. Y. N. Y.)*. **59**, 499–524 (2015).
67. Fry, D. *et al.* Anisotropy of sheared carbon-nanotube suspensions. *Phys. Rev. Lett.* **95**, 038304 (2005).
68. Miller, E. & Rothstein, J. P. Transient evolution of shear-banding wormlike micellar solutions. *J. Nonnewton. Fluid Mech.* **143**, 22–37 (2007).
69. Schubert, B. A., Kaler, E. W. & Wagner, N. J. The Microstructure and Rheology of Mixed Cationic/Anionic Wormlike Micelles. *Langmuir* **19**, 4079–4089 (2003).
70. Hu, Y., Wang, S. Q. & Jamieson, A. M. Rheological and flow birefringence studies of a shear-thickening complex fluid—A surfactant model system. *J. Rheol. (N. Y. N. Y.)*. **37**, 531–546 (1993).
71. Cathey, C. A. & Fuller, G. G. The Optical and Mechanical Response of Flexible Polymer-Solutions to Extensional Flow. *J. Nonnewton. Fluid Mech.* **34**, 63–88 (1990).
72. Farrell, C. J., Keller, A., Miles, M. J. & Pope, D. P. Conformational Relaxation-Time in Polymer-Solutions by Elongational Flow Experiments .1. Determination of Extensional Relaxation-Time and Its Molecular-Weight Dependence. *Polymer (Guildf)*. **21**, 1292–1294 (1980).
73. Scrivener, O. *et al.* Dynamical behaviour of drag-reducing polymer solutions. *J. Nonnewton. Fluid Mech.* **5**, 475–495 (1979).
74. Islam, M. T., Vanapalli, S. A. & Solomon, M. J. Inertial Effects on Polymer Chain Scission in Planar Elongational Cross-Slot Flow. *Macromolecules* **37**, 1023–1030 (2004).
75. Lee, E. C., Solomon, M. J. & Muller, S. J. Molecular Orientation and Deformation of Polymer Solutions under Shear: A Flow Light Scattering Study. *Macromolecules* **30**, 7313–7321 (1997).
76. Bauer, B. J., Hobbie, E. K. & Becker, M. L. Small-Angle Neutron Scattering from Labeled Single-Wall Carbon Nanotubes. *Macromolecules* **39**, 2637–2642 (2006).
77. Wang, H. *et al.* Dispersing Single-Walled Carbon Nanotubes with Surfactants: A Small Angle Neutron Scattering Study. *Nano Lett.* **4**, 1789–1793 (2004).
78. Zhou, W. *et al.* Small angle neutron scattering from single-wall carbon nanotube

- suspensions: evidence for isolated rigid rods and rod networks. *Chem. Phys. Lett.* **384**, 185–189 (2004).
79. Yurekli, K., Mitchell, C. a & Krishnamoorti, R. Small-Angle Neutron Scattering from Surfactant-Assisted Aqueous Dispersions of Carbon Nanotubes. *J. Am. Chem. Soc.* **126**, 9902–9903 (2004).
 80. Schaefer, D. W. *et al.* Structure and dispersion of carbon nanotubes. *J. Appl. Crystallogr.* **36**, 553–557 (2003).
 81. Schaefer, D. W., Zhao, J., Brown, J. M., Anderson, D. P. & Tomlin, D. W. Morphology of dispersed carbon single-walled nanotubes. *Chem. Phys. Lett.* **375**, 369–375 (2003).
 82. Magid, L. J., Li, Z. & Butler, P. D. Flexibility of Elongated Sodium Dodecyl Sulfate Micelles in Aqueous Sodium Chloride: A Small-Angle Neutron Scattering Study. *Langmuir* **16**, 10028–10036 (2000).
 83. Arleth, L., Bergström, M. & Pedersen, J. S. Small-Angle Neutron Scattering Study of the Growth Behavior, Flexibility, and Intermicellar Interactions of Wormlike SDS Micelles in NaBr Aqueous Solutions. *Langmuir* **18**, 5343–5353 (2002).
 84. Bergström, L. M., Bastardo, L. A. & Garamus, V. M. A small-angle neutron and static light scattering study of micelles formed in aqueous mixtures of a nonionic alkylglucoside and an anionic surfactant. *J. Phys. Chem. B* **109**, 12387–93 (2005).
 85. Berret, J.-F., Gamez-Corrales, R., Séréro, Y., Molino, F. & Lindner, P. Shear-induced micellar growth in dilute surfactant solutions. *Europhys. Lett.* **54**, 605–611 (2001).
 86. Li, X., Imae, T., Leisner, D. & López-Quintela, M. A. Lamellar Structures of Anionic Poly(amido amine) Dendrimers with Oppositely Charged Didodecyldimethylammonium Bromide. *J. Phys. Chem. B* **106**, 12170–12177 (2002).
 87. Hollamby, M. J. Practical applications of small-angle neutron scattering. *Phys. Chem. Chem. Phys.* **15**, 10566 (2013).
 88. Pedersen, J. S. & Svaneborg, C. Scattering from block copolymer micelles. *Curr. Opin. Colloid Interface Sci.* **7**, 158–166 (2002).
 89. Shrestha, L. K., Sharma, S. C., Sato, T., Glatter, O. & Aramaki, K. Small-angle X-ray scattering (SAXS) study on nonionic fluorinated micelles in aqueous system. *J. Colloid Interface Sci.* **316**, 815–824 (2007).
 90. Sugiyama, M., Nakamura, Y. & Norisuye, T. Dilute-Solution Properties of Polystyrene Polymacromonomer Having Side Chains of over 100 Monomeric Units. *Polym. J.* **40**, 109–115 (2007).
 91. Calabrese, M. A., Rogers, S. A., Murphy, R. P. & Wagner, N. J. The rheology and microstructure of branched micelles under shear. *J. Rheol. (N. Y. N. Y.)* **59**, 1299–1328 (2015).

92. Gurnon, A. K., Lopez-Barron, C. R., Eberle, A. P. R., Porcar, L. & Wagner, N. J. Spatiotemporal stress and structure evolution in dynamically sheared polymer-like micellar solutions. *Soft Matter* **10**, 2889–98 (2014).
93. Caputo, F. E., Ugaz, V. M., Burghardt, W. R. & Berret, J.-F. Transient 1–2 plane small-angle x-ray scattering measurements of micellar orientation in aligning and tumbling nematic surfactant solutions. *J. Rheol. (N. Y. N. Y.)* **46**, 927 (2002).
94. Caputo, F. E. & Burghardt, W. R. Real-Time 1–2 Plane SAXS Measurements of Molecular Orientation in Sheared Liquid Crystalline Polymers. *Macromolecules* **34**, 6684–6694 (2001).
95. Pujari, S. *et al.* Shear-induced anisotropy of concentrated multiwalled carbon nanotube suspensions using x-ray scattering. *J. Rheol. (N. Y. N. Y.)* **55**, 1033 (2011).
96. Pujari, S. *et al.* X-ray scattering measurements of particle orientation in a sheared polymer/clay dispersion. *Rheol. Acta* **50**, 3–16 (2010).
97. Pujari, S. *et al.* Orientation dynamics in multiwalled carbon nanotube dispersions under shear flow. *J. Chem. Phys.* **130**, 214903 (2009).
98. McCready, E. M. & Burghardt, W. R. In situ SAXS studies of structural relaxation of an ordered block copolymer melt following cessation of uniaxial extensional flow. *Macromolecules* **48**, 264–271 (2015).
99. Mao, R., McCready, E. M. & Burghardt, W. R. Structural response of an ordered block copolymer melt to uniaxial extensional flow. *Soft Matter* **10**, 6198–207 (2014).
100. Kundu, S. K., Gupta, S., Stellbrink, J., Willner, L. & Richter, D. Relating structure and flow of soft colloids. *Eur. Phys. J. Spec. Top.* **222**, 2757–2772 (2013).
101. Kisilak, M. *et al.* An x-ray extensional flow cell. *Rev. Sci. Instrum.* **72**, 4305–4307 (2001).
102. Idziak, S. H. J. *et al.* Undulating membrane structure under mixed extensional-shear flow. *Eur. Phys. J. E* **6**, 139–145 (2001).
103. Alves, M. A. Design of a cross-slot flow channel for extensional viscosity measurements. *Xvth Int. Congr. Rheol. - Soc. Rheol. 80th Annu. Meet. Pts 1 2* **1027**, 240–242 (2008).
104. Haward, S. J., Oliveira, M. S. N., Alves, M. A. & McKinley, G. H. Optimized Cross-Slot Flow Geometry for Microfluidic Extensional Rheometry. *Phys. Rev. Lett.* **109**, 128301 (2012).
105. Lutz-Bueno, V., Kohlbrecher, J. & Fischer, P. Shear thickening, temporal shear oscillations, and degradation of dilute equimolar CTAB/NaSal wormlike solutions. *Rheol. Acta* **52**, 297–312 (2013).
106. Cullity, B. D. & Stock, S. R. Elements of X-ray diffraction, 3rd edition. *Prentice Hall* Chapter 1 (2001). doi:citeulike-article-id:3998040
107. Bragg, W. H. & Bragg, W. L. The Reflection of X-rays by Crystals. *Proc. R. Soc. A Math.*

- Phys. Eng. Sci.* **88**, 428–438 (1913).
108. Roe, R. J. *Methods of X-ray and neutron scattering in polymer science*. (Oxford University Press, 2002).
 109. Baltá-Calleja, F. J., . V. C. G. & Vonk, C. G. *X-ray Scattering of Synthetic Polymers*. (Elsevier, 1989). at http://books.google.com/books/about/X_ray_scattering_of_synthetic_polymers.html?id=FBvwAAAAMAAJ&pgis=1
 110. Yang, J. Viscoelastic wormlike micelles and their applications. *Curr. Opin. Colloid Interface Sci.* **7**, 276–281 (2002).
 111. Advani, S. G. & Tucker, C. L. The Use of Tensors to Describe and Predict Fiber Orientation in Short Fiber Composites. *J. Rheol. (N. Y. N. Y.)* **31**, 751–784 (1987).
 112. White, J. L. & Spruiell, J. E. The specification of orientation and its development in polymer processing. *Polym. Eng. Sci.* **23**, 247–256 (1983).
 113. Roland, C. M. *Viscoelastic Behavior of Rubbery Materials. Viscoelastic Behavior of Rubbery Materials* (2011). doi:10.1093/acprof:oso/9780199571574.001.0001
 114. Hammersley, A. THE FIT2D HOME PAGE. (2016). at <http://www.esrf.eu/computing/scientific/FIT2D/>
 115. Toby, B. H. & Von Dreele, R. B. GSAS-II : the genesis of a modern open-source all purpose crystallography software package. *J. Appl. Crystallogr.* **46**, 544–549 (2013).
 116. Rahatekar, S. S. *et al.* Optical microstructure and viscosity enhancement for an epoxy resin matrix containing multiwall carbon nanotubes. *J. Rheol. (N. Y. N. Y.)* **50**, 599–610 (2006).
 117. Ma, A. W. K., Mackley, M. R. & Chinesta, F. The microstructure and rheology of carbon nanotube suspensions. *Int. J. Mater. Form.* **1**, 75–81 (2008).
 118. Hobbie, E. K. *et al.* Optical measurements of structure and orientation in sheared carbon-nanotube suspensions. *Rev. Sci. Instrum.* **74**, 1244–1250 (2003).
 119. Hobbie, E. K. Shear rheology of carbon nanotube suspensions. *Rheol. Acta* **49**, 323–334 (2010).
 120. Chatterjee, T. & Krishnamoorti, R. Rheology of polymer carbon nanotubes composites. *Soft Matter* **9**, 9515 (2013).
 121. Yu, M. Strength and Breaking Mechanism of Multiwalled Carbon Nanotubes Under Tensile Load. *Science (80-.)* **287**, 637–640 (2000).
 122. Ma, A. W. K., Chinesta, F., Tuladhar, T. & Mackley, M. R. Filament stretching of carbon nanotube suspensions. *Rheol. Acta* **47**, 447–457 (2008).
 123. Tiwari, M. K., Bazilevsky, A. V., Yarin, A. L. & Megaridis, C. M. Elongational and shear

- rheology of carbon nanotube suspensions. *Rheol. Acta* **48**, 597–609 (2009).
124. Darsono, N., Mizunuma, H. & Obara, H. Extensional Flow of Carbon Nanotube Dispersion and Its Influence on Electrical Conductivity. *Nihon Reoroji Gakkaishi* **40**, 101–109 (2012).
 125. Dong, R.-Y. & Cao, B.-Y. Superhigh-speed unidirectional rotation of a carbon nanotube in a sheared fluid and its decoupled dynamics. *RSC Adv.* **5**, 88719–88724 (2015).
 126. Eken, A. E., Tozzi, E. J., Klingenberg, D. J. & Bauhofer, W. A simulation study on the effects of shear flow on the microstructure and electrical properties of carbon nanotube/polymer composites. *Polymer (Guildf)*. **52**, 5178–5185 (2011).
 127. Eken, A. E., Tozzi, E. J., Klingenberg, D. J. & Bauhofer, W. Combined effects of nanotube aspect ratio and shear rate on the carbon nanotube/polymer composites. *Polymer (Guildf)*. **53**, 4493–4500 (2012).
 128. Ma, W. K. A., Chinesta, F., Ammar, A. & Mackley, M. R. Rheological modeling of carbon nanotube aggregate suspensions. *J. Rheol. (N. Y. N. Y)*. **52**, 1311 (2008).
 129. Chatterjee, T., Jackson, A. & Krishnamoorti, R. Hierarchical Structure of Carbon Nanotube Networks. *J. Am. Chem. Soc.* **130**, 6934–6935 (2008).
 130. Lin-Gibson, S., Pathak, J. A., Grulke, E. A., Wang, H. & Hobbie, E. K. Elastic flow instability in nanotube suspensions. *Phys. Rev. Lett.* **92**, 048302 (2004).
 131. Karpushkin, E., Lapshina, M. & Sergeyev, V. Shear-induced structure evolution of carbon nanotubes dispersions in polyacrylonitrile–dimethylsulfoxide solution. in 040004 (2015). doi:10.1063/1.4918892
 132. Niu, R., Gong, J., Xu, D., Tang, T. & Sun, Z.-Y. Flow-induced structure and rheological properties of multiwall carbon nanotube/polydimethylsiloxane composites. *RSC Adv.* **4**, 62759–62768 (2014).
 133. Kharchenko, S. B., Douglas, J. F., Obrzut, J., Grulke, E. A. & Migler, K. B. Flow-induced properties of nanotube-filled polymer materials. *Nat. Mater.* **3**, 564–568 (2004).
 134. Hu, G., Zhao, C., Zhang, S., Yang, M. & Wang, Z. Low percolation thresholds of electrical conductivity and rheology in poly(ethylene terephthalate) through the networks of multi-walled carbon nanotubes. *Polymer (Guildf)*. **47**, 480–488 (2006).
 135. Dijkstra, D. J., Cirstea, M. & Nakamura, N. The orientational behavior of multiwall carbon nanotubes in polycarbonate in simple shear flow. *Rheol. Acta* **49**, 769–780 (2010).
 136. Schulz, S. C. & Bauhofer, W. Shear influenced network dynamics and electrical conductivity recovery in carbon nanotube/epoxy suspensions. *Polymer (Guildf)*. **51**, 5500–5505 (2010).
 137. Schulz, S. C. *et al.* Combined electrical and rheological properties of shear induced multiwall carbon nanotube agglomerates in epoxy suspensions. *Eur. Polym. J.* **47**, 2069–

- 2077 (2011).
138. Cassagnau, P. Linear viscoelasticity and dynamics of suspensions and molten polymers filled with nanoparticles of different aspect ratios. *Polymer (Guildf)*. **54**, 4762–4775 (2013).
 139. Hobbie, E. K. & Fry, D. J. Nonequilibrium Phase Diagram of Sticky Nanotube Suspensions. *Phys. Rev. Lett.* **97**, 036101 (2006).
 140. Tung, W.-S., Composto, R. J., Clarke, N. & Winey, K. I. Anisotropic Polymer Conformations in Aligned SWCNT/PS Nanocomposites. *ACS Macro Lett.* **4**, 916–920 (2015).
 141. Lindsey, C. P. & Patterson, G. D. Detailed comparison of the Williams–Watts and Cole–Davidson functions. *J. Chem. Phys.* **73**, 3348 (1980).
 142. Fuller, G. G. *Optical Rheometry of Complex Fluids*. (Oxford University Press, 1995). at <<https://global.oup.com/academic/product/optical-rheometry-of-complex-fluids-9780195097184?cc=us&lang=en>>
 143. Ma, A. W. K., Chinesta, F. & Mackley, M. R. The rheology and modeling of chemically treated carbon nanotubes suspensions. *J. Rheol. (N. Y. N. Y)*. **53**, 547 (2009).
 144. Khalkhal, F., Carreau, P. J. & Ausias, G. Effect of flow history on linear viscoelastic properties and the evolution of the structure of multiwalled carbon nanotube suspensions in an epoxy. *J. Rheol. (N. Y. N. Y)*. **55**, 153 (2011).
 145. Khalkhal, F. & Carreau, P. J. Scaling behavior of the elastic properties of non-dilute MWCNT–epoxy suspensions. *Rheol. Acta* **50**, 717–728 (2011).
 146. Yokozeki, T., Carolin Schulz, S., Buschhorn, S. T. & Schulte, K. Investigation of shear thinning behavior and microstructures of MWCNT/epoxy and CNF/epoxy suspensions under steady shear conditions. *Eur. Polym. J.* **48**, 1042–1049 (2012).
 147. White, K. L., Li, P., Sumi, Y. & Sue, H.-J. Rheology of Disentangled Multiwalled Carbon Nanotubes Dispersed in Uncured Epoxy Fluid. *J. Phys. Chem. B* **118**, 362–371 (2014).
 148. Doi, M. & Edwards, S. F. *The Theory of Polymer Dynamics. International Series of Monographs on Physics* (Clarendon Press, 1988).
 149. Larson, R. G. *The Structure and Rheology of Complex Fluids*. (Oxford UP, 1999).
 150. Johnston, D. C. Stretched exponential relaxation arising from a continuous sum of exponential decays. *Phys. Rev. B* **74**, 184430 (2006).
 151. Cueto, E. *et al.* Rheological modeling and forming process simulation of CNT nanocomposites. *Int. J. Mater. Form.* **3**, 1327–1338 (2010).
 152. Cruz, C., Illoul, L., Chinesta, F. & Régnier, G. Effects of a bent structure on the linear viscoelastic response of diluted carbon nanotube suspensions. *Rheol. Acta* **49**, 1141–1155 (2010).

153. Natale, G., Heuzey, M. C., Carreau, P. J., Ausias, G. & Férec, J. Rheological modeling of carbon nanotube suspensions with rod-rod interactions. *AIChE J.* **60**, 1476–1487 (2014).
154. Natale, G. ., Ausias, G. ., Férec, J. ., Heuzey, M. C. . & Carreau, P. J. . Modeling interactions in carbon nanotube suspensions: Transient shear flow. *J. Rheol. (N. Y. N. Y.)*. **60**, 1069–1083 (2016).
155. Ma, A. W. K., Chinesta, F., Mackley, M. R. & Ammar, A. The rheological modelling of carbon nanotube (CNT) suspensions in steady shear flows. *Int. J. Mater. Form.* **1**, 83–88 (2008).
156. Larson, R. G. in *Constitutive Equations for Polymer Melts and Solutions* 219–270 (1988). doi:10.1016/B978-0-409-90119-1.50013-0
157. Fan, Z. & Advani, S. G. Characterization of orientation state of carbon nanotubes in shear flow. *Polymer (Guildf)*. **46**, 5232–5240 (2005).
158. Iso, Y., Cohen, C. & Koch, D. L. Orientation in simple shear flow of semi-dilute fiber suspensions 2. Highly elastic fluids. *J. Nonnewton. Fluid Mech.* **62**, 135–153 (1996).
159. SCHAEFER, D. W. Polymers, Fractals, and Ceramic Materials. *Science (80-.)*. **243**, 1023–1027 (1989).
160. Ouchi, M., Takahashi, T. & Shirakashi, M. Shear-induced structure change and flow-instability in start-up Couette flow of aqueous, wormlike micelle solution. *J. Rheol. (N. Y. N. Y.)*. **50**, 341–352 (2006).
161. Dreiss, C. A. Wormlike micelles: where do we stand? Recent developments, linear rheology and scattering techniques. *Soft Matter* **3**, 956 (2007).
162. Berret, J.-F. Rheology of Wormlike Micelles : Equilibrium Properties and Shear Banding Transition. (2004). at <<http://arxiv.org/abs/cond-mat/0406681>>
163. Cates, M. E. Reptation of Living Polymers - Dynamics of Entangled Polymers in the Presence of Reversible Chain-Scission Reactions. *Macromolecules* **20**, 2289–2296 (1987).
164. Cates, M. E. & Candau, S. J. Statics and Dynamics of Worm-Like Surfactant Micelles. *J. Physics-Condensed Matter* **2**, 6869–6892 (1990).
165. Müller, A. J., Torres, M. F. & Sáez, A. E. Effect of the Flow Field on the Rheological Behavior of Aqueous Cetyltrimethylammonium p -Toluenesulfonate Solutions. *Langmuir* **20**, 3838–3841 (2004).
166. Kadoma, I. A., Ylitalo, C., VanEgmond, J. W. & Egmond, J. W. Structural transitions in wormlike micelles. *Rheol. Acta* **36**, 1–12 (1997).
167. Moss, G. R. & Rothstein, J. P. Flow of wormlike micelle solutions past a confined circular cylinder. *J. Nonnewton. Fluid Mech.* **165**, 1505–1515 (2010).
168. Fischer, P. & Rehage, H. Non-linear flow properties of viscoelastic surfactant solutions. *Rheol. Acta* **36**, 13–27 (1997).

169. Hu, Y. T. & Lips, A. Kinetics and mechanism of shear banding in an entangled micellar solution. *J. Rheol. (N. Y. N. Y.)* **49**, 1001–1027 (2005).
170. Decruppe, J. P., Lerouge, S. & Berret, J. F. Insight in shear banding under transient flow. *Phys. Rev. E* **63**, 022501 (2001).
171. Thareja, P. *et al.* Shear-induced phase separation (SIPS) with shear banding in solutions of cationic surfactant and salt. *J. Rheol. (N. Y. N. Y.)* **55**, 1375–1397 (2011).
172. Britton, M. M. & Callaghan, P. T. Shear banding instability in wormlike micellar solutions. *Eur. Phys. J. B* **7**, 237–249 (1999).
173. Cressely, R. & Hartmann, V. Rheological behaviour and shear thickening exhibited by aqueous CTAB micellar solutions. *Eur. Phys. J. B* **6**, 57–62 (1998).
174. Vasudevan, M., Shen, A., Khomami, B. & Sureshkumar, R. Self-similar shear thickening behavior in CTAB/NaSal surfactant solutions. *J. Rheol. (N. Y. N. Y.)* **52**, 527–550 (2008).
175. Liu, C. H. & Pine, D. J. Shear-induced gelation and fracture in micellar solutions. *Phys. Rev. Lett.* **77**, 2121–2124 (1996).
176. Hu, Y. T., Boltenhagen, P. & Pine, D. J. Shear thickening in low-concentration solutions of wormlike micelles. I. Direct visualization of transient behavior and phase transitions. *J. Rheol. (N. Y. N. Y.)* **42**, 1185–1208 (1998).
177. Oda, R. *et al.* Time-Resolved Small-Angle Neutron Scattering Study of Shear-Thickening Surfactant Solutions after the Cessation of Flow. *Langmuir* **16**, 4859–4863 (2000).
178. Prud'homme, R. K. & Warr, G. G. Elongational Flow of Solutions of Rodlike Micelles. *Langmuir* **10**, 3419–3426 (1994).
179. Bhardwaj, A., Miller, E. & Rothstein, J. P. Filament stretching and capillary breakup extensional rheometry measurements of viscoelastic wormlike micelle solutions. *J. Rheol. (N. Y. N. Y.)* **51**, 693–719 (2007).
180. Kim, W.-J. & Yang, S.-M. Effects of Sodium Salicylate on the Microstructure of an Aqueous Micellar Solution and Its Rheological Responses. *J. Colloid Interface Sci.* **232**, 225–234 (2000).
181. Kato, M., Takahashi, T. & Shirakashi, M. Steady Planar Elongational Viscosity of CTAB/NaSal Aqueous Solutions Measured in a 4-Roll Mill Flow Cell. *Nihon Reoroji Gakkaishi* **30**, 283–287 (2002).
182. Chellamuthu, M. & Rothstein, J. P. Distinguishing between linear and branched wormlike micelle solutions using extensional rheology measurements. *J. Rheol. (N. Y. N. Y.)* **52**, 865 (2008).
183. Wheeler, E. K., Izu, P. & Fuller, G. G. Structure and rheology of wormlike micelles. *Rheol. Acta* **35**, 139–149 (1996).
184. Weston, J. S. *et al.* Simultaneous slit rheometry and in situ neutron scattering. *Rheol. Acta*

- 57, 241–250 (2018).
185. Wang, S.-Q., Hu, Y. & Jamieson, A. M. in *Structure and Flow in Surfactant Solutions* **578**, 278–287 (1994).
 186. Dehmoune, J., Decruppe, J. P., Greffier, O., Xu, H. & Lindner, P. Shear Thickening in Three Surfactants of the Alkyl Family C_nTAB: Small Angle Neutron Scattering and Rheological Study. *Langmuir* **25**, 7271–7278 (2009).
 187. Lerouge, S., Decruppe, J. P. & Humbert, C. Shear Banding in a Micellar Solution under Transient Flow. *Phys. Rev. Lett.* **81**, 5457–5460 (1998).
 188. Chen, S. & Rothstein, J. P. Flow of a wormlike micelle solution past a falling sphere. *J. Nonnewton. Fluid Mech.* **116**, 205–234 (2004).
 189. Azzouzi, H., Decruppe, J. P., Lerouge, S. & Greffier, O. Temporal oscillations of the shear stress and scattered light in a shear-banding-shear-thickening micellar solution. *Eur. Phys. J. E* **17**, 507–514 (2005).
 190. Shikata, T., Hirata, H., Takatori, E. & Osaki, K. Nonlinear Viscoelastic Behavior of Aqueous Detergent Solutions. *J. Nonnewton. Fluid Mech.* **28**, 171–182 (1988).
 191. Poole, R., Alves, M. & Oliveira, P. Purely Elastic Flow Asymmetries. *Phys. Rev. Lett.* **99**, 164503 (2007).
 192. Rocha, G. N., Poole, R. J., Alves, M. A. & Oliveira, P. J. On extensibility effects in the cross-slot flow bifurcation. *J. Nonnewton. Fluid Mech.* **156**, 58–69 (2009).
 193. Soltero, J. F. A. *et al.* Rheological behavior in the didodecyldimethylammonium bromide/water system. *Colloid Polym. Sci.* **278**, 37–47 (2000).
 194. Partal, P. *et al.* Rheology and Microstructural Transitions in the Lamellar Phase of a Cationic Surfactant. *Langmuir* **17**, 1331–1337 (2001).
 195. Sierro, P. & Roux, D. Structure of a Lyotropic Lamellar Phase under Shear. *Phys. Rev. Lett.* **78**, 1496–1499 (1997).
 196. Martin, H. P. *et al.* Complex fluids under microflow probed by SAXS: rapid microfabrication and analysis. *J. Phys. Conf. Ser.* **247**, 012050 (2010).
 197. Panizza, P., Colin, A., Coulon, C. & Roux, D. A dynamic study of onion phases under shear flow: size changes. *Eur. Phys. J. B* **4**, 65–74 (1998).
 198. Berni, M. A review of the rheology of the lamellar phase in surfactant systems. *Adv. Colloid Interface Sci.* **98**, 217–243 (2002).
 199. Mortensen, K. Structural studies of lamellar surfactant systems under shear. *Curr. Opin. Colloid Interface Sci.* **6**, 140–145 (2001).
 200. Dubois, M. & Zemb, T. Phase behavior and scattering of double-chain surfactants in diluted aqueous solutions. *Langmuir* **7**, 1352–1360 (1991).

201. Yang, H., Wang, J., Yang, S. & Zhang, W. Aggregate Conformation and Rheological Properties of Didodecyldimethylammonium Bromide in Aqueous Solution. *J. Dispers. Sci. Technol.* **31**, 650–653 (2010).
202. Syringe Warmers and Accessories. at <https://www.harvardapparatus.com/electrophysiology/temperature-control/syringe-warmers-and-accessories.html>
203. Council, A. C. U. S. *Resin Production & Sales*. (2018). at <https://plastics.americanchemistry.com/Plastics-Statistics/ACC-PIPS-Year-End-2017-Resin-Stats-vs-2016.pdf>
204. Lamberti, G. Flow induced crystallisation of polymers. *Chem. Soc. Rev.* **43**, 2240–2252 (2014).
205. Hoffman, J. D., Davis, G. T. & Lauritzen, Jr., J. I. in *Treatise on Solid State Chemistry Volume 3 Crystalline and Noncrystalline Solids* (ed. N. Hannay) XVI, 774 (Springer US, 1976). doi:10.1007/978-1-4684-2664-9
206. Sidelman, N., Rosenberg, Y. & Richter, S. Peptide-based spherulitic films—formation and properties. *J. Colloid Interface Sci.* **343**, 387–391 (2010).
207. Ehrenstein, G. W. *Polymeric Materials: Structure, Properties, Applications*. (Carl Hanser Verlag GmbH & Co, 2001).
208. Stephen Lower. *Polymers and Plastics*. (2018). at [https://chem.libretexts.org/Textbook_Maps/General_Chemistry/Book%3A_Chem1_\(Lower\)/07%3A_Solids_and_Liquids/7.09%3A_Polymers_and_Plastics](https://chem.libretexts.org/Textbook_Maps/General_Chemistry/Book%3A_Chem1_(Lower)/07%3A_Solids_and_Liquids/7.09%3A_Polymers_and_Plastics)
209. Janeschitz-Kriegl, H. & Ratajski, E. Some fundamental aspects of the kinetics of flow-induced crystallization of polymers. *Colloid Polym. Sci.* **288**, 1525–1537 (2010).
210. van Meerveld, J., Peters, G. W. M. & Hütter, M. Towards a rheological classification of flow induced crystallization experiments of polymer melts. *Rheol. Acta* **44**, 119–134 (2004).
211. Pennings, A. J., Mark, J. M. A. A. & Kiel, A. M. Hydrodynamically induced crystallization of polymers from solution. *Kolloid-Zeitschrift Zeitschrift für Polym.* **237**, 336–358 (1970).
212. Hsiao, B. S., Yang, L., Somani, R. H., Avila-Orta, C. A. & Zhu, L. Unexpected Shish-Kebab Structure in a Sheared Polyethylene Melt. *Phys. Rev. Lett.* **94**, 117802 (2005).
213. Matsuba, G., Kaji, K., Nishida, K., Kanaya, T. & Imai, M. Conformational Change and Orientation Fluctuations Prior to the Crystallization of Syndiotactic Polystyrene. *Macromolecules* **32**, 8932–8937 (1999).
214. Lamberti, G. & Brucato, V. Real-time orientation and crystallinity measurements during the isotactic polypropylene film-casting process. *J. Polym. Sci. Part B Polym. Phys.* **41**, 998–1008 (2003).

215. Su, F. *et al.* Coupling of Multiscale Orderings during Flow-Induced Crystallization of Isotactic Polypropylene. *Macromolecules* **50**, 1991–1997 (2017).
216. Kumaraswamy, G., Kornfield, J. A., Yeh, F. J. & Hsiao, B. S. Shear-enhanced crystallization in isotactic polypropylene. 3. Evidence for a kinetic pathway to nucleation. *Macromolecules* **35**, 1762–1769 (2002).
217. Fernandez-Ballester, L. *et al.* Simultaneous birefringence, small- and wide-angle X-ray scattering to detect precursors and characterize morphology development during flow-induced crystallization of polymers. *J. Synchrotron Radiat.* **15**, 185–190 (2008).
218. Okada, T., Saito, H. & Inoue, T. Time-resolved light scattering studies on the early stage of crystallization in isotactic polypropylene. *Macromolecules* **25**, 1908–1911 (1992).
219. Pogodina, N. V., Siddiquee, S. K., van Egmond, J. W. & Winter, H. H. Correlation of Rheology and Light Scattering in Isotactic Polypropylene during Early Stages of Crystallization. *Macromolecules* **32**, 1167–1174 (1999).
220. Fukushima, H., Ogino, Y., Matsuba, G., Nishida, K. & Kanaya, T. Crystallization of polyethylene under shear flow as studied by time resolved depolarized light scattering. Effects of shear rate and shear strain. *Polymer (Guildf)*. **46**, 1878–1885 (2005).
221. Keum, J. K. *et al.* in *Scattering Methods and the Properties of Polymer Materials* **130**, 114–126 (Springer Berlin Heidelberg, 2005).
222. van Drongelen, M., Roozmond, P. C. & Peters, G. W. M. in 207–242 (Springer, Cham, 2016). doi:10.1007/12_2015_344
223. Kornfield, J. A., Kumaraswamy, G. & Issaian, A. M. Recent Advances in Understanding Flow Effects on Polymer Crystallization. *Ind. Eng. Chem. Res.* **41**, 6383–6392 (2002).
224. Hadinata, C., Gabriel, C., Ruellman, M. & Laun, H. M. Comparison of shear-induced crystallization behavior of PB-1 samples with different molecular weight distribution. *J. Rheol. (N. Y. N. Y)*. **49**, 327–349 (2005).
225. Liu, Y. *et al.* Extensional rheometer for in situ x-ray scattering study on flow-induced crystallization of polymer. *Rev. Sci. Instrum.* **82**, 045104 (2011).
226. Ma, Z., Balzano, L., van Erp, T., Portale, G. & Peters, G. W. M. Short-Term Flow Induced Crystallization in Isotactic Polypropylene: How Short Is Short? *Macromolecules* **46**, 9249–9258 (2013).
227. Roozmond, P. C., Janssens, V., Van Puyvelde, P. & Peters, G. W. M. Suspension-like hardening behavior of HDPE and time-hardening superposition. *Rheol. Acta* **51**, 97–109 (2012).
228. Luciani, L., Seppälä, J. & Löfgren, B. Poly-1-butene: Its preparation, properties and challenges. *Prog. Polym. Sci.* **13**, 37–62 (1988).
229. Ugaz, V. M. & Burghardt, W. R. In Situ X-ray Scattering Study of a Model Thermotropic

- Copolyester under Shear: Evidence and Consequences of Flow-Aligning Behavior. *Macromolecules* **31**, 8474–8484 (1998).
230. L. Heeley, E. *et al.* Shear-induced crystallization of polyethylene studied by small- and wide-angle X-ray scattering (SAXS/WAXS) techniques. *PhysChemComm* **5**, 158 (2002).
231. Matsuba, G. *et al.* In situ small-angle X-ray and neutron scattering measurements on a blend of deuterated and hydrogenated polyethylenes during uniaxial drawing. *Polym. J.* **45**, 293–299 (2012).
232. Terrill, N. J. *et al.* Density fluctuations: The nucleation event in isotactic polypropylene crystallization. *Polymer (Guildf)*. **39**, 2381–2385 (1998).
233. Wang, Z.-G., Hsiao, B. S., Sirota, E. B. & Srinivas, S. A simultaneous small- and wide-angle X-ray scattering study of the early stages of melt crystallization in polyethylene. *Polymer (Guildf)*. **41**, 8825–8832 (2000).
234. Somani, R. H. *et al.* Structure Development during Shear Flow Induced Crystallization of i-PP: In Situ Wide-Angle X-ray Diffraction Study. *Macromolecules* **34**, 5902–5909 (2001).
235. Mao, Y. *et al.* Wide-Angle X-ray Scattering Study on Shear-Induced Crystallization of Propylene-1-Butylene Random Copolymer: Experiment and Diffraction Pattern Simulation. *Macromolecules* **44**, 558–565 (2011).
236. Somani, R. H. *et al.* Structure Development during Shear Flow-Induced Crystallization of i-PP: In-Situ Small-Angle X-ray Scattering Study. *Macromolecules* **33**, 9385–9394 (2000).
237. Hermans, J. J., Hermans, P. H., Vermaas, D. & Weidinger, A. Quantitative evaluation of orientation in cellulose fibres from the X-ray fibre diagram. *Recl. des Trav. Chim. des Pays-Bas* **65**, 427–447 (1946).
238. Mitchell, G. R. & Windle, A. H. in *Developments in Crystalline Polymers* 115–175 (Springer Netherlands, 1988). doi:10.1007/978-94-009-1341-7_3
239. Burger, C., Hsiao, B. S. & Chu, B. Preferred Orientation in Polymer Fiber Scattering. *Polym. Rev.* **50**, 91–111 (2010).
240. Shao, H., Jiang, D., Zhang, M., Yao, W. & Huang, B. Characterization of the polymorphic transformation of poly(1-butene) based on FTIR and mechanical properties. *J. Polym. Res.* **19**, 9919 (2012).
241. Eder, G., Janeschitz-Kriegl, H. & Liedauer, S. in *Solidification Processes in Polymers* 129–131 (Steinkopff, 1992). doi:10.1007/BFb0115587